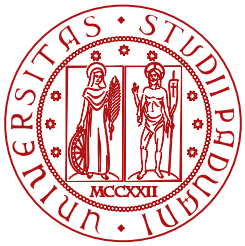

Università degli studi di Padova

Dipartimento di Fisica e Astronomia “Galileo Galilei”

---

Philosophiae Doctoral Course in Physics

Cycle XXXVI

# Study of the reconstruction of $\nu_\mu$CC QE events from the Booster Neutrino Beam with the ICARUS detector

Thesis written with the financial support of the European Union
Horizon 2020 Programme, Marie Skłodowska-Curie Actions (MSCA)

Coordinator:

**Prof. Giulio Monaco**

Supervisor:

**Prof. Daniele Gibin**

Ph.D. Candidate:

**Maria Artero Pons**

Academic Year 2022/2023

*A Simone,*
*i a la meva família.*

# Abstract

Liquid Argon Time Projection Chamber (LArTPC) detectors offer charged particle imaging capabilities with impressive spatial resolution. Precise event reconstruction procedures are mandatory to fully exploit the potential of this technology. The Short Baseline Neutrino program (SBN) makes use of this novel technology to carry out sensitive searches for new physics of neutrinos at the GeV energy scale. ICARUS is the far detector of the program, located at 600 m from the Booster Neutrino Beam (BNB) target and operating at a shallow depth. Recent results from the Neutrino-4 experiment at a Russian nuclear reactor have claimed a $\bar{\nu}_e$ oscillation signature at short baseline, thus the early phase of ICARUS is intended to test the Neutrino-4 oscillation hypothesis by studying the $\nu_\mu$ disappearance channel with the BNB beam. In this thesis a validation of the ICARUS detector and reconstruction algorithms performance is presented along with a proposed automatic selection to identify simple event topologies towards a final BNB $\nu_\mu$ disappearance analysis. Visual selected neutrinos were initially used to assess the reconstruction performance and demonstrate ICARUS' capability to carry out precise calorimetric studies, particle identification and complete kinematic reconstruction of $\nu_\mu$ CC quasi-elastic interactions. With the additional input of simulated events, the automatic selection procedure to identify neutrino interactions with exactly two particles in the final state, one muon and one proton ($1\mu 1$p), was developed and optimized. A detailed evaluation of the proposed selection is presented indicating that a distorted $\nu_\mu$ survival probability should be visible in the presence of sterile neutrinos. A final data-simulation comparison with a limited statistics dataset is presented showing promising results towards a final analysis with full statistics and systematic uncertainties.

# Acknowledgments

First of all, I would like to express my deepest gratitude to my supervisor, Daniele Gibin who trusted me since the very first moment and consistently exhibited enthusiasm in discussing new results while patiently addressing my countless questions. Your advice and guidance has been essential throughout this work.

I also wish to express my sincere appreciation to Christian Farnese, who proved to be my lifesaver every time things did not work (which occurred quite frequently) and made all my travels more exciting. Additionally, I want to convey my heartfelt thanks to Alberto Guglielmi, whose leadership has helped create an incredible research group and who made me feel like one of them from the very beginning. My gratitude also extends to Filippo Varanini, Riccardo Triozzi and Magda Cicerchia who were always accessible, generously sharing their knowledge and expertise.

Furthermore, I had the privilege of collaborating with amazing members of ICARUS, who, in various ways, facilitated my integration into the system, enabling me to make my modest contribution to this huge and remarkable effort. A special acknowledgment goes to Simone Donati, who provided me with the opportunity to join INTENSE, allowing me to enjoy this journey even more.

También quiero dar las gracias a Fermi Güell por ser la primera persona en hacerme descubrir la pasión por la física y ayudarme a emprender este apasionante viaje. A Clara Cuesta y a Carmen Palomares, gracias por ayudarme a construir los peldaños que me han llevado hasta aquí.

A mis dos mejores compis de aventuras, Bea y Paula, esto también es gracias a vosotras. Os debo mi felicidad durante los años de univeridad y mis mejores recuerdos de verano.

A toda mi familia, que me han apoyado en todo momento y han sabido ayudarme en cada ocasión. Mama, papa, Marc, os estoy eternamente agradecida, gracias por vuestro apoyo incondicional y por haberme escuchado siempre, incluso cuando explicaba mis estudios y os parecía chino. Y en especial a mi abuela, que se fue antes de que empezara esta aventura y, aún estando orgullosa, estoy segura de que me hubiera dicho que cerca de casa también tenía que haber oportunidades.

E infine, a te, Simone, che sei diventato la mia casa e mi hai insegnato tante cose... Hai reso questi tre anni incredibili e niente di tutto questo sarebbe stato possibile senza di te. Grazie, per **tutto**.

# Contents

# Chapter 1

# Introduction

The formulation of the Standard Model (SM) of particle physics has been of great scientific success, receiving important theoretical and experimental contributions over the last 60 years. In the SM, neutrinos belong to the lepton family and come in three flavours: electron neutrinos, muon neutrinos and tau neutrinos. They are omnipresent and particularly intriguing, being one of the most abundant particles in the universe but also one of the least understood. This is mainly because they are neutral and interact only through the weak force with the other particles, making their detection and study challenging. A lot of interest was raised after the Nobel discovery of neutrino oscillation: the phenomenon implies not only that the three neutrinos change their flavour when traveling but also that they are massive, contrary to the predictions of the SM. Knowing more about neutrino oscillation could help answer fundamental questions, which are currently open. One such mystery relates to the number of neutrino species. While not contained in the minimal SM version, a variety of experimental results have suggested that additional neutrino flavours, with quite different properties, could exist.

Anomalies from accelerator experiments (LSND and MiniBooNE), reactors and radioactive sources have been reported in the last 20 years, unable to fit inside the 3-flavour oscillation scheme. These results suggest the existence of a new sterile neutrino state, characterized by an eV-scale mass state and by a small mixing to the active flavours, that would drive short-distance oscillations. Recent results from the reactor Neutrino-4 collaboration have also shown a hint of an oscillatory signature which could be associated with sterile neutrinos. The existing anomalies are currently under investigation by dedicated neutrino oscillation experiments, providing exciting yet partially contradictory results on the active-sterile scenario. Thus, a coherent general description is far from being complete.

The Short Baseline Neutrino (SBN) program based at Fermilab, is designed to address the possible existence of eV mass-scale sterile neutrinos in both appearance and disappearance channels. It consists of large Liquid Argon Time Projection Chambers (LArTPCs) sitting along the Booster Neutrino Beam (BNB), where near and far detector locations have been optimized to achieve world-leading sensitivity. The joint effort will enable the coverage of the full LSND 99% C.L allowed region at $\sim 5\sigma$ studying the $\nu_e$ appearance, while at the same time performing a sensitive search in the $\nu_\mu$ disappearance channel. Neutrino spectra are virtually identical for the near and far detectors, as are the interaction cross sections, consequently the associated systematic uncertainties are expected to cancel out in the near-far comparison. Furthermore, given the same detection technology, many detector systematic uncertainties nearly cancel out as well, when comparing the measurements at both locations. On top of that, the superb detector capabilities of the LArTPC technology, allow a unique identification and reconstruction of neutrino interactions together with an efficient rejection of background events, particularly from neutral current interactions.

ICARUS is the far detector of the program, located at 600 m from the Booster target. In addition to the BNB neutrinos, ICARUS is also exposed $\sim 6^\circ$ off-axis to the higher energy

Neutrinos from the Main Injector (NuMI) beam, which has an enriched component of $\nu_e$. The analysis of these events will provide an independent cross check to the BNB oscillation results and neutrino-argon cross-sections measurements crucial for oscillation analysis and systematic constraints, in view of the future long baseline experiments.

While the near detector is preparing to start physics operation, ICARUS-standalone phase is addressed to test the recent Neutrino-4 oscillation claim exploiting its $\sim$ mm 3D reconstruction and excellent calorimetric capabilities. The Neutrino-4 oscillation-like signal for $\bar{\nu}_e$ events can be initially investigated in ICARUS with the BNB searching for the $\nu_\mu$ disappearance as a function of the neutrino energy. Analogous more direct searches for $\nu_e$ disappearance using the NuMI beam will follow. This thesis focuses on this first goal, studying the selection and reconstruction of $\nu_\mu$ charged current interactions. As a first step, studies have been performed on contained events with a simple topology: a single muon and a single proton in the final state. Several analyses were carried out to demonstrate the particle identification tool performance and the capability to fully reconstruct events with a set of visually scanned neutrinos. The experience gained was used to develop a robust strategy to automatically select a pure sample of well-reconstructed neutrino event topology. As a result, a possible selection is presented together with a preliminary comparison with real data.

The organization of this work is as follows:

Chapter 2 describes the history of neutrino physics, providing a general overview with special emphasis on the neutrino mixing and oscillation phenomenon. The current experimental status of neutrino oscillations is presented, along with the anomalies that have led to the hypothesis of new neutrino states.

An overview of the Short Baseline Neutrino program is given in Chapter 3, describing both the neutrino beams and the novel LArTPC technology principle. A description of each detector with its common and unique characteristics is also provided here.

Chapter 4 focuses on the ICARUS detector, its previous underground operation and the initial results on its present performance. An up-to-date report of the ICARUS and SBN program situation is given at the end of the chapter.

A specific description of how event reconstruction takes place in ICARUS is presented in Chapter 5, where some details about the signal processing chain are given. Fundamental concepts such as particle identification or neutrino energy reconstruction are exposed here in view of the performed neutrino analysis.

The final neutrino event selection approach is described in detail in Chapter 6, illustrating all the previous studies to optimize the selection. These benefited from a sample of visually selected events, which turned out to be crucial to define the ideal selection cuts. Finally, the purity and efficiency of the proposed selection are reported, along with a neutrino data validation.

Appendix A offers some calibration studies I performed at the early ICARUS phase, including the evaluation of containment conditions, a possible wire TPC equalization strategy and the measurement of the flatness of the central cathode.

# Chapter 2

# The Physics of Neutrinos

Neutrinos are elementary particles described by the Standard Model of particle physics and the second most abundant particles in the universe after photons. The neutrino is so named because it is electrically neutral (neutr-) and its rest mass is so small (-ino) that it was long thought to be zero. Neutrinos only interact via the weak and gravitational force, and cannot undergo electromagnetic or strong interactions. As it is well known the weak force has a very short range, while gravitational interaction is extremely weak due to the mass of the neutrino. Thus, they typically pass through normal matter unaffected, making its detection and study challenging.

## 2.1 Neutrinos in a nutshell

The history of neutrinos begins in 1914 when $\beta$-decay was studied by James Chadwick [1]. Experimental results showed that the emitted electron had a continuous energy spectrum, unlike the $\alpha$ and $\gamma$ decays, where a mono-energetic spectrum was observed. On the other hand, if the well-understood law of energy conservation had to be fulfilled, such a spectrum was expected to be a delta peak at the kinetic energy of the outgoing electron. This unexpected result presented a severe crisis in physics as it could have hinted at a violation of energy conservation law. To restore that equilibrium, Wolfgang Pauli proposed in 1930 the existence of a new neutral and very light fermion that was also emitted in beta decay along with the electron [2]; giving a possible explanation to the observed continuous energy spectrum.

Enrico Fermi named Pauli's particle *neutrino*, meaning 'little neutral one', as *neutron* was already taken after its discovery in 1932.

In 1933 and based on Pauli's hypothesis, Fermi proposed a theory of $\beta$ decay as a four-fermion point interaction, which involved a neutron decaying to a proton, to produce an electron and a neutrino [3]. Fermi's theory was also able to explain the shape of the observed $\beta$ spectrum. The close agreement between theoretical prediction and experimental data led to the acceptance of the neutrino hypothesis, even though neutrinos had not been explicitly seen. Bethe and Peierls attempted to define a neutrino interaction cross-section using the assumptions required by Fermi's $\beta$-theory and concluded that, if these assumptions held true, its interaction was too weak for a neutrino to ever be observed [4].

26 years passed before any evidence of neutrinos was found experimentally. During that time a lot of work was done to build the theoretical framework and determine possible ways to observe what appeared to be an 'undetectable' particle. The problem of the low neutrino interaction cross section was solved using a large flux of $\nu$ produced by a nuclear reactor and the invention of a novel detection technique. This synergy led to the discovery of the neutrino by Reines and Cowan, in their experiment at the Savanah River Plant in South Carolina [5]. They had previously indicated that these particles had been found in 1953 through the detection of positrons and neutrons following fission-fragment decay in large reactor experiment. However, the reactor-induced and cosmic backgrounds were too large to be confident in the results obtained [6]. As

a consequence, the experiment was updated to incorporate significant background mitigation techniques, such as moving the experiment underground.
In 1956 Reines and Cowan were finally able to announce the discovery of the *neutrino* [5]. They measured the positron and the neutron resulting from the interaction of a neutrino (in reality an anti-neutrino) with a proton. The so-called inverse beta decay (IBD) process:

$$\bar{\nu} + p \longrightarrow n + e^{+} \ . \tag{2.1}$$

Reines and Cowan's experiment used a nuclear reactor as a neutrino source. The idea was to build a large detector filled with liquid scintillator loaded with Cd to increase the probability of capturing a neutron. In the IBD, the positron undergoes matter–antimatter annihilation yielding a prompt flash of light, while the neutron is radioactively captured on Cd producing a delayed light. The timing and spatial coincidence between the prompt light and delayed neutron capture, few $\mu$s later, provides a powerful means to discriminate the neutrino signature of the inverse beta decay from background noise. To exploit that characteristic signature, the detector was composed of two tanks of water, surrounded by liquid scintillator to detect the light. The rate of neutrino events was compared to the reactor-based background, resulting in a signal rate 20 times higher than expected, which allowed Reines and Cowan to claim the discovery.
During the years preceding the discovery of the neutrino, the muon was also discovered [7]. In 1959 Bruno Pontecorvo took under examination the nature of neutrinos, wondering whether neutrinos produced alongside electrons were the same as those produced with muons. Does $\nu_e = \nu_\mu$ or $\nu_e \neq \nu_\mu$? [8]
Lower than expected experimental limits were set on the process $\mu \longrightarrow e + \gamma$, suggesting the conservation of the family lepton number and the expectation that the process $\nu_\mu + n \longrightarrow p + e^{-}$ was forbidden. Therefore if neutrinos produced together with muons cannot induce electrons when interacting, $\nu_\mu$ and $\nu_e$ had to be different particles.
In 1962 the muon neutrino was discovered at the Brookhaven National Laboratory [9], confirming that more than one type of neutrino exists. In their experiment Leon Lederman, Melvin Schwartz and Jack Steinberger used a beam of neutrinos created from the in-flight decay of pions and kaons. The muon neutrino interaction products were detected in a spark chamber where the topological signature of outgoing muons was distinguished from that of electrons. If more types of neutrinos existed, only muons were expected to be observed; otherwise $\nu_\mu = \nu_e$ would produce equal rates of outgoing muons and electrons. A clear predominance of single muon events was found in data, leading to the conclusion that another type of neutrino existed.
When the tau lepton was discovered in 1975, it was natural to think that a third type of neutrino coupled to lepton could exist. The neutrino family was enlarged in 2001, when the DONUT experiment observed the tau neutrino [10]. Accelerated protons were used to produce charmed mesons which subsequently decayed into tau neutrinos. To eliminate as many unwanted background particles as possible, a system of strong magnets and shielding were used to filter out essentially all particles except the neutrinos. The beam would then pass through several sheets of nuclear emulsion and in very rare occasion, a tau neutrino would interact with an iron nucleus from the iron plates sandwiched with layers of emulsion. The products of the collision would be a shower of particles including an observable tau particle. These electrically charge particles would leave visible tracks in the emulsion and could be electronically registered by a system of scintillators and drift chambers.

DONUT experiment photographically developed the emulsion sheets in order to connect all the traces left in the planes and reconstruct the path of each particle to subsequently identify neutrino interactions. Their characteristic properties were the sudden appearance of several particles without any track leading up to them. Furthermore, the smoking gun signature of a tau neutrino was a track showing a king after few millimeters, indicating the decay of a tau lepton. Four tau particle events were unambiguously observed in DONUT experiment, with a significant low probability of coming from background sources, and thus allowing the collaboration to prove the existence of the tau neutrino.

Around 1990 the ALEPH detector at the Large Electron Positron (LEP) collider ruled out the possibility of there being a fourth active neutrino flavour. The experiment measured the invisible width of the Z boson, $Z \longrightarrow \nu\bar{\nu}$, strongly restricting the number of active neutrinos to 3 [11]. The most up to date limit comes from the combination of all LEP experiments, reporting the following value

$$N_\nu = \frac{\Gamma_{inv}}{\Gamma_{\nu\bar{\nu}}} = 2.984 \pm 0.008 \; . \tag{2.2}$$

This restriction is within the Standard Model benchmark, so there is no prohibition for additional neutrinos to exist as long as they do not participate in standard model interactions. These hypothetical particles are often called *sterile* neutrinos and so far, no unequivocal experimental evidence has been found.

In 1957 Pontecorvo proposed for the first time the possibility that neutrinos changed their flavour while travelling in vacuum or trough matter. This idea aroused from an analogy with the $K^0 \longleftrightarrow \overline{K}^0$ oscillations [12], so his concept was presented as neutrino oscillations, $\nu \longleftrightarrow \bar{\nu}$. Following the discovery of the muon neutrino, in 1969 he expanded his proposal of neutrino oscillations to include the transition between the known flavours ($\nu_e$ and $\nu_\mu$).

After the brief introduction of all the involved pieces, it is interesting to discuss a series of experiments that from 1968 to 2002 led to the discovery of the mechanism of neutrino oscillations.

## 2.2 First hints of neutrino oscillation

### 2.2.1 Solar neutrino problem

The Standard Solar Model (SSM) predicts a certain electron neutrino flux [13], due to the fusion reactions occurring in the sun. The solar neutrino production and the flux for each reaction as a function of the neutrino energy described by the SSM are shown in the following Figure 2.1.

In 1968, Ray Davis, Don Harmer and Kenneth Hoffman carried out the first experiment to detect solar neutrinos to verify the SSM [15]. The Homestake detector contained 615 tons of perchlorethylene ($C_2Cl_4$) located 1478 m underground in the Homestake gold mine in South Dakota. A radiochemical procedure based on the inverse $\beta$-decay reaction was used,

$$\nu_e + {}^{37}Cl \longrightarrow {}^{37}Ar + e^- \; . \tag{2.3}$$

The ${}^{37}Ar$ produced by neutrino capture on stable ${}^{37}Cl$, decays by electron capture back to ${}^{37}Cl$ with a half-life of 35 days. The proposed reaction has a threshold of 0.814 MeV, hence Homestake was only sensitive to solar electron neutrinos from the *pep* reaction and those emitted by the decay of ${}^{7}Be$ and the high energy component of ${}^{8}B$. On the other hand, it was transparent to other neutrino flavours as discussed below.

The ${}^{37}Ar$ activity produced by $\nu_e$ was removed by purging with helium gas. The recovered Ar was purified by gas chromatography and transferred into a proportional counter. The purification procedure was an extremely important step, since it was mandatory to remove all the impurities that might have entered during the various manufacturing, storage and transfer operations and that could compromise the measurement. The sample for each run, of approximately 3 months, was assayed for almost twelve ${}^{37}Ar$ half-lives and a maximum likelihood fit was used to resolve the ${}^{37}Ar$ decays from the counter background.

Surprisingly, the events seen by the experiment were only about a third of the predicted number by the SSM. This is usually referred to as the *solar neutrino problem*. The results indicated some good news, as the reaction in Eq. 2.3 was indeed taking place, but also some bad news, as there was a factor three discrepancy between experimental observation and theoretical calculation [16]. At that moment, there were three possible resolutions to the discrepancy; there was a theoretical overestimation in the calculation of neutrino production by a factor of three; something happened to the neutrinos as they travelled from the sun to the earth; or all neutrinos

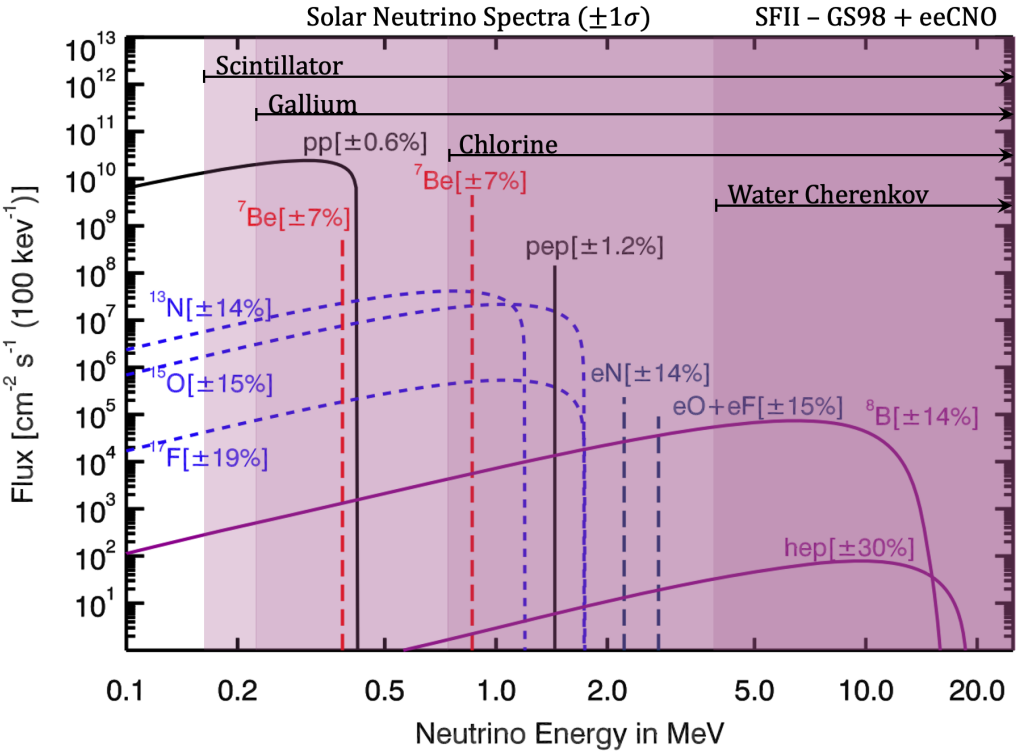


Figure 2.1: Spectrum of solar neutrino fluxes predicted by SSM. Fluxes produced by the electron capture in $^{13}N$, $^{15}O$ and $^{17}F$, often known as ecCNO neutrinos, have been added. Solid lines represent neutrinos from the pp chain while the dashed ones are for neutrinos from the CNO cycle. Picture taken from Ref. [14] and modified to include sensitivity of various experimental approaches.

reached the earth but the detector was inefficient in detecting all of them. The third option was soon ruled out by calibrating the detector with an intense source of neutrinos. The first one was also disregarded as the modelling of the sun improved, largely reducing the uncertainties which could not explain anymore the deficit. Physicist were forced to accept that some aspect of neutrino propagation between the sun and the earth was responsible for the shortfall in recorded events.

The neutrino oscillation proposal was not widely accepted for two reasons. Firstly because at that time, the existence of tau neutrino was unknown, hence the mixing between two flavours could at most produce a suppression of 1/2 rather than the necessary 1/3.

An eventual component of $\nu_\mu$ from the sun could not contribute to the $^{37}Ar$ production via the analogous interaction

$$\nu_\mu + {}^{37}Cl \longrightarrow {}^{37}Ar + \mu^- \ , \tag{2.4}$$

as in this case, the neutrino would need at least 104.4 MeV of energy to overcome the reaction threshold. Hence, the $\nu_e$ solar neutrinos that have turned into $\nu_\mu$, would simply pass through the detector, leaving no signal at all. It is legitimate to make an analogous reasoning for the $\nu_\tau$, which has an even larger mass than the muon.

The second reason was that a Large Mixing Angle (LMA) solution was needed between the two neutrino species to explain the 1/2 reduction. From the analysis of the available data at that time, several regions were allowed in terms of the variables governing the two flavour neutrino mixing parameters. However, the data showed strong evidence in favor of the LMA region, in which both the mixing angle and the mass difference between the two neutrinos was large. For the time being, physicists were prejudiced against large mixing of particles and had to wait a few years to observe spectacular proof of the correctness of the LMA region.

After the discovery of the tau lepton and tau neutrino, it was possible to obtain 1/3 suppression, considering the mixing of electron neutrinos with muon and tau neutrinos. However, the second problem still aroused doubts among the experts. It was not until 1985 when two Russian theorists, proposed a dynamical mechanism by which small mixing could be amplified into large mixing under certain conditions [17].

The solar neutrino problem was confirmed in the late 80's by the real-time water Cherenkov Kamiokande experiment [18] with 3000 tons of water and located 1 km underground. The experiment was able to observe solar neutrinos through the elastic scattering (ES) reaction $\nu + e^- \longrightarrow \nu + e^-$ which is mainly sensitive to electron neutrinos, whose cross section is about six times larger than the cross section of muon and tau neutrinos. Unlike radiochemical detectors, in which the reaction rate is integrated between extractions, Cherenkov detectors are real-time experiments, since the light produced in the water by the recoil of the electron during the reaction can be immediately observed. The solar neutrino signal was discriminated from the background exploiting the fact that the recoil electron preserves the directionality of the incoming neutrino; more details about the principle of the Cherenkov detector will be described in the upcoming section. The energy threshold of Kamiokande was 6.5 MeV, allowing only detection of $^8B$ neutrinos. After 1995, the Kamiokande experiment was upgraded by the bigger Super-Kamiokande experiment, same depth but with 50 ktons of water, achieving a high accuracy measurement of the flux of solar $^8B$ neutrinos with an energy threshold of 3.5 MeV. The flux ratio between the measurement and the predictions from the SSM model reported by Super-Kamiokande was $0.465 \pm 0.015$ [19], confirming once again the solar neutrino deficit.

In the early 90's two radiochemical experiments GALLEX [20] (30.3 tons of $^{71}Ga$ and 1.4 km underground) and SAGE [21] (50 tons of $^{71}Ga$ and 2 km underground) started the observation of solar electron neutrinos through the following charged-current reaction

$$\nu_e + {}^{71}Ga \longrightarrow {}^{71}Ge + e^- \ , \tag{2.5}$$

which has an energy threshold of 0.233 MeV. It allowed the detection of the *pp* cycle neutrinos, besides the $^7Be$, $^8B$ and other more energetic neutrinos. The combined results of the two experiments, plus a posterior upgrade of GALLEX, confirmed the solar neutrino problem, reporting a ratio between experimental and theoretical fluxes of $0.56 \pm 0.03$. This result meant, not only that neutrinos were disappearing, but also that their disappearance probability was a function of the neutrino's energy.

Sudbury Neutrino Observatory (SNO) experiment [22] was designed to provide a definitive answer, addressing the open questions of the mixing angle and the truthfulness of the electron neutrino oscillating into different flavours. Being a water Cherenkov detector, heavy water ($D_2O$) was used to enable the detection of both electron neutrino flux and the total neutrino flux, by collecting the emitted Cherenkov light, see Figure 2.2.

Due to the energy thresholds, SNO detector observed $^8B$ neutrinos via three different reactions.

$$\nu_e + d \longrightarrow p + p + e^- \qquad \text{Charged Current (CC)} \qquad E^{SNO}_{\text{th,CC}} = 8.2 \text{ MeV} \tag{2.6}$$

$$\nu_x + d \longrightarrow p + n + \nu_x \qquad \text{Neutral Current (NC)} \qquad E^{SNO}_{\text{th,NC}} = 2.2 \text{ MeV} \tag{2.7}$$

where $\nu_x$ stands for any of the three neutrino types; in addition to the ES reaction with $E^{SNO}_{\text{th,ES}} = 7.0 MeV$. The charged current interaction is sensitive only to the electron neutrino, while neutral current interactions have equal sensitivity to all three flavours. By comparing the data from each interaction channel, it was possible to measure the composition of the neutrino flux and provide a model independent test of neutrino flavour change. In case of no oscillations, the neutrino fluxes from the three interactions, should be equal, since there are only electron neutrinos coming from the Sun. However, the results of the CC reaction were in perfect agreement with those of previous experiments, showing that only 1/3 of the electron neutrinos were reaching the earth [23].

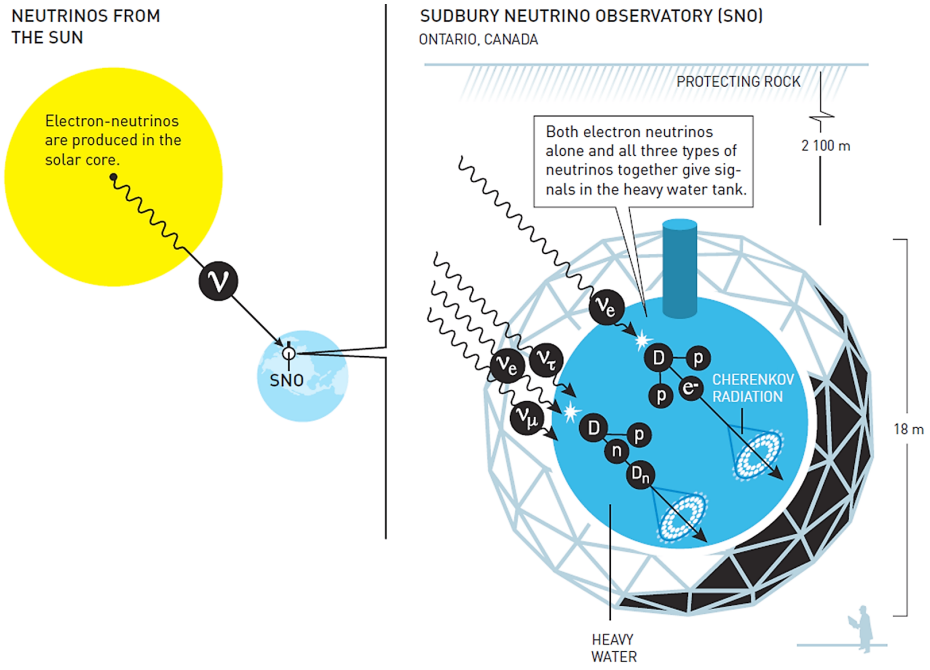


Figure 2.2: Schematic drawing of the SNO experiment, where the water Cherenkov detection principle is shown. Picture taken from Ref. [24].

Instead, the NC events gave a measurement of the total solar neutrino flux, showing a good agreement with the SSM theoretical predictions. SNO was able to test if the deficit of solar $\nu_e$ was due to changes in the flavour composition of the solar neutrino beam, since the ratio CC/NC gave a comparison of the number of $\nu_e$ interactions with those from all active flavours, completely independent of the solar model. The latest results of SNO claim a ratio between the CC and NC [25] of

$$\frac{\phi_{CC}}{\phi_{NC}} = 0.301 \pm 0.033 \,, \tag{2.8}$$

which differs from unit by more than 20 standard deviations and is a very convincing proof that solar electron neutrinos have transformed into muon and/or tau neutrinos on their way to the earth. The reasoning behind it is that these converted neutrinos were incapable of driving the CC interaction, while they could undergo without problems the NC reaction. For establishing the phenomenon of the oscillation of electron neutrinos from the sun into muon and tau neutrinos the SNO Experiment and Arthur McDonald (its leader) were awarded in 2015 with the Nobel Prize.

### 2.2.2 Atmospheric neutrino problem

A similar puzzle was found by the Irvine-Michigan-Brookhaven (IMB) [26] and Kamiokande [18] experiments in 1986, who were primarily looking for proton decay and could observe atmospheric neutrinos of $\sim$ 1 GeV energy. Atmospheric neutrinos are produced when high-energy protons from outer space interact with the atoms in the atmosphere. These collisions lead to abundant production of pions which decay according to the following chain

$$\begin{aligned} \pi^+ &\longrightarrow \mu^+ + \nu_\mu \\ &\hookrightarrow e^+ + \nu_e + \bar{\nu}_\mu \quad . \end{aligned} \tag{2.9}$$

Large amount of neutrinos and antineutrinos are produced in the final states. Their flux is

much smaller than the one from solar neutrinos, but atmospheric neutrinos are more energetic with $E_\nu > 200$ MeV. This larger energy enable neutrinos to produce muons in the final state, therefore it is possible to distinguish between the interaction of a $\nu_e$ from $\nu_\mu$ based on weather the final state contains an electron or a muon. Most atmospheric neutrino detectors cannot determine the charge of the final state particles, meaning they cannot distinguish between the interactions of neutrinos and anti-neutrinos. It is then usual, to group neutrinos and anti-neutrinos together. As a consequence, it is possible to derive from Eq. 2.9, that for every electron neutrino produced, there are two muon neutrino emitted, giving a $(\nu_e + \bar{\nu}_e) : (\nu_\mu + \bar{\nu}_\mu) = 1 : 2$ ratio.

IMB and Kamiokande experiments were after a sign of proton decay predicted by grand unified theories. Since these interactions take place at huge energy scales, their effect at ordinary energies is strongly suppressed and enormous experiments are designed to achieve a non negligible possibility of observing an event. Both experiments were water Cherenkov detectors surrounded by photomultipliers tubes. Ultra-relativistic charged particles, moving through water, create Cherenkov light which can be used to detect emitted particles. As the proton decay interaction was expected to barely occur, it was mandatory to work out all possible random events which could mimic the proton decay signal. Atmospheric neutrinos were a big source of background events, as they could occasionally interact with a nucleus (either hydrogen or oxygen) and produce charged particles. The emitted particle would be a muon if the incoming neutrino was $\nu_\mu$, while electrons would be detected if the interaction occurred with a $\nu_e$. Considering that the muon is 200 times more massive than the electron, it loses energy in a much slower scale, greatly impacting the emitted Cherenkov light pattern. Thus it is possible to identify if the interaction which produced the charged particle was due to a $\nu_\mu$ or $\nu_e$. Muon Cherenkov light rings have sharp edges and relatively empty interiors, while electron rings have fuzzy edges with full interiors. The difference arises from how the two particles lose energy as they propagate through water. At the typical energies at what atmospheric neutrinos produce muons, their behaviour in water is similar to rectilinear tracks, whose length is related to its kinetic energy. Muons mostly loss energy through ionization at a rate proportional to their energy, while electrons generate electromagnetic showers along their longitudinal direction, the loss rate of which varies only logarithmically with the energy of the electron.

IMB and Kamiokande were only able to set a lower limit on proton lifetime, however comparing their neutrino event rates with the theoretical expectations, they observed a lower than expected rate of muon neutrinos. In order to avoid large uncertainties in the theoretical expectations, the experiments had to come up with an ingenious method. The main source of uncertainty came from the derivation of cosmic ray fluxes. The uncertainty equally affects both the muon and electron neutrino interaction rates. Thus, if one takes the ratio of this two rates, the uncertainties cancels out and the ratio can be predicted quite accurately. The observed ratio was found to be around 0.7 of the predicted ratio.

To resolve this unexpected result, a similar experiment but five times larger in scale was built, Super Kamiokande. This upgraded experiment conclusively proved in 1998 that the muon neutrinos produced in the atmosphere were oscillating into tau neutrinos [27].

The observation principle was the same as previous experiments, but its larger size increased the rate of interactions. In addition, the photon-multipliers tubes were designed with exceptional light sensitivity, allowing a highly efficient reconstruction of the Cherenkov light cone. This improvement led super Kamiokande study the rate of interactions not only as a function of the incoming energy but also with respect to its direction.

At higher energies, there is a fairly good correlation between the direction of the neutrino and the produced charged particle. An important concept is the azimuthal asymmetry; neglecting the geomagnetic effect (affecting low energy cosmic rays[1]) it is expected to have the same flux

[1] At low energies, the directional flux of atmospheric neutrinos depends on the effect of the geomagnetic field on the parent cosmic ray primaries and secondaries. However, this effect disappears at high energies, above few

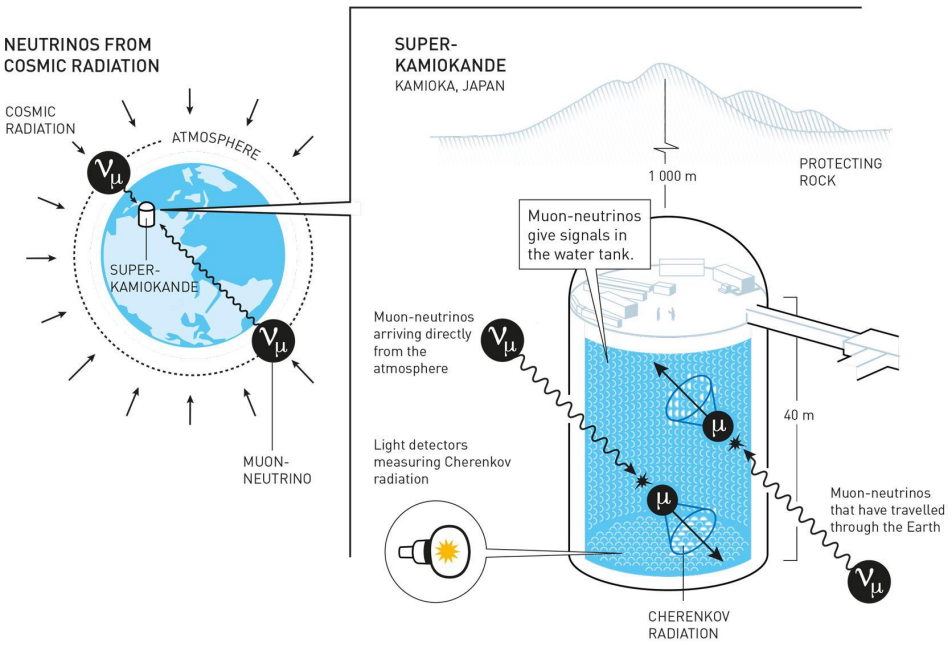


Figure 2.3: Schematic drawing of the Super-Kamiokande experiment, where the detection principle is shown. Picture taken from Ref. [24].

for any given incidence angle, either coming from above or below the detector.

For electrons and muons going in the downward direction of the detector, there must have been a neutrino coming from above which produced that particle, or in other words, the neutrino must have crossed the whole atmosphere before interacting (few km). Instead if the charged particle was seen in the upward direction, the corresponding neutrino must have come from below, which means that it was produced on the other side of the earth. Hence the scenario presented a wide variety of neutrino energies in the range of 200 MeV to 10 GeV, travelling distance from 10 to 13,000 km. Super Kamiokande observed a deficit in the up-going muon neutrinos and discovered that depending on the neutrino energy and distance traveled, different neutrinos oscillate with different probabilities [27]. The large deficit of $\nu_\mu$ in contrast to the small deficit for $\nu_e$ could only be explained by the oscillation of high energy $\nu_\mu$ into $\nu_\tau$, which could not be detected by the experiment. Thus the Super Kamiokande experiment conclusively settled the atmospheric neutrino problem earning a Nobel Prize to the leader of the group, Takaaki Kajita.

This will be further developed in the following section, after the detailed introduction to the neutrino oscillation mechanism, where the technicalities of the atmospheric neutrino oscillations will be presented.

The 2015 Nobel Prize was shared by the leaders of the experiments who solved the solar and atmospheric problems, in particular "for the discovery of neutrino oscillation, which shows that neutrinos have mass" opening a new chapter in particle physics. After the discovery, many experiments have been built to observe neutrino oscillations and constrain the parameters that drive them. Their main results and the current understanding of neutrino oscillations will be summarised in Section 2.8.

GeV.

## 2.3 Neutrinos in the Standard Model

Neutrinos, as elementary particles, are described by the Standard Model (SM) of particle physics, being a self-consistent theory capable of describing three of the four fundamental interactions that govern our Universe: strong, electromagnetic and weak interactions. The SM is a gauge theory [28] and it is the result of the direct product of three groups $SU(3)_C \otimes SU(2)_L \otimes U(1)_Y$, where C stands for colour, L for left-handedness, and Y for hypercharge. This representation describe the strong interaction, the weak isospin and the hypercharge groups, respectively.

The handedness or chirality of a particle is a Lorentz-invariant quantum mechanical property related to its spin. In the case of massless or highly-energetic particles, the physical interpretation of this quantity is identical to its helicity, in which a massless particle whose spin is (anti)aligned with its direction of motion is said to have a (negative)positive helicity and (left)right-handed chirality. In contrast, the helicity of massive particles corresponds to a superposition of both left and right handed-chiral states. The W-boson couples only with left-handed particles or right-handed antiparticles, while the Z-boson can couple to all of them.

In the SM there are three types of neutrinos, one for each of the three charged leptons: $\nu_e$, $\nu_\mu$ and $\nu_\tau$ with their corresponding antiparticles. Neutrinos are fermions that do not have strong nor electromagnetic interactions. Consequently, they are singlets of the subgroup $SU(3)_C \otimes U(1)_{EM}$. Fermions are grouped as doublets for chiral left-handed fields $\psi_L$ and singlets for right-handed fields, $\psi_R$.

$$\psi_L = \begin{pmatrix} \nu_e \\ e \end{pmatrix}, \begin{pmatrix} \nu_\mu \\ \mu \end{pmatrix}, \begin{pmatrix} \nu_\tau \\ \tau \end{pmatrix} \quad \text{and} \quad \psi_R = e_R, \mu_R, \tau_R \, . \tag{2.10}$$

Active neutrinos are usually referred to neutrinos that are part of these lepton doublets, as only (right)left-handed (anti)neutrinos have been observed so far. Sterile neutrinos are defined as having no SM gauge interactions, that is, they are singlets of the complete SM gauge group. Thus the SM, being the gauge theory able to describe all known particle interactions, contains no sterile neutrinos and extensions of the SM would be needed if one would like to accommodate them.

$SU(2)_L$ gauge invariance dictates the form of the weak charged current (CC) interactions, between neutrinos and their corresponding charged leptons, and neutral current (NC), among themselves, to be

$$\mathcal{L}^{CC}(x) = -\frac{g}{2\sqrt{2}} j_\alpha^{CC} W^\alpha(x) + h.c \, , \tag{2.11}$$

$$\mathcal{L}^{NC}(x) = -\frac{g}{2\cos\theta_W} j_\alpha^{NC}(x) Z^\alpha(x) + h.c \, . \tag{2.12}$$

With h.c its hermitian conjugate. In this expressions,

$$j_\alpha^{CC}(x) = 2 \sum_{\beta=e,\mu,\tau} \bar{\nu}_{\beta L}(x) \gamma_\alpha l_{\beta L}(x) \tag{2.13}$$

represents the leptonic charged current and

$$j_\alpha^{NC}(x) = 2 \sum_{\beta=e,\mu,\tau} \bar{\nu}_{\beta L}(x) \gamma_\alpha \nu_{\beta L}(x) \tag{2.14}$$

is the neutrino neutral current. $W^\alpha(x)$ and $Z^\alpha(x)$ are the fields of the $W^\pm$ and $Z^0$ vector bosons, and $g$ the electroweak coupling constant, which defines its strength. $\theta_W$ is the Weinberg or weak mixing angle and relates the masses of $W^\pm$ and $Z^0$ bosons as $\cos\theta_W = M_W/M_Z$.

## 2.4 Neutrino mass

An interesting and actively studied question is that of the neutrino mass, which still remains open. In theory, all particles of the SM should be massless in order to preserve the gauge invariance. However, the Higgs mechanism, also known as spontaneous symmetry breaking, allows particles to acquire mass [29] through a Yukawa coupling. To conserve the isospin invariance, the Higgs has to be combined with the fermion doublet and singlet together. As seen from Eq. 2.10, charged leptons have both left and right-hand components, being able to interact with the Higgs field and causing them to acquire some mass. Instead, neutrinos do not have the right-handed singlet and remain massless in the SM. An additional consequence of being massless particles is that the flavour of neutrinos must be preserved during their propagation, however several experiments have shown neutrino mixing, indicating that neutrinos need to have non-zero masses; this will be the main topic of Section 2.6.

Typically, mass is included in the SM with the Dirac mass term in the Lagrangian: $m_D\bar{\nu}\nu$. The neutrino spinor can be decomposed into its chiral components $\nu = \nu_L + \nu_R$ resulting in[2]

$$m_D\bar{\nu}\nu = m_D(\overline{\nu_L + \nu_R})(\nu_L + \nu_R) = m_D(\bar{\nu}_L\nu_R + \bar{\nu}_R\nu_L) \, . \tag{2.15}$$

A Dirac mass for the neutrino would require the existence of a right-handed neutrino, which has not been observed in electroweak interaction. This could be a possible candidate for sterile neutrinos, with the exclusive function of giving neutrinos mass without participating in electroweak interactions. In addition, Eq. 2.15 also requires neutrinos to be Dirac particles, which means that neutrino and antineutrino are different particles.

Alternatively, the neutrino can just be a purely left-handed field and have a Majorana mass. In this case additional mass terms need to be introduced in the Lagrangian. For a general spinor, these are:

$$\mathcal{L}_M = -\frac{1}{2}\bar{\nu}_L M_M \nu_L^C + h.c \, , \tag{2.16}$$

where $M_M$ is the Majorana mass matrix, $\nu_L^T = (\nu_{eL}, \nu_{\mu L}, \nu_{\tau L})$ and $\nu^C$ is the charge conjugated. Using a unitary transformation $U$ to diagonalize $M_M$, the previous equation can rewritten as,

$$\mathcal{L}_M = -\frac{1}{2}\bar{\nu}^M m \nu^M \, , \tag{2.17}$$

with $\nu^M = U^\dagger\nu_L + \left(U^\dagger\nu_L\right)^C = (\nu_1, \nu_2, \nu_3)^T$ and $m = (m_1, m_2, m_3)$ a diagonal matrix. It is straight forward to see that

$$\left(\nu^M\right)^C = \nu^M \, . \tag{2.18}$$

Thus the fields of the neutrinos with definite mass satisfy the Majorana condition

$$\nu_i^C = \nu_i \, , \tag{2.19}$$

and are the so called Majorana neutrinos. This condition implies that both neutrino and antineutrino states are described by only one field, unlike the case of charged states where two different fields are required. Being neutrinos Majorana particles would imply not only that neutrinos and antineutrinos are the same particle, but also that the lepton number is not conserved.

The field $\nu_M$ is defined as the sum of left and right handed components

$$\nu^M = \nu_L^M + \nu_R^M \, , \tag{2.20}$$

[2]Last equivalence of the Eq. 2.15 hold because $\psi_{L,R} = P_{L,R}\psi$ with $P_{L,R}$ projectors and due to the properties of the gamma matrices.

but also as

$$\nu^M = U^\dagger \nu_L + \left(U^\dagger \nu_L\right)^C \ . \tag{2.21}$$

Simply by comparison one can see that $\nu_L^M = U^\dagger \nu_L$ and $\nu_R^M = \left(U^\dagger \nu_L\right)^C$, i.e. the left- and right-hand components of the Majorana fields are not independent from each other, $\nu_R^M = \left(\nu_L^M\right)^C$. Therefore $\nu_{i,R} = (\nu_{i,L})^C$ with $i = 1, 2, 3$ and consequently

$$\nu_i = \nu_{i,L} + (\nu_{i,L})^C \ . \tag{2.22}$$

A mass term like $m\bar{\nu}_L \, (\nu_L)^C$ would break the lepton number by two units.

The most general Lorentz invariant mass term is a combination of both cases:

$$\mathcal{L} = -\frac{1}{2} \left(\bar{\nu}_L, \bar{\nu}_L^C\right) \begin{pmatrix} m_L & m_D \\ m_D & m_R \end{pmatrix} \begin{pmatrix} \nu_R^C \\ \nu_R \end{pmatrix} + h.c. \ . \tag{2.23}$$

where $\nu_L$, $\nu_R^C$ represent the known neutrino interactions, while $\nu_L^C$, $\nu_R$ represent the sterile neutrino. $m_L$ and $m_R$ are the left and right handed Majorana masses. The mass eigenstates can be obtained if one diagonalizes the mass matrix, obtaining the corresponding eigenvalues,

$$m_{1,2} = \frac{1}{2} \left[ (m_L + m_R) \pm \sqrt{(m_L - m_R)^2 + 4m_D^2} \right] \ . \tag{2.24}$$

The case with both Majorana masses equal to 0, $m_L = m_R = 0$, corresponds to the pure Dirac case, conversely $m_D = 0$ is the pure Majorana case.

One could choose different values for $m_L$, $m_R$ and $m_D$, that will give different physical masses, but the interesting behaviour occurs when $m_L = 0$ and $m_R \gg m_D$. It was already mentioned that the SM explicitly forbids the left-handed Majorana term, hence $m_L = 0$, but says nothing about the right-handed Majorana term, so this choice of parameters is sensible. This is the famous *seesaw* model and was proposed in 1979 to explain the smallness of the neutrino masses. With these values, it is possible to obtain the following eigenvalues:

- A light mass of $m_1 = m_D^2/m_R$ that would correspond to the active neutrino mass
- A heavy mass of $m_2 = m_R \left(1 + m_D^2/m_R^2\right) \approx m_R$ for the sterile neutrino

If $m_R$ is set to a very large value then the physical neutrino with mass $m_2$ also acquires a very large mass. On the other hand, the physical mass of the other neutrino $m_1$, becomes very small as it is suppressed by a factor $1/m_R$. Computing the eigenstates, i.e. the physical neutrino states, for this choice one finds that $\nu_1$ is mostly the familiar left-handed light Majorana neutrino, while $\nu_2$ corresponds almost entirely to the heavy sterile right-handed partner. The seesaw mechanism provides an explanation for the small mass of neutrino with respect to the other charged leptons, but it requires the neutrino to be a Majorana particle and the existence of an extremely heavy partner to the neutrino.

A detailed summary of the different models that could explain neutrino masses can be found in Ref. [30].

## 2.5 Neutrino Interactions

In most experiments, neutrinos are detected when they interact with protons and neutrons making up the detector active material. It was already mentioned that neutrinos interact via either the charged or neutral weak currents, and they may scatter off the target nucleons via a number of processes. Neutral current interactions, mediated by the $Z^0$ boson, are characterised by having a neutrino of the same flavour in both the initial and the final state. NC do not change the nature of fundamental particles involved but do transfer energy and momentum between

them. On the other hand, charged current interactions, mediated by the $W$ boson, replace the neutrino in the final state by a charged lepton of the same flavour. Feynman diagrams illustrating examples of these interactions are shown in Figure 2.4.

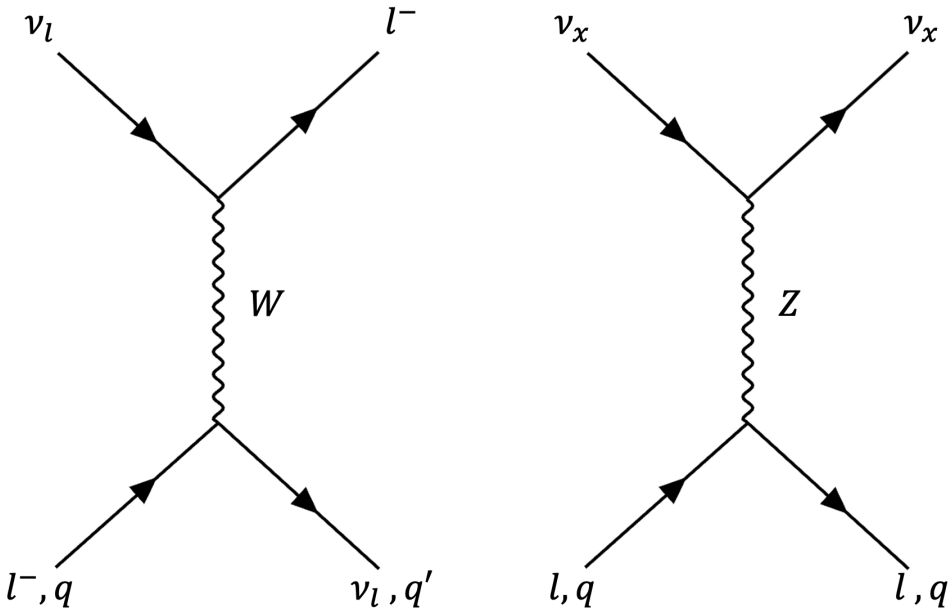


Figure 2.4: Feynman diagrams illustrating examples of neutrino interactions, left CC interaction mediated by the W boson, while right there is a NC interaction mediated by the Z boson. $l$ and $q$ stand for a generic lepton and quark respectively, while $\nu_x$ denotes any neutrino flavour. Time increases from left to right.

The energy of the neutrino is an important factor to determine the phenomenology of the interaction. At high energies, about 7 GeV and above, the predominant interaction is the so-called deep inelastic scattering (DIS). Given enough energy, the neutrino can resolve the individual quark constituents of the nucleon and manifests in the creation of an hadronic shower. At lower energies, the fact that the quarks are bound within the nucleons and these bound inside the nuclei play an important role. Interaction modes include[3]:

- elastic and quasi-elastic scattering (QE): Neutrinos can elastically scatter an entire nucleon liberating a nucleon (or multiple nucleons) from the target. In the case of charged current neutrino scattering, this process is referred to as quasi-elastic scattering, whereas for neutral current scattering this is traditionally referred to as elastic scattering.
- resonance production: Neutrinos can excite the target nucleon to a resonance state. The resultant baryonic resonance ($\Delta$, $N^*$) quickly decays to a variety of possible mesonic final states producing combinations of nucleons and mesons.
- n-particle n-hole (npnh): conceptually similar to QE, with the added complexity that the neutrino interacts with more than one bound nucleon inside the nuclei at once.

The contribution of each process varies with the neutrino energy and flavour. This dependence is different for neutrinos and antineutrinos and can be observed in the following Figure 2.5 for muon flavour in both cases,

$$\nu_\mu N \longrightarrow \mu^- X \ , \tag{2.25}$$

$$\bar{\nu}_\mu N \longrightarrow \mu^+ X \ . \tag{2.26}$$

[3] in addition to DIS, whose contribution decreases as the energy is reduced

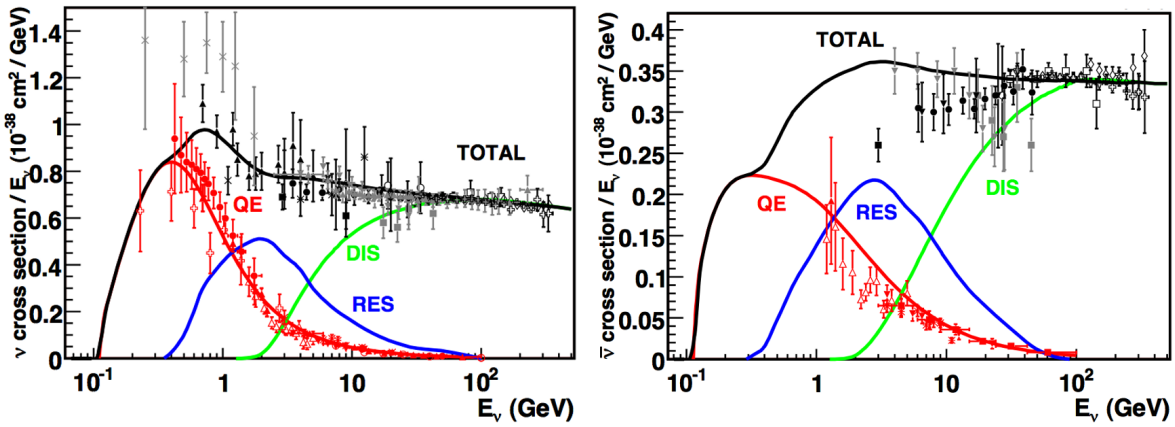


Figure 2.5: Existing muon neutrino (left) and anti-neutrino (right) charged current cross section data on a neutral nucleus and predictions as a function of neutrino energy; including the region covered by short baseline neutrino experiments. The total cross-section for CC events is included, as well as a breakdown of interaction-specific data predictions for QE, RES and DIS interactions. The energy dependence of the $2p2h$ cross-section has large theoretical uncertainties and is not shown. Figure from Ref. [31].

These results have been accumulated over many decades using a variety of neutrino targets and detector technologies. There are some relevant features in these figures; in first place, the total cross section approaches a linear dependence on neutrino energy. This scaling behaviour is a prediction of the quark parton model (Feynman 1969, [32]) and expected if point-like scattering off quarks dominates the scattering mechanism. Secondly, low energy region are not typically as well measured as their high energy counterparts. This is due to the lack of statistics data available and the challenges of trying to describe all various underlying physical processes that can participate in this low energy regime. Lastly, antineutrino cross sections are typically less well measured, as statistics tend to be smaller and backgrounds larger for these cases.

For a typical energy range of neutrino oscillation experiment, multiple processes are simultaneously relevant. This implies that having a precise understanding of the neutrino interaction cross section is essential to perform oscillation experiments.

## 2.6 Neutrino Mixing and Oscillations

In the active paradigm neutrinos exist in two forms, each with 3 variants: flavour eigenstates, $\nu_e$, $\nu_\mu$, $\nu_\tau$, and mass eigenstates, $\nu_1$, $\nu_2$, $\nu_3$. The flavour eigenstates undergo weak interactions and are experimentally detectable, while mass eigenstates dictate the propagation of neutrinos in space and time. The flavour eigenstates are superpositions of the mass eigenstates, and its composition evolves along the trajectory of the neutrinos due to the differences in momenta of the mass eigenstates. This phenomenon is the so called neutrino flavour oscillations and can be understood as a quantum mechanical interference effect. The treatment follows that in Ref. [33].

In order to determine the probability of oscillations occurring between neutrino flavour states in space, it is necessary to define their behaviour in time.

A generic flavour state $|\nu_\alpha\rangle$, $\alpha \in \{e, \mu, \tau\}$ can be expressed as a linear combination of mass states $|\nu_i\rangle$, $i \in \{1, 2, 3\}$:

$$|\nu_\alpha\rangle = \sum_{k=1,2,3} U^*_{\alpha k} |\nu_k\rangle \ , \tag{2.27}$$

where U is a unitary matrix called the PMNS (Pontecorvo, Maki, Nakagawa, Sakata) matrix.

In the standard picture with 3 flavours and nonzero neutrino masses, this mixing matrix can be written in terms of three mixing angles $(\theta_1, \theta_2, \theta_3)$ and one complex CP-violating phase $\delta_{CP}$:

$$U = \begin{pmatrix} 1 & 0 & 0 \\ 0 & c_{23} & s_{23} \\ 0 & -s_{23} & c_{23} \end{pmatrix} \begin{pmatrix} c_{13} & 0 & s_{13}e^{-i\delta_{CP}} \\ 0 & 1 & 0 \\ -s_{13}e^{i\delta_{CP}} & 0 & c_{13} \end{pmatrix} \begin{pmatrix} c_{12} & s_{12} & 0 \\ -s_{12} & c_{12} & 0 \\ 0 & 0 & 1 \end{pmatrix} , \tag{2.28}$$

with $s_{ij} = \sin\theta_{ij}$, $c_{ij} = \cos\theta_{ij}$, $\theta_{ij} = [0, \pi/2)$ and $\delta_{CP} = [0, 2\pi]$. Other parameters can be absorbed into an overall phase and will not lead to any physically observable effect, for instance additional CP-violating phases due to the nature of Majorana neutrinos.

By breaking down the PMNS matrix this way, it is possible to highlight the main components. The matrix that contains $\theta_{12}$ is referred to as the solar mixing matrix, the parameters of which are mainly determined by solar neutrino experiments. For the same reason, the matrix containing $\theta_{23}$ is often called the atmospheric mixing matrix. Finally, the reactor matrix contains $\theta_{13}$ and the complex phase. Note that if $\delta_{CP}$ is not equal to 0 or $\pi$, the matrix will have nontrivial complex entries leading to subtle distortions in the oscillation probabilities and also to differences between neutrinos and antineutrinos oscillations. The PMNS matrix is analogous to the Cabibbo-Kobayashi-Maskawa (CKM) matrix in the quark sector, however the first one has larger off-diagonal terms than the CKM matrix.

The mass states $|\nu_k\rangle$ are eigenstates of the free-particle Hamiltonian $\mathcal{H}$,

$$\mathcal{H}\,|\nu_k\rangle = E_k\,|\nu_k\rangle \ , \tag{2.29}$$

where the energy eigenvalue is

$$E_k = \sqrt{\vec{p}^{\,2} + m_k^2}\,, \tag{2.30}$$

with $\vec{p}$ and $m_k$ the momentum and mass of the neutrino state.

The time evolution of the mass eigenstates is subject to the Schrödinger equation and can be defined by a plane wave solution:

$$i\frac{d}{dt}\,|\nu_k(t)\rangle = \mathcal{H}\,|\nu_k(t)\rangle = E_k\,|\nu_k(t)\rangle \Longrightarrow |\nu_k(t)\rangle = e^{-iE_kt}\,|\nu_k\rangle \ , \tag{2.31}$$

where $t \neq 0$ and $|\nu_k\rangle = |\nu_k(t=0)\rangle$. Substituting this result into Eq. 2.27, a flavour state $|\nu_\alpha(t)\rangle$ at a generic time $t$ can be written as

$$|\nu_\alpha(t)\rangle = \sum_k U^*_{\alpha k} e^{-iE_kt}\,|\nu_k\rangle \ . \tag{2.32}$$

Thanks to the unitary relation of U

$$\sum_\alpha U^*_{\alpha k} U_{\alpha j} = \delta_{jk}\ , \tag{2.33}$$

the massive states can be written in terms of the flavour states,

$$|\nu_k\rangle = \sum_{\alpha=e,\mu,\tau} U_{\alpha k}\,|\nu_\alpha\rangle \ . \tag{2.34}$$

Going back to Eq. 2.32, the flavour eigenstate will evolve as

$$|\nu_\alpha(t)\rangle = \sum_k U^*_{\alpha k} e^{-iE_kt}\,|\nu_k\rangle = \sum_\gamma \left( \sum_k U^*_{\alpha k} e^{-iE_kt} U_{\gamma k} \right) |\nu_\gamma\rangle \ . \tag{2.35}$$

This implies that, even if the initial state was a pure flavour state $|\nu_\alpha\rangle$, after a certain time $t$, it becomes a superposition of all flavour states. Hence, the probability of measuring a neutrino in a flavour state $|\nu_\beta\rangle$, at a specific time $t$, given the neutrino was initially in a $|\nu_\alpha\rangle$ state is:

$$P_{\nu_\alpha \to \nu_\beta}(t) = |\langle \nu_\beta | \nu_\alpha(t) \rangle|^2 = \left| \sum_\gamma \left( \sum_k U^*_{\alpha k} U_{\gamma k} e^{-iE_k t} \right) \langle \nu_\beta | \nu_\gamma \rangle \right|^2 , \tag{2.36}$$

where $\langle \nu_\beta | \nu_\gamma \rangle = \delta_{\beta\gamma}$. Expanding the squared amplitude of the $|\nu_\alpha\rangle \to |\nu_\beta\rangle$ transition after a time $t$, gives

$$P_{\nu_\alpha \to \nu_\beta}(t) = \left| \sum_k U^*_{\alpha k} U_{\beta k} e^{-iE_k t} \right|^2 = \sum_{k,j=1,2,3} U^*_{\alpha k} U_{\beta k} U_{\alpha j} U^*_{\beta j} e^{-i(E_k - E_j)t} . \tag{2.37}$$

A rigorous evaluation of this probability requires a wave packet treatment of the neutrino evolution, rather than the simplified plane wave approximation discussed here. However, the same result can be achieved by assuming the relativistic approximation where all neutrino masses are considered negligible and all the mass eigenstates have the same energy $E$, equal to the modulus of their momentum: $p_k = E_k = E$. Since the energy $E_k$ and momentum $p_k$ of the $k^{th}$ mass eigenstate are related by the relativistic dispersion relation

$$E_k^2 = p_k^2 + m_k^2 , \tag{2.38}$$

the aforementioned approximation allows to derive the following relation,

$$E_k = p_k \sqrt{1 + \left( \frac{m_k}{p_k} \right)^2} \approx E + \frac{m_k^2}{2E} , \tag{2.39}$$

and thus,

$$E_k - E_j \approx \frac{\Delta m^2_{kj}}{2E} . \tag{2.40}$$

With the definition of the mass-squared difference, $\Delta m^2_{kj} \equiv m_k^2 - m_j^2$. Note that only two of these values are independent, because of the following equality,

$$\Delta m^2_{12} + \Delta m^2_{23} + \Delta m^2_{31} = 0 . \tag{2.41}$$

The transition probability can then be expressed as

$$P_{\nu_\alpha \to \nu_\beta}(t) = \sum_{k,j=1,2,3} U^*_{\alpha k} U_{\beta k} U_{\alpha j} U^*_{\beta j} \exp\left( -i \frac{\Delta m^2_{kj} L}{2E} \right) . \tag{2.42}$$

Where the relation $t = L$ for ultra-relativistic neutrinos (in natural units) was used and motivated by the fact that real experiments do not measure the neutrino travel time, but the source-detector distance $L$ is known.

It is often useful to separate the real and imaginary parts of the product of the different PMNS matrix to get

$$\begin{aligned} P_{\nu_\alpha \to \nu_\beta}(L,E) = \delta_{\alpha\beta} &- 4 \sum_{k>j} \Re[U^*_{\alpha k} U_{\beta k} U_{\alpha j} U^*_{\beta j}] \sin^2 \left( \frac{\Delta m^2_{kj} L}{4E} \right) \\ &\pm 2 \sum_{k>j} \Im[U^*_{\alpha k} U_{\beta k} U_{\alpha j} U^*_{\beta j}] \sin \left( \frac{\Delta m^2_{kj} L}{2E} \right) , \end{aligned} \tag{2.43}$$

where the $(+)$ and $(-)$ signs are for the neutrino and anti-neutrino cases respectively. $\Re(z)$ and $\Im(z)$ represent the real and imaginary components of a complex number $z$.

The first term corresponds to no oscillation at all. The middle one corresponds to the three-flavour oscillation, in which the component defined by the real part of the PMNS matrix elements characterizes the amplitude of the oscillation, while the component driven by the mass splitting defines the oscillation phase. The oscillation probability also depends on the ratio $L/E$, but this is typically fixed by the experimental conditions and from constants of nature. Finally, the last term accounts for the impact of CP-violation.

The oscillation probabilities of the channels with $\alpha \neq \beta$ are usually called transition probabilities, whereas the oscillation probabilities of the channels with $\alpha = \beta$ are usually called survival probabilities.

From Eq. 2.43, it follows that oscillation experiments are not sensitive to the absolute value of neutrino masses, but only to their squared mass differences. Thanks to matter effects, which will be soon explained, it is known that $\Delta m^2_{21} > 0$. On the other hand, atmospheric mass splitting $\Delta m^2_{31}$ is essentially measured only via neutrino oscillations in vacuum and hence its sign remains unknown at the moment. As a consequence, there are two possibilities for the ordering of neutrino masses:

- Spectrum with Normal Ordering (NO), where $m_1 < m_2 < m_3$ and $\Delta m^2_{31} > 0$
- Spectrum Inverted Ordering (IO) with $m_3 < m_1 < m_2$ and $\Delta m^2_{31} < 0$

The two possible hierarchical neutrino mass scenarios are shown in Figure 2.6. It provides a graphical representation of the neutrino flavour content of each neutrino mass eigenstates given the current preferred values of the oscillation parameters. At present, even if some $\delta_{CP}$ values are more favoured than others, the precise value of the CP violating phase is still a mystery, hence the figure shows the different compositions as a function of that angle. Note that even if $\delta_{CP}$ ranges from 0 to $2\pi$ the figure only shows values up to $\pi$, this is because there is an horizontal reflection symmetry. Neutrino oscillation parameters slightly depend on the mass ordering, as will be soon shown.

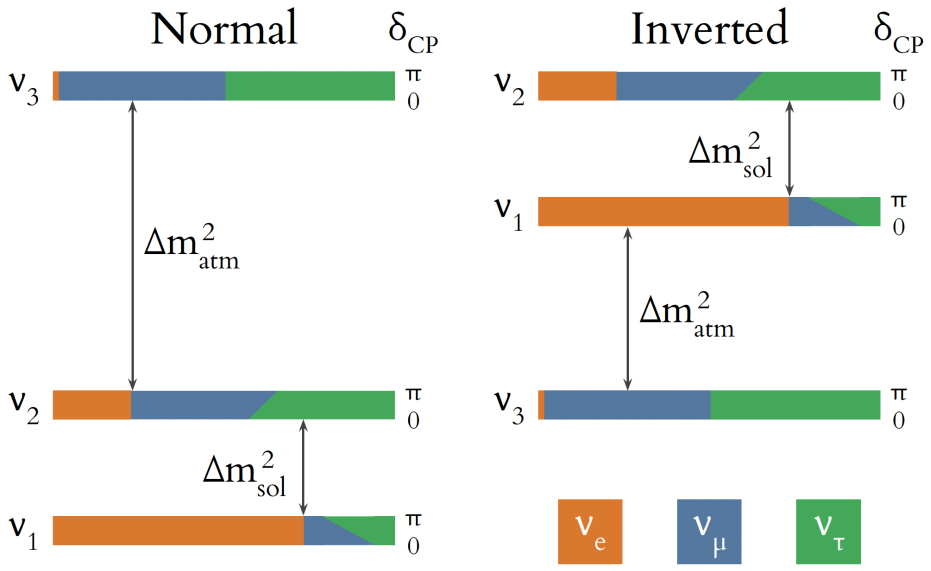


Figure 2.6: Schematic drawing of the neutrino flavour eigenstate composition for the mass eigenstates in case of normal or inverted hierarchies.

Sometimes in the literature the determination of the neutrino mass spectrum is referred to as determination of the neutrino hierarchy. This could be misleading, since the lightest neutrino mass could be comparable to the other two masses, i.e. $m_1 \approx m_2 \approx m_3 \gg \sqrt{|\Delta m^2_{32}|}$, and the

spectrum might not be hierarchical but degenerate. Clearly the observation of flavour oscillations imply a lower bound on the mass of the heavier neutrino as $|m_i| \geq \sqrt{\left|\Delta m^2_{ij}\right|}$, however it cannot provide an upper bound on $m_i$. Information of the mass scale of neutrino is provided by other type of experiments. The most-model independent observable for the determination of the mass of the electron neutrino is the shape of the endpoint of the beta decay spectrum. Other probes of the absolute value of the neutrino masses includes double beta decays, if neutrino are of Majorana type, or large-scale structures of the Universe which are sensitive to the total mass of neutrinos. Even if the latter might be model dependent, several constraints have been put in place as experiments improved their sensitivity. Some of their results will be briefly discussed in Section 2.8.6.

### 2.6.1 Two-flavour oscillations

Modifications can be made to the three-flavour neutrino oscillation framework in order to either simplify the model or add complexities which arise in nature, for instance introducing additional neutrino states or adjusting the oscillation description to matter propagation.

For a given distance $L$ and energy $E$ the oscillatory behaviour is typically dominated by one of the mass splittings. In many cases, the phenomenology of neutrino oscillations can therefore be well approximated by the two-flavour scenario. This scenario will have a single mass splitting and the unitary matrix, in this case $2 \times 2$, only requires a single real mixing angle, $\theta$:

$$U = \begin{pmatrix} \nu_\alpha \\ \nu_\beta \end{pmatrix} \begin{pmatrix} \cos\theta & \sin\theta \\ -\sin\theta & \cos\theta \end{pmatrix} \begin{pmatrix} \nu_1 \\ \nu_2 \end{pmatrix} . \tag{2.44}$$

The oscillation probability of a neutrino in the initial flavour state $|\nu_\alpha\rangle$ to be found in the flavour state $|\nu_\beta\rangle$ after travelling a distance $L$ reduces to

$$P_{\nu_\alpha \to \nu_\beta}(L, E) = \left| \delta_{\alpha\beta} - \sin^2(2\theta) \sin^2\left(\frac{\Delta m^2 L}{4E}\right) \right| \quad \text{(natural units)} \tag{2.45}$$

$$= \left| \delta_{\alpha\beta} - \sin^2(2\theta) \sin^2\left(1.27 \frac{\Delta m^2[eV^2] L[m]}{E[MeV]}\right) \right| \quad \text{(SI units)} \tag{2.46}$$

where

$$L_{max}[m] = \frac{\pi}{2} \frac{1}{1.27} \frac{E[MeV]}{\Delta m^2[eV^2]} , \tag{2.47}$$

is the location of the first oscillation maximum. The oscillation amplitude is governed by the mixing angle, while the frequency is determined by the mass splitting.

Phenomenologically the observable oscillation effects can be divided into three regimes, as seen in Figure 2.7:

- $4E \gg \Delta m^2 L$: the oscillatory term vanishes and there is no observable effect
- $4E \sim \Delta m^2 L$: the oscillatory behaviour is observed as a function of energy or distance
- $4E \ll \Delta m^2 L$ the oscillations become increasingly rapid until the experimental resolution is no longer sufficient. The observed flux then averages out at $|\delta_{\alpha\beta} - \frac{1}{2}\sin^2(2\theta)|$

From here one can see that typically, an experiment will be sensitive to a mass splitting around

$$|\Delta m^2| \sim \frac{E}{L} , \tag{2.48}$$

where $E$ is the energy of the detected neutrinos and $L$ is the distance travelled before reaching the detector, i.e. the *baseline*. These two parameters are therefore the main considerations when designing a neutrino oscillation experiment to ensure maximum sensitivity to the physics.

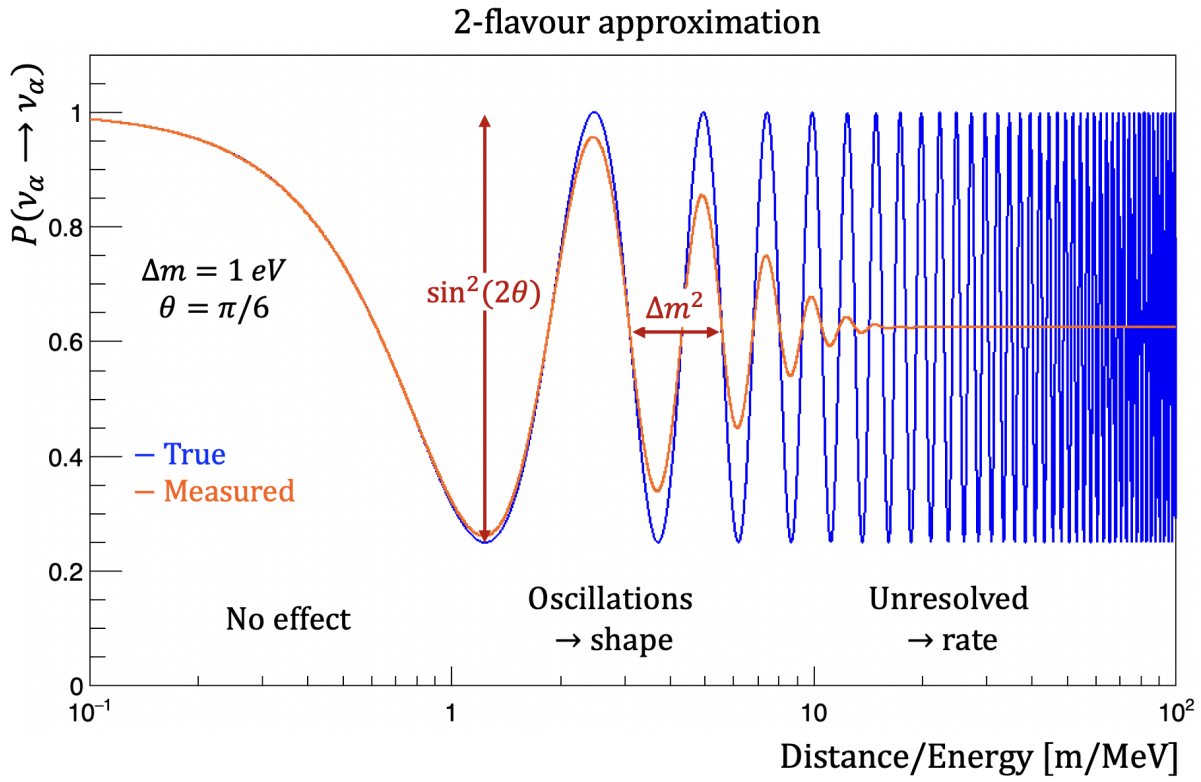


Figure 2.7: Survival probability as a function of the ratio: distance L over energy E, in a 2-flavour model. Values of $\Delta m^2$ and $\theta$ are chosen just for illustrative purposes.

The two-flavour approximation is not sufficient to describe the entire active neutrino oscillation picture, nevertheless it is possible to choose wisely the values of the baseline and neutrino energy to gain sensitivity on a particular oscillation channel while suppressing the rest. This effectively results in the two flavour neutrino oscillation approximation with some error. Such error is not so important in just verifying the existence of the neutrino masses. However, current interest in neutrino physics is, not only focused in verifying the finite neutrino masses, but also in determining the precise values of the mixing parameters. The allowed region of the mass differences and the mixing angles may be affected due to this error and one should consider the full three neutrino framework to perform precise measurements.

## 2.7 Matter effects in neutrino oscillations

So far, the neutrino oscillation mechanism has only been discussed for propagation in vacuum, such that all neutrino flavour eigenstates interact equally. The presence of matter can drastically change the pattern of neutrino oscillations, given that neutrinos can interact with the particles forming the matter.

These matter effects primarily involve neutral and charged-current scattering of neutrinos off electrons and nucleons in a medium, as indicated in Figure 2.8. These two interactions need to be treated separately, due to the fact that neutral-current scattering impacts all active neutrino flavours equally, whereas the charged-current scattering occurs only for electron neutrinos off electrons in matter [34].

Accordingly, the Hamiltonian of the neutrino system in matter $\mathcal{H}_m$, differs from the Hamiltonian in vacuum $\mathcal{H}_0$, $\mathcal{H}_m = \mathcal{H}_0 + \mathcal{H}_{int}$ , where $\mathcal{H}_{int}$ describes the interaction of neutrinos with particles in the medium. The incoherent elastic and the quasi-elastic scattering, in which the states of the initial particles change in the process (destroying the coherence between the

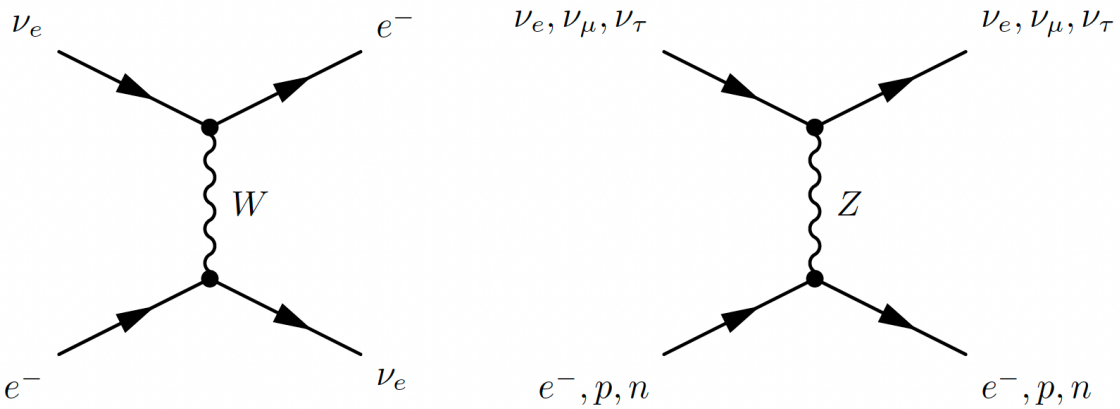


Figure 2.8: Feynman diagrams of the coherent elastic scattering process that generates the CC potential through W exchange and NC potential through Z exchange. Picture taken from Ref. [34].

neutrino states), have negligible cross sections. But when neutrinos propagate in dense matter, they can also interact coherently with the particles in the medium. By definition, in coherent interactions, the medium remains unchanged so it is possible to have interference of the forward scattered and the unscattered neutrino waves which enhances the effect of matter in the neutrino propagation. In this latter case, the effect of the medium is introduced in the evolution equation for the neutrinos in the form of an effective potential which depends on the density and composition of the matter [17].

The corresponding charged-current potential for electron neutrinos is

$$V_{CC} = \sqrt{2} G_F n_e \ , \tag{2.49}$$

where $G_F$ is the Fermi weak coupling constant and $n_e$ the electron density of the medium. The analogous potential for $\nu_\mu$ and $\nu_\tau$ due to its CC interactions, is found to be 0 for most media since neither $\mu$'s nor $\tau$'s are often present.

The effective potential for any active neutrino due to the neutral current interactions in neutral matter is

$$V_{NC} = -\frac{1}{\sqrt{2}} G_F n_n \ , \tag{2.50}$$

which only depends on the neutron density of the medium. Since the neutral current potential affects all neutrino flavours equally, it can be eliminated from the evolution equation as it only contributes to an overall unobservable phase.

In the case of antineutrinos, one would only have to change the signs of both effective potentials. This change gives different oscillation probabilities for neutrinos and antineutrinos and it is key to determine the ordering of the neutrino mass eigenstates. A detailed calculation of the oscillation probabilities through matter can be found in Ref. [34].

It is useful to analyze what happens in a simplified two neutrino scenario $\nu_e - \nu_\mu$. The Hamiltonian with matter effects would be written in the flavour basis as

$$H = \frac{1}{2E} U^T \begin{pmatrix} 0 & 0 \\ 0 & \Delta m^2 \end{pmatrix} U + \begin{pmatrix} V_{CC} & 0 \\ 0 & 0 \end{pmatrix} \ , \tag{2.51}$$

where U was defined in Eq. 2.44. $\Delta m^2_m$ and $\sin^2 2\theta_m$ are the effective mass splitting and mixing amplitude that diagonalize the new Hamiltonian, defined as:

$$\Delta m^2_m = \sqrt{(\Delta m^2 \cos 2\theta - 2E_\nu V_{CC})^2 + (\Delta m^2 \sin 2\theta)^2} \ , \tag{2.52}$$

$$\sin 2\theta_m = \frac{\Delta m^2 \sin 2\theta}{\Delta m_m^2} \ , \tag{2.53}$$

The muon neutrino appearance probability in an electron neutrino beam, propagating through constant matter density becomes,

$$P_m\left(\nu_e \to \nu_\mu\right) = \sin^2 2\theta_m \sin^2\left(\frac{\Delta m_m^2 L}{4E_\nu}\right) \ . \tag{2.54}$$

Maximal mixing is achieved when $\sin^2 2\theta_m = 1$, which implies that the first term of $\Delta m_m^2$ should vanish, i.e. $\Delta m^2 \cos 2\theta = 2E_\nu V_{CC}$. This condition is satisfied regardless of the value of the vacuum mixing angle, meaning that even if the vacuum mixing is tiny, there might still be some value of the electron number density where a total transition between flavours is possible. This is known as the Mikheyev-Smirnov-Wolfenstein (MSW) resonance.

The relation between the eigenstates in matter and the flavour states are given in terms of $\theta_m$, which depends on the matter density and the neutrino energy,

$$\nu_e = \cos\theta_m \nu_{1m} + \sin\theta_m \nu_{2m} \qquad \nu_\mu = \cos\theta_m \nu_{2m} - \sin\theta_m \nu_{1m} \ . \tag{2.55}$$

The eigenstates dependence on the density of matter can be seen in Figure 2.9, where the Resonance region was defined as $\theta_m$ between 40° and 50°. At high density situations $2E_\nu V_{CC} \gg \Delta m^2 \cos 2\theta$, flavour eigenstates are $\nu_e \simeq \nu_{2m}$ and $\nu_\mu \simeq \nu_{1m}$; instead, vanishing density, i.e. vacuum condition $2E_\nu V_{CC} \ll \Delta m^2 \cos 2\theta$, leads to the original vacuum states previously described.

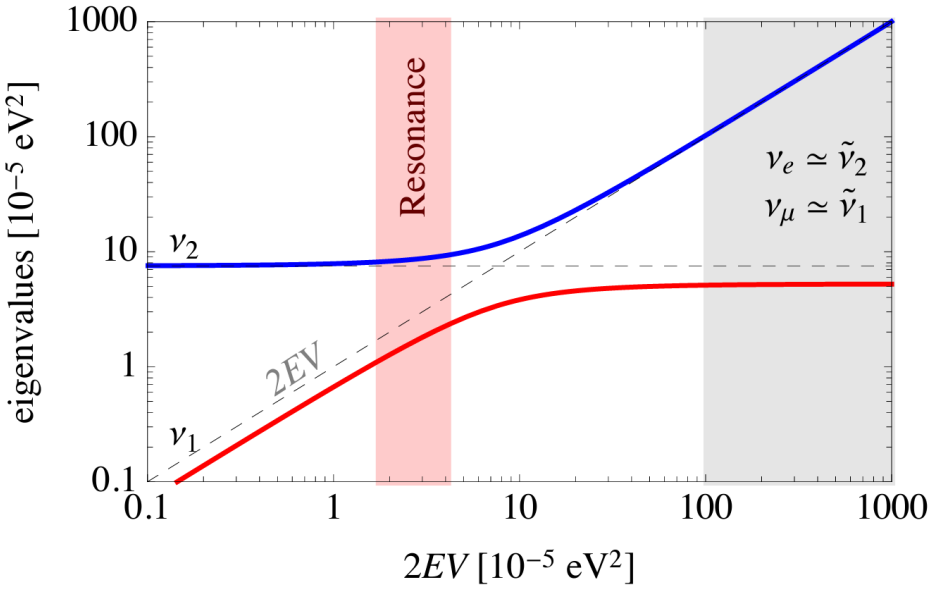


Figure 2.9: Level crossing diagram for neutrinos propagating in matter. A simplified two neutrino framework was assumed, with $\Delta m_{21}^2 = 7.5 \times 10^{-3}\ eV^2$ and $\sin^2\theta = 0.3$ for vacuum. Picture taken from Ref. [35].

The dashed lines - the electron-electron and muon-muon diagonal elements of the $m_\nu^2$ matrix - intersect at the level crossing density $n_e$ given by $n_e = \Delta m^2 \cos 2\theta / 2\sqrt{2} E_\nu G_F$.

Neutrinos produced in the Sun, where the electron density is large, would fall in the gray shaded area. There, the electron neutrino mostly coincides with the second mass eigenstates and the contribution of the other mass eigenstate is very small; as a consequence, neutrino oscillations are strongly suppressed in that region.

As the density decreases along the trajectory and assuming it does so slowly (adiabatic condition), the propagation eigenstate gradually turn into a mass eigenstate (for example $\nu_{2m} \rightarrow \nu_2$ ), following the solid lines in Figure 2.9. Outside the Sun, $\nu_{2m} \approx \nu_2$, and the mass eigenstate begins to propagate freely through the vacuum. Instead, if the density changes quickly, the $\nu_m$ state would follow the dashed lines and jump over the level crossing, as if the matter eigenstates would cross. This happens when the levels get very close, i.e. for a small vacuum mixing angle. The full treatment of neutrino oscillations in matter is beyond the scope of this section, however more detailed studies can be found in literature, such as Ref. [36].

Few important observations are worth mentioning:

1. If $\sin 2\theta = 0$, then $\sin_m 2\theta = 0$ as well, regardless of the potential. For there to be oscillations in matter, one must already have the possibility of vacuum mixing.

2. If the matter is very dense, i.e. $\Delta V \longrightarrow \infty$, then $\sin_m 2\theta \longrightarrow 0$. In very dense matter, oscillations cannot occur via matter effects, as illustrated in Figure 2.9.

3. If one chooses $\cos 2\theta > 0$, setting the order of the mass eigenstates, the resonance condition can be fulfilled for neutrinos ($V_{CC} > 0$) only if $\Delta m^2 > 0$, and for antineutrinos ($V_{CC} < 0$) only when $\Delta m^2 < 0$. One can exploit that dependency to obtain an estimate for the sign of the mass split difference, since it was previously seen that this is not possible via vacuum oscillations. Matter effects produced by the Sun have allowed solar neutrino oscillation experiments to determine the sign of $\Delta m^2_{21}$, while $\Delta m^2_{32}$ is still unknown.

## 2.8 Experimental Study of Neutrino Oscillations

Neutrino oscillations have been experimentally studied using various neutrino sources and detection techniques as summarized in Figure 2.10. Its experimental status and present anomalies are reviewed here.

### 2.8.1 Solar neutrinos

The solar neutrino problem that led to the Nobel prize award was reviewed in Section 2.2.1. However, other experiments have made their contribution towards a more precise measurement of the parameters that define the solar neutrino oscillations. In addition to the already mentioned experiments, a real-time measurement of solar neutrinos was performed by the Kamiokande experiment [38]. The Kamiokande detector was a 3 kt water-Cherenkov detector in the Kamioka mine. Super-Kamiokande, the successor of Kamiokande, started operation in 1996. Both experiments were able to observe solar neutrinos using the $\nu - e$ elastic scattering (ES), which occurs through both charged and neutral current interaction. Even if the cross section for $\nu_e$ is around 6 times larger than for $\nu_\mu$, $\nu_\tau$, it gives to the experiment sensitivity to all types of active neutrinos. Because the energy thresholds for both experiments are 6.5 MeV and 3.5 MeV respectively, they are primarily sensitive to $^8B$ neutrinos. The results from Kamiokande and Super-Kamiokande showed significantly smaller values of solar neutrinos with respect to the theoretical prediction [39].

In 2001, SNO reported the initial results of CC measurements, which combined with the high statistics measurement from Super-Kamiokande, provided a direct evidence for the existence of non$-\nu_e$ component in solar neutrino flux [40]. One year later the NC measurements was able to confirm that hypothesis with $5.3\sigma$ of statistical significance [41]. Figure 2.11 shows the fluxes of electron neutrinos $\phi(\nu_e)$ and muon and tau neutrinos $\phi(\nu_{\mu,\tau})$ with the 68% , 95% and 99% joint probability contours obtained with the SNO data. The Super-Kamiokande ES flux is also shown, as well as the SSM prediction.

In order to better understand the SSM and study in depth the MSW effect, measurements of solar neutrinos other than the $^8B$ are important. The Borexino experiment at Gran Sasso

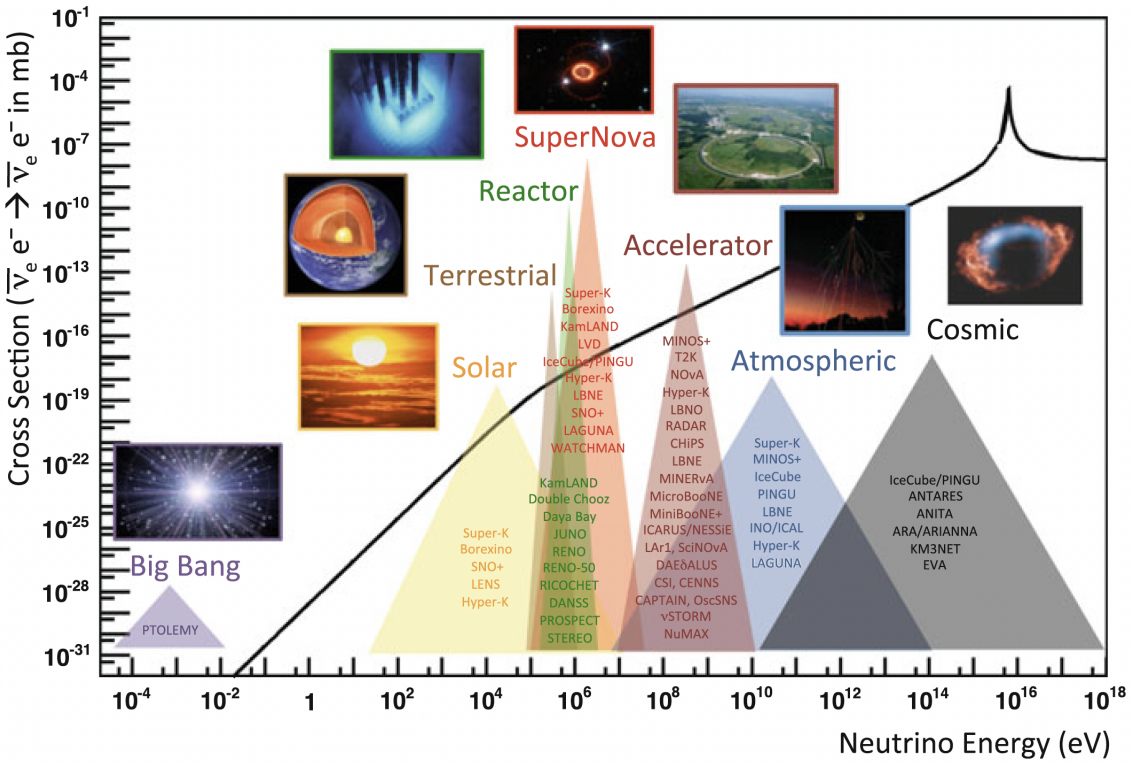


Figure 2.10: Neutrino interaction cross section as a function of energy, showing typical energy regimes accessible by different neutrino sources and experiments. The curve shows the scattering cross section for $\bar{\nu}_e e^- \longrightarrow \bar{\nu}_e e^-$ on free electrons. Figure from Ref. [37].

detects solar neutrino via $\nu - e$ scattering in real time with a much lower energy threshold. With a 300 t of ultra-pure liquid scintillator, it can achieve 0.19 MeV of energy threshold. Borexino reported the first real-time detection of $^7Be$ solar neutrinos [43], and also measured the fluxes for other reactions of the neutrino chain production. The data from all the experiments can be combined together to obtain the $\nu_e$ survival probability as a function of neutrino energy [44], indicating that the measurements were consistent with the MSW-LMA[4] solution of the solar neutrino problem.

### Gallium Anomaly

In 1968, first results from the Homestake chlorine solar neutrino experiment were announce. Ray Davis' radiochemical detector made use of the reaction $\nu_e + {}^{37}Cl \to {}^{37}Ar + e^-$ to observe $^8B$ and $^7Be$ solar neutrinos ($E_{thre} = 0.814$ MeV). Later on, $^{71}Ga$ was proposed as the target for radiochemical solar neutrino experiments due to the inferior 234 keV threshold of the reaction $\nu_e + {}^{71}Ga \longrightarrow {}^{71}Ge + e^-$ and 11.43 day half-life of $^{71}Ge$. The low threshold could provide sensitivity to the low-energy pp neutrinos, which are those generated in the first step of the pp chain via proton-proton fusion. Experiments using gallium as the detector medium are the so-called "Gallium radioactive source experiments".

In the 1970s work began to cross check the results claimed by the Homestake experiment by exposing detectors to a well-calibrated artificial neutrino source. GALLEX was a solar neutrino experiment that performed also some tests under controlled conditions, employing gallium as a $GaCl_3$ solution. After an exposure of about three weeks, the Germanium produced

[4] In the early fits to the neutrino data, three potential MSW solutions were frequently discussed, designated by small mixing angle (SMA, $\Delta m^2_{21} \sim 5.4 \times 10^{-6}\ eV^2$, $\sin^2 2\theta \sim 0.006$), large mixing angle (LMA, $\Delta m^2_{21} \sim 1.8 \times 10^{-5}\ eV^2$, $\sin^2 2\theta \sim 0.76$) and low probability and low mass (LOW, $\Delta m^2_{21} \sim 8 \times 10^{-8}$ eV, $\sin^2 2\theta \sim 0.96$) solutions.

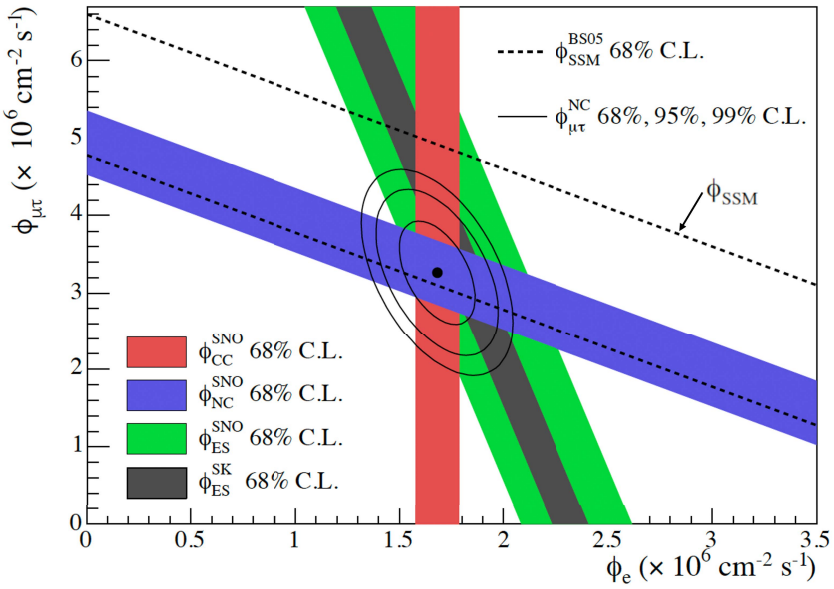


Figure 2.11: Fluxes of $^8B$ solar neutrinos, $\phi(\nu_e)$ and $\phi(\nu_{\mu,\tau})$ from SNO and SK experiments. The bands represent $1\sigma$ error and the contours the joint probability for both fluxes. The standard solar model $1\sigma$-prediction is also shown in dashed lines. Figure from Ref. [42].

via $\nu_e + {}^{71}Ga \longrightarrow {}^{71}Ge + e^-$, was recovered as $GeCl_4$ by purging nitrogen gas. The Ge-containing gas was further concentrated and purified, being finally counted following a procedure similar to those used in the chlorine experiments.

SAGE was another solar experiment that, in addition to its solar neutrino measurements, it performed some follow-up calibration measurements using gallium metal. The produced $^{71}Ge$ was separated from the metal thanks to a particular liquid solution that produced an emulsion and allowed the $^{71}Ge$ to be extracted as $GeCl_4$. The gas was further purified and counted similarly as in the GALLEX experiment.

In the mid 1990's and early 2000's, four high-activity, artificial source experiments were conducted: three with $^{51}Cr$ and one with $^{37}Ar$. These sources emitted electron neutrinos through the following electron capture (EC) processes:

$$e^- + {}^{51}Cr \longrightarrow {}^{51}V + \nu_e \qquad \text{and} \qquad e^- + {}^{37}Ar \longrightarrow {}^{37}Cl + \nu_e \; .$$

Taking into account the atomic properties of both radioactive isotopes, the energy of the emitted neutrinos would be $E_\nu \sim 810$ keV for Ar and $E_\nu \sim 746$ keV for Cr. In case of $^{51}Cr$ there was a $\sim 10\%$ probability of capture to the first excited state of $^{51}V$, which produced neutrinos with an average energy of $\sim 426$ keV. The ejected $\nu_e$ subsequently interact with the main component of the detector through the process $\nu_e + {}^{71}Ga \longrightarrow {}^{71}Ge + e^-$. The $^{71}Ge$ atoms produced by this reaction were extracted from the gallium using chemical mechanisms in order to determine the number of neutrinos produced by the radioactive sources and that had interacted with the detector media. After the counting procedure, the activity of the source was computed and compared to each theoretically predicted activity. The ratio between these two numbers was reported for both collaborations: GALLEX did two run tests using $^{51}Cr$ and reported ratios of $R_{Cr_1} = 0.953 \pm 0.11$ and $R_{Cr_2} = 0.812^{+0.10}_{-0.11}$, while SAGE also performed two calibration runs, changing the radioactive source. Its results were $R_{Cr} = 0.95 \pm 0.12$ and $R_{Ar} = 0.791^{+0.084}_{-0.078}$.

Typical precision achieved in each GALLEX and SAGE was $\gtrsim 10\%$. When combined, the four experiments yield a ratio of observed to expected counts of $R_{avg} = 0.86 \pm 0.05$, which is $\sim 2.5\sigma$ away from unity [45]. Although, the discrepancy was not statistically sufficient, it generated a great deal of speculation as to possible causes and became known as the *Gallium*

*anomaly*. In particular, the discrepancy has been often understood as tentative evidence for sterile neutrinos and $\nu_e \to \nu_s$ oscillations.

To explore the deficit of electron neutrinos previously reported in GALLEX and SAGE, the Baksan Experiment on Sterile Transitions (BEST) was designed. It is a two-distance oscillation experiment with 47 tonnes of liquid Ga metal, which exploits the same gallium reaction as previous experiments, see Figure 2.12. The radioactive source was placed at the center of the two zones of the Ga target, in order to irradiate the two volumes simultaneously. This strategy allowed to measure the production rates of $^{71}Ge$ at two different distances. The two target zones were separated at the meter scale, which was at the same scale as BEST's highest sensitivity to the oscillatory behaviour of $\nu_e$. Neutrino oscillations at this short scale would be indicated by slightly different deficits in the $^{71}Ge$ production rates within the two zones.

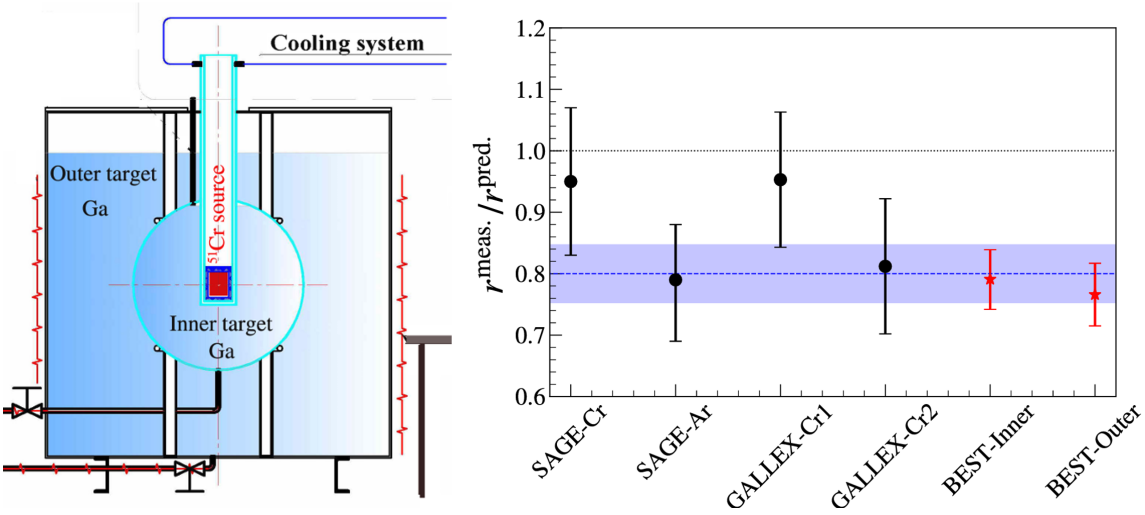


Figure 2.12: Left: Cartoon of the BEST experiment configuration showing the two nested vessels. Right: Ratio of the measured $^{71}Ge$ production rate to predicted rate for all 6 measurements described in the text. The dotted blue line (shading) is the best fit (uncertainty) to all 6 results. Figures from Ref. [45].

The measured-to-expected ratios found for BEST nested vessels were $R_{in} = 0.79 \pm 0.05$ and $R_{out} = 0.77 \pm 0.05$. The values differed significantly from unity, but were in agreement with each other within uncertainties. The result for all six measurements are displayed in Figure 2.12. The weighted average value of combining data sets for all Ga experiments is $R_{combined} = 0.82 \pm 0.03$, [45]. While the original Ga anomaly had a significance of about $2.2\sigma$, with the inclusion of BEST's results, the significance rise up to $\sim 4\sigma$.

Many cross checks of either the experimental procedure or theoretical uncertainties have been made to all gallium experiments, yet no possible explanation was found that could possible account for a $\sim 20\%$ reduction in the counting rate.

BEST results have been attributed to $\nu_e \longrightarrow \nu_s$, however the absence of any distance dependence means there is no direct evidence supporting this hypothesis. If neutrino oscillations were to happen, they would have to occur on a smaller scale than the size of the experiment.

The parameter space allowed for all combined Ga source experiments under the hypothesis of an active-to-sterile neutrino oscillation, will be presented later on.

### 2.8.2 Atmospheric neutrinos

Atmospheric neutrinos were presented in Section 2.2.2 along with the puzzle that bears his name. Kamiokande and IMB experiments were described as early experiments looking for nucleon decays, which encountered the need to study atmospheric neutrinos to precisely control their backgrounds.

After some unexpected results not predicted by the standard model, the solution to the atmospheric neutrino anomaly came from Super-Kamiokande in 1998, [27]. The zenith angle distributions of $\mu-$like events showed a clear deficit of upward-going events, while no significant asymmetry was observed for $e-$like events, results can be seen in Figure 2.13.

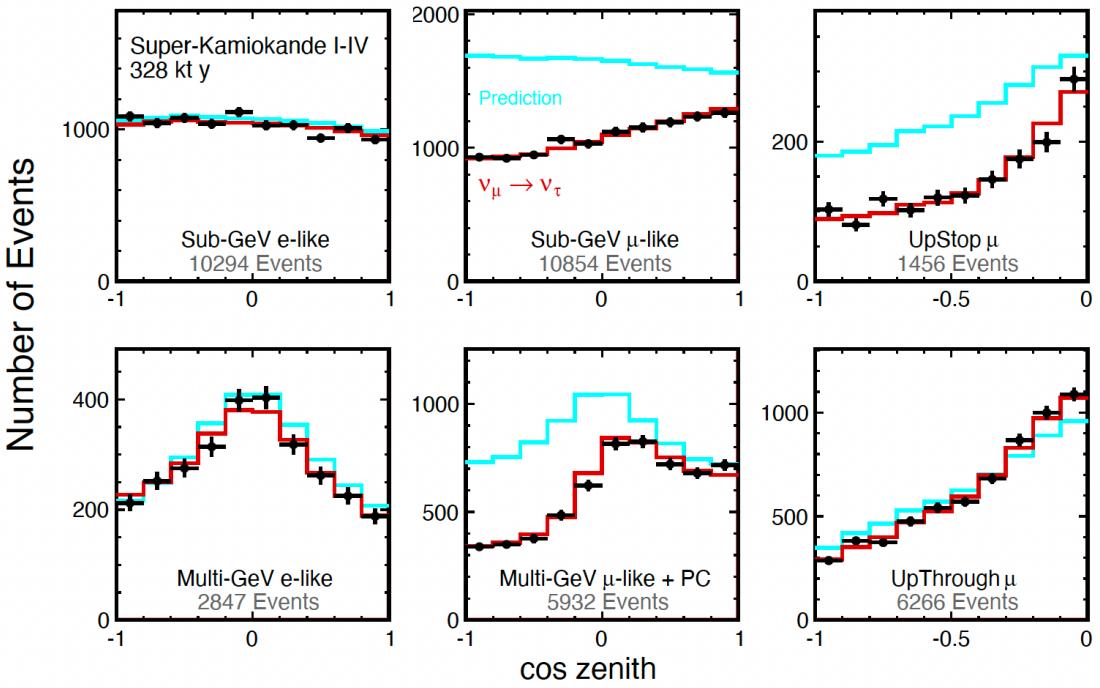


Figure 2.13: Zenith angle distributions of Super-Kamiokande neutrino events. The blue histograms show the non-oscillated Monte Carlo prediction while the red histograms show the best-fit expectations for neutrino oscillations. Picture taken from Ref. [33]

Atmospheric neutrinos have a broad range of energy, going from hundreds of MeV to more than TeV. Super-Kamiokande used the multi-GeV $\mu-$like events alone to measure the asymmetry (A) between upward and downward-going events showing a clear deviation from 0 by more than $6\sigma$ for $\mu$-like events, whereas the e-like asymmetry was consistent with 0 .

$$A_{\mu}^{up-down} = -0.296 \pm 0.048 \pm 0.01$$

$$A_{e}^{up-down} = -0.036 \pm 0.067 \pm 0.02$$

This result was considered as a model-independent evidence that part of the upward-going atmospheric muon neutrino flux was disappearing. The most likely explanation of the up-down muon asymmetry was neutrino oscillations, since the source-detector distance covered by upward-going neutrinos was much larger than that one covered by downward-going neutrinos. In other words, downward-going neutrinos did not have enough time to oscillate, while the distance traveled by upward-going neutrinos was large enough to produce a transition.

However, SK data, could not discriminate the flavour channel of the atmospheric neutrino oscillations, either $\nu_\mu \rightleftharpoons \nu_e$ or $\nu_\mu \longrightarrow \nu_\tau$.

Long baseline (LBL) experiments are sensitive to the same range of $\Delta m^2$ probed by atmospheric neutrino experiments[5]. Thus they can be used to confirm and improve the results of atmospheric neutrinos experiments. Two reactor $\bar{\nu}_e$-disappearance experiments, CHOOZ [46]

[5]Considering the wide spectrum of neutrino energies in atmospheric experiments, from $\sim$ 100 MeV to $\sim$ TeV, and their range of pathlengths, from $\sim$ 10 km to about $1.3 \times 10^4$ km, the sensitivity of atmospheric experiments covers a wide interval of $\Delta m^2 \in (10^{-4}, 10)\ eV^2$.

and Palo Verde [47], did not measure any $\bar{\nu}_e$ disappearance, excluding the $\nu_\mu \rightleftharpoons \nu_e$ oscillation solution of the atmospheric neutrino anomaly. In addition this channel was also disfavoured by the data shown in Figure 2.13; if $\nu_\mu$ were turning into $\nu_e$, one would expect an excess of $\nu_e$ coming from below, however no anomaly was seen in the electron-like data.

SK data favoured the $\nu_\mu \longrightarrow \nu_\tau$ channel also over the $\nu_\mu \longrightarrow \nu_s$ channel, where $\nu_s$ stands for sterile neutrino. This is due to the fact that no matter effects for neutrino oscillation through the Earth was appreciated in $\mu$-like events. In $\nu_\mu \longrightarrow \nu_\tau$ transitions, there are no matter effect, as both flavours are subject to the same interaction with matter, in contrast $\nu_\mu \longrightarrow \nu_s$ transitions would be affected by matter effects as $\nu_s$ do not interact with matter by definition, causing an asymmetry between $\nu_\mu$- and $\nu_s$-matter effects.

In 2005, SK reported a best-fit values in the $\sin^2 2\theta$ - $\Delta m^2$ plane for $\nu_\mu \longrightarrow \nu_\tau$ of $\sin^2 2\theta = 1.00$ and $\Delta m^2 = 2.1 \times 10^{-3}\ eV^2$, [48].

This results were later confirmed by other atmospheric neutrino experiments such as MACRO [49] and Soudan 2 [50].

The Soudan 2 experiment was located 710 m underground in the Soudan underground Mine State Park in USA, beneath an overburden of 2070 meter water equivalent (m.w.e.). The main detector was an iron tracking calorimeter which operated as a time projection chamber. It had a total fiducial mass of 770 tons and took data from 1989 to 2001. Soudan 2 measured the ratio between the electron and muon ratios of observed to predicted events, for sub GeV neutrinos, reporting a value in agreement with those measured in IMB and SK experiments. Figure 2.14 shows the 90% allowed region in the $\sin^2 2\theta - \Delta m^2$ plane for $\nu_\mu \longrightarrow \nu_\tau$ oscillations found by Soudan 2, compared with the SK and the Monopole Astrophysics and Cosmic Ray Observatory (MACRO) experiment allowed regions. The overlap between curves show the compatibility of the results. Soudan 2 allowed region is much larger than that of the SK experiment, this is due to the small statistics collected in Soudan 2 with respect to SK. Nevertheless, such confirmation was of utmost importance, since it was obtained through a completely different technology from the previously used water Cherenkov detectors.

The other confirmation of SK's results came from the MACRO, a large area multipurpose underground experiment designed to search for rare events in the penetrating cosmic radiation. The detector was placed in the Gran Sasso National Laboratories in Italy, under $\simeq 3700$ m.w.e., which defines a minimum muon energy on surface of $\sim 1.3$ TeV in order to reach MACRO detector. The primary goal of MACRO was to search for magnetic monopoles, however its design, optimized for high resolution tracking and timing, allowed MACRO to operate also as a neutrino detector and cosmic ray observatory. Upward going muons were identified by a streamer tube system (for tracking) and a scintillator technique (for time-of-flight measurement), and separated from the downward-going muons background. Data was taken from 1989 to 2000 and several strategies were adopted in order to overcome uncertainties due to the calculation of neutrino fluxes and to optimize the oscillation signal. As a first step, the experiment considered the ratio between the number of events with reconstructed neutrino energy lower than 30 GeV and higher than 130 GeV. The experimental ratio reported was $R = 0.85 \pm 0.16$ to be compared with the Monte Carlo prediction in case of no oscillations $R = 1.50 \pm 0.25$ or with $R = 1.00 \pm 0.17$ in an oscillated scenario (using their best fit values, with maximal mixing $\sin^2 2\theta = 1$ and $\Delta m^2 = 2.5 \times 10^{-3}\ eV^2$).

Finally, MACRO also took advantage of the zenith angle distribution of upward through-going muons, finding that the $\nu_\mu \longrightarrow \nu_s$ oscillations were disfavoured at 99% confidence level compared to the $\nu_\mu \longrightarrow \nu_\tau$ channel.

Combining the information from the energy estimate and angular distributions MACRO reported a deficit of events corresponding to more than $4\sigma$, which could be explained considering oscillations of $\nu_\mu$ to $\nu_\tau$. The 90% confidence level allowed region of MACRO data set is shown in Figure 2.14, where agreement is found between the curves of the three aforementioned experiments.

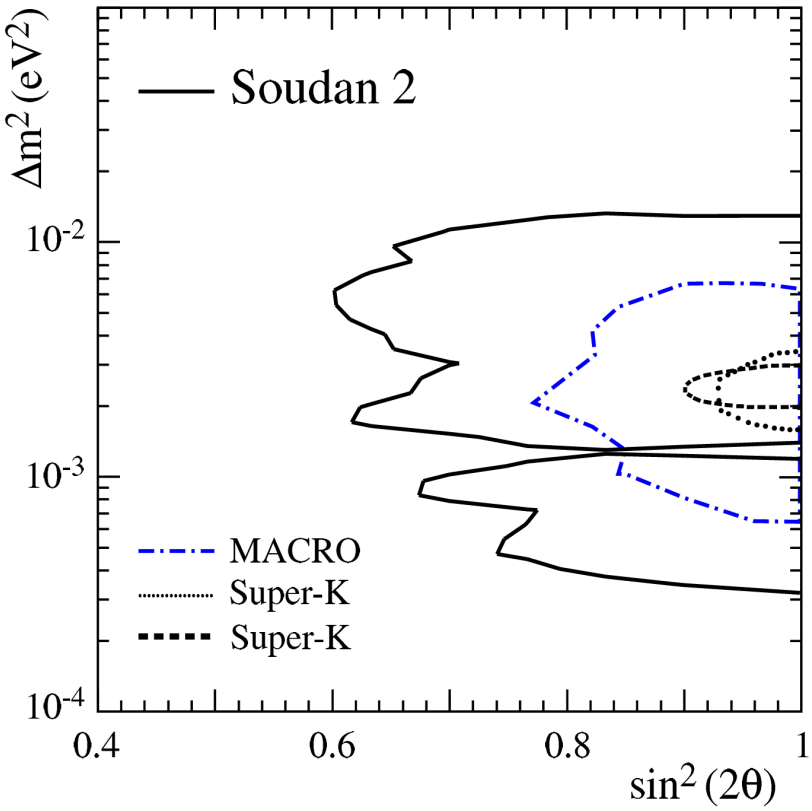


Figure 2.14: 90% confidence allowed regions in the $\sin^2 2\theta, \Delta m^2$ parameter space for Soudan 2 (solid line), MACRO (blue line) and Super-Kamiokande zenith angle (dotted line) and energy (dashed line) analyses. Picture taken from Ref. [51]

In order to find direct experimental proof of $\nu_\mu - \nu_\tau$ oscillation, an appearance signal of $\nu_\tau$ was searched for in the atmospheric neutrino data. Due to the high energy threshold (more than 3.5 GeV) of $\nu_\tau$ CC interactions and the short lifetime of the $\tau$ lepton (0.3 ps), the observation of this transition was very challenging. Super-Kamiokande reported evidence of $\nu_\tau$ appearance with atmospheric neutrino data with $4.6\sigma$ significance [52]. However, the definitive observation of $\nu_\mu \longrightarrow \nu_\tau$ was made by the long-baseline experiment, OPERA [53] and recently confirmed by the IceCube collaboration [54].

Neutrino telescopes such as ANTARES and IceCube were primarily built for high-energy neutrino astronomy, nevertheless they can also measure neutrino oscillations with atmospheric neutrinos. Both experiments consist of arrays of PMTs placed in the Mediterranean Sea and the Antarctic ice, respectively. By observing the charged current interaction of up-going $\nu_\mu$, they are able to measure $\nu_\mu$ disappearance, [55, 56].

There are several projects for atmospheric neutrino observations under preparation, for example ORCA in the KM3NeT project [57] in the Mediterranean Sea, IceCube Upgrade [58] at the South Pole and ICAL[6] planned at the India-based Neutrino Observatory [59]. Future large underground detectors as Hyper-Kamiokande in Japan [60] or DUNE in the US [61] will also be able to study atmospheric neutrinos.

[6]ICAL will be a 50 kt magnetized iron tracking calorimetry detector, in contrast to the PMT based technology used by the previous experiments.

### 2.8.3 Reactor antineutrinos

Reactor neutrinos have also played a crucial role in neutrino oscillations. They have helped to understand the solar anomaly and provided unique information on the $\theta_{13}$ mixing angle.

Nuclear reactors are the major source of human-generated neutrinos. They are very intense, pure and isotropic sources of $\bar{\nu_e}$'s in the MeV energy region, generated in nuclear fission of heavy isotopes[7]. The neutrino flux from the reactor can be estimated based on the thermal power output and fuel composition as a function of time.

$\bar{\nu_e}$ disappearance is the only available channel to study neutrino flavour changes with reactor experiments. Charged current interactions cannot happen if a reactor $\bar{\nu_e}$ changes its flavour to $\bar{\nu_\mu}$ or $\bar{\nu_\tau}$, as its energy is not sufficient to produce heavier charged leptons. The inverse beta decay (IBD) $\bar{\nu_e} + p \longrightarrow e^+ + n$ provides a way to detect $\bar{\nu_e}$ in the relevant energy region. The energy released by the prompt signal from the positron is related to the incoming neutrino energy. In addition, the delayed coincidence in time of the $\gamma$ emitted by the neutron capture is very efficient in terms of suppressing the backgrounds. Scintillation liquids are often used to build large detectors, where the hydrogen is the target of the inverse beta decay. These detectors are often loaded with gadolinium to increase the neutron detection efficiency, because of a large neutron capture cross-section and higher energy of the emitted $\gamma$ rays[8].

Such technique was used in the CHOOZ experiment [46], which was looking for $\bar{\nu_e}$ disappearance from the CHOOZ nuclear power plant in France during the 1990s. No evidence for $\nu_e \longrightarrow \nu_\mu$ oscillations at the $10^{-3}$ scale were found, which resulted in stringent upper-bound limits of the mixing angle depending on the $\Delta m^2$. Despite the negative result, CHOOZ constraints were extremely relevant to the global interpretation of solar and atmospheric neutrino data in the framework of three neutrino mixing.

Table 2.1 shows a list of reactor $\bar{\nu}$ experiments measuring neutrino oscillations. Note that the experiments are designed with a wide range of baselines, in order to account for the different scale of mass splittings found by the solar and atmospheric neutrino experiments. Experiments with longer baselines $\mathcal{O}(100)$ km are sensitive to $\Delta m^2$ of $10^{-4} - 10^{-5}\ eV^2$, while shorter baselines $\sim \mathcal{O}(1)$ km, have sensitivities in the range of $10^{-2} - 10^{-3}\ eV^2$.

| Name | Reactor Power ($GW_{th}$) | Baseline (km) | Detector mass (t) | Year |
|---|---|---|---|---|
| KamLAND | various | 180 (in ave.) | 1000 | 2001- |
| Double Chooz | $4.25 \times 2$ | 1.05 | 8.3 | 2011-2018 |
| Daya Bay | $2.9 \times 6$ | 1.65 | $20 \times 4$ | 2011-202 |
| RENO | $2.8 \times 6$ | 1.38 | 16 | 2011- |

Table 2.1: List of reactor antineutrino oscillations experiments and characteristics

The neutrino oscillation in the solar range was confirmed by the KamLAND long-baseline reactor experiment. KamLAND was a 1 kton liquid scintillator detector located at the original Kamiokande cavern, $\sim$ 2700 m.w.e of depth and an average distance of 180 km from the nuclear power plant. They were looking for the disappearance of electron neutrinos at $L/E \sim 10^{-5}\ eV^2$, in the oscillation range indicated by the solar data.

The collaboration reported their first results in 2002 showing evidence for reactor $\bar{\nu_e}$ disappearance at the 99.95% confidence level [62]. The proof came from the measurement of the ratio of observed $\bar{\nu_e}$ events over expectations without oscillations as a function of the reactor distance. The deficit measured by KamLAND, $R = 0.611 \pm 0.085 \pm 0.041$ is shown in the left plot of Figure 2.15 and is also compared to the previous unsuccessful experiments. This result was consistent

[7] The four main isotopes contributing to the antineutrino flux are $^{235}$U, $^{238}$U, $^{239}$Pu and $^{241}$Pu.

[8] The total energy is about 8 MeV for the Gadolinium, in contrast to the 2.2 MeV $\gamma$-emitted for the neutron capture by hydrogen.

with large value of the mixing angle corresponding to the LMA solution, reported by the solar neutrino experiments.

In 2004, KamLAND presented the first evidence of $\bar{\nu}_e$ spectrum distortion consistent with neutrino oscillations expectations. New results including more statistics, increased the significance of the spectral distortion above $5\sigma$, allowing unequivocal interpretation of the KamLAND results in terms of $\bar{\nu}_e$ oscillations. Figure 2.15 right, shows the allowed contours in the oscillation parameter space for solar and KamLAND data, individually and combined, from the three-flavour oscillation analysis when $\theta_{13}$ is not constrained.

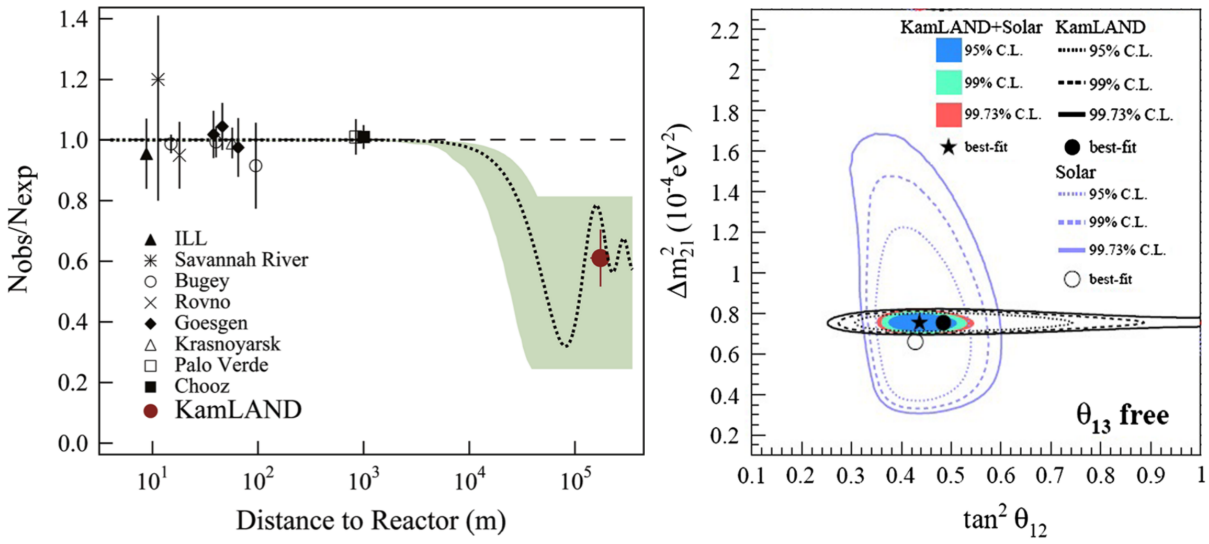


Figure 2.15: Left: Ratio of measured to expected $\bar{\nu}_e$ flux from reactor experiments. The green shaded region indicates the range of flux predictions corresponding to the 95% C.L. Right: Three flavour neutrino oscillation analysis including solar and KamLAND data. Plots from Ref. [63]

Following the establishment of neutrino oscillations, the measurement of the remaining mixing angle $\theta_{13}$ was set as the next major milestone. To be sensitive to a small value below the limit set by early reactor detectors (such as CHOOZ and Palo Verde [47]), experiments with two detectors were proposed. Examples of those are Double Chooz [64] in France, Daya Bay [65] in China and RENO [66] in Korea. These three experiments employed a similar detector design and all three collaborations published their first results in 2012, establishing with great significance a non-zero value of $\theta_{13}$.

$$\sin^2 2\theta_{13} = 0.087 \pm 0.041 \pm 0.030 \qquad \text{Double CHOOZ}$$
$$\sin^2 2\theta_{13} = 0.092 \pm 0.016 \pm 0.005 \qquad \text{Daya Bay}$$
$$\sin^2 2\theta_{13} = 0.113 \pm 0.013 \pm 0.019 \qquad \text{RENO}$$

In all of them, as well as in NEOS experiment [67], an excess of $\bar{\nu}_e$ events over the expected energy spectrum was observed around 5 MeV, present in both near and far detectors and scaling with the reactor power, which still lacks explanation.

With a medium-baseline of $\sim$ 50 km and fine energy measurement, reactor antineutrino experiments have significant sensitivity to the mass ordering. While the sign of the solar mass splitting is known thanks to how matter affects neutrino oscillations, the atmospheric mass splitting will be addressed with reactor antineutrinos experiments which only rely on the oscillation interference between $\Delta m^2_{31}$ and $\Delta m^2_{32}$. JUNO experiment [68], actually under construction, aims to determine the mass ordering as its primary goal with this latter approach.

**Reactor Neutrino Anomaly** The antineutrino fluxes produced by the fissionable isotopes have been calculated several times since the discovery of neutrinos in the Cowan and Reines reactor experiment. In 2011, new calculations by Mueller [69] and Huber [70] (HM model) predicted reactor antineutrino fluxes that were about 5% larger than previous estimations and larger than the fluxes measured in several short-baseline reactor neutrino experiments. This discrepancy is known as the "*Reactor Antineutrino Anomaly*" (RAA) [71]. Such disagreement is quantified with the average ratio across experiments, reporting a value of $R = 0.925^{+0.025}_{-0.023}$ with a significance of $2.9\sigma$, where the updated HM model was used.

Besides the HM, which is the basis of the RAA, several models have been proposed to better define the reactor antineutrino fluxes. A detailed review of the current status can be found in this Ref. [72]. Newer calculations relying on more recent measurements of the decays of $^{235}U$ were published, resulting in a better agreement with the experimental data. The most up-to-date calculation, using the Kurchatov Institute (KI) model results in $R = 0.975^{+0.022}_{-0.021}$, lowering down the discrepancy to $1.1\sigma$ significance. Results are shown in Figure 2.16.

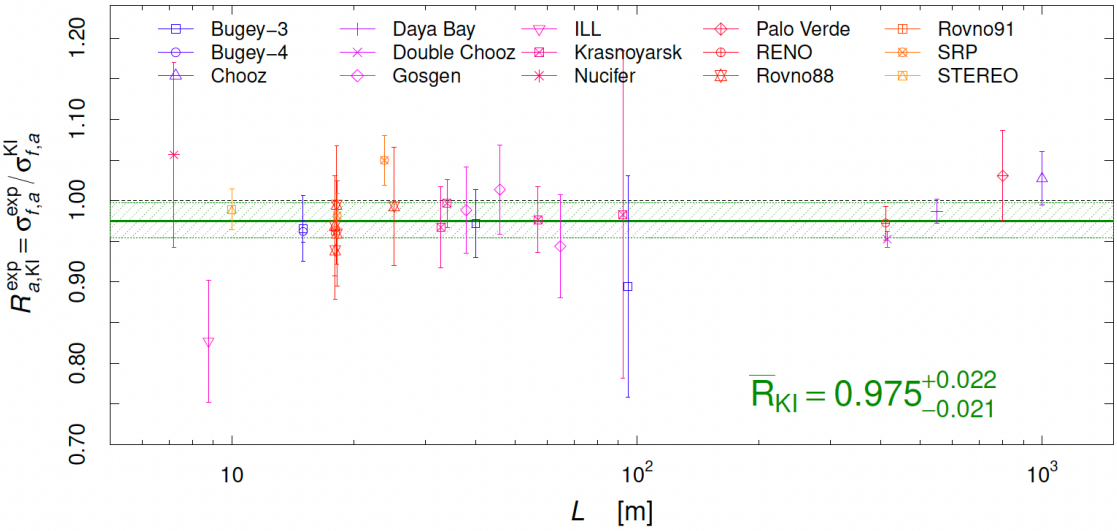


Figure 2.16: Ratio of measured and expected IBD yields for the reactor experiments considered in the analysis as a function of the reactor-detector distance (L) for the KI model. The horizontal green band shows the average ratio $\bar{R}$ and its uncertainty. Picture taken from Ref. [72]

Possible hints of neutrino oscillation at a scale of $\Delta m^2 \sim 1\ eV^2$ have motivated reactor experiments at a very-short-baseline $L \sim \mathcal{O}(10m)$ from the core. These newer generation of experiments attempted to measure the inverse $\beta$ decay yield at different distances through segmented or movable detectors. Exploiting relative comparisons, these were sensitive to baseline dependent spectral distortions induced by oscillations without having to rely on neutrino flux predictions. Examples of such experiments are NEOS [67], DANSS [73], STEREO [74], PROSPECT [75] and NEUTRINO-4 [76]. The first four reported null results, disfavouring and further weakening the RAA. NEUTRINO-4 experiment was the only one claiming evidence of a signal at the $2.9\sigma$ level and will be further discussed.

This anomaly is still under study both by the experimental community, with a set of follow-up measurements performed at short-baselines using either reactor or accelerator $\nu$ sources, and by the theoretical community looking for improvements of the reactor flux calculations.

### NEUTRINO-4 Anomaly

Neutrino-4 experiment is a 1.8 $m^3$ Gd-doped liquid scintillator detector divided into 10 rows, each one consisting of 5 sections of 0.225 m × 0.225 m × 0.85 m. The total volume of the detector

is 1.8 $m^3$, yet the first and last detector rows are used as shielding, reducing the detector fiducial volume to 1.42 $m^3$.

The experimental setup is constructed to measure the flux and spectrum of the reactor antineutrinos $\bar{\nu}_e$ as a function of distance to the center of the active zone of the SM-3 reactor (Dimitrovgrad, Russia). Thanks to the movable platform, the detector is able to sample baselines from 6 to 12 m.

Neutrino-4 selection technique includes time intervals and topological criteria to discriminate inverse $\beta$ decay events from background. Prompt ($e^+$) and corresponding delayed ($\gamma$ from neutrino capture by Gd) signals have to occur in 300 $\mu$s time window, were only events with a time gap less than 100 $\mu$s are considered as correlated, while the rest become a basis for estimation of accidental coincidence background. The background is one of the main problems of the experiment; the correlated background might occur due to fast neutrons, where the prompt signal is produced by the recoil proton emitted in the elastic scattering of a neutrino on hydrogen (being one of the main components of the scintillator).

When attempting to study neutrino oscillations, the correct analysis method involves using averaged ON-OFF signal spectrum for each distance.

However measurements in the mode when reactor was ON and OFF are preferred to be close in time in order to better compensate for temporal fluctuations of the cosmic background. This can be done taking advantage of the short reactor on (off) cycles of 8-10 (2-5) days, where signal and background measurements few days apart are possible.

The detector collected data between 2016-2021. Measurements with the reactor on were carried out for a total of 720 calendar days, recording $\sim$ 300 events/day while additional 860 days of reactor off mode allowed extensive background measurements as well. The experiment performed a sterile neutrino search in the $L/E$ space and reported a $2.9\sigma$ evidence of neutrino oscillation effect with the best-fit at [76]:

$$\sin^2(2\theta_{14}) = 0.36 \pm 0.12(stat) \quad \text{and} \quad \Delta m^2_{14} = 7.3 \pm 0.13(stat) \pm 1.16(syst)\ eV^2\ .$$

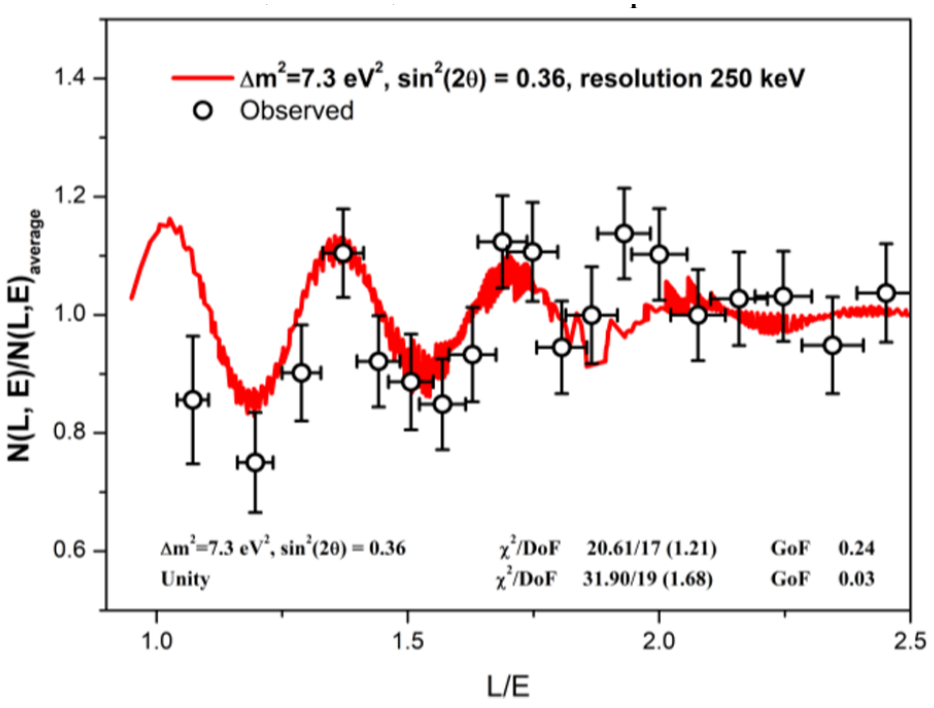


Figure 2.17: $L/E$ distribution of background subtracted neutrino rates reported by the Neutrino-4 experiment, showing the oscillatory curve of the neutrino signal. The red line is the expected behaviour considering the best-fit values. Figure taken from Ref. [77].

The claim of Neutrino-4 was of strong impact to the community, as their allowed regions for an additional neutrino state were strongly rejected by other experiments, such as PROSPECT or STEREO. Recently, the Neutrino-4 collaboration has published some joint analysis with the GALLEX, SAGE and BEST experiments, claiming a good agreement with their results and further increasing the confidence level [77].

The Neutrino-4 experiment is planning to upgrade their current experimental facility to increase statistical precision. The upgraded detector will contain 4 identical modules, each consisting of a square grid of 25 segments, thus triplicating the volume. At the same time, there are other experiments which are addressing the sterile neutrino problem. For instance, the Short-Baseline (SBN) experiment based at Fermilab which will be explained in detail in Chapter 3.

### 2.8.4 Accelerator Neutrinos

Conventional neutrino beams from accelerators are produced by colliding high-energy protons onto a target, producing $\pi$ and $K$, which in turn decay into neutrinos. Undecayed mesons and muons are stopped in a beam dump and soil. Pions are the most abundant product of high energy collisions, hence the usual neutrino beams contain a dominant amount of muon-type neutrinos or antineutrinos.

In order to have a better control of the beam, focusing devices called magnetic horns are used to concentrate the neutrino beam flux towards the desired direction. One can choose the dominant component of the beam to be either neutrinos or antineutrinos by focusing positive or negative mesons with the magnetic horns. Even with the focusing horns, wrong sign neutrinos contaminate the beam, as well as a small amount of $\nu_e/\bar{\nu}_e$ coming from kaon and muon decays.

In order to maximize the sensitivity of the experiment, the ratio of baseline and neutrino energy ($L/E$) should be chosen to match the oscillation effects to be studied.

Several detectors at accelerators have adopted the new off-axis configuration, which yields an almost monochromatic neutrino flux in a detector slightly shifted by a small angle from the axis of a high intensity neutrino beam. For an on-axis detector, the neutrino energy is proportional to the pion energy, leading to a wide neutrino energy spectrum if the range of pion energies is wide. However, as soon as one moves slightly off-axis, the energy of the neutrino beam is more independent from the pion energy and pions with different energies produce neutrinos in a similar low-energy region. As a result, a narrower energy spectrum is obtain, which can be exploit to reduce systematic uncertainties in cross section and oscillation analysis[9].

Another advantage of the off-axis configuration is that, as neutrino energy is much smaller than the pion energy, the neutrino oscillation length is shorter and there is an enhanced sensitivity to small values of $\Delta m^2$. The problem with this technique is the reduced neutrino flux, thus large detectors and intense sources are needed. The off-axis beam method was first introduced in 1995 [78] and has been adopted in T2K and NO$\nu$A experiments. Figure 2.18 shows the neutrino energy spectrum measured by NO$\nu$A for different off-axis angles, where the spectrum becomes more narrow and peaked at lower energies as the off-axis angle increases.

There are different scales of baselines for accelerator-based experiments according to the desired study range of $\Delta m^2$. Atmospheric mass splitting of $\Delta m^2 \sim 2.5 \times 10^{-3}\ eV^2$ gives rise to the first oscillation maximum at $L/E \sim 500\ GeV/km$, hence a $\sim 1\ GeV$ accelerator neutrino beam will require a long baseline of few hundred to thousand km. On the other hand, searches for a possible oscillation at the $\sim 1\ eV^2$ scale, only require $\sim 1$ km baseline if studied with $\sim 1$ $GeV$ neutrinos from accelerators.

#### Long-baseline experiments

[9] Taking into account that the incoming neutrino energy is unknown in an event by event basis, neutrino flux predictions are often an important source of systematic uncertainties.

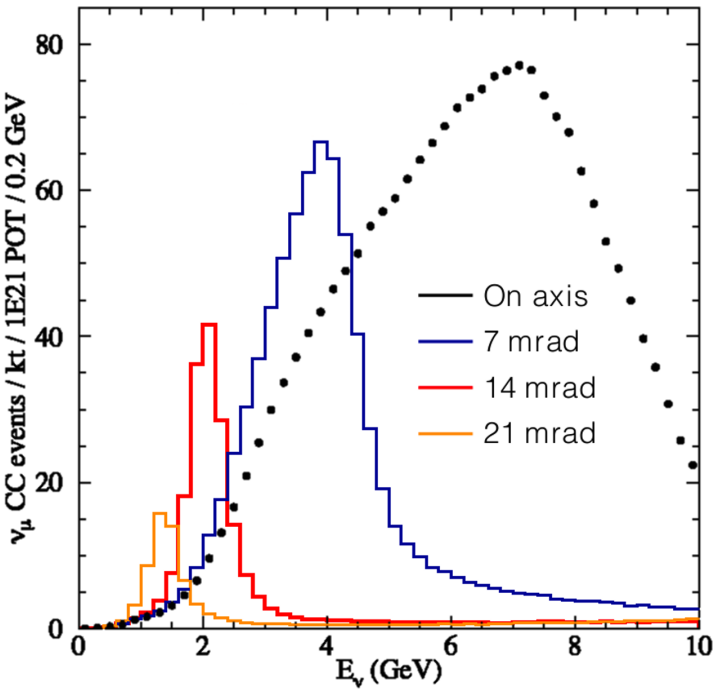


Figure 2.18: Charged current $\nu_\mu$ event rates for the NO$\nu$A experiment at various off-axis locations relative to its source beam. Figure from NO$\nu$A Collaboration.

Many long-baseline experiments use two detectors to reduce the systematic uncertainties arising from neutrino flux and neutrino-nucleus interactions. Both detectors typically use the same technology and target nucleus. In this way, the systematic uncertainties relative to the neutrino flux, energy spectrum, interaction cross-section and detector response largely cancel out in the near far comparison. Even with this clever approach, one should be aware that the neutrino flux is inevitably different between the near and the far detectors characterized by nonidentical angular acceptance.

The first long-baseline experiment was the K2K which used a neutrino beam from KEK 12 GeV proton synchrotron with a baseline of 250 km. K2K confirmed the $\nu_\mu$ disappearance originally reported by the Super-Kamiokande atmospheric neutrino observation [79].

The MINOS experiment used the NuMI beam from Fermilab, a near detector, at 1 km downstream, and a far detector, 735 km away from the production target. It was an iron-scintillator tracking calorimeter detector that was able to combine accelerator and atmospheric neutrino data to measure oscillation parameters using both appearance and disappearance channels [80].

Long-baseline experiments were also based in Europe, using the CNGS neutrino beamline from CERN to LNGS with about 730 km of baseline. In particular, the beam energy was chosen so that CC interactions of $\nu_\tau$ had enough energy to occur and a direct confirmation of $\nu_\tau$ appearance was possible. The Oscillation Project with Emulsion-tRacking Apparatus (OPERA) was able to confirm the $\nu_\mu \longrightarrow \nu_\tau$ oscillation appearance with a statistical significance of $6.1\sigma$ [53]. ICARUS [81] was another experiment exposed to the CNGS, with a complete different technology with respect to the one employed by OPERA and was operated in Gran Sasso from 2010 to 2012 exploring $\nu_\mu \longrightarrow \nu_e$ transitions in the CNGS $\nu$ beam. ICARUS Liquid Argon Time Projection technology (LArTPC) and its data taking operation will be exhaustively detailed in the next chapters.

All these experiments were part of the first generation of long-baseline experiments aiming to confirm the existence of neutrino oscillations. A further step arrived with the second-generation experiments whose goal was to observe the $\nu_\mu \longrightarrow \nu_e$ oscillation, together with precise measurements of the unknown parameters of neutrino oscillations, i.e. search for CP violation,

measurement of the mass ordering and the octant of $\theta_{23}$.

The T2K experiment started in 2010 and was the first long-baseline experiment to employ an off-axis neutrino beam. In 2014, T2K was able to confirm $\nu_\mu \longrightarrow \nu_e$ oscillations with more than $7\sigma$ [82], proving again that a non-zero amplitude generated by the $\theta_{13}$ mixing angle was mandatory (within the $3\nu$ mixing framework). By combining data from neutrino and antineutrino mode, T2K was also able to report some hint of CP violation [83].

Another experiment using the off-axis configuration was the NO$\nu$A experiment in US. The experiment started in 2014 and after years of data taking was able to prove $\nu_e$ appearance from $\nu_\mu$ beam for both neutrino and antineutrino modes [84, 85]. It also reported some limits to the CP-violating phase.

Two large scale long-baseline experiments are under preparation to address most of the unknowns from the neutrino oscillation paradigms, for instance making more precise measurements. Their physics program will also include searches for nucleon decays as well as study of supernova neutrinos. DUNE [61] will be a 1300 km long-baseline experiment based in the US, exploiting the liquid argon time projection chamber technology. On the opposite side of the globe, the Hyper-Kamiokande experiment (Japan) will be a water Cherenkov detector with a 295 km baseline.

#### Short-baseline experiments

It has been presented in this section that several anomalies have emerged between existing oscillation data and the three flavour neutrino framework; short-baseline experiments are no exception. What is common to all these anomalous measurements is that the experiments detect neutrinos at short-baselines ($L \sim 10$ m $-$ 1 km), which induce faster oscillations and consequently undetectable by long-baseline experiments (sensitive to $\Delta m^2 \sim 0.1 - 100\ eV^2$).

#### LSND Anomaly

The LSND detector (Liquid Scintillator Neutrino Detector) [86] was the first oscillation experiment to report positive result in the short baseline scenario. It operated at Los Alamos between 1993 and 1998, searching for $\bar{\nu}_\mu \longrightarrow \bar{\nu}_e$ oscillations through the appearance of $\bar{\nu}_e$ in the single near detector, located 29.8 m from the neutrino source. A 800 MeV proton beam was used to produce pions that stopped in the target. Most of the $\pi^-$'s were absorbed by the nuclei inside the target, while $\pi^+$'s and their daughter $\mu^+$'s decayed and produced muon neutrinos through the following sequence: $\pi^+ \longrightarrow \mu^+ + \nu_\mu$ and $\mu^+ \longrightarrow e^+ + \nu_e + \bar{\nu}_\mu$. As a result, the produced neutrinos were mostly $\nu_\mu$, $\bar{\nu}_\mu$ and $\nu_e$ with a minimal intrinsic contamination of $\bar{\nu}_e$.

The signal selection proceeded via the identification of a positron from inverse beta decay, followed by detection of a 2.2 MeV photon from subsequent neutron capture that is correlated with the positron both in time and position. This powerful signature is schematically illustrated in the following Figure 2.19. The detector was a Cherenkov tank surrounded by photomultipliers allowing particle identification and precise determination of both energy and angle of the outgoing positron.

A series of LSND measurements were published, all in support of an excess of events observed over that expected from beam-on and beam-off neutrino background. The final results published in 2001 [88] reported an excess of $87.9 \pm 22.4(\text{stat}) \pm 6.0(\text{sys})$ $\bar{\nu}_e$ events more than expected in absence of neutrino oscillations. Because of the double signature, interpreting the excess of events due to particles other than $\bar{\nu}_e$ is difficult. If this excess is interpreted as $\bar{\nu}_\mu$ oscillation to $\bar{\nu}_e$, under the short-baseline approximation $\Delta m^2_{21} \approx \Delta m^2_{31} = 0$, then the best fit oscillation point is at

$$[\sin^2(2\theta), \Delta m^2_{23}] = (0.003, 1.2\, eV^2)\ .$$

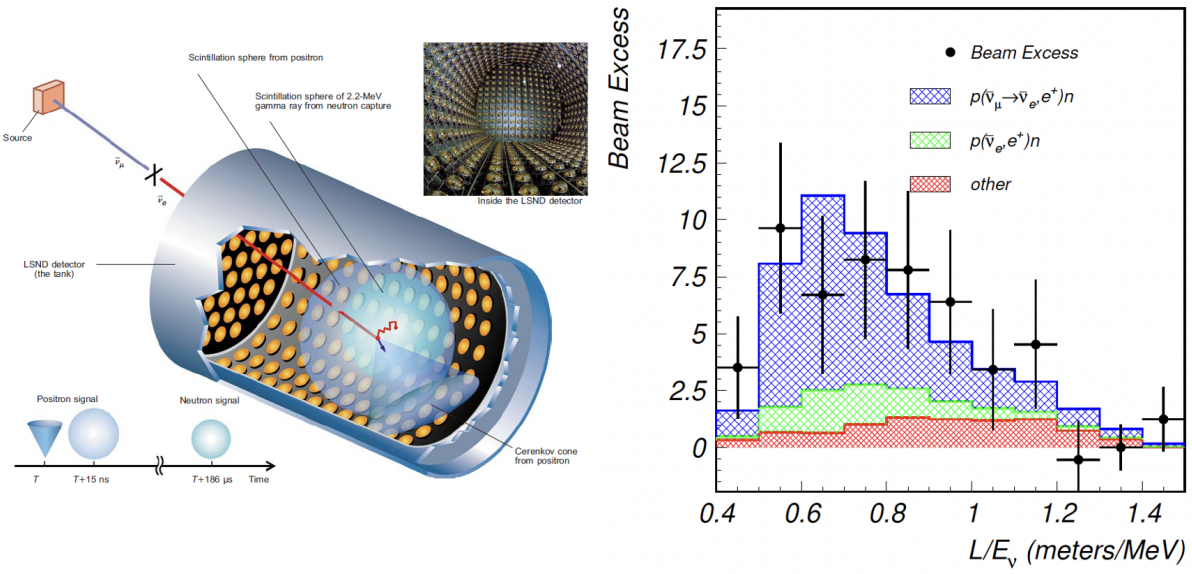


Figure 2.19: Left: LSND experiment, consisting of a cylindrical liquid scintillator equipped with over a thousand photomultipliers, able to measure $\bar{\nu}_e$ exploiting the double signature of $e^+$ followed by neutron capture. Figure from Ref. [87]. Right: LSND anomalous events as a function of $L/E_\nu$ for a subset of total events. The red and green histograms show the beam's expected contamination of $\bar{\nu}_e$, while the blue histogram represents the distribution under the light sterile neutrino hypothesis for the best-fit value, reported in the text, to the data (black dots). More information can be found in Ref. [88], from which this figure was taken from.

It is known that solar and atmospheric experiments give rise to two well defined mass scales $\Delta m^2_{12} = 8\times10^{-5}\ eV^2$ and $|\Delta m^2_{23}| = 2.3\times10^{-3}\ eV^2$. The LSND result imply then 3 independent mass splitting, and therefore at least one additional neutrino state[10], as can be seen in Figure 2.20.

### MiniBooNE Low Energy Excess

The LSND evidence for two-neutrino oscillation beginning in the late 1990's prompted the need for an independent follow-up experiment to test the results. Such test needed to rely on different systematics and methodology, while preserving sensitivity to the same $\Delta m^2$ and $\sin^2(2\theta_{\mu e})$. A $\pi^+$ decay-in-flight accelerator beam can produce $\nu_\mu$-dominated flux with higher mean energy, providing an opportunity for an independent test at longer baseline and through different detection methods. This independent test was realized by the MiniBooNE Cherenkov detector [91] using the Booster Neutrino Beam (BNB) at US Fermi National Accelerator Laboratory, able to provide a $\sim$ 99.5% pure $\nu_\mu$ beam with a mean $E_\nu \sim 600$ MeV. The detector was shaped as a sphere of roughly 5 m of radius and filled with about 800 t of mineral oil. Surrounded by a thousand photomultipliers, MiniBooNE could detect various final states through different types of Cherenkov "rings" as illustrated in Figure 2.21, being able to differentiate between electrons, muons, charged and neutral pions.

A crucial point to understand the MiniBooNE's results is to be aware of its capabilities and limitations. The experiment was not only insensitive to the difference between electrons and photons, but also to the discrimination between protons and neutrons. Therefore, to reconstruct the incoming neutrino energy, the interactions were assumed to be quasi-elastic, i.e. elastic on

[10] Obviously the introduction of a new neutrino state has to be in agreement with all previous experiments and measurements. For instance with the LEP experiment strongly constraining the number of active neutrino flavours.

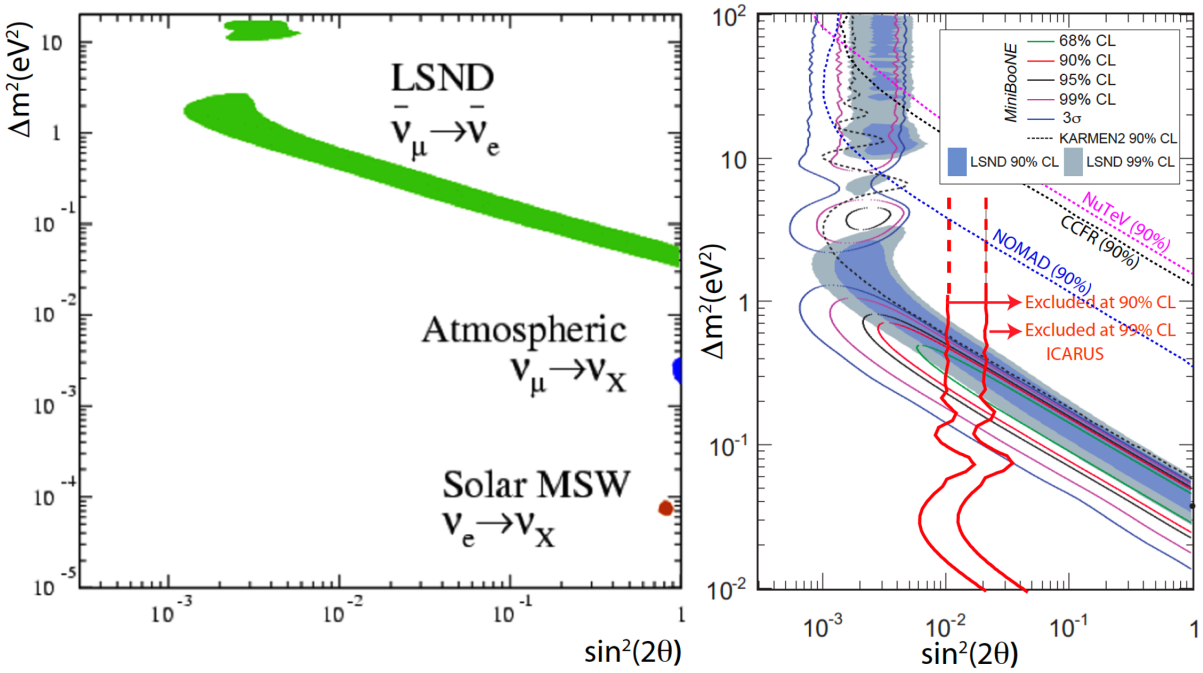


Figure 2.20: Left: Two dimensional plot of $\Delta m^2$ vs $\sin^2 2\theta$ showing the allowed regions including atmospheric, solar and LSND data. Figure from Ref. [89]. Right: Same parameter space plane showing the LSND allowed regions in comparison with the main published experiments sensitive to the $\nu_\mu \longrightarrow \nu_e$ anomaly, from Ref. [90].

a single, unbounded nucleon, which is mostly the case at the experiment energy range.

The first results from MiniBooNE, published in 2007, showed no evidence for oscillations within two-neutrino $\nu_\mu \longrightarrow \nu_e$ appearance paradigm [93]. However this result was performed only for events with neutrino reconstructed energy $E_\nu^{QE} > 475$ MeV, and a further examination to the region below this energy showed an excess of events, often referred to as the MiniBooNE "Low Energy Excess" (LEE).

Since those first results, MiniBooNE ran for approximately ten more years, collecting BNB data in both neutrino and antineutrino running modes. MiniBooNE's final results [94] are reproduced in Figure 2.22, showing an excess of data over background prediction in both $\nu$ and $\bar{\nu}$ data sets, as a function of the reconstructed electron candidate energy. The excess is predominantly evident below 600 MeV and presents an overall discrepancy of $4.8\sigma$ when combining all data sets. The significance was mostly dominated by systematics and corresponds to $560.6 \pm 119.6$ and $77.4 \pm 28.5$ excess events in neutrino and antineutrino running modes respectively. The final best-fit parameters for the full $\nu$ and $\bar{\nu}$ data sets, were found to be

$$[\sin^2(2\theta), \Delta m^2_{23}] = (0.807, 0.043\, eV^2)\ .$$

Figure 2.23 shows the radial coordinate of the interaction vertex, pointing towards an excess related to the beam and not simply a background effect. The excess is concentrated in the inner part of the detector, similar to the standard neutrino interactions, excluding its possible relationship with backgrounds close to the boundary of the detector.

These observations have helped motivate and understand conventional interpretations involving energy misreconstruction due to mismodeled nuclear effects, mis-estimated backgrounds, as well as other beyond-SM physics as the source of the MiniBooNE anomaly. The MicroBooNE experiment [96] was proposed in 2008 to provide a direct test of the MiniBooNE excess where a completely different technology was employed to overcome potential inefficiencies.

Many checks were performed on the MiniBooNE data to ensure the correct estimation of

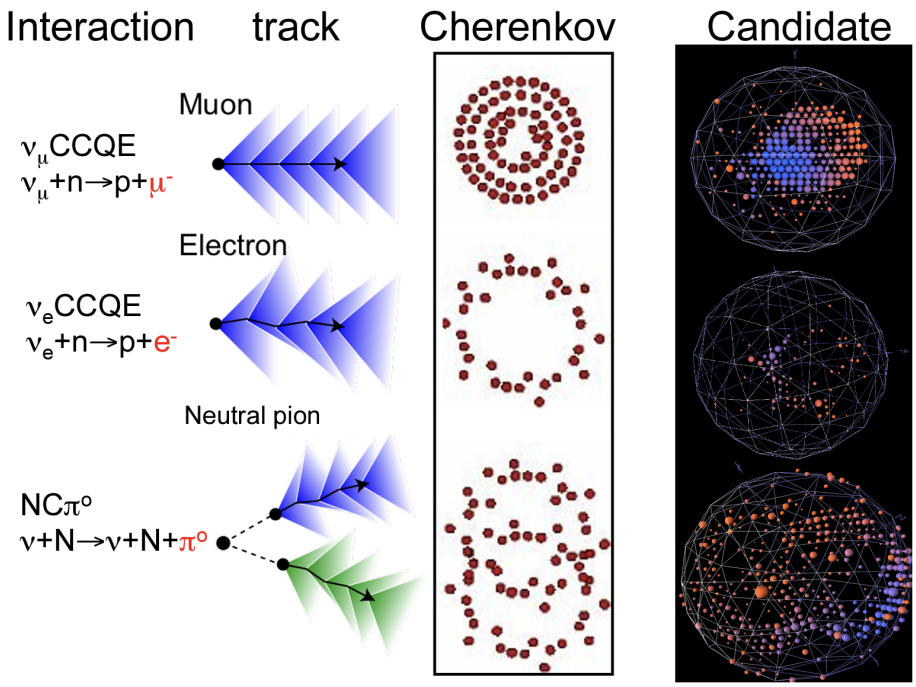


Figure 2.21: MiniBooNE particle reconstruction. From top to bottom, a muon neutrino charged-current quasi-elastic (CCQE) interaction, an electron neutrino CCQE, a neutral current and finally a neutral pion production interaction. The second and third columns show the characteristics of tracks and Cherenkov rings, and the last column shows the event display of candidate events. Figure taken from Ref. [92].

backgrounds, however no relevant contribution was identified that could explain the excess of events. On the right-hand plot of Fig. 2.20 different MiniBooNE CL contours for $\bar{\nu}_\mu \longrightarrow \bar{\nu}_e$ oscillations are shown, where the allowed regions are in agreement with the previous results of LSND.

In 2013, results from the ICARUS experiment on the search for a $\nu_\mu \longrightarrow \nu_e$ signal due to the LSND anomaly with the CNGS neutrino beam were presented. ICARUS' results strongly limited the allowed options for the LSND anomaly to a narrow region around $[sin^2(2\theta), \Delta m^2_{23}] = (0.005, 0.5\, eV^2)$, where an overall agreement with LSND and MiniBooNE results was found. ICARUS exclusion curves are shown in Figure 2.20 as well.

A conclusive result clarifying at $5\sigma$ level the nature of the LSND anomaly and the possible existence of sterile neutrinos is still needed. LSND and MiniBooNE were single detector experiments, so two innovative concepts have been chosen for the short-baseline neutrino (SBN) program at Fermilab [97], with the aim of further investigating the reported excess. In first place, the use of Liquid argon time projection chamber (LArTPC) technology provides excellent tracking and reconstruction capabilities; secondly, the multi-detector design measuring the same neutrino spectrum at 3 different distances from the target should be a straight forward evidence in case any spectra is distorted due to oscillations. The SBN program in which MicroBooNE also takes part, will be described in more detail in the next chapter.

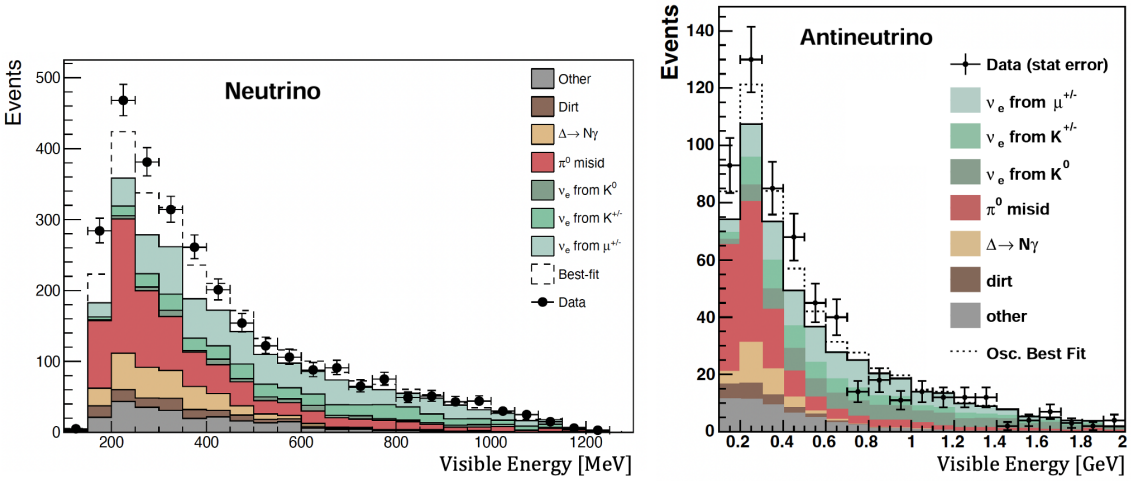


Figure 2.22: Final MiniBooNE results corresponding to $18.75 \times 10^{20}$ proton on target (POT) in neutrino mode (left figure, from Ref. [94]) and $11.27 \times 10^{20}$ in antineutrino mode (right figure, from Ref. [95]) for the reconstructed visible energy. Note that the analysis were done with different data samples, the best fit line does not correspond to the exact same point in the sterile parameter space.

### 2.8.5 Combined Analysis of Experimental Results

#### The $3\nu$ Paradigm

From the experimental situation described above one can conclude several results:

- Several long-baseline experiments were able to prove the $\nu_\mu \longrightarrow \nu_\tau$ appearance in a muon neutrino beam. However an independent cross check came from the atmospheric $\nu_\mu/\bar{\nu}_\mu$ disappearance most likely converting to $\nu_\tau/\bar{\nu}_\tau$, where the results show an energy and distance dependence in agreement with the one predicted by the mass-induced oscillations.

- Accelerator $\nu_\mu/\bar{\nu}_\mu$ disappearance occurs over distances of hundreds km, oscillating to the electron (anti)neutrino flavour. The clear oscillation behaviour seen in the energy spectrum is in fair agreement with the effect observed in atmospheric experiments.

- Solar $\nu_e$ oscillates to $\nu_\mu/\nu_\tau$, where the energy dependence is well described by massive neutrino conversion inside the Sun material according to the MSW effect.

- Reactor antineutrinos disappear over distances of $\sim 1.5$ km and $\sim 200$ km with different probabilities. These are generated by two different mass splitting values; at short distance in agreement with the $\nu_\mu$-disappearance observed in accelerators while at more longer baselines compatible with the MSW conversion in the Sun.

From these results, it can be stated that the three-flavour oscillation is of great success when describing the processes of all these 4 situations. However several anomalies were presented which can not be explained within the $3\nu$ framework and might point towards the existence of additional neutrino states with masses at the eV scale. The simplest extension of the active neutrino picture together with its implication will be described in the following section. An up-to-date description of the current situation will also be given.

In total, the $3\nu$ oscillation analysis of the existing data involves six parameters: 2 mass differences, 3 mixing angle and 1 CP phase. The different experiments that have been described all along this Chapter provide information on different subsets of these parameters, which are

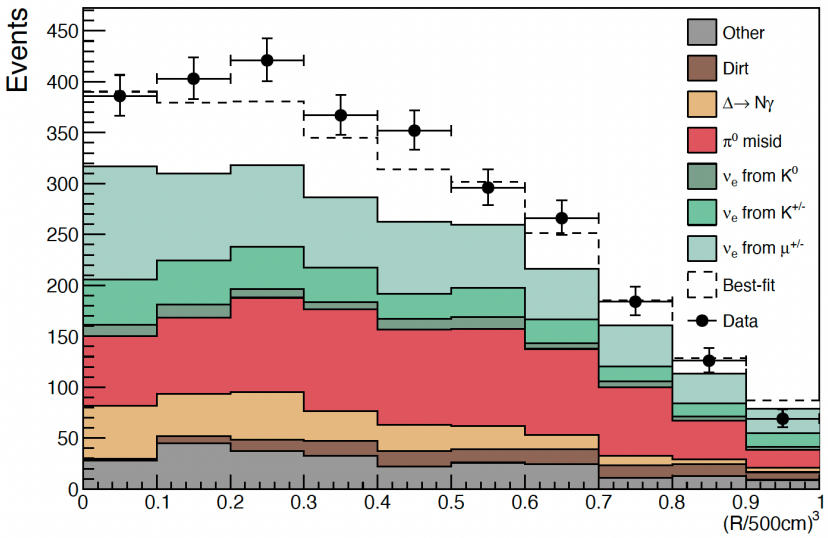


Figure 2.23: The final MiniBooNE results in neutrino mode in terms of the reconstructed radial position of the spherical detector. Figure taken from Ref. [94].

summarized in Table 2.2. The dominant contribution (standalone measurements) has been discriminated from its possible contribution when combining results from different experiments (important). It is then clear that the determination of all parameters requires global analysis of the data from different experiments.

| Experiment | Dominant | Important |
|---|---|---|
| Solar Experiments | $\theta_{12}$ | $\Delta m^2_{21}$, $\theta_{13}$ |
| Reactor LBL (KamLAND) | $\Delta m^2_{21}$ | $\theta_{12}$, $\theta_{13}$ |
| Reactor MBL (Daya Bay, RENO, Double Chooz) | $\theta_{13}$, $\Delta m^2_{31,32}$ | |
| Atmos. Exp (SK, IceCube - DeepCore ) | | $\theta_{23}$, $\lvert\Delta m^2_{31,32}\rvert$, $\theta_{13}$, $\delta_{CP}$ |
| Accel LBL $\nu_\mu$ (K2K, MINOS, T2K, NO$\nu$A) | $\theta_{23}$, $\lvert\Delta m^2_{31,32}\rvert$ | |
| Accel LBL $\nu_e$ (MINOS, T2K, NO$\nu$A) | $\delta_{CP}$ | $\theta_{13}$, $\theta_{23}$ |

Table 2.2: Experiments contributing to the present determination of the oscillation parameters. Table from Ref. [33], where a more detail description can be found.

Over the years, the responsibility of combining the data from all the experiments to determine the oscillation parameters have been in the hands of some phenomenological groups. It is of no surprise that the determination of the parameters show some dependence on variations of the statistical treatment performed, as well as on the data samples included. Table 2.3 shows the results of one of the latest global analysis.

Different analysis find consistent results, in particular on the $\theta_{12}$, $\theta_{13}$, $\Delta m^2_{21}$ and $|\Delta m^2_{32}|$ parameters. On the other hand, there are some issues which still require clarification, such as

- Ordering discrimination: In all the latest analysis the best fit is for the normal mass ordering. Inverted ordering is disfavoured with $\Delta\chi^2$ ranging from slightly above $2\sigma$ (driven by the combination of long-baseline accelerators and short-baseline reactor data) to $3\sigma$ when Super-Kamiokande atmospheric data is added.

- Determination of the octant of $\theta_{23}$: whether the value lies in the first ($\theta_{23} < \pi/4$) or second octant ($\theta_{23} > \pi/4$). All analysis find some preference for the second octant but with statistical significance well below $3\sigma$.

- Measurement of the leptonic CP phase, $\delta_{CP}$: the best fit for the complex phase in the normal ordering configuration is at $\delta_{CP} \sim 120°$, but CP conservation ($\delta_{CP} \sim 180°$) is still allowed at a confidence level of $1 - 2\sigma$. The significance of the CP violation is strongly reduced in the global analysis due to the null results observed by NO$\nu$A.

Next generation experiments, some of them described in the text, are going to address these problems aiming to achieve more precise measurements and detailed knowledge of the current anomalies in the near future.

| Parameter | Best Fit $\pm 1\sigma$ | $3\sigma$ Range |
|---|---|---|
| $\Delta m^2_{21}$ $[10^{-5} eV^2]$ | $7.34^{+0.17}_{-0.14}$ | 6.92 - 7.91 |
| $\Delta m^2_{32}$ $[10^{-3} eV^2]$ (NO) | $2.419^{+0.035}_{-0.032}$ | 2.319 - 2.521 |
| $\Delta m^2_{32}$ $[10^{-3} eV^2]$ (IO) | $-2.478^{+0.035}_{-0.033}$ | -2.577 - -2.375 |
| $\sin^2\theta_{12}$ $[10^{-1}]$ (NO) | $3.04^{+0.14}_{-0.13}$ | 2.65 - 3.46 |
| $\theta_{12}$ [°] (NO) | $33.46^{+0.87}_{-0.88}$ | 30.98 - 36.03 |
| $\sin^2\theta_{12}$ $[10^{-1}]$ (IO) | $3.03^{+0.14}_{-0.13}$ | 2.64 - 3.45 |
| $\theta_{12}$ [°] (IO) | $33.40^{+0.87}_{-0.81}$ | 30.92 - 35.97 |
| $\sin^2\theta_{23}$ $[10^{-1}]$ (NO) | $5.51^{+0.19}_{-0.80}$ | 4.30 - 6.02 |
| $\theta_{23}$ [°] (NO) | $47.9^{+1.1}_{-4.0}$ | 41.0 - 50.9 |
| $\sin^2\theta_{23}$ $[10^{-1}]$ (IO) | $5.57^{+0.17}_{-0.24}$ | 4.44 - 6.03 |
| $\theta_{23}$ [°] (IO) | $48.2^{+1.0}_{-1.4}$ | 41.8 - 50.9 |
| $\sin^2\theta_{13}$ $[10^{-2}]$ (NO) | $2.14^{+0.09}_{-0.07}$ | 1.90 - 2.39 |
| $\theta_{13}$ [°] (NO) | $8.41^{+0.18}_{-0.14}$ | 7.9 - 8.9 |
| $\sin^2\theta_{13}$ $[10^{-2}]$ (IO) | $2.18^{+0.08}_{-0.07}$ | 1.95 - 2.43 |
| $\theta_{13}$ [°] (IO) | $8.49^{+0.15}_{-0.14}$ | 8.0 - 9.0 |
| $\delta_{CP}$ [°] (NO) | $238^{+41}_{-33}$ | 149 - 358 |
| $\delta_{CP}$ [°] (IO) | $247^{+26}_{-27}$ | 193 - 346 |

Table 2.3: $3\nu$ oscillation parameters obtained from a fit to global data. The numbers labeled as NO (IO) are obtained assuming the normal (inverted) ordering configuration. Results are reported from Ref. [98].

### 2.8.6 Direct measurements of neutrino mass

The properties of neutrinos and especially their rest mass play an important role in cosmology, particle and astroparticle physics. Neutrino oscillation experiments provide compelling evidence that neutrinos are massive but they cannot provide any hint about the absolute mass value, neither of their Dirac or Majorana nature. There are two complementary approaches for measuring neutrino masses in laboratory experiments: one is the precise spectroscopy of beta decay and its kinematic endpoint, while the other one is the search for neutrinoless double beta decay (also known as $0\nu\beta\beta$).

The only model-independent information on the neutrino masses can be extracted from energy-momentum conservation relation in reactions in which a neutrino or antineutrino is involved. In 1933 Fermi proposed such a kinematic search for the $\nu_e$ neutrino mass in the end part of the beta spectra in $^3H \longrightarrow {}^3He + e^- + \bar{\nu}_e$ decay. By definition, $\beta$-decays are transitions that always occur between mirror nuclei, which are pairs of nuclei with equal numbers of protons and neutrons plus an extra proton in one case an extra neutron in the other. Tritium $\beta$-decay is a superallowed transition between mirror nuclei, where superallowed refers to allowed transitions between nuclei belonging to the same isospin multiplet. As a consequence, the nuclear matrix elements are independent of the electron energy and the electron spectrum is exclusively determined by the phase space:

$$\frac{dN}{dE} = Cp_eE_eE_\nu p_\nu F(Z,E_e) = Cp_eE_e(Q_\beta - T)\sqrt{(Q_\beta - T)^2 - m_{\nu_e}^{eff}}F(Z,E_e)\ . \tag{2.56}$$

Where C is a constant and $F(Z,E_e)$ is the Fermi function which describes the electromagnetic interaction of the produced electron with the final state nucleus. The neutrino energy is given by $E_\nu = Q_\beta - T$, with electron kinetic energy $T = E_e - m_e$ and $Q_\beta$ the Q-value of the process, being the total energy of the leptons minus the electron mass ($Q_\beta = M_i - M_f - m_e$). The maximal kinetic energy of the electron is $T_{max} = Q_\beta - m_{\nu_e}^{eff}$, which is equivalent to the Q-value only if massless neutrinos are assumed. Finally, the neutrino momentum is given by

$$p_\nu = \sqrt{E_\nu^2 - m_{\nu_e}^{eff\,2}} = \sqrt{(Q_\beta - T)^2 - m_{\nu_e}^{eff\,2}}\ , \tag{2.57}$$

which gives the neutrino mass dependency in $\beta$-decays. This relation is satisfied regardless of the Dirac or Majorana nature of neutrinos, thus the direct measurement of neutrino mass with $\beta$-decay experiments do not give any information on the Dirac or Majorana origin of the neutrino mass.

If $m_{\nu_e}^{eff}$ is small, its effect on the electron spectrum is maximal at the upper end of the energy spectrum (end point), where kinetic energy is close to maximal and $Q_\beta - T \simeq m_{\nu_e}^{eff}$. However, few events occur near the end point, precisely, the relative number of events present in an interval of energy $\Delta T$ below the end point is given by

$$\frac{n(\Delta T)}{n} \propto \left(\frac{\Delta T}{Q_\beta}\right)^3\ . \tag{2.58}$$

It is clear then, that in order to maximize the number of events in the region of interest the Q-value needs to be as small as possible. The most stringent information on the electron neutrino mass using this method has been obtained with tritium, which has a $Q_\beta = 18.574$ keV being one of the smallest among all known $\beta$-decays. In addition the tritium half-life is relatively short (12.3 years), which implies an acceptable number of observed events during the experiment lifetime. Finally, the simple atomic structure of tritium leads a more accurate calculation of atomic effects with respect to those of heavier atoms.

The Kurie function is defined as

$$K(T) \equiv \sqrt{\frac{dN}{dE}\frac{1}{p_eE_eF(Z,E_e)}}\ . \tag{2.59}$$

and if the electron neutrino mass is zero,it has a linear behaviour with respect to the kinetic energy, $K(T) = Q_\beta - T$. Instead, a non-vanishing neutrino mass provokes a distortion from the straight-line T-dependence and there is an early falloff of the electron spectrum near the end point, which is shifted from $T_{max} = Q_\beta$ to $T_{max} = Q_\beta - m_{\nu_e}^{eff}$, indicated in Figure 2.24 as point B. Information on the value of the neutrino mass is obtained by looking for a distortion of the Kurie plot rather than measuring the shift of the end point, as the latter has a very small event rate. The most recent result using tritium decay comes from KATRIN [99], employing a molecular gaseous tritium source with a sophisticated array of subdetectors that combine strong magnetic fields, a spectrometer and a silicon detector downstream. No indication of $m_{\nu_e}^{eff} \neq 0$ has been found so far, hence KATRIN has set an upper limit of $m_{\nu_e}^{eff} < 1.1$ eV at 90% CL. The detector is still operative nowadays and it is expected to reach a sensitivity of $\sim 0.2$ eV.

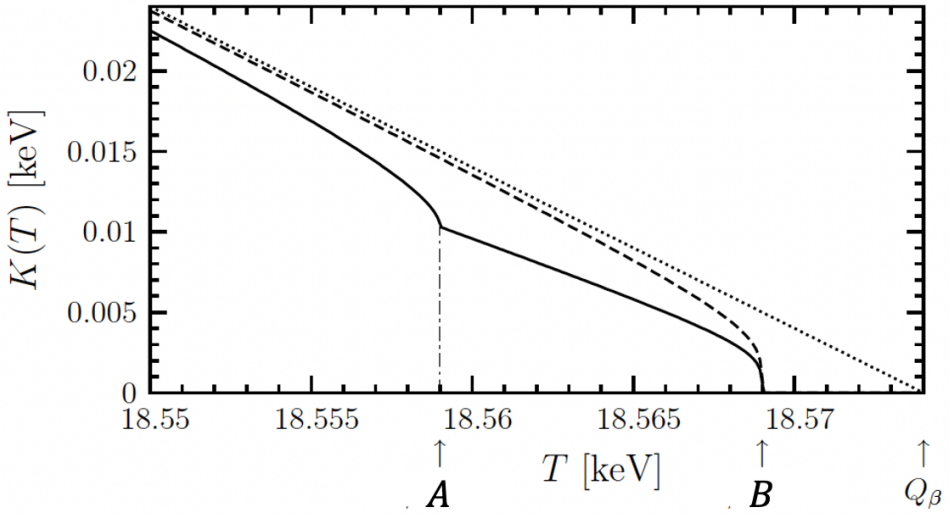


Figure 2.24: Kurie plot from tritium $\beta$-decay. Dotted line shows the linear behaiour of the function for $m_{\nu_e}^{eff} = 0$. Dashed line is the Kurie function for $m_{\nu_e}^{eff} = 5$ eV, while the solid line describes the same function for two neutrino mixing with $m_1 = 5$ eV, $m_2 = 15$ eV, producing distortions at B and A respectively, and $|Ue_1|^2 = |Ue_2|^2 = 1/2$, $|Ue_3|^2 = 0$. Figure from Ref. [34]

Alternative isotopes to tritium are $^{163}$Ho and $^{187}$Re with $Q$-values of 2.8 keV and 2.47 eV respectively, which are still far from being competitive with tritium but are expected to have considerable improvements in the future.

Accurate measurements of the kinematics in the decay of charged pions can give analogous information on the $\nu_\mu$ and $\nu_\tau$ masses, Ref. [33].

$$m_{\nu_\mu}^{eff} < 190 \text{ keV (90\% CL)} \qquad \text{from } \pi^- \longrightarrow \mu^- + \bar{\nu}_\mu \,,$$
$$m_{\nu_\tau}^{eff} < 18.2 \text{ MeV (95\% CL)} \qquad \text{from } \tau^- \longrightarrow n\pi + \nu_\tau \,.$$

In the case of neutrino mixing, the electron neutrino is a superposition of the massive neutrinos ($\nu_i$) with weights given by the $U_{ei}$ elements of the neutrino mixing matrix. The distortion of the beta spectrum would then be governed by the sum of the individual spectra generated incoherently by each final neutrino state ($^3H \longrightarrow {}^3He + e^- + \bar{\nu}_i$). The main characteristics of the mixing-induced distortions of the Kurie functions are

- A shift of the end point of the spectrum from $T = Q_\beta$ to $T = Q_\beta - m_{lightest}$
- Kinks at the electron kinetic energies $T_i = Q_\beta - m_i$, for $\nu_i \neq \nu_{lightest}$, with sizes that are determined by the value of $|U_{ei}|^2$.

This is also illustrated in Figure 2.24, where point B indicates the kink due to a $m_1 = 5$ eV and A is caused by $m_2 = 15$ eV.

$\beta$-decay experiments have the possibility of revealing a possible mixing of the electron neutrinos with more than three massive neutrinos, especially if the additional massive neutrinos are heavier than few eV, as the Kurie spectrum would suffer further distortions.

In the $3\nu$ mixing scenario, and recalling the standard parametrization of the mixing matrix already presented, the effective electron neutrino mass in $\beta$-decays, can be described and bounded to

$$1.1eV \geq m_{\nu_e}^{eff} = \sqrt{\sum_i m_i^2 |U_{ei}|^2} = \begin{cases} \sqrt{m_0^2 + \Delta m_{21}^2 (1 - c_{13}^2 c_{12}^2) + \Delta m_{32}^2 s_{13}^2} & \text{in NO,} \\ \sqrt{m_0^2 + \Delta m_{21}^2 c_{13}^2 c_{12}^2 - \Delta m_{32}^2 c_{13}^2} & \text{in IO,} \end{cases} \tag{2.60}$$

where $m_0$ is the lightest neutrino mass, corresponding to $m_1$ for NO and $m_3$ for IO spectrum. Given the present knowledge of the neutrino mass differences and their mixing from oscillation experiments, it is possible to use the equation above to set allowed values for $m_{\nu_e}^{eff}$ as a function of the lightest neutrino mass state and depending on the mass ordering; using the best fit values reported in Table 2.3 the lower bounds are $m_{\nu_e}^{eff} > 0.048$ eV for IO and $m_{\nu_e}^{eff} > 0.0085$ eV for NO at 95% CL.

Direct information on neutrino masses can also be obtained from neutrinoless double beta decay ($0\nu\beta\beta$) searches. This process violates the total lepton number by two units and requires Majorana neutrinos, thus in case of positive results, the process would prove that neutrinos are their own antiparticles.

The neutrinoless double beta decay was proposed by W.H. Furry in 1939 and is forbidden in the standard model. Under the hypothesis of massive Majorana neutrinos, a nucleus which can decay through a $2\beta_{2\nu}$ process can also decay through a $2\beta_{0\nu}$ process, even though their lifetimes are very different. A $2\beta_{0\nu}$ decay can be generated at lower order in perturbation theory by the term represented in Figure 2.25 left. However, this process can also occur through other mechanism besides the exchange of a Majorana massive neutrinos such as processes involving new interactions or new particles beyond the standard model. It is reasonable to believe that these additional contributions would not exactly cancel the standard process shown in Figure 2.25 as this would require a fine-tuned arrangement of masses and mixings at all orders of perturbation theory, nonetheless the effective Majorana mass could be slightly modified.

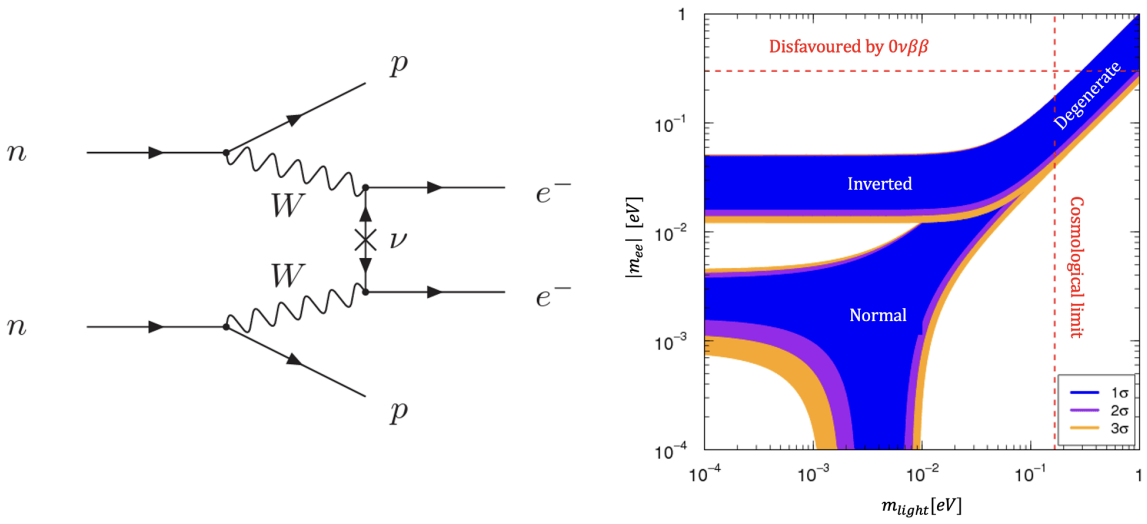


Figure 2.25: Left: Feynman diagram for neutrinoless double beta decay. Right: Effective Majorana neutrino mass as a function of the lightest neutrino mass for different mass ordering schemes. Picture taken from EXO-200 Collaboration.

The observable determined by the $0\nu\beta\beta$ experiments is the half-life of the decay, which sets a limit on the effective Majorana neutrino mass. Under the assumption that the Majorana neutrino mass is the only source of lepton number violation at low energies, the decay half-life of a certain nucleus is given by:

$$[T^{0\nu}_{1/2}]^{-1} = G^{0\nu}|M^{0\nu}|^2 \left(\frac{m_{ee}}{m_e}\right)^2 . \tag{2.61}$$

Where $G^{0\nu}$ and $M^{0\nu}$ are the phase space integral taking into account the final atomic state and the nuclear matrix element of the transition, respectively. While $G^{0\nu}$ can be computed with rather small uncertainties, $M^{0\nu}$ is more challenging, as it requires an accurate nuclear model. $m_{ee}$ is the effective Majorana mass of $\nu_e$ given by

$$m_{ee} = \left|\sum_i m_i U^2_{ei}\right| ,$$

which, in addition to the masses and mixing parameters for Dirac neutrinos, also depends on the CP violating and Majorana phases.

There are 35 candidate nuclei for double beta decay, however experiments using $^{136}$Xe and $^{76}$Ge have reported the most sensitive results of $0\nu\beta\beta$ search. Because of uncertainties related to the nuclear matrix element, the complementarity of technologies and different backgrounds, it is important to pursue searches with as many isotopes as possible to have a better understanding and more robust results.

In case of $\beta\beta$ decay, a continuous energy spectrum corresponding to the two emitted neutrinos up to the end point should be observed. On the contrary, a $0\nu\beta\beta$ decay, should only see a line coming from the two electron energies, since no neutrinos are carrying away part of the energy of the process. In order to be sensitive to $0\nu\beta\beta$, a good energy resolution to separate the mentioned energy line from possible background is mandatory. The energy from electrons is measured with either ionization, scintillation or through phonons; in some experiments a combination of both techniques is used to enhance the sensitivity.

Among the experiments using ionization detection, ultra-high purity germanium detector provides the best sensitivity thanks to high energy resolution and an almost background free scenario. GERDA used a total of 20 kg of broad energy germanium to achieve a background-free research. Final results from GERDA set the half-life limit of $0\nu\beta\beta$ for $^{76}$Ge to $T_{1/2} > 1.8 \times 10^{26}$ years at 90% CL [100]. GERDA and Majorana collaborations have joint efforts to develop LEGEND [101], a more massive experiment which is expected to reach a discovery sensitivity of half-life beyond $10^{28}$ years.

Liquid scintillator detectors are another alternative, which is being employed by the KamLAND -Zen [102] and SNO+ [103] experiments. KamLAND detector has added an inner, very radiopure balloon to hold 380 kg of xenon. By purifying the scintillator, background levels were highly reduce and KamLAND-Zen was able to report a half-life limit of $T_{1/2} > 1.07 \times 10^{26}$ years at 90% CL. SNO detector was also upgraded to include $^{130}$Te in its vessel and search for $0\nu\beta\beta$.

Time projection chambers are also a good environment for such decays, as ionization and scintillation information can be used simultaneously. Examples of such experiments are EXO-200 [104] and NEXT [105] which use liquid xenon TPCs.

Using the reported half-life limit of GERDA and KamLAND-Zen and the appropriate nuclear matrix elements, the corresponding upper bounds on the effective Majorana mass at 90% CL are:

$$m_{ee} < 79 - 180 \text{ meV} \qquad \text{for GERDA,}$$
$$m_{ee} < 61 - 165 \text{ meV} \qquad \text{for KamLAND-Zen.}$$

Using the experimental best fit results, the effective Majorana mass can be parameterized in terms of the lightest neutrino mass. Due to the lack of knowledge about the Majorana phases the

allowed range for $m_{ee}$, as a function of $m_{lightest}$ and for a given mass ordering, is substantially broader than the one obtained with spectroscopy beta decay procedures, as shown in Figure 2.25 right.

Last but not least, it is well known that neutrinos leave detectable traces at cosmological scales that can be used to constrain neutrino properties. Cosmology is sensitive to the total number of active neutrinos, neutrino species and their masses, while being blind to their mixing angles and CP violation phases. Hence cosmological constraints are complementary to measurements from terrestrial neutrino experiments. Several experiments have tried to constrain $\sum m_\nu$ resulting in different upper bounds depending on which data sets are included and which models are considered. The strongest bound to date comes from eBOSS experiment (using Lyman-alpha forest spectroscopy) combined with Planck 18 experiment and baryonic acoustic oscillations data, which sets $\sum m_\nu < 0.087$ eV at 95% CL. Global results seem to have a preference towards the normal hierarchy while putting inverted hierarchy under pressure. More details about neutrinos in cosmology and future plans to address remaining unknowns can be found in Ref. [33].

### 2.8.7 Beyond $3\nu$

Following the discussion from previous section, it is clear that many efforts have been put together to slightly modify the standard model in order to accommodate the observed new results. Independently of which extension of the SM one prefers, it must contain only three light active neutrinos. If more than three neutrinos are required, one must add sterile neutrinos to the particle content of the model, such that they are unable to interact via the weak force. These kind of particles would be unobservable both directly and indirectly in current neutrino oscillation experiments, and their existence would only be inferred through inconsistencies with the active-only neutrino oscillation picture. Small admixture between sterile and active states is expected, in order to not substantially alter the phenomenology of three-neutrino mixing beyond what is allowed by current limits. These constraints are coming not only from atmospheric and solar neutrino data, but also from LEP experiment and cosmological observations restricting the total number of active neutrinos.

The anomalies hint towards the existence of an additional mass eigenstate at around $\Delta m^2 \sim 1\ eV^2$, such that the oscillations of active neutrinos to this new sterile state are fast, being undetectable by long-baseline experiments. Introducing additional mass states results in a large number of extra parameters in the model; however, the simplest extension to the active neutrino picture is the $3+1$ (active+sterile) model, where an extra neutrino flavour $\nu_s$ is added.

The three neutrino flavours and the sterile neutrino are mixtures of four neutrino mass eigenstates. Parametrically, one can extend the $3 \times 3$ leptonic mixing matrix to a $4 \times 4$ matrix $U_{\alpha i}$, where $\alpha = e, \mu, \tau, s$ and $i = 1, 2, 3, 4$. The new oscillation parameters are now: the three usual mixing angles and CP violating phase, plus three extra mixing angles and two extra CP phases. Lacking any other coupling with the active neutrinos, the sterile state $\nu_s$ itself as well as its associated mixing parameters $U_{si}$ for $i \in 1, 2, 3$, are generally considered experimentally non-accessible. This is in contrast to the mass eigenstate $\nu_4$, as the active neutrinos will now be generated with a $\nu_4$ component, as schematically shown in Figure 2.26, for the normal ordering scenario. This will affect neutrino oscillation phenomenology, as $\nu_4$ will propagate with a different phase velocity compared to other mass eigenstate, modifying the $3\nu$ oscillation probabilities. If experimental conditions fulfill $4E \sim \Delta m^2_{4i} L$ the oscillatory behaviour due to sterile neutrinos would be observable.

The separation of scales between the large sterile neutrino mass splitting $\Delta m^2_{41}$ and the smaller $3\nu$ splittings, corresponding to the solar and atmospheric mass-squared differences, allows to effectively consider degenerate active mass states with equal masses. This is commonly called the *short-baseline approximation*. In the $\sim 1\ eV^2$ region, short baseline experiments do not constrain $|U_{\tau 4}|$, because the neutrino energy required for the optimal $L/E$ resolution is well below

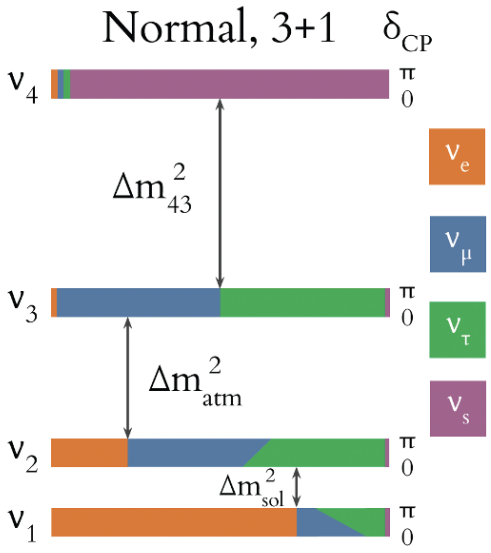


Figure 2.26: The sterile neutrino mass splitting, $\Delta m^2_{43} \approx \Delta m^2_{41}$ is included in the normal-ordering scheme to demonstrate the (3+1) model correction to the active neutrino picture. Not to scale, $\Delta m^2_{41}$ is expected to be at least 10 times larger than the active mass splitting.

the $\tau$ production threshold of 3.48 GeV for the incident neutrino energy needed to produce a $\tau$ lepton. Therefore, the global fits to the short baseline data sets in the 3+1 model are constraining $\Delta m^2_{41}$, $|U_{e4}|$ and $|U_{\mu 4}|$. For that reason, sterile neutrino oscillation in short baseline experiments are made via one of the following three channels: $\nu_\mu$ disappearance [$\nu_\mu \longrightarrow \nu_\mu$], $\nu_e$ appearance [$\nu_\mu \longrightarrow \nu_e$] or $\nu_e$ disappearance [$\nu_e \longrightarrow \nu_e$]. Measurement might also be made through the antineutrino channels, and for both modes the sensitivity of the measurement is dependent on the energy, baseline and neutrino source of the experiments, as previously demonstrated. By observing all three oscillation channels it is possible to over-constrain the system and perform consistency tests of the different results.

In each disappearance experiment, a deficit in the observed event rate relative to predictions given by the $3\nu$-model could indicate that the active neutrino flavour eigenstate is oscillating to a sterile flavour eigenstate. Similarly, for the appearance channel, an excess of observed events might be due to the oscillation of a sterile flavour state into an active flavour state.

The appearance and disappearance formulas for 3+1 model, under the short baseline oscillation approximation, are then given by the following expressions, [106]:

$$P(\nu_\mu \longrightarrow \nu_\mu) \simeq 1 - \sin^2(2\theta_{\mu\mu}) \sin^2\left(\frac{\Delta m^2_{41} L}{4E_\nu}\right) , \tag{2.62}$$

$$P(\nu_\mu \longrightarrow \nu_e) \simeq \sin^2(2\theta_{\mu e}) \sin^2\left(\frac{\Delta m^2_{41} L}{4E_\nu}\right) , \tag{2.63}$$

$$P(\nu_e \longrightarrow \nu_e) \simeq 1 - \sin^2(2\theta_{ee}) \sin^2\left(\frac{\Delta m^2_{41} L}{4E_\nu}\right) . \tag{2.64}$$

Where the effective sterile mixing angles are defined as

$$\sin^2(2\theta_{\mu\mu}) = 4|U_{\mu 4}|^2(1 - |U_{\mu 4}|^2) \,, \tag{2.65}$$

$$\sin^2(2\theta_{\mu e}) = 4|U_{\mu 4}|^2|U_{e4}|^2 \,, \tag{2.66}$$

$$\sin^2(2\theta_{ee}) = 4|U_{e4}|^2(1 - |U_{e4}|^2) \,, \tag{2.67}$$

fulfilling the unitary condition $|U_{e4}|^2 + |U_{\mu 4}|^2 + |U_{\tau 4}|^2 + |U_{s4}|^2 = 1$. It is possible to observe from these equations that if both $|U_{\mu 4}|^2$ and $|U_{e4}|^2$ are nonzero, then all three probabilities described above must occur at the same $L/E_\nu$. More explicitly, at linear order in the mixing elements, the amplitudes of appearance and disappearance probabilities are related by $4\sin^2(2\theta_{\mu e}) \sim \sin^2(2\theta_{ee})\sin^2(2\theta_{\mu\mu})$. This relation implies a constraint between the possible results in appearance and disappearance experiments. Hence, it is not trivial to find consistent description to all the short baseline (SBL) anomalies.

The present status of the 3+1 model is best examined through a global fit analysis, in which each set of data from short-baseline experiments contribute to a single statistical model according to the strength of their results. Global fits have been performed independently by several groups and all of them have found a strong preference for a 3+1 model compared to the SM. This result is mainly driven by the LSND and MiniBooNE results, however a significant tension among data sets is also present; making the 3+1 model highly unlikely to be the definitive answer. The problem is that LSND and MiniBooNE require large mixings, implying big disappearance amplitudes, which are in strong tension with experimental results.

Figure 2.27 shows the preferred region in the 3+1 model parameter space of all short-baseline appearance experiments (red region), compared to the excluded region by all disappearance experiments (blue line) at 99.73% CL for two degrees of freedom.

Note that the region to the right of the blue line is excluded, and that includes the entirety of the appearance allowed region, concluding that the 3+1 scenario is excluded at $4.7\sigma$ level.

Within the 4 neutrino flavour approximation, one could also think of different configurations of neutrino states. In addition to the 3+1 model, where a group of three close-by neutrino masses is separated from a fourth massive state responsible for the SBL oscillation, there is also the possibility of a 2+2 scheme. In this latter one there are two pairs of close masses, one pair responsible for solar results and the other one responsible for the atmospheric, which are separated by a gap of $\mathcal{O}(\sim eV^2)$. These scheme would modify the values expected for the solar and atmospheric results, and therefore it was tested in the past. As no deviation was seen, the model was soon ruled out beyond $3 - 4\sigma$ [108].

Another possible solution would be to introduce more states to the $3\nu$ framework. This allows some additional freedom when fitting neutrino and antineutrino data from LSND and MicroBooNE, however it still holds true that a non zero appearance $\nu_\mu \longrightarrow \nu_e$ should be accompanied by a disappearance result in both e and $\mu$ channels. As a result, the tension between appearance and disappearance results still remains.

Many more explanations have been raised during the last decade, still a coherent picture where all anomalies fit together is missing. Several experiments have been build or are under construction to address this problem, in particular the Short-Baseline Neutrino (SBN) program at Fermilab aims to solve this issue exploiting its multi-detector configuration exposed to a $\nu_\mu$ beam.

This program represents an exciting opportunity to search for light sterile neutrinos. Both $\nu_e$ appearance and $\nu_\mu$ disappearance channels will be simultaneously investigated, allowing to confirm or reject at $\geq 5\sigma$ the light sterile neutrino oscillation interpretation.

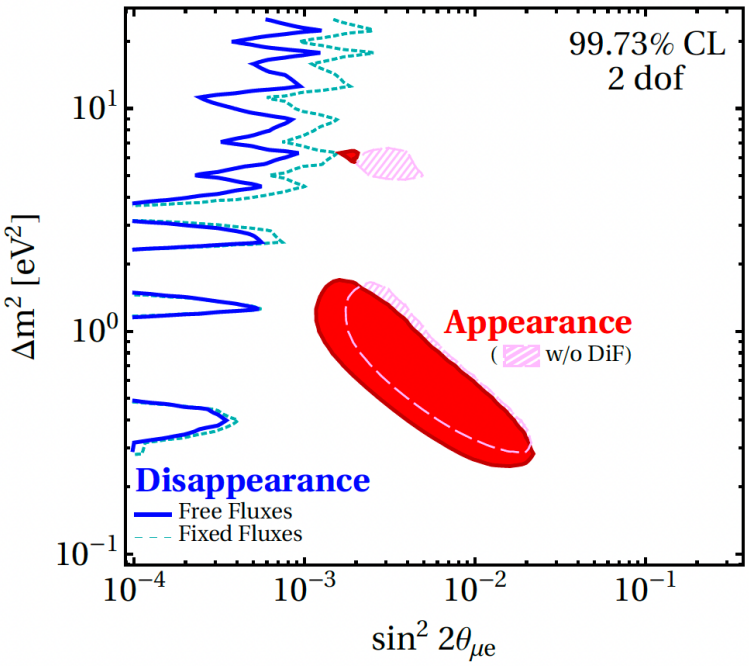


Figure 2.27: All appearance and disappearance constraints combined in the $\sin^2(2\theta_{\mu e})$ , $\Delta m^2_{41}$ parameter space. The blue curves show limits from the disappearance data sets using free reactor fluxes (solid) or fixed reactor fluxes (dashed). The areas are based on the appearance data sets using LSND results with decays at rest + decays in flight (red) or only decays at rest (pink). Figure taken from Ref. [107].

# Chapter 3

# The Short Baseline Neutrino program

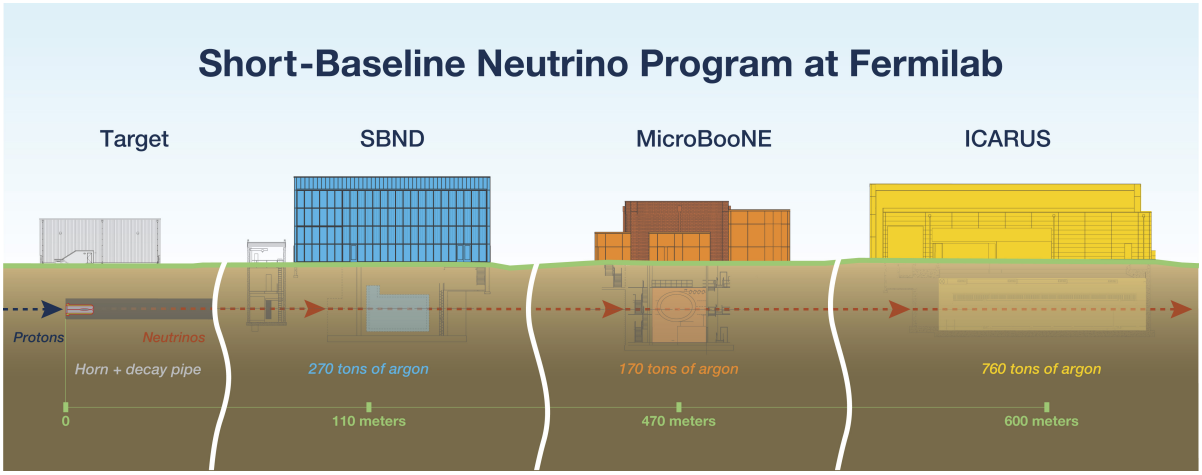


Figure 3.1: Fermilab's Short-Baseline Neutrino Program uses three detectors sitting along the same neutrino beam. The Short-Baseline Near Detector is closest to where the neutrino beam is created. MicroBooNE, the first of the three detectors to become operational, sits in the middle. ICARUS, the largest of the three, is the furthest. Figure from Fermilab Creative Services.

The Short-Baseline Neutrino (SBN) program at Fermilab presents an exciting opportunity in experimental neutrino physics. SBN will carry out precision searches for new physics in neutrinos recording millions of neutrino CC and NC interactions on argon to unveil the physics of neutrinos at the GeV energy scale. SBN is designed to address the possible existence of eV mass-scale sterile neutrinos. The search for light sterile neutrinos at SBN is motivated by a set of anomalous results in past neutrino data, mainly driven by the LSND and MiniBooNE experiments. Follow-up experiments are mandatory to either confirm or rule out the existence of these new neutrino states.

SBN will test this important question using multiple, functionally identical detectors sitting along the same neutrino beam, which is the key to the experiment's world-leading sensitivity. A discovery would reveal new physics and open the doors to further experimentation of this area, while a clear null result from SBN would help close the long-standing puzzle of anomalies in the neutrino physics field.

The SBN program, consists of three large liquid argon time projection chambers (LArTPC) sitting along the Booster Neutrino Beam (BNB) at the Fermi National Accelerator Laboratory (Fermilab or FNAL) in Illinois. Figure 3.1 shows from left to right the neutrino beam target area, the Near Detector (SBND), the intermediate detector (MicroBooNE) and the far detector

(ICARUS T600).

The Short-Baseline Near Detector (SBND) is a 112 t active mass LArTPC located at 110 m from the neutrino production target. The near detector will be able to characterize the neutrino beam before any substantial oscillation, greatly reducing the systematic uncertainties in a search for oscillation signals downstream the BNB. The SBND detector is in the final stages of installation and is getting ready for data-taking, expected to begin in 2024.

The MicroBooNE detector is an 89 t active mass LArTPC, sited at 470 m along the beam. The detector has been collecting data from BNB since October 2015 and completed its physics run in early 2020. The collaboration has published interesting results on the LEE from 2016-2018 data [109, 110] and further results are expected soon from the full data set.

Finally ICARUS-T600 is the far detector of the program, with 476 t active mass and placed at 600 m from target and which has been refurbished and upgraded for an optimal performance in SBN. The detector commissioning phase concluded in June 2022, and has been collecting physics data since that moment.

The physics goal of the SBN program are summarized here, however a more detailed description of all the opportunities offered by the experiment can be found in Ref. [97].

### Oscillation searches and sterile neutrino sensitivity

The joint effort among the three LArTPC detectors will provide a world-leading sterile neutrino search experiment. A very sensitive search of $\nu_\mu \longrightarrow \nu_e$ appearance signal will cover the full LSND 99% C.L allowed region at $\sim 5\sigma$. The locations of the near and far detectors are optimized for maximal sensitivity in the most relevant ranges of oscillation parameters, under the hypothesis of a $\sim$ 1 eV sterile neutrino. From Figure 2.27, the global $\nu_e$ appearance data showed an allowed region defined by $\Delta m^2 = [0.3, 1.5]\ eV^2$ and $\sin^2(2\theta_{\mu e}) = [0.002, 0.015]$. Figure 3.2 shows the shape of oscillation probability for two sets of parameters in this allowed region. Oscillations are visible at the far detector in both cases, while a small oscillation signal begin to appear at the near detector if a high $\Delta m^2$ is chosen. This feature does not compromise the experiment, as its precise design preserves a strong sensitivity up to several $eV^2$.

Precision oscillation studies are mandatory to observe a clean signal, hence SBN will exploit the highly correlated event rates in the near-far detector configuration to achieve a significant cancellation of the flux and cross section uncertainties. At this point, the main source of uncertainties will be due to systematic effects. To address them, the collaboration will benefit from the knowledge learnt by other experiments during these past years and is currently developing more sophisticated tools to precisely evaluate detector uncertainties.

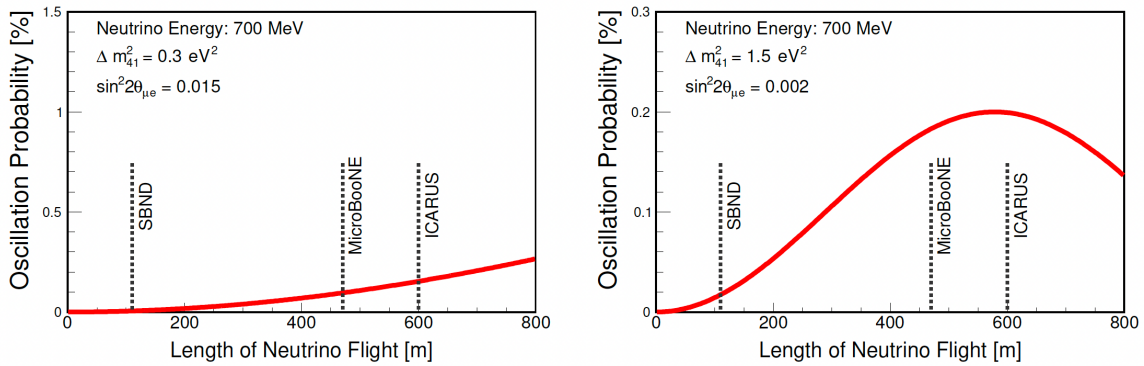


Figure 3.2: $\nu_\mu \longrightarrow \nu_e$ oscillation probability as a function of the baseline, considering a BNB neutrino of peak energy 700 MeV for two different sets of oscillation parameters inside the appearance allowed region described in the text. Figure taken from Ref. [111].

On the other hand, the huge event statistics at the near detector will also allow a simultaneous sensitive search in the $\nu_\mu \longrightarrow \nu_\mu$ disappearance channel. The projected sensitivities to the $\nu_e$ appearance and $\nu_\mu$ disappearance are shown in 3.3, where a 3+1 sterile neutrino model is assumed. The sensitivities correspond to an integrated exposure of $6.6 \times 10^{20}$ protons on target (POT) for BNB, at both the near and far detectors.

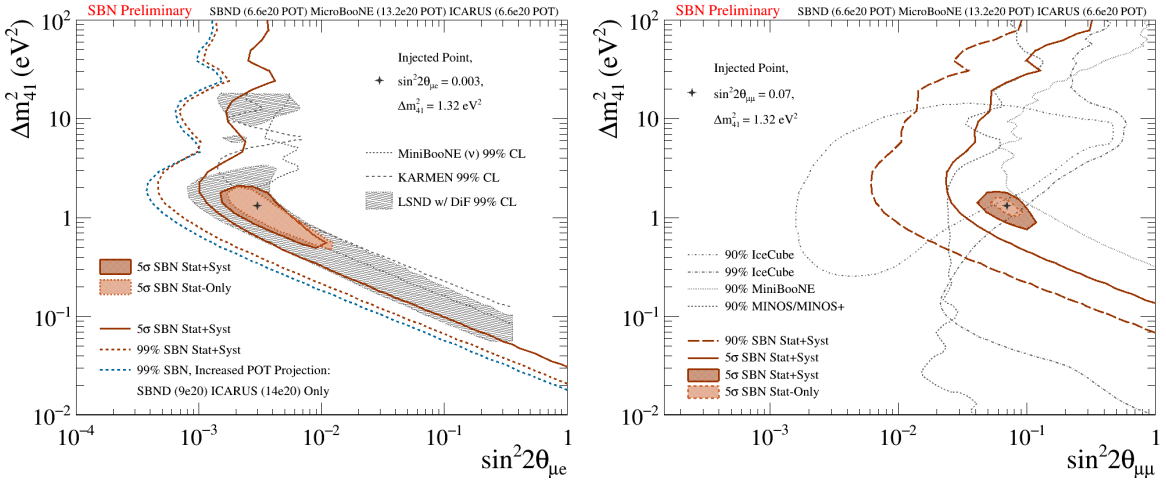


Figure 3.3: SBN $5\sigma$ sensitivity to a light sterile neutrino in the appearance and disappearance channels

The POT values shown in the figures are those from the SBN proposal [97], however BNB will operate until a long-term shutdown in early 2027 allowing to collect at least twice more statistics than planned for ICARUS+SBND and increase by a factor of 3 the expected statistics for ICARUS alone.

It was already pointed out that non-zero values for $\sin^2(2\theta_{\mu e})$ and $\sin^2(2\theta_{\mu\mu})$ are necessarily accompanied by non-zero values of $\sin^2(2\theta_{ee})$. This latter channel will be studied by both SBND and ICARUS exploiting the BNB and NuMI beams, respectively. SBND will collect more than 2 million $\nu$ interactions per year assuming an exposure of $2.2 \times 10^{20}$ POT, of which 12,000 events are expected to be $\nu_e$ due to the intrinsic contamination of the BNB ($\sim 0.5\%$ $\nu_e/\bar{\nu}_e$). For what concerns ICARUS, taking advantage of its privileged position at 6° off-axis from the higher energy NuMI beam, a large neutrino event sample in the 0-3 GeV energy range will be recorded. ICARUS will see about 10,000 $\nu_e$ NuMI off-axis events per year thanks to the enriched component of the beam ($\sim 5\%$ $\nu_e$).

Finally the SBN program will also address the MiniBooNE LEE. The ability of the LArTPC technology to reduce the main backgrounds that affected the MiniBooNE experiment will be a key point to clarify the anomaly.

### Neutrino-Argon Cross-section Measurement

The interaction cross-sections need to be well understood to enable high-sensitivity neutrino oscillation measurements for the discovery of new physics. This is of vital importance for experiments involving complex scattering of neutrinos with heavy nuclei, like SBN whose detection medium is Argon. SBN will study neutrino-argon cross-sections with millions of interactions using the well characterized neutrino fluxes from the BNB.

The closest detector will observe the largest flux providing an ideal scenario to conduct precision studies, achieving the world's highest statistics cross section measurements for many $\nu$-Ar scattering processes. MicroBooNE was the first detector to start operation and has been able to produce a number of precise cross-section measurements studying the BNB [112, 113].

At the same time, MicroBooNE and ICARUS can also study neutrino-argon cross sections exploiting the NuMI beam.

All together, SBN has the potential to broaden the knowledge of physics in the low-energy neutrino-nucleus scattering. This analysis will provide key information at energies relevant to the future long baseline experiments with multikiloton LArTPC detectors, such as DUNE [61].

#### Search for Beyond Standard Model Physics

Last but not least, thanks to the excellent event reconstruction achieved with LArTPC technology and the intense neutrino flux, SBN presents an optimal venue to search for exotic new physics. The Beyond Standard Model physics program includes large extra dimension models, Lorentz/CPT symmetry violation searches, non-standard interactions and dark neutrino sectors, among many others. A list of them with a brief description can be found in Ref. [111].

## 3.1 The Booster Neutrino Beam

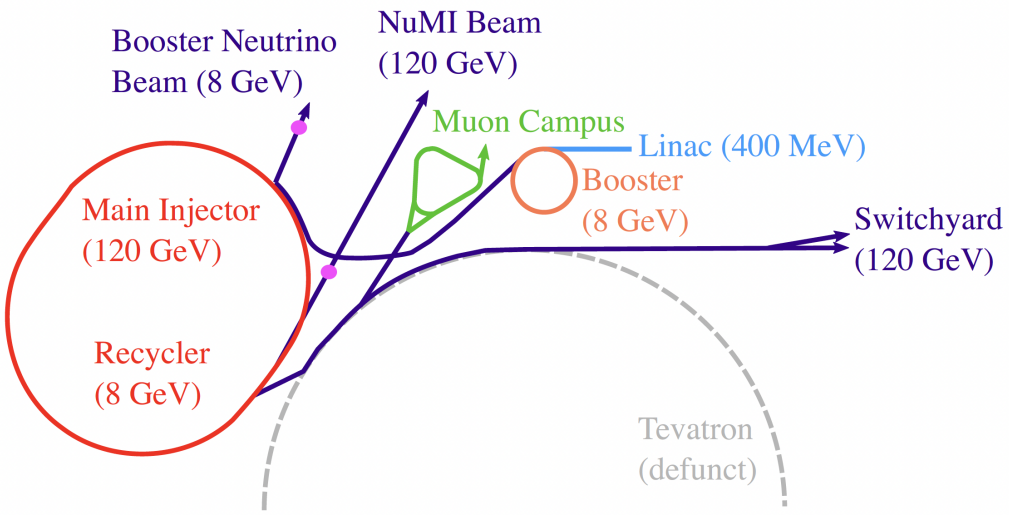


Figure 3.4: Fermilab accelerator complex. The path of neutrinos before reaching the detectors is shown. Pink points show the position of the target where protons collide to produce secondary hadrons. Note the slightly different inclination of BNB and NuMI beams. Figure taken from Ref. [114]

The SBN program makes use of the Booster Neutrino Beam (BNB) at Fermilab. It is generated by extracting protons from the 400 MeV Linac, accelerating them to 8 GeV kinetic energy in the Booster synchrotron and, subsequently firing them on a beryllium target to produce a secondary beam of hadrons, mainly pions. The fluxes are well understood thanks to a detailed simulation developed by MiniBooNE collaboration [115] and to the hadron production data acquired by the HARP experiment [116]. Secondary particles are focused by a magnetic polarising horn supplied with 174 kA in 143 $\mu$s pulses in coincident with the proton delivery. Based on the horn polarization, positive or negative particles are selected and collimated while the others ones are defocused. The focused mesons are allowed to propagate through a 50 m long tunnel where the majority of them will decay to produce $\nu_\mu$ and $\nu_e$. The dominant decay channel for pions is via $\pi^+ \to \mu + \nu_\mu$ and the analog for $\pi^-$, which has a branching ratio of $\sim 99.988\%$. The length of the decay pipe is chosen to maximise the production of $\nu_\mu/\bar{\nu}_\mu$ while minimising the probability of secondary muons decaying into $\nu_e/\bar{\nu}_e$. The remaining particles are absorbed

into a concrete and steel absorber at the end of the 50 m decay region to ensure no further weak decays occur that might contaminate the beam.

The Booster spill length is 1.6 $\mu s$ with nominally $\sim 5 \times 10^{12}$ protons per spill delivered to the beryllium target. The beam structure is a series of 81 bunches of protons each $\sim$ 2 ns wide and 19 ns apart with an average spill delivery rate of 5 Hz. The neutrino fluxes observed at the three SBN detector locations are shown in Figure 3.5. The neutrinos produced in the BNB are peaked around $\sim$ 0.7 GeV and range between 0 and 3 GeV across the spectrum. The composition of the flux in the neutrino mode is energy dependent, but dominated by a $\sim$ 93.6 % $\nu_\mu$, followed by a $\sim$ 5.9% $\bar{\nu}_\mu$ contribution and an intrinsic $\nu_e/\bar{\nu}_e$ contamination at the level of 0.5%, at energies below 1.5 GeV. A substantial portion of the electron neutrino contamination originates from the pion $\rightarrow$ muon decay chain with the remaining portion coming from the $K^+$ and $K^0$ decays.

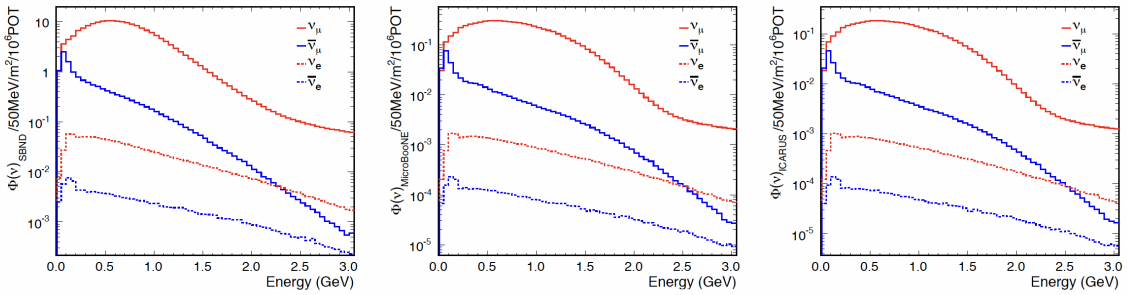


Figure 3.5: Neutrino components of the flux distribution for each SBN detector. Left-hand side plot corresponds to the nearest detector, SBND, while the the rightmost distribution shows the furthest detector, ICARUS. Solid lines indicate the muonic contribution, red for neutrino and blue for antineutrino modes, while the dashed lines represent to the electronic contamination. Figure taken from Ref. [97]

BNB has the ability to run in neutrino and antineutrino modes, exploiting its full potential. This depends on the polarization of the magnetic horns: forward horn current (FHC) focuses $\pi^+$'s to produce a $\nu_\mu$-dominated beam, while reversed horn current (RHC) collimates the $\pi^+$'s to obtain a $\bar{\nu}_\mu$-dominated beam. However there is no near term plan to change the actual FHC mode to RHC.

## 3.2 Neutrinos at the Main Injector Beam

The Neutrinos at the Main Injector (NuMI) beam is the world's most powerful neutrino beam from 120 GeV protons extracted from the Fermilab Main Injector. Protons originate in the Linac and are accelerated up to 8 GeV in the Booster. Once protons reach the nominal energy they are transferred in the Main Injector, whose circumference is 7 times the circumference of the Booster. This allows the injection and storage of seven Booster batches, however a maximum of six proton batches can be accelerated as the last slot is used for the pulse kicker rise time. With some sophisticated techniques and hardware improvements the proton intensity was significantly increased in the past, and nowadays protons are accelerated up to 120 GeV. Afterwards, they are fired towards the MINOS Far detector to a graphite target placed at 350 m. From the collision, hadrons are produced and will be focused by two magnetic horns before entering a 675 m long decay pipe where they decay to neutrinos or antineutrinos.

Pions and kaons constitute a major portion of the hadrons and predominantly decay via the modes $\pi^+ \rightarrow \mu^+ + \nu_\mu$ and $K^+ \rightarrow \mu^+ + \nu_\mu$, yielding a $\nu_\mu$ beam. There is also a few percent $\bar{\nu}_\mu$ component coming from the negative hadrons and a small contamination of $\nu_e$ due to subdominant electronic decay modes of $K^+$, $K^0$ and tertiary muons. Similarly to BNB,

the current of the NuMI horns can be reversed in order to produce a neutrino or antineutrino dominant beam.

An hadron monitor is located at the end of the decay volume just in front of the 5 m thick absorber to record the profile of the residual hadrons. The 240 m of rock following the absorber stops the remaining muons in the beam but allows the neutrinos to pass undisturbed.

NuMI is able to deliver up to $6.5 \times 10^{13}$ protons per spill with a beam pulse width of 9.6 $\mu s$. ICARUS detector will also exploit this beam, focusing primarily on the interaction rates of neutrinos in Ar nuclei. ICARUS lies 795 m downstream the NuMI beam at an off axis angle of 5.7° which translates to a significant flux of both muon an electron flavour neutrinos and antineutrinos.

## 3.3 Time Projection Chamber technology

A Time Projection Chamber (TPC) is a type of detector that allows a 3D reconstruction of particle trajectories. It was first proposed by David Nygren in the 1970s [117], his idea was to have a detector able to identify a ionizing crossing particle from its energy deposition and to reconstruct its track three-dimensionally. Carlo Rubbia proposed in 1977 to scale the TPC technology towards much bigger volumes for neutrino physics using ultra pure liquid argon (LAr) as the active volume [118]. The combination of high 3D imaging resolution and large active volume, makes the LAr-TPC an excellent technology for neutrino physics.

The ICARUS collaboration was the first to successfully utilise this technology with the goal of studying solar neutrinos, proton decay and cosmic neutrino interactions. After its great success, the LArTPC technology has consistently been improving through its use in experiments designed to perform research and development, while at the same time making groundbreaking physics measurements.

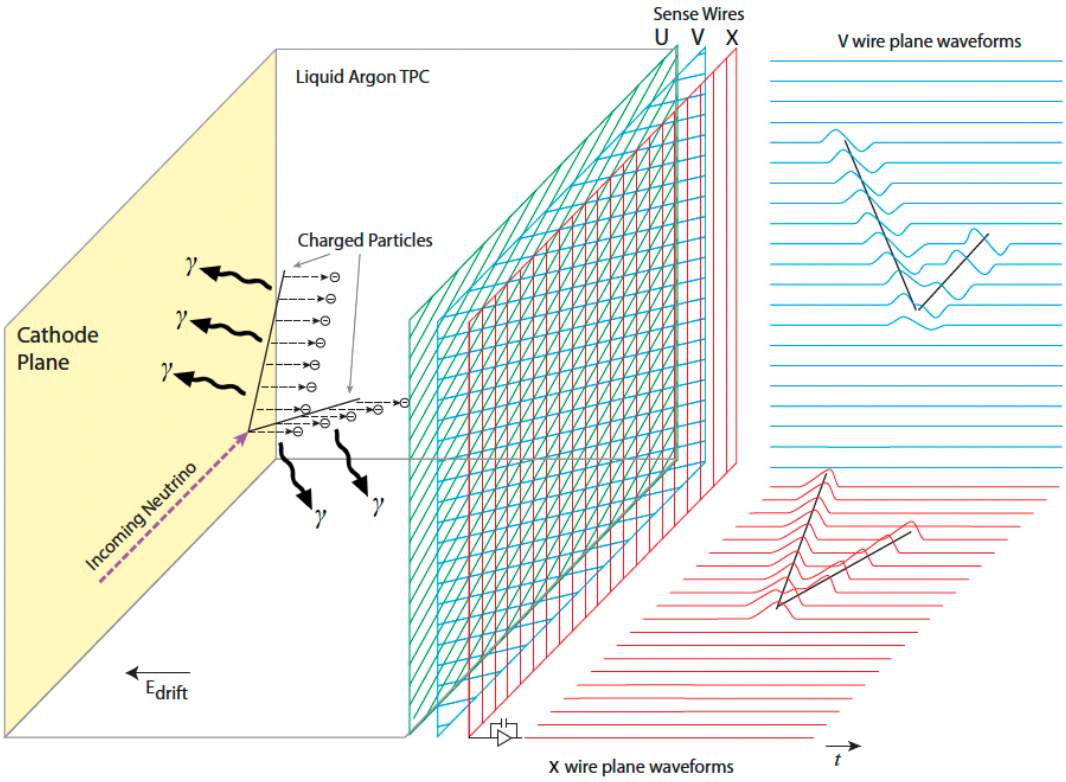


Figure 3.6: General operating principle of a liquid argon time-projection chamber. Figure taken from Ref. [119]

The basic idea of a TPC is shown in Figure 3.6, consisting of an active volume filled with gas or liquid where the particles crossing the medium lose enough energy to ionize the target atoms. The electrons produced in the ionization process are drifted by an uniform electric field towards a position-sensitive anode that provides a 2D projection of the particle trajectory. The anode segmentation defines the spatial resolution with which the detector is able to reconstruct the tracks. The arrival time of the drifted electrons is further used to reconstruct the missing coordinate allowing a complete 3D track reconstruction. First TPCs were filled with noble gases, later on liquids were introduced. The advantage of using liquids comes from their higher density, the greater mobility of their ionization charges and a reduced electron-ion recombination with respect to the gas phase.

Being noble liquid scintillators, the energy of the emitted photons is not sufficient to be absorbed via photoelectric effect, therefore Argon has the characteristic to be transparent to its own scintillation light. The light produced by the particles crossing the TPC volume can be collected and used in combination with the information extracted from the drifted charges.

Several liquefied noble gases can be used in a TPC (He, Ne, Ar, Kr and Xe), however the choice of liquid argon TPC is motivated by it having a number of desirable properties:

1. Liquid argon has a high density 1.39 $g/cm^3$ and high atomic mass; this increases the neutrino cross-section.

2. It does not attach electrons and hence it permits long drift lifetimes: being Ar a noble gas, the energy absorbed from charged particles crossing the detector can only be used to ionize the argon and produce scintillation photons. As a result, minimal energy is absorbed in the argon maximising the efficiency of the electron production. At the same time, this allows long drift lifetimes in which ionization electrons can cross the entire TPC without being captured.

3. High electron mobility, allowing electrons to be drifted quickly under an electric field.

4. The LAr radiation length of $X_0 = 14$ cm allows mm-scale calorimetry sampling of neutrino events while having a precise discrimination between electron and photo-induced activities, without the need of huge detector volumes. Photons produced at the primary vertex usually have a gap between the interaction and the starting point of the electromagnetic shower; in addition, the ionization pattern in the first centimeters of the shower is consistent with two minimum ionizing particles (MIP), in contrast to the single MIP signature characteristic of an electron track.

5. It is cheap and easy to obtain: Ar is the third most abundant gas in Earth's atmosphere ($\sim 1/\%$) and can be liquefied by liquid nitrogen, making it the cheapest noble gas available and ideal for large-scale detector volumes.

6. Can be highly purified: many of the organic impurities are frozen out from its liquid form to very low levels.

Liquid argon is a very attractive target for neutrinos due to its high density, however it is important to take into account that the complicated structure of the argon nucleus will give rise to nuclear effects which must be treated with special effort. The cryogenic temperatures at which the noble elements are in the liquid phase also introduces the need for additional design considerations to ensure stable and safe operations. A summary of the physical properties of liquid argon can be found in Ref. [33, 120].

## 3.4 LArTPC across the Short Baseline Neutrino program

All three detectors from the SBN program utilise the LArTPC technology. Increasing the number of features which are functionally identical among the three detectors allows an important cancellation of systematic uncertainties when performing joint oscillation analyses. Despite the great effort to maintain all detectors as similar as possible, they are not identical and each one exhibits a number of unique features. This allows to test a wide range of possible configurations to optimize the physics potential for next-generation LArTPC experiments.

This section will provide a detailed description of the three SBN detectors and an up to date review of their current status.

### 3.4.1 The Liquid Argon TPC

The charged particles observed following the neutrino interactions in LArTPC are reconstructed collecting the ionization electrons and scintillation photons produced along the trajectories of the particles. Depending on their behaviour such trajectories might take the form of tracks or electromagnetic showers. In both cases, the 3D image produced by the TPC provides detailed information to reconstruct the final state topology of neutrino interactions allowing to perform geometric and calorimetric analysis.

In LArTPCs, the liquid argon is highly purified so that the ionization traces can be transported with minimal attenuation over distances of the order of meters. Ionization electrons are drifted across the TPC under the influence of a uniform electric field, until they reach sense planes located at one side of the active volume. The electric field is created by introducing a potential difference between the cathode and anode planes and gradually stepping that voltage down in magnitude across a field cage. Non-uniformities in the electric field, diffusion and recombination of the charge and space charge effects modify the precise reconstruction of charge particles. These features will be described in Chapter 5 and more details can be found in Appendix A, however an accurate calibration of them is critical to perform precise measurements.

The anode plane is arranged parallel to the cathode plane and made up of three sense wire planes with a characteristic pitch and held at a precise bias voltage. The planes continuously read out the signals induced by the ionization electrons drifting towards them. The electrostatic potentials of the sequence of anode planes allow ionization electrons to pass undisturbed by the first two planes (referred to as induction planes) before being collected and recorded in a wire in the last plane (referred to as the collection plane). The signals that the ionization electrons create on the anode wires are recorded in terms of waveforms, and detector effects, such as noise, are subsequently removed. A further step is applied, using a deconvolution filter to separate individual waveform signals on a single wire. A sophisticated treatment has been developed over the years to improve the signal discrimination from the detector response effects, as well as to achieve a more precise reconstruction. More details will be given in Section 5.5.

The 3 dimensional position at which an ionization electron was produced in the detector starts with finding the 2D projection in the wire planes. The three wire planes are usually orientated in $+60°$, $-60°$ and $0°$ with respect to the horizontal, so that for each induced current coming from the same electron one can determine where the affected wires cross one another to set the y-z position.

The remaining x-position is calculated using timing information, meaning the recorded drift time of the ionization. The drift time is the difference between the arrival times of ionization signals on the wires ($t_m$) and the time the interaction took place in the detector ($t_0$). The latter one can be provided by an accelerator clock synchronized to the beam (beam timing information) or from a trigger provided by the light collection system. Given a known electron drift velocity ($v_d$) one can set the x-position to

$$x = v_d \times (t_m - t_0) \, . \tag{3.1}$$

The characteristics of the waveforms observed in each wire provide a measure of the energy deposition of the traversing particles near a specific wire. The identification of the particle is possible measuring the energy loss per unit path (dE/dx) which is proportional to the collected charge per wire and unit time ($dQ/dx$), making the TPC a good calorimeter. The particle identification will be of uttermost importance as oscillation and reconstruction studies cannot be performed without that information.

Not all the energy deposited by ionizing particles goes to the production of electron-ion pairs, $Ar^+ + e^-$. When the energy is not enough to release the electron from the Coulomb potential produced by the argon atom, ionizing particles can only excite argon atoms $Ar^*$. When an ionized or excited argon atom couples to a neutral Ar, it produces the molecular states of $Ar_2^+$ and $Ar_2^*$, respectively; where $Ar_2^+$ eventually recombines with a free electron producing $Ar_2^*$ as well. These molecular argon excimers[1] ($Ar_2^*$) in its turn decay producing two atoms of Ar and scintillation light. In both processes the decay of the final state results in the emission of a vacuum ultraviolet (VUV) photon peaked at $\sim$ 128 nm [121]. These scintillation processes are described by:

$$\begin{aligned} \text{Excitation}: \; & Ar^* + Ar \longrightarrow Ar_2^* \longrightarrow 2Ar + \gamma \,, \\ \text{Recombination}: \; & Ar^+ + Ar \longrightarrow Ar_2^+ + e^- \longrightarrow Ar_2^* \longrightarrow 2Ar + \gamma \,. \end{aligned}$$

The recombination process requires an electron cloud surrounding the $Ar_2^+$ to occur, hence the scintillation yield due to recombination will be dependent of the electric field; in particular, in LArTPCs where the ionization electrons are drifted towards the anode, the recombination process is highly suppressed.

The VUV scintillation light emission is determined by the de-excitation through a transition to the ground energy level from one of the two lowest electronic excited states: the singlet ($^1\sum_u^+ \longrightarrow {}^1\sum_g^+$) or the triplet ($^3\sum_u^+ \longrightarrow {}^1\sum_g^+$)[2]. These two states have approximately the same energy with respect to the dissociative ground state, however their lifetimes are very different. The second transition is strongly suppressed, as it involves a forbidden spin transition. This transition, despite being forbidden, occurs on rare occasions through spin-orbital coupling mixing in a much slower time scale than the singlet transition. In liquid argon the mean lifetime of the singlet state is $\tau_{fast} = (6 \pm 2)$ ns (*early light*), while the triplet state has a $\tau_{slow} = (1590 \pm 100)$ ns (*late light*). A schematic drawing of the ionization mechanism and scintillation light emission are shown in Figure 3.7.

The ratio between the populations of the singlet and triplet states is strongly dependent on the ionization density of the track (dE/dx), ranging from 1:3 in case of minimum ionizing particles up to 3:1 in case of $\alpha$-particles [97].

The production of scintillation photons is proportional to the energy deposited by the ionizing particle. The typical light yield in liquid argon is $\sim$ 40,000 photons per MeV of deposited energy in absence of a drift field. Under the influence of a 500 V/cm drift field, this amount decreases to $\sim$ 24,000 $\gamma$/MeV, as the recombination process is strongly reduced [123].

In order to be detected, scintillation photons are usually shifted from the vacuum ultraviolet to the visible spectra to match the quantum efficiencies of available photodetectors, which generally peak around 430-450 nm. This has been typically achieved using a fluorescent material to downshift the direct scintillation light, either coated on top of the photomultiplier tubes (PMT) or with plates mounted in front of them. In a general case the photon detection system is composed of a wall of PMTs, however additional components have been introduced in the SBN

[1] An excimer (originally short for excited dimer) is a short-lived molecule formed from two species, at least one of which was in an excited state.

[2] Molecular orbitals which are left unchanged under an inversion through the center of symmetry in a molecule are said to have gerade (g) symmetry, from the German word for even. Those which undergo a change in sign under such inversion are said to have ungerade (u) symmetry, from the German word for odd.

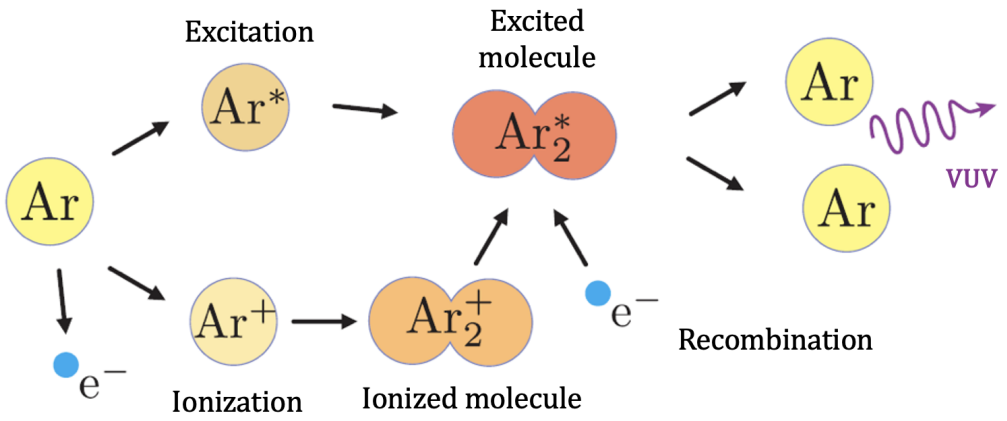


Figure 3.7: Scintillation and ionization mechanisms in liquid argon. Picture taken from Ref. [122]

detectors with the main goal of research and development for future LArTPC experiments. The light collection systems of SBN are immersed in the liquid argon and facing into the detector volume, but always located outside of the electric field region.

Since the typical scintillation time is more than three orders of magnitude smaller than the electron drift time, the photon signal can be used as time origin for the charge events $t_0$, and in addition, supply trigger information to an electronic readout system. In the case of surface LArTPC experiments, all electrons that reach the anode plane during a predefined readout window are recorded, those arriving outside of this window are not. Hence, the window is defined to occur in coincidence with the beam spill time and to last for a duration of at least the maximum drift time of the ionization electrons produced by the neutrino interactions. This method also aims to minimise the number of recorded cosmic ray muons which cross the detector during the readout window. Since all three detectors of the SBN program operate at shallow depth, the main background to neutrino interactions will be dominated by cosmic rays. The light collection system is of crucial importance when it comes to distinguish detector activity that is in-time with the beam (and therefore most possibly originated from beam interactions) from activity which is out-of-time (and therefore probably not associated with the beam), in addition to also benefiting the trigger and event reconstruction.

Finally the yz-position of an interaction can also be inferred from the light system, providing an important cross check validation.

LArTPC detectors are intrinsically a slow technology, with drift times in the millisecond range, hence detectors at the surface record significant cosmic activity with each readout (between 5-15 cosmic muons are seen per readout in the case of the SBN detectors). For this reason the near and far detector of SBN have been designed to include an external cosmic ray tagger detector system (CRT) with nearly $4\pi$ coverage and based on solid scintillator technology to achieve hit timing resolution of a few nanoseconds. In addition, both the near and far detector buildings are designed to support 3 m of concrete overburden directly above the pits where the detectors are installed. This shielding should absorb more than 99% of the photon and hadron contents of cosmic showers hitting the experimental halls. The shielding and CRTs provide a powerful combination for cosmic background mitigation which is essential to the physics goals of SBN.

### 3.4.2 The SBN Near Detector: SBND

The Short Baseline Near Detector (SBND) is the near detector in the SBN program positioned at 110 m from the BNB target. It has a dimension of 5.0 m (L) × 4.0 m (W) × 4.0 m (H), holding

in total 112 tons of liquid argon in its active volume. The detector will operate mostly following the general setup described above, however there is a number of functional differences briefly mentioned here; for a more detailed review of the full detector properties and technicalities see Ref. [97].

Unlike the general TPCs, SBND TPC consists of four anode plane assemblies (APAs) and two central cathode plane assemblies (CPAs), resulting in two drift regions each with a 2 m drift length, as shown in the left hand side Figure 3.8.

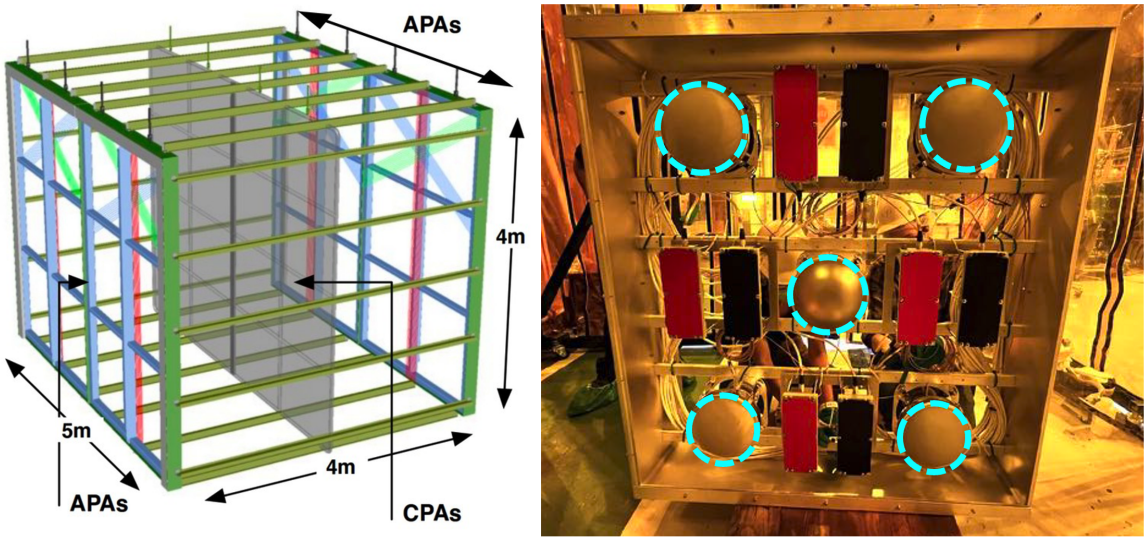


Figure 3.8: Left: SBND TPC, showing the position of the anode and cathode plane assemblies, from Ref. [124]. Right: Photon detection system where all the different components are shown. Blue rings indicate the PMTs, where the center one is uncoated while the remaining 4 are coated with TPB. The pairs of X-ARAPUCA are also visible, being the red and black rectangles. The picture is courtesy of the SBND Collaboration.

The APAs and CPAs are large-scale elements with an area of 4.0 × 2.5 m each [124]. The cathode planes lie side-by-side in the join position between the two TPCs, while the anode planes are positioned in pairs one next to the other on the opposite wall to the cathode plane in each TPC. This configuration produces 2 electric fields and therefore 2 opposite drifting directions. The drift direction is perpendicular to the neutrino beam and has a maximal drift time of 1.3 ms, for the nominal drift field of 500 $V/cm$. Limiting the distance electrons are able to drift across the TPC is necessary to prevent diffusion and attenuation due to interaction with impurities. The solution reached by SBND has been to divide the detector into a multiple module system.

Each APA consists of a steel frame supporting three planes of 150 $\mu m$ copper-beryllium wires at pitch and plane spacing of 3 mm. Each one hosts a total of 2816 wires across the induction and collection planes, resulting in a total of 11,264 readout channels for the whole detector. The wires are orientated at $\pm 60°$ and $0°$ to the vertical plane and similarly to the other two detectors in the SBN program, the configuration of the wire positioning and spacing allows a high resolution in terms of geometric and calorimetric reconstruction. This, at the same time enables electron/photon separation with very similar efficiencies among the three detectors.

Each of the two joined cathode planes consists of a stainless outer frame composed of 8 subframes. The subframe panel design was chosen to have two wire mesh panels, in order to hold a reflective foil coated in wavelength shifting tetraphenyl butadiene (TPB) between them. The goal is to maximise the light yield of the detector by reflecting any of the scintillation photons emitted by the interacting particles which travel in the opposite direction to the photon detection system (PDS).

SBND has a composite PDS that enhances the amount of light collected and simultaneously

provides, a great opportunity for R&D in the scintillation detection in liquid argon. The PDS is divided in 24 modules equally distributed behind each APAs, containing 5 PMTs plus 4 X-ARAPUCA pairs, as shown in the right picture of Figure 3.8.

Thanks to the reflective cathode, SBND will be able to record both direct and indirect scintillation light, all of which is naturally produced with wavelengths in the vacuum ultraviolet (VUV) range, $\lambda = 128$ nm and $E = 9.69$ eV. Employed PMTs are not sensible to the VUV light, therefore the light has to be shifted to higher wavelengths in order to be detected. For this purpose the interface between the LAr target and the PMTs is usually coated with a wavelength shifter (WLS), being compounds that absorb photons and re-emit them at an equal or larger wavelength. TPB is the most used material in LAr-based experiments and is coated on top of some SBND PMTs.

Direct photons require WLS PMTs, while the indirect photons are already shifted into the visible range when reflected into the CPAs and therefore need to be detected with uncoated PMTs. For this reason out of the 5 PMTs in each module, 4 are TPB-coated and 1 is left uncoated.

The X-ARAPUCA[3] is a novel light collection device aiming to record scintillation photons with extremely high efficiency [125]. The mechanism is to trap photons inside a highly reflective box and detect them through silicon photomultipliers (SiPM) placed at the sides of the WLS slabs.

The entire TPC is housed in a stainless steel membrane cryostat, which holds a similar design and serves as a prototype for the DUNE experiment. The SBND TPC is supported from the cryostat roof which contains the feed-throughs for all detector cables and high voltage system, see Figure 3.9. The entire front-end electronics chain is immersed in the LAr and operates at 87 K to achieve an optimal signal to noise ratio, in addition to minimising the amount of cables need to be fed out of the cryostat.

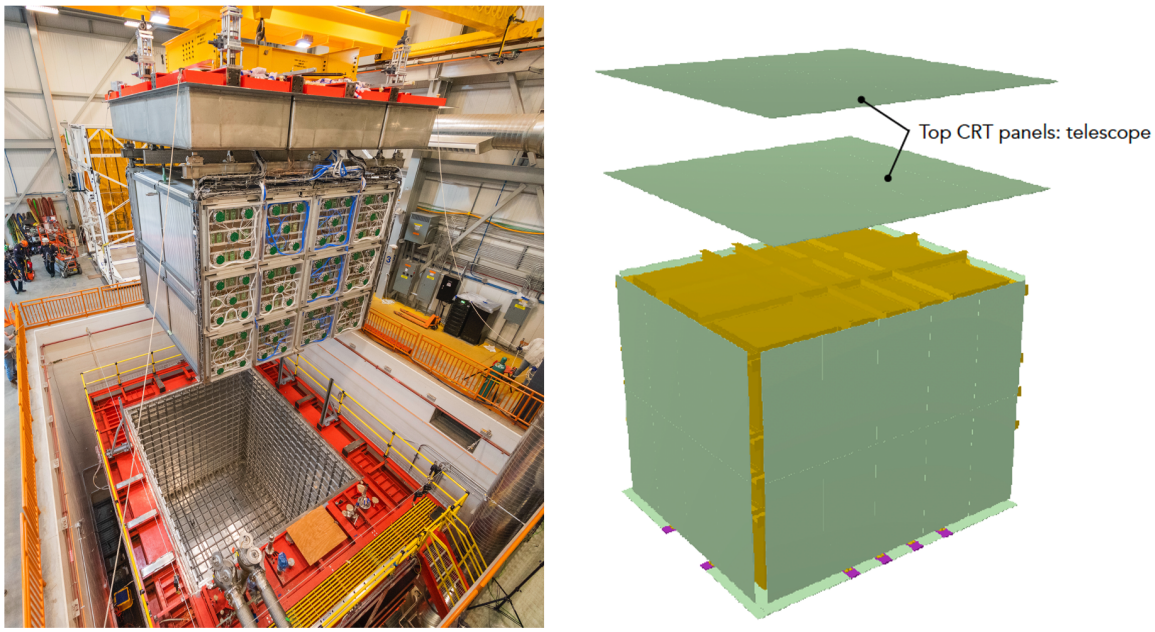


Figure 3.9: Left: SBND TPC on the day the detector was successfully lowered into the cryostat. The TPC is shown hanging from the cryostat lid, where a wall PDS modules are visible. Right: Technical design drawing of the CRT system surrounding the SBND cryostat and including the additional plane above the top face of the detector working as a telescope. Both pictures are courtesy of the SBND Collaboration.

[3]The term ARAPUCA is the indigenous Guarani word for “a trap to catch birds”.

SBND resides on the surface of the Earth and therefore is under the influence of a huge flux of cosmic ray muons. Even if muons do not contribute significantly to the background for the sterile neutrino search, they produce $\gamma$-rays which in turn produce photons. These photons could possibly mimic the $\nu_e$-like interaction signature and therefore need to be addressed carefully. The addition of a cosmic ray tagging system (CRT) that detects cosmic ray muons and measures their time and position relative to events internal to the TPC, is a way to mitigate the cosmic ray background. From SBND simulations an average of 3 cosmic rays for every neutrino event will cross the active volume in coincidence with the neutrino beam.

In order to mitigate cosmic ray events a $4\pi$ solid angle coverage of the TPC is highly desirable. In addition, cosmic rays entering the detector from the top are significantly more frequent than those entering from any other side of the detector. Hence, there will be 7 CRT planes in total, one covering each detector face plus an additional plane 2 m above the CRT plane covering the top surface of the TPC, as shown in Figure 3.9 right. The two top-face modules form a telescope that provides a coordinate resolution below 2 cm. After some new studies performed by the SBND collaboration it seems that the cosmic reduction achieved with the CRT is sufficient to rule out the need for an overburden, hence SBND will not proceed with its installation.

The SBND detector is currently under construction; TPC assembly was completed in June 2022, including the wire planes, the cathode, the field cage closure and the installation of the TPC cold electronics. The PDS was installed in September 2022 right before completing the detector assembly in October 2022. The detector was successfully lowered into the cryostat on April 25th, where it is now ready to finalize the remaining pieces of the installation. Cryogenic commissioning of the detector is expected to begin in late summer 2023, allowing the detector to become operational and start recording the first neutrinos in mid-2024.

### 3.4.3 The MicroBooNE Detector

The MicroBooNE LArTPC detector is the intermediate detector of SBN, at a baseline of 470 m and with a total active mass of 85 t of LAr [126]. The inner TPC is a rectangular box of 10.4 m long in the beam direction, 2.56 m wide in the drift direction and 2.33 m tall in the vertical direction. The detector is enclosed within a cylindrical cryostat containing the liquid argon and maintaining it at an operation temperature of 87 K, as shown in Figure 3.10.

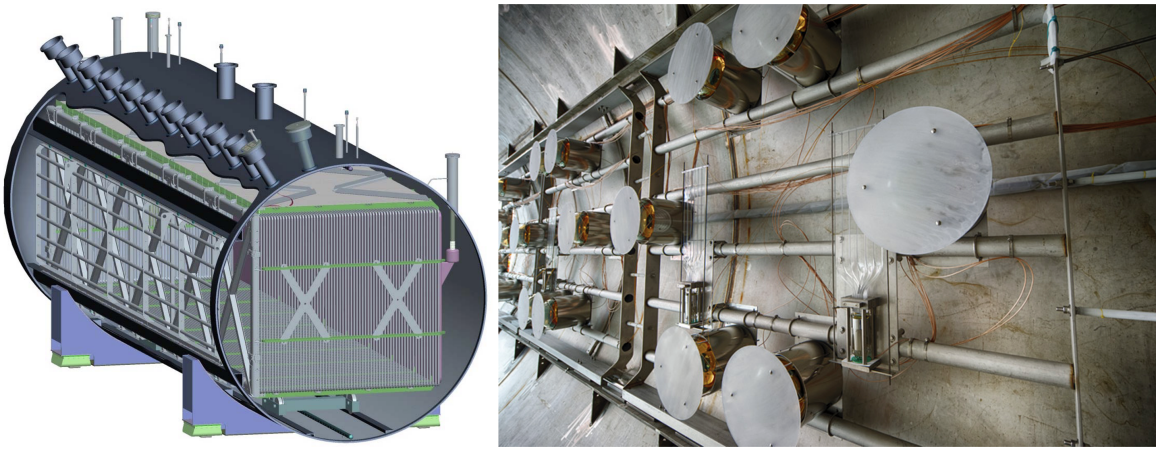

Figure 3.10: Left: Schematic diagram of the MicroBooNE LArTPC as arranged inside the cryostat. This is placed with its longest side in the beam direction, the anode plane on the right-hand side as seen from the beam, while the cathode is positioned on its left side. Right: picture of the optical units mounted in MicroBooNE right before the LArTPC installation. The picture shows the PMTs with its top TPB plate together with the light guide paddles. Figures taken from Ref. [126].

In contrast to the near and far detectors, MicroBooNE has a single TPC configuration. The three sense wire planes are oriented and spaced similarly to SBND, resulting into 2400 wires for each induction plane and 3456 wires for the collection plane. The single anode to cathode planes in the detector create a nominal electric field of 273 V/cm in contrast to the 500 V/cm used by the SBND and ICARUS detectors. In this field, the ionized electrons drift at a typical velocity of $\sim 1.1\ mm/\mu s$, corresponding to a maximum drift length of 2.53 m.

The MicroBooNE photon detection system is installed behind the TPC anode plane and consists of 32 8-inch cryogenic PMTs, equipped with TPB coated acrylic front plates. The reason why MicroBooNE chose to separate the PMT from the WLS plate is basically for simplicity of quality control and installation. In addition to the PMTs, there is a secondary system consisting of four light guide paddles. These paddles were introduced for R&D studies for future LArTPC and are placed near the primary optical units to allow a comparison of their performance, see Figure 3.10 right.

Sited nearly the Earth's surface, the MicroBooNE detector is also exposed to a high rate of cosmic ray muons. Due to a relatively long readout window for collecting the drifting charge, 2.2 ms which almost doubles the one from SBND, MicroBooNE collects signals from an average of 24 cosmics in its data acquisition window of 4.8 ms per event. A CRT system was therefore designed for the detector and put in place after the first data run. It consisted of 73 scintillating modules made of plastic scintillating strips situated on the top, bottom and along sides parallel to the neutrino beam. The design achieved a coverage of 85% of cosmics muons passing the TPC and a detailed review of its characteristics and construction can be found in Ref. [127].

The MicroBooNE detector took neutrino beam physics data from February 2016 to March 2020. The data-taking period is divided into five Runs that each correspond to about one year of data. The collaboration has recently presented a first set of searches related to the MiniBooNE low energy excess targeting multiple final-state topologies of CC $\nu_e$ interactions and NC $\Delta$ resonance decay that produces a single photon in the final state [128]. These results disfavor the hypothesis that the MiniBooNE low-energy excess originates exclusively from additional $\nu_e$ interactions, requiring a more sophisticated mechanism to explain the MiniBooNE observations. The recent analysis makes use of the data collected from February 2016 to September 2018, referred to as Run 1 to 3 and corresponding to a $\sim 6.4 \times 10^{20}$ POT for BNB. They present no evidence of sterile neutrino oscillations but rather a consistency with the $3\nu$ hypothesis within $1\sigma$ significance. This result allows to test part of the sterile neutrino parameter space suggested by other experimental anomalies, however it cannot completely rule out the 3+1 model. Further analysis including the data sets from Run 4 and 5 are expected to improve the sensitivity taking advantage of the higher statistics.

### 3.4.4 The SBN Far Detector: ICARUS

The ICARUS-T600 (Imaging Cosmic And Rare Underground Signals) cryogenic detector is the first large-scale operating LAr-TPC containing 760 tones of ultra-pure LAr, of which 476 tons are active [97]. Its construction finalized many years of R&D studies by the ICARUS Collaboration, with prototypes of growing mass developed both in laboratory and with industry involvement [129, 130]. Being the far detector of SBN, it is located at 600 m from the BNB target and consists of two large and identical adjacent modules with internal dimensions $3.6 \times 3.9 \times 19.6\ m^3$. Each module houses two LAr-TPC separated by a common cathode with a maximum drift distance of 1.5 m, equivalent to 0.96 ms drift time for the nominal 500 V/cm electric drift field. The cathode is built up by an array of nine panels made of punched stain-less, enabling a 58% optical transparency between the two drift regions. The anode of each TPC consists of a system of three parallel wire planes (17.95 m $\times$ 3.16 m surface) positioned 3 mm apart from each other. Wires are made of stainless steel with a diameter of 150 $\mu$m and length ranging from 9.42 m to 0.49 m depending on the position of the wire in the plane itself. Two coplanar adjacent sets of horizontal wires form the Induction 1 plane, while both Induction 2 and Collection planes are inclined at

$+60°$ and $-60°$ respectively with respect to the horizontal direction (not the vertical as in the other SBN detectors). This orientation was decided due to the fact that ICARUS was originally designed as a cosmic ray detector, which primarily enter from the top and cross the detector exiting downwards. Detecting the rays with a set of horizontal wires would then maximise the number crossed by a down-going cosmic ray. A total of 53,248 wires are mounted on the whole detector (four chambers) with a 3 mm wire pitch[4]. As in SBND and MicroBooNE, ICARUS applies an appropriate bias voltage to induce a non-destructive signal from the ionization charge in the first two planes (Induction 1 and 2 planes), whereas the ionization charge is fully collected by the last Collection plane.

In contrast to the SBND reflective cathode, all scintillation light produced inside the ICARUS TPCs are in the VUV regime and therefore it requires only PMT provided with wavelength-shifting. ICARUS light detection system consists of 360 PMTs deployed behind the wire chambers, evenly distributed and resulting in 90 PMTs per TPC, to collect the scintillation light and used for triggering purposes.

### Previous operation of ICARUS

The pre-assembly of the ICARUS T600 detector began in 1999 in Pavia (Italy) where one of its two 300-tons modules was brought into operation in 2001. A test run lasting three months was carried out with exposure to only cosmic rays on the surface to test for the first time the detector features and performance [131]. After the test, the detector was de-commissioned and in 2004 the two cryostats were transported to the Hall B of the underground Gran Sasso National Laboratories (LNGS), see Figure 3.11. In the first months of 2010 the detector was brought into operation taking data with the CERN to Gran Sasso (CNGS) neutrino beam and with cosmic rays. In 2013 ICARUS concluded a very successful 3-year long run, being exposed to the CNGS beam from October 2010 to December 2012. A total of about 3,000 CNGS neutrino events were collected, corresponding to $8.6 \times 10^{19}$ protons on target with an efficiency greater than 93 %. Additional data was also collected with cosmic rays, to study atmospheric neutrinos and proton decay. From the technological point of view ICARUS ran successfully, featuring a smooth operation, excellent electronic live time and high reliability. All in one, the detector demonstrated the feasibility of LAr-TPC technology at the kiloton scale in a deep underground environment as well as paved the way to the construction of the next generation of experiments.

The solutions adopted by the ICARUS detector for the argon recirculation and purification systems permitted to reach an impressive result in terms of argon purity, $< 50$ parts per trillion (ppt) of $O_2$ equivalent contaminant. In 2013 the highest electron lifetime of 16 ms was achieved, corresponding to a 20 ppt $O_2$ equivalent LAr contamination [132], where electron lifetime was determined with a 3% precision dominated by charge fluctuations. This result demonstrates the effectiveness of the single phase LAr-TPC detectors, proving that the construction of huge detectors with longer drift distance are viable. With the achieved purity level a drift distance of 5 m would suffer from a maximum signal attenuation of only 23 %.

Thanks to the detector exposure of the CNGS neutrino beam and collection of cosmic rays, the event reconstruction of these proved the high-level performance and physical potential of the LAr-TPC technology. Due to the high resolution and granularity of the detector, ICARUS reported a resolution of $\sim 1\ mm^3$ on an overall active volume of 340 $m^3$. This allowed the identification of the nature of particles by studying the event topology and the energy deposition per track length ($dE/dx$) as a function of the particle range. A dedicated program was developed to achieve precise 3D track reconstruction [133] and a neural network was used for particle identification. ICARUS claimed a complete identification of electrons taking advantage of its characteristic electromagnetic showering ( presents a behaviour well separated from $\pi^0$ reconstructed through its decay photons), the $dE/dx$ comparison and a $\pi^0$ invariant mass

[4]In each wire plane, the pitch is intended as orthogonal to the wires' direction.

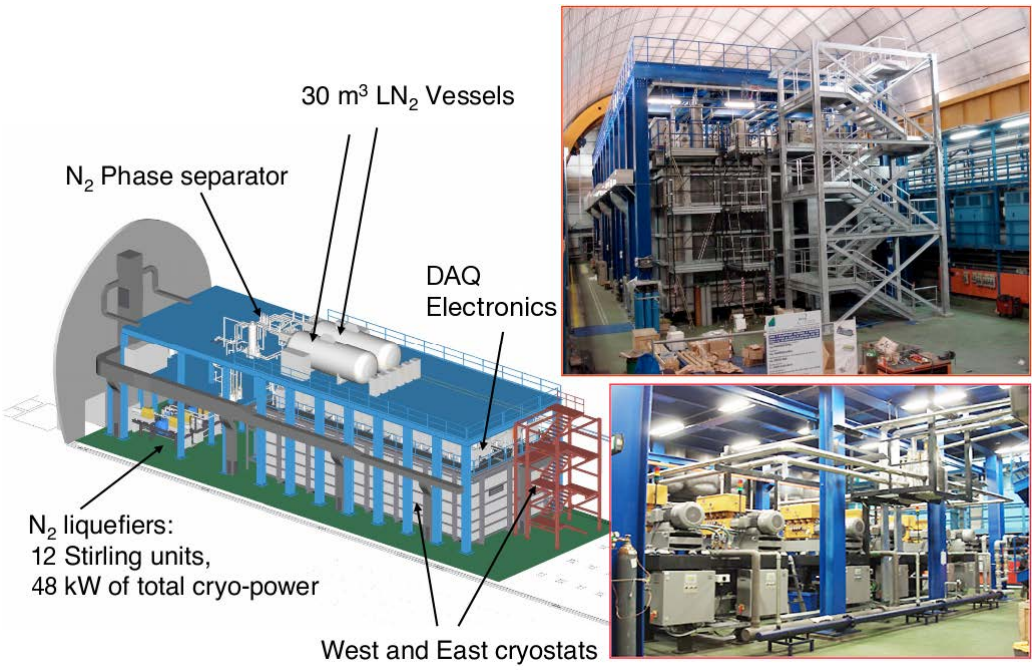


Figure 3.11: Left: Schematic diagram of the whole ICARUS-T600 plant in Hall B at LNGS. Right top: photo of the detector installation. Right-bottom: details of the cryo-cooler plant. Figure taken from Ref. [81].

measurement at the level of $10^{-3}$. In addition the high density of sampling ($\sim 2\%$ of a radiation length) and the remarkable signal to noise ratio of $\sim 10/1$ on individual wires reported by ICARUS, allowed to efficiently identify charged current $\nu_e$ interactions, while rejecting neutral currents to a negligible level. As a consequence, ICARUS demonstrated its unprecedented $e/\gamma$ identification capabilities confirming the expectations for a LArTPC detector, see Figure 3.12.

Another big milestone that was achieved during the underground operation concerns the good homogeneous calorimetric response of the detector [133]. The electromagnetic energy resolution was estimated to be $\sigma_E/E \approx 3\%/\sqrt{E(\text{GeV})}$, in agreement with the $\pi^0 \longrightarrow \gamma\gamma$ invariant mass measurements in the sub-GeV energy range. On the other hand the estimated resolution for hadronic showers was reported to be $\sigma_E/E \approx 30\%/\sqrt{E(\text{GeV})}$.

Further studies were done to measure the muon momentum by means of multiple Coulomb scattering (MCS), as it is a crucial ingredient to the reconstruction of $\nu_\mu$CC events in LArTPC in the absence of a magnetic field. The method exploited the multiple scattering along the tracks, studying its displacements with respect to a straight line. The analysis showed a $\sim 14\%$ average resolution in the sub-GeV energy range (0.4-4 GeV/c), covering an energy region relevant for the next SBN and long base-line neutrino experiments [135].

Finally, events related to the cosmic rays were also studied identifying a handful number of atmospheric neutrino interactions corresponding to an exposure of 0.43 kton $\cdot$ year : 6 $\nu_\mu$CC and 8 $\nu_e$CC. These events were fully reconstructed and the agreement with the expectations demonstrated that the automatic search for the $\nu_e$CC in the sub-GeV range, required for the study of the BNB neutrinos at FNAL and other long baseline neutrino experiments, was feasible [136].

### ICARUS-T600 overhauling at CERN

In order to prepare the detector for SBN data taking, at the end of the LNGS operations, ICARUS was disassembled and moved to CERN to undergo an intensive overhaul before being shipped to FNAL. In contrast to the hostile environment in which ICARUS operated on

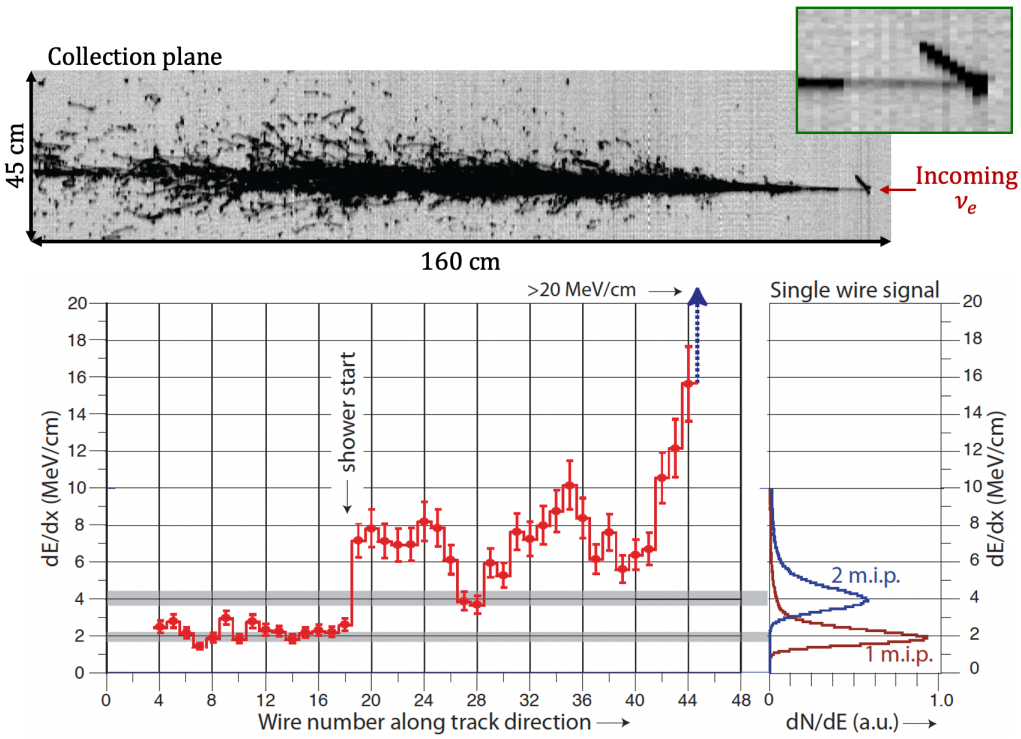


Figure 3.12: $\nu_e$ charged-current quasi-elastic event collected in ICARUS during the LNGS run. The top image shows the clear electron signature and an additional hadronic track at the primary vertex, seen in Collection. The bottom plot reports the evolution of $dE/dx$ from a single track to the electromagnetic shower produced by the initial electron along the individual wires, showing good agreement with the 1 MIP and 2 MIP hypothesis. Figure from Ref. [134].

LNGS, the SBN program offers a completely different venue. As previously mention, ICARUS takes data at shallow depth and, even if a 3-meter concrete overburden is build on top of the detector, a considerably large number of cosmic muons ($\sim$ 11) are expected to cross the detector randomly in the 1 ms drift time during each recorded event. Hence, ICARUS was moved to the CERN's Neutrino Platform for a complete overhauling, preserving most of the existing operational equipment while upgrading some components with up-to-date technology.

The refurbishing mainly consisted of: the realization of new cold vessels for LAr containment with purely passive insulation, based on a similar technology as the SBND; a complete review and maintenance of the cryogenics and LAr purification equipment; flattening of the TPC cathode, the punched hole stainless steel panels underwent a thermal treatment improving the planarity to a few mm; the implementation of a new light collection system, to allow a more precise event localization and disentangle beam events from the cosmogenic background; and finally a new, higher performance TPC read-out electronics with updated slow control systems and cabling.

A new light detection system that is sensitive to the photons produced by the LAr scintillation is a fundamental feature for the ICARUS operation at shallow depth. The system needs to be able to localize the track associated with every light pulse along the 20 m of the longitudinal detector direction with an accuracy better than 1 m ($\mathcal{O}$(1 ns) time resolution). In this way, the light collection system would be able to provide unambiguously the absolute timing for each track and to identify, among the several tracks in the LAr-TPC image, the event in coincidence with the BNB and NuMI beam spill gates. The detection process in the LAr-TPC is initiated by the trigger signal opening a long "imaging" readout window, in which tracks are recorded in a time sequence and collected serially by the readout planes, while the electrons travel towards the end of the drift path. The full image of the event is therefore progressively extracted from the drift time distributions and from many readout wires.

ICARUS light detection system consists of 360 8-inch Hamamatsu R5912-MOD PMTs deployed behind the 4 wires chambers, resulting in 90 PMTs per TPC and yielding a 5% photocathode coverage [137]. This greatly increases the number of PMTs, recalling that before the overhauling there were a total of only 74 PMTs. To make them sensitive to the VUV light, each PMT glass is provided with a $\sim 0.2\ mg/cm^2$ coating of TPB. All PMTs were mounted onto the wire chamber mechanical frames using a supporting system that allows the PMT to be positioned about 5 mm behind the Collection planes wires, as shown in Figure 3.13. Given that PMTs might induce spurious signal on wire planes a stainless steel grid cage surrounds each PMT with the goal of providing an electrostatic shielding to mitigate the induction of these fake signals.

Figure 3.13: Inner view of one ICARUS module with the two TPCs separated by the common central cathode and showing the new 8" PMT system behind the wire planes. Figure courtesy of CERN, where the picture was taken during the refurbishing in a clean room.

Finally, the light detection setup was complemented by a laser calibration system allowing for gain equalization, timing and monitoring of all the PMTs. More detailed information can be found in Ref. [138].

The other major upgrade was regarding the TPC electronics. The electronics initially equipping ICARUS during the LNGS operation were designed to allow a continuous read-out, digitization and independent waveform recording of signals from each wire of the TPC for the entire drift time. Starting from an analogue low noise warm front-end amplifier followed by a multiplexed 10-bit analog-digital converter (ADC), with sampling rate of 400 ns, and by a digital VME (Versa Module Eurocard) module that provided local storage, data compression and trigger information. The custom design low-noise ICARUS system used in the LNGS run performed efficiently with a signal to noise ratio $\sim 10$, allowing collection of several thousands of neutrino and cosmic events with unprecedented imaging quality. However, the signal shaping chosen at that time presented some limitations on signals produced by the intermediate Induction 2 wire plane, in particular in the presence of dense showers. The described architecture, even if still valid, presents nowadays major improvements, taking advantage of new, better performing and compact electronic devices. The new electronics designed for the ICARUS surface operation at FNAL should improve the performance of the system and drastically reduce the costs and vol-

ume by using more advance components. Given the foreseen shallow depth and the high rate of cosmics, the original data acquisition system (DAQ) presented a strong limitation to the allowed data rate collection. Even though the new system maintains the previous architecture, allowing a continuous triggerable multi-buffered waveform recorder for each wire of the detector, exploits a more advanced design. Each channel has a dedicated serial 12-bit ADC and the analog and digital parts are now integrated in one electronic module that serves 64 channels. The VME standard was abandoned in favor of a serial bus architecture with optical links allowing a Gb/s band-width data transmission.

TPC wire signals are extracted from the cryostat through proprietary flanges on top of the chimneys and fed into the front-end amplifiers. The flanges were also modified from the original ones in order to accommodate electronic modules and Decoupling Biasing Boards (DBBs) directly inserted on the external and internal sides of the flanges, respectively. The DBB has two main functions, first to bias each wire and secondly, to convey the signal to the amplifiers by means of blocking capacitors. The design, prototyping and performance of new ICARUS front-end electronics chain has been extensively tested prior installation. It was demonstrated, among other features, the improved capability to efficiently handle the signals in the intermediate Induction 2 plane with a significant increase of signal to noise ratio with respect to previous performances. Finally nine A2795 boards are housed in a custom "mini-crate' mounted onto the feed-through flange on top of the chimney designed for the transmission of the TPC wire signals. This was an important achievement as it dramatically reduced the volume of the front-end electronics for each flange, as shown in Figure 3.14. Each set of nine boards in a single crate are read out through two fibers. The full TPC electronics, composed of 96 mini-crates, is synchronized by a serial link cable which sends clock, trigger and commands information. A detailed review of the TPC electronics upgrade can be found in Ref. [139].

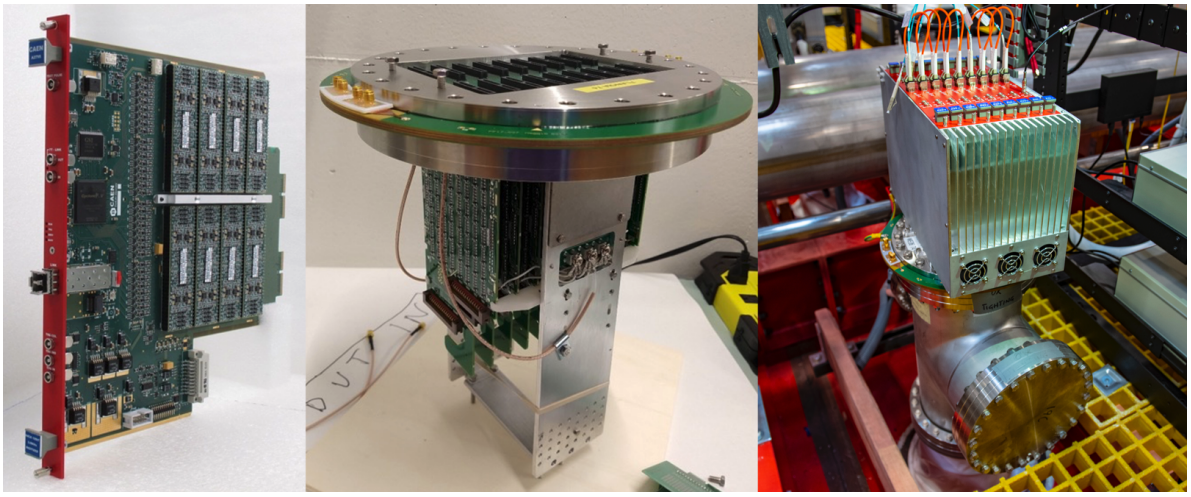

Figure 3.14: Left: A2795 custom board housing 64 amplifiers, analog-digital converter, digital control and optical link. Middle: An assembled feed-through with nine DBB and the biasing cables. Right: A mini-crate populated by nine A2795 boards installed on a feed-through flange and placed on top of the chimney. Figures taken from Ref. [139].

### ICARUS at FNAL

After the overhauling activities at CERN, ICARUS was shipped to Fermilab in July 2017 and installed in the SBN far detector experimental hall in August 2018. Figure 3.15 left, shows a picture of the installation of the ICARUS cryostats inside the far detector pit. Work began soon after that moment to install and test all main subsystems before the cryogenic commissioning. The installation of the various components of the detector is shown in the middle and right

pictures of Figure 3.15.

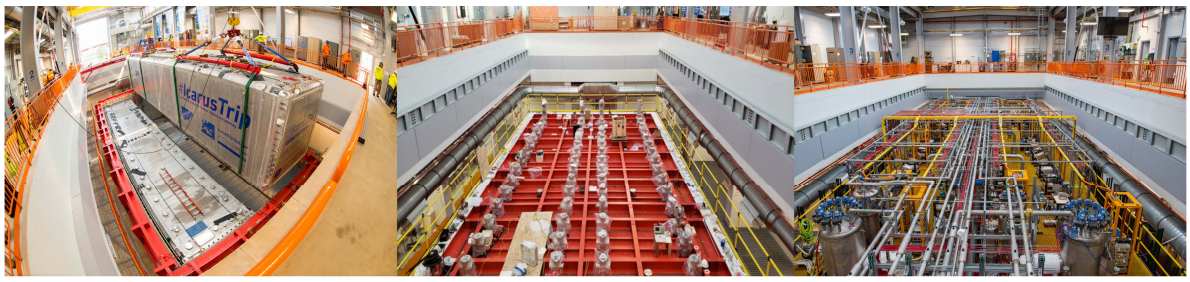

Figure 3.15: Left: Installation of one of the two ICARUS T300 modules inside the pit of the SBN far detector building, August 2018. Middle: Status of the detector by December 2018, where the TPC, PMT and laser feed-through flanges were installed. Right: ICARUS detector right before the start of data taking for commissioning, showing the installation of the mini-crates and the cryogenic plant. Photos from Fermilab Creative Services.

The ICARUS cryogenic plant was designed, built and installed at Fermilab thanks to a joined effort from CERN, Istituto Nazionale di Fisica Nucleare (INFN) and Fermilab to ensure an optimal performance of the detector. Previous operation at LNGS demonstrated the very high reliability of the existing cryogenic plant, therefore the adopted strategy was carried over to the new detector operations with few exceptions due to their different locations. The new design followed closely the original implementation at LNGS, however the cryogenic and purification system was completely renewed. One main difference is the re-liquefaction system; at LNGS the residual nitrogen gas produced in the various processes was converted back to liquid by a dedicated re-liquefaction system composed of twelve cryo-coolers. This was designed to work in closed loop for safe operation in confined spaces. In contrast, at Fermilab the cooling circuit is operated in an open loop, namely the re-liquefaction cryo-coolers is no longer used and instead, the residual nitrogen gas is vented to the atmosphere.

The main components of the cryogenic and purification system are listed below:

- 273 $m^3$ LAr containers, hosting the TPC detectors and the LAr scintillation light system.
- Cold shields consisting of set of heat exchangers filled with $LN_2$, completely surrounding the main LAr containers. They are designed to prevent heat coming from the thermal insulation, to reach the LAr volumes.
- Thermal insulation panels surrounding the cold shields and made of $\sim$ 600 mm thick polyurethane foam.
- $LN_2$ cooling circuits (piping, circulation pumps, regulating valves, etc) serving the cold shields and purifying units.
- Warm vessel, providing enclosure and mechanical support for the thermal insulation.
- 4 argon gas recirculation units, two per cold vessel, that re-condense and purify the argon flowing from the gas phase on top of the main LAr containers.
- 2 liquid argon recirculation units, one per cold vessel, ensuring the circulation of argon from the cold vessel through a set of purifiers before injecting it back into the cold vessel.
- Cryogenic control system including a data display and recording, automation and alarming options.
- $LN_2$ and LAr storage dewars and its relative transfer lines

- Purification unit used for the filling of the cold vessels. The unit is equipped with a regeneration system and a set of gas analysers.

The ICARUS cryogenic plant was fully designed, delivered and installed at the SBN Far Detector Hall by July 2019, in parallel with the TPC electronic and PMT system installation activities.

**Cosmic Background rejection strategies**

The shallow depth at which ICARUS operates at FNAL, exposes the detector to an abundant flux of cosmic rays while collecting neutrinos from BNB and NuMI beams ($\sim$ 11Hz), as these can induce several additional and uncorrelated triggers during the 1 ms drift time. Cosmic particles entering anywhere in the detector during the neutrino beam spill[5] may interact in the liquid argon generating scintillation light as well as an event trigger; this is the so called *in-time* activity. If instead the interaction occurs outside the beam spill gate but within the drift time, the cosmic activity is then tagged as *out of time*. On average around 11 cosmic tracks are expected to cross the entire detector volume during each drift window, generating a background that needs to be identified and suppressed. To cope with this challenging condition which could potentially spoil out the search for anomalous oscillation signal induced by sterile neutrinos, the detector setup includes a $\sim$ 3m concrete overburden (OB), to reduce the flux of cosmic rays, complemented by a $4\pi$ coverage CRT system, to tag the remaining incoming charged particles.

Cosmic background rejection strategies are of uttermost relevance for the $\nu_\mu \longrightarrow \nu_e$ channel, as the oscillation study relies on the tiny intrinsic $\nu_e$ component in the BNB beam. Any additional contribution of background faking $\nu_e$CC interactions would result into a reduction of the oscillation sensitivity. Photons associated with cosmic muons represent the primary background for identifying $\nu_e$ candidates, since electrons produced through Compton scattering or pair production can mimic a genuine $\nu_e$CC event.

Furthermore, due to ICARUS larger size and distance from the target in comparison with SBND, exposes the detector to a $\sim$ 4 times larger rate of cosmic rays while the neutrino interaction rate is reduced by a factor 10.

**ICARUS CRT: description and installation** The CRT system is a subdetector external to the cryostat intended to identify charged particles passing through or near the TPC active volume. Timestamps associated to a particle tagged by the CRT are compared with timestamps from PMT signals, exploiting the few ns time resolution of each system. This comparison allows the determination of weather an interaction inside the TPC originated from an outside cosmic ray or from an internal interaction.

The CRT system covers a surface area of $\sim$ 1100 $m^2$ and consists of a top, side and bottom subsystems with comparable timing and spatial resolutions. The three different systems complement each other to provide a $\sim$ 95% possibility of identify through going cosmics.

The ICARUS Top CRT system is divided in 123 detector modules: 84 are placed horizontally on top of the cryostats while the remaining 39 are vertical modules along the perimeter of the cryostat top surface. This configuration was chosen so that more than 80% of the cosmic muons flux would be intercepted by the Top CRT. Each hodoscope module is a 1.86 $\times$ 1.86 $m^2$ aluminium box containing two orthogonal layers of eight scintillator bars for position reconstruction purposes. These scintillator bars are 23 cm wide and 184 cm long and have a different thickness depending on the layer, 1 cm for the top layer and 1.5 cm for the bottom one. In total, 2000 scintillator bars were used to build the whole Top CRT system. Each scintillator strip is instrumented with two wave-length shifting (WLS) fibers that collect the light. The fibers are read-out only from one end by a Silicon Photo-Multiplier (SiPM) therefore, the

[5] 1.6 $\mu$s for BNB and 9.6 $\mu$s for NuMI

opposite end-site mirrors the light into the SiPM to enhance the light yield. There are 32 SiPM in each module, and its signal is routed via micro-coaxial cables to a printed circuit board patch panel connected to a Front End Board (FEB). As the ultimate goal of the CRT modules is determining the precise position of crossing muons, the FEB requires a coincidence between two SiPM signals of the same bar and triggers only when a logic coincidence is found between the two scintillator layers. The top CRT was build and designed from scratch by INFN and CERN. The construction of the modules began in April 2019 and concluded in February 2020, to later be shipped to Fermilab in summer 2021. The installation of Top CRT modules was carried out and completed in December 2021.

The ICARUS Side CRT makes use of scintillator modules formerly used by the MINOS experiment. Each module is composed of twenty adjacent strips of $800 \times 4 \times 1\ cm^3$ polystyrene scintillator. The scintillator is contained in a metal envelope and each strip has an embedded WLS fiber running down the middle. These fibers are collected at the end of the modules and connected to the optical readout, consisting of an array of ten Hamamatsu SiPM. Each SiPM reads out two fibers and corresponds to a single electronic readout channel on CAEN FEB. ICARUS Side CRT system is double layered, with an inner and outer layer of MINOS modules to apply coincidence logic between the two. The south Side CRT wall is the only one that exploits a configuration in which the two scintillator layers are arranged orthogonally in an X-Y configuration. To this end, the modules oriented vertically were cut in half. This particular configuration provides an improved position reconstruction on the southern side of the TPCs, corresponding to the upstream direction along the BNB beam. East and west walls utilize full length MINOS modules mounted with the strips arranged horizontally and parallel to the cryostat. Due to the proximity of the north wall to the liquid argon filtering system, the north module uses cut MINOS modules, mounted horizontally, of different lengths to maximize the coverage of the available surface. All full length modules are read-out on both ends of the scintillator strips, while the cut modules are read-out on one end only. The full side CRT system is composed of 2710 read-out channels with 136 full and 81 cut modules in total. The Side CRT system was installed over the period from November 2019 to April 2021.

Finally, the Bottom CRT consists of 14 modules, divided into two daisy chains of 7 modules each, and positioned underneath the TPC warm vessel. The modules have been inherited from the Double Chooz experiment and each one consists of 64 polystyrene scintillator strips divided equally into two layers. Scintillation light is collected in a WLS optical fiber and read-out at one end of each strip by an Hamamatsu multianode PMT, while being mirrored at the other end. Bottom CRT panels were installed before the warm vessel deployment.

The whole ICARUS CRT system can bee seen in Figure 3.16 and Figure 3.17.


Figure 3.16: Pictures of the Top CRT subsystem, where the horizontal (left) and vertical (right) plane modules are shown on its final configuration. Photos from Ref. [140].

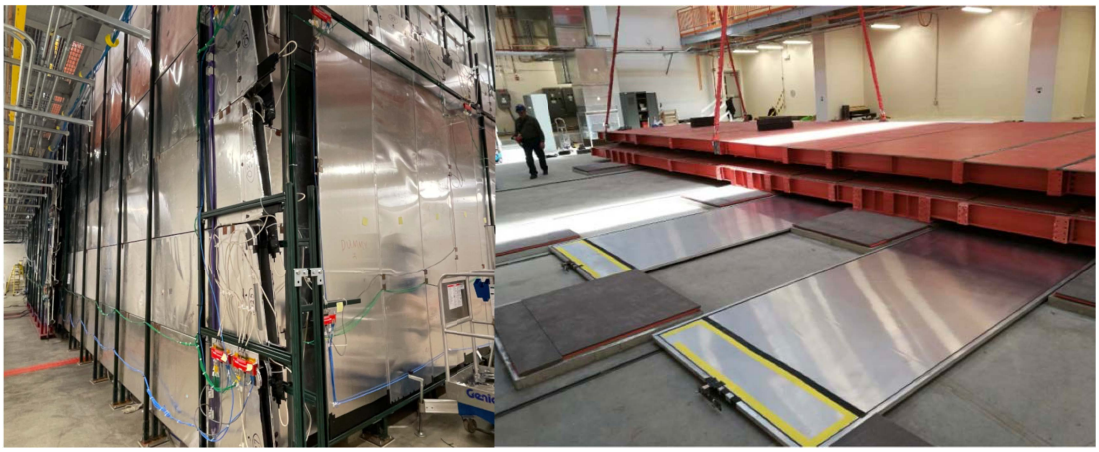

Figure 3.17: Left: Picture of the Side CRT south and west walls seen from the ICARUS building ground pit. Right: Fully installed Bottom CRT module during the warm vessel deployment. Photos from Ref. [140].

**ICARUS Overburden: motivation and installation** In order to evaluate the impact of placing a concrete overburden on top of the detector detailed Monte Carlo (MC) calculations were performed to asses the cosmic ray rate crossing the ICARUS detector.

Cosmic ray fluxes were simulated using CORSIKA as implemented in the LArSoft framework [141], more details will be given in Chapter 5. This provides two alternative models to describe the primary cosmics impinging on top of Earth's atmosphere: the first option is the so-called Constant Mass Composition Model and includes substantial amounts of both light and heavy elements; the second alternative is the proton-only model, where only primary protons are responsible for the reduced simulated flux of particles through the detector. Previous work from MicroBooNE collaboration showed that the second simplified method is adequate to describe the cosmic ray muon fluxes, and hence was used to perform the MC study. Cosmic primary particles are sampled from a data library generated by CORSIKA uniformly distributed on top of the cryostats; each particle with kinetic energy greater or equal to 50 MeV and producing some activity inside or in the immediate surrounding of the detector is fed as input to the MC simulation. These particles are then propagated with GEANT4 [142] exploiting an accurate description of the detector geometry and composition of the experimental setup. All secondary particle information is saved down to a 1 MeV energy threshold.

To understand the role of the overburden in the reduction of cosmics reaching the active detector, an event statistics for 3 years of data taking (total exposure of $6.6 \times 10^{20}$ POTs) was simulated. The impact of the overburden is shown in Figure 3.18, where the presence of different particles, of cosmogenic origin, inside the active volume with and without the overburden is quantified.

The overburden reduces the dominant muon flux by $\sim 25\%$, filtering out muons with kinetic energy $E_K < 1.5$ GeV. There is a more effective suppression for primary hadrons, with a reduction by a factor $\sim 540$ for protons and $\sim 210$ for neutrons, while the electromagnetic cosmic ray component is almost fully eliminated. These studies confirmed the need for an overburden in order to perform sterile neutrino searches and to reach the necessary reduction of the cosmic background to $\nu_e$ CC events.

The Overburden was placed 10 cm above the ICARUS Top CRT system and consist of three layers of concrete blocks, each approximately 1 meter tall. This gives a height of 2.845 m, or 6 m water equivalent, with a total mass of 5 million pounds. The overburden installation started in April 2022, once the Top CRT commissioning was completed. The first layer of the overburden was build with low radioactive material, while the second and third layer of the overburden were taken from previous Fermilab experiments. Before being installed, each concrete block was

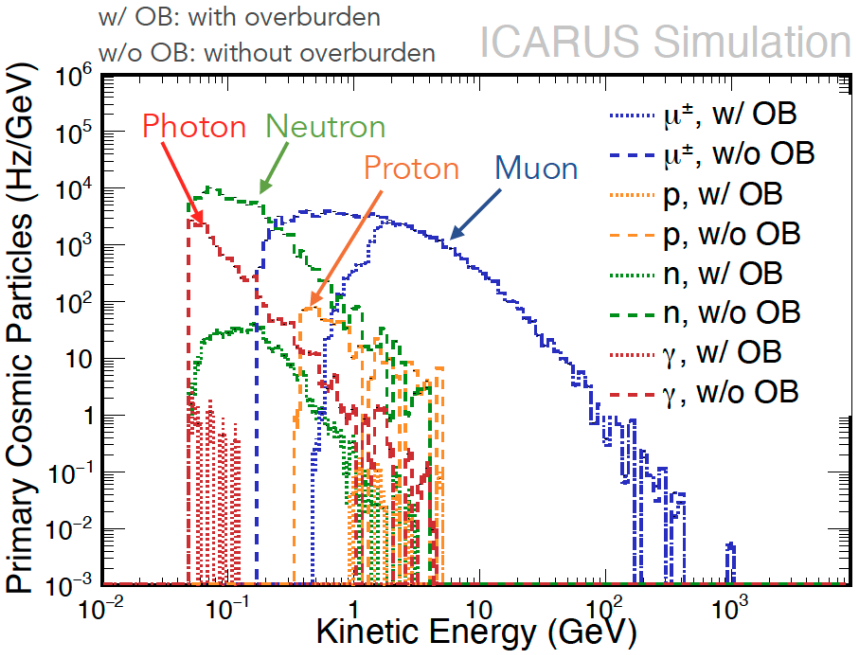


Figure 3.18: Overburden impact on the spectrum of primary cosmics for different particles. Dashed lines represent the number of primary cosmics particles intersecting the active volume when a complete geometry description of the detector and surrounding materials is used, but no overburden is simulated. Dotted lines instead show the same quantity when a 2.845 m concrete overburden is added on top of the detector. Plot taken from Ref. [143].

tested with a Geiger counter to ensure a low value of radioactivity. The installation of the last concrete block was completed on June 7, 2022 marking the beginning of ICARUS physics data taking phase. A picture of the fully completed overburden is shown in Fig 3.19.

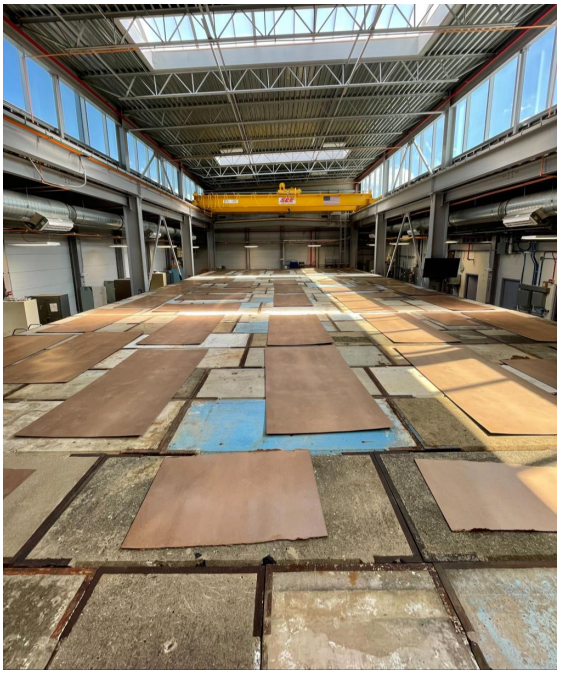

Figure 3.19: Picture of ICARUS after the full installation of the 3 overburden concrete layers. Picture taken from Ref. [140].

# Chapter 4

# ICARUS Initial Operation

After a complete description of the SBN Program, its physical goals, and a detailed definition of its 3 detectors, it is now possible to shift focus and describe the activities that have been taking place at the ICARUS detector.

## 4.1 ICARUS standalone physics program

In addition to the physics program of SBN, a new opportunity has arisen; the claim of the observation of a sterile neutrino signal in the reactor Neutrino-4 experiment has already been presented, however it has not been emphasised that such an oscillatory pattern, if present, should be visible with both $\nu_\mu$ and $\nu_e$.

The Neutrino-4 oscillation-like signal for $\nu_\mu$ events can be observed by ICARUS at the BNB studying the $\nu_\mu$ disappearance channel as a function of the neutrino energy, averaged over the length of the pion decay tunnel. The top plot of Figure 4.1 shows the survival oscillation probability in the presence of the Neutrino-4 anomaly and the expected ICARUS results after 3 months of data taking with the BNB. The calculation of black dots was performed in 0.02 steps of L/E and considering the best fit of Neutrino-4 parameters, $\Delta m^2 = 7.25\ eV^2$ and $\sin^2(2\theta) = 0.26$. Instead ICARUS expectations were calculated considering only contained $\nu_\mu$CC QE interactions with a muon of length greater than 50 cm, to enhance $\mu$ identification and suppression of charged $\pi$ backgrounds. The calculation was performed in 0.1 L/E steps and only statistical errors were reported. Preliminary trigger studies showed a total reduction of $\sim 3\%$ on $\nu_\mu$CC QE contained events at low neutrino energy, further increasing the statistical uncertainty at higher L/E values. In addition, and as a first approximation, an smearing on the energy of $\sim 3\%$ was applied to account for detector energy resolution and uncertainty on the BNB neutrino flux. With this requirements, ICARUS is expected to collect $\sim$ 11500 $\nu_\mu$CC events in this 3 months. It is possible to see that the oscillation pattern is not spoiled when the precision on reconstructed neutrino energy for contained $\nu_\mu$CC QE events is accounted for, confirming the possibility to unambiguously observe the Neutrino-4 like signal with the Booster neutrino beam.

In addition to BNB, ICARUS also records neutrinos from the NuMI beam. While BNB is greatly dominated by $\nu_\mu$ from pion production decays, the off-axis location of the detector with respect to the NuMI target makes kaons the primary source of neutrinos. This leads to a much larger contribution of the $\nu_e$ signal and allows to perform a sensitive disappearance search in the $\nu_e$ channel. By considering one year of data taking at NuMI and proceeding in an analogous manner, ICARUS expects to record $\sim$ 5200 $\nu_e$CC interactions with a fully contained electromagnetic shower. In this case, the expected values were computed in 0.06 L/E steps and only statistical errors were reported, as given the optimal ICARUS energy resolution observed at LNGS for electrons and electromagnetic showers, the effect of energy reconstruction is expected to be marginal. Despite the almost 725 m long NuMI decay tunnel, most of the $\nu_e$ are produced by kaons decaying close to the target. As seen in the bottom plot of Figure 4.1, this does

not wash out the characteristic oscillatory pattern foreseen in the presence of the Neutrino-4 anomaly. This measurement will be sufficient to verify conclusively the Neutrino-4 observation from another neutrino source.

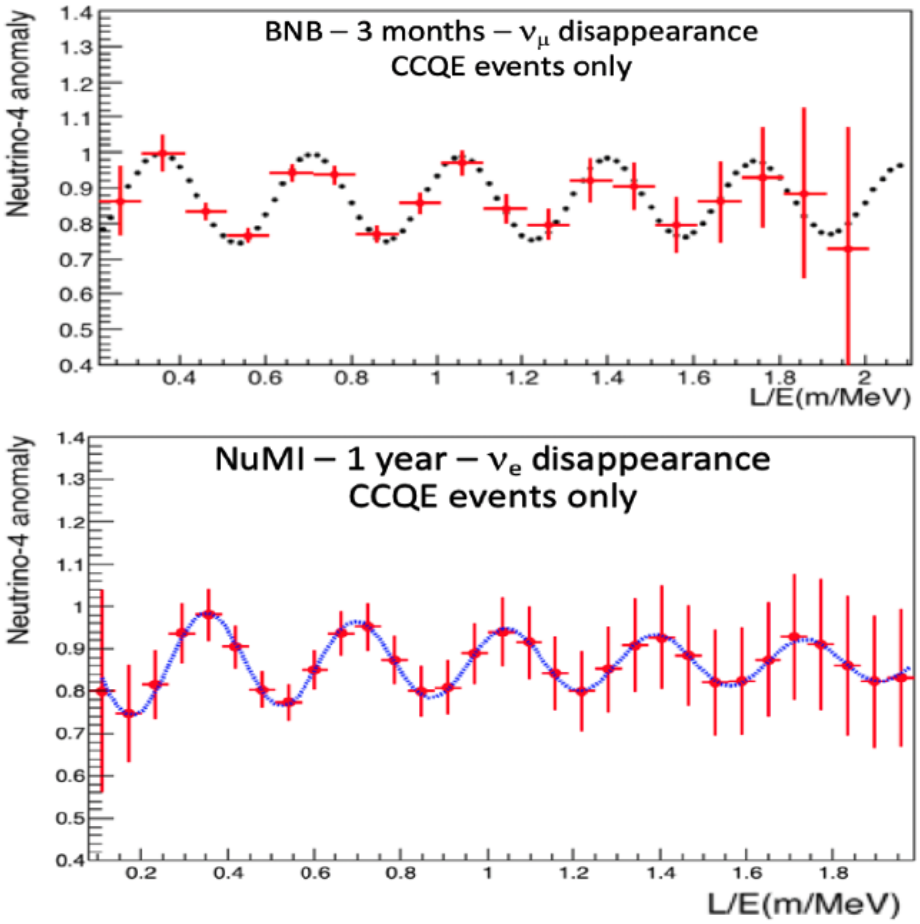


Figure 4.1: Predicted survival neutrino oscillation probability for Neutrino-4 anomaly (top black and bottom blue dots) for the best fit ($\Delta m^2_{N4} = 7.25, \sin^2 2\theta_{N4} = 0.26$) and expected signature observed at ICARUS after 3 month of BNB data (top plot, red) or 1 year of NuMI data (bottom plot, red). Plots taken from Ref. [144].

## 4.2 ICARUS-T600 commissioning

After the placement of the two ICARUS modules in the pit in August 2018, all subsystems were installed in the detector and its components checked for correct operation. PMT and TPC systems were placed and tested to measure the PMT gain and dark rate together with activities to examine the full TPC system for noise monitoring purposes. In addition dedicated runs were also carried out for specific PMT calibration with a laser system, to assess data acquisition system upgrades and to perform longevity test, among others. In parallel, the cryogenic equipment was installed and its commissioning started on February 13, 2020 when preparatory activities for liquid argon filling took place. The filling was completed on April 19 and the system was fully stabilized thanks to the correct operation of the liquid recirculation circuit on May 2020. During the cryogenic commissioning, several activities both related to monitoring the status of the detector and to developments for the incoming commissioning data taking phase, were ongoing. The detector activation took place on August 27, 2020 when the TPC wire planes and the cathode high voltage (HV) were taken to nominal voltage. The three wire planes are biased

at -250V, -30V and 250V for Induction 1, Induction 2 and Collection planes respectively, while the cathode high voltage is set to -75 kV.

The detector started its data taking with a random 5 Hz trigger, collecting cosmic-ray interaction events for calibration purposes. One of the first measurements carried out was the free electron lifetime $\tau_{ele}$. This parameter is crucial to monitor the liquid argon condition in the TPCs and to ensure a precise measurement of the energy deposition from the ionization charge signal of collected events. If $\tau_{ele}$ is below 3 ms, impurities prevent an efficient detection and reconstruction of ionizing events inside the active volume. On the other hand, the higher the $\tau_{ele}$ the better, as the probability that an ionization electron is capture by any impurity decreases. The LAr purity is continuously monitored by measuring the charge attenuation along the drift path of the electron ionization signals generated by cosmic ray track crossing the detector, which are used as standard candles. One of the methods used to have a fast, real time measurement of the purity, is the one developed during the ICARUS Gran Sasso run [132]. This method was employed during the commissioning phase were a run by run measurement was of great relevance to monitor the correct operation of the detector in its initial phase.

To characterize the performance of ICARUS subsystems, a variety of measurements were done starting in August 2020.

The whole light detection system was tested at Fermilab before the detector cooling down. A total of 357 out of the 360 PMTs were found to be properly functioning in accordance with tests performed at CERN [138]. Same situation was reported after the LAr filling, demonstrating the ability of PMT to work at cryogenic temperatures. A PMT signal recorded by the light detection system is shown in Figure 4.2, presenting the characteristic shape of the fast and slow light components. During the PMT commissioning a calibration and equalization campaign was carried out, achieving a 1 ns precision between PMT channel delay response and a final equalization below 1%.

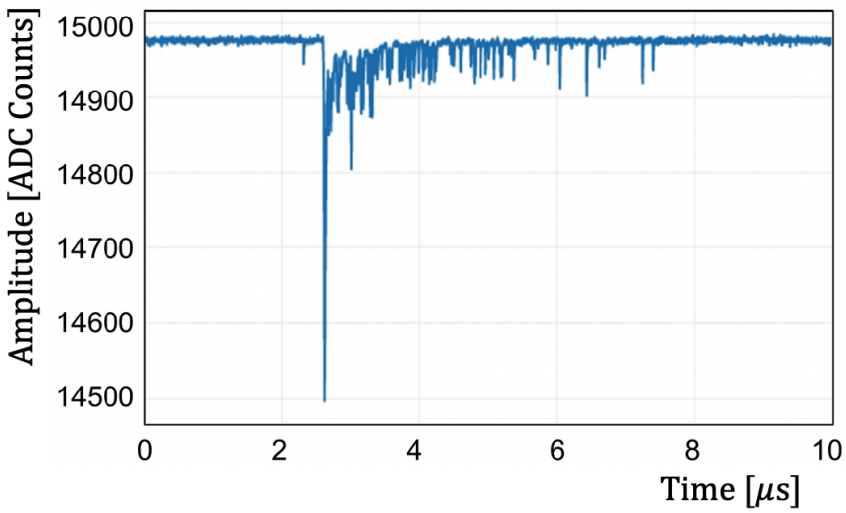


Figure 4.2: PMT signal recorded by the light detection system electronics. Taken from Ref. [128].

TPC commissioning began soon after the liquid argon purity was good enough to precisely study the detector response with ionization signals from cosmogenic activity. TPC noise level were evaluated by measuring the RMS of waveforms from the TPC readout, with an equivalent noise charge of roughly 550 $e^-$/ADC [139]. Noise is characterized by an incoherent component, varying wire by wire, and a significant component correlated over an electronic front-end board, corresponding to 64 adjacent wires. Measured TPC noise levels are shown in Figure 4.3 left, before and after the filtering of coherent noise. A custom made coherent noise filtering algorithm identifies the coherent component as the median ADC value at each tick across all 64 channels of

the readout board, allowing a precise separation of the coherent and intrinsic noise components. In order not to bias the noise measurements, recorded waveforms containing signals were identified by a threshold based algorithm and removed from consideration. In addition, the described measurements were repeated with the cathode high voltage (HV) turned off, finding consistent results. The agreement indicated not only that a negligible amount of TPC noise was caused by cathode HV interference, but also it was possible to validate the ionization signal identification methodology. Figure 4.3 right shows the Fast Fourier transform of the same noise waveforms for each of the three wire planes, averaged over the entire detector, before and after the application of the coherent noise filtering. The intrinsic noise spectrum was found to agree with the expected Rayleigh distribution, demonstrating that the filtering algorithm was able to almost completely eliminate the extrinsic noise component. Given the same length of wires, Collection and Induction 2 planes present a similar normalization, contrary to the slightly different shape found in Induction 1. This is due to the longer wires present in this latter plane resulting in a higher capacitance, and thus increasing the intrinsic noise levels. More details on how noise is eliminated when physical signals are present will be given in the TPC reconstruction chapter, in particular Subsection 5.5.1.

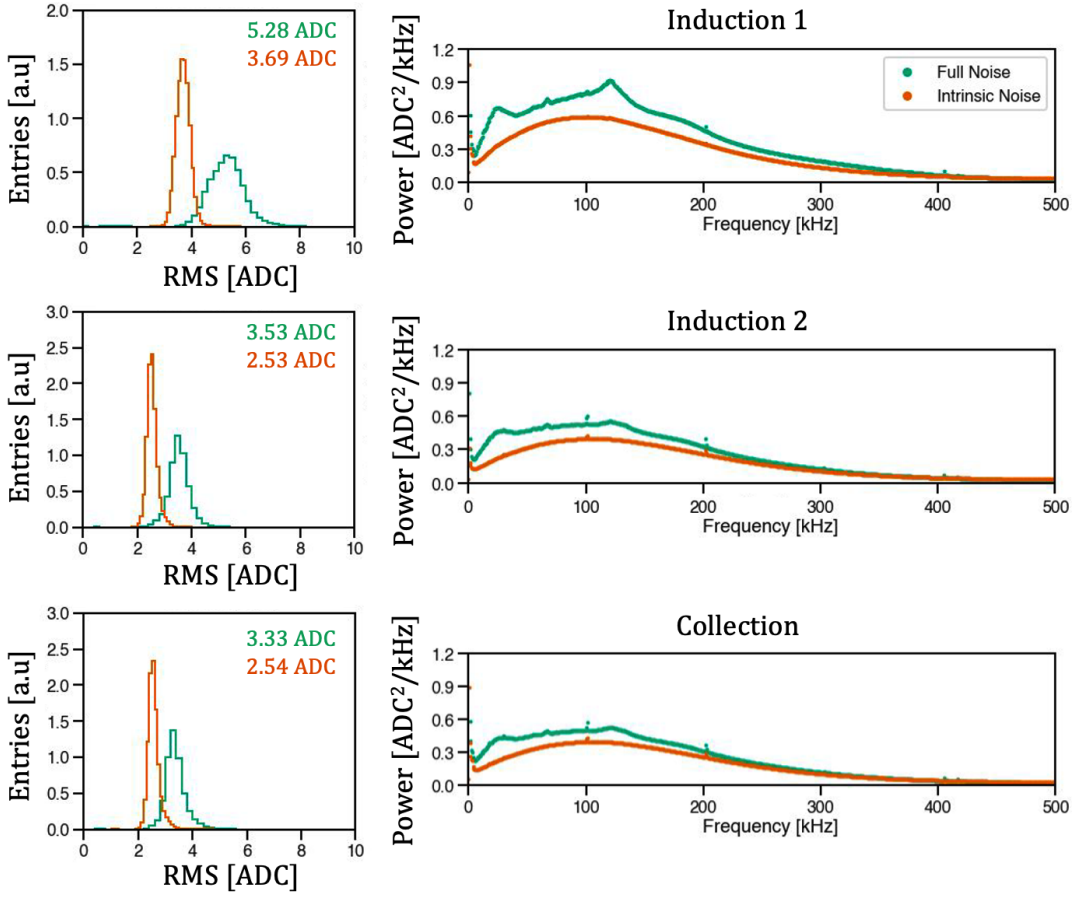


Figure 4.3: Left: TPC noise levels at ICARUS before and after filtering out the coherent noise. Results are shown for each plane together with the mean values of each distribution. Right: Corresponding Fast Fourier transforms of noise waveforms data collected in ICARUS in each plane, showing the raw and noise filtered spectra. First row corresponds to Induction 1 plane, middle and bottom rows present the Induction 2 and Collection plane, respectively. The legend applies for all plots similarly. Taken from Ref. [128]

Ionization signals from anode-cathode crossing cosmic muons were used to address other measurements, for instance to evaluate the peak signal-to-noise ratio, to determine the ionization

drift velocity, to quantify the space charge effects and to set the energy scale calibration for minimum ionization particles. More details can be found in Ref. [145], however some of this items will be analyzed later in detail.

Last but not least, the CRT system was also tested before and after its installation. Once all CRT panels were installed the cosmic rate over time was obtained. The rates for each wall of the side CRT as a function of time are constant, as shown in Figure 4.4. The higher rates on the north wall are due to the proximity with the cryogenic pumps; as a consequence, these modules are not only exposed to the incidence of cosmic rays on the surface, but also to an additional rate of electrical noise. Similar effect, even if smaller, is also seen in the west north and east north modules which are also relatively near to the cryogenic equipment. Top CRT cosmic rates were monitored during the commissioning phase, where a significant variation can be seen in Figure 4.4 due to the overburden installation. For horizontal Top CRT modules the mean rate was $\sim$ 610 Hz, dropping off until 330 Hz after the full installation of the overburden. Excluding some rate variation due to concrete blocks installation, the CRT rates have shown to be stable on a time scale of months.

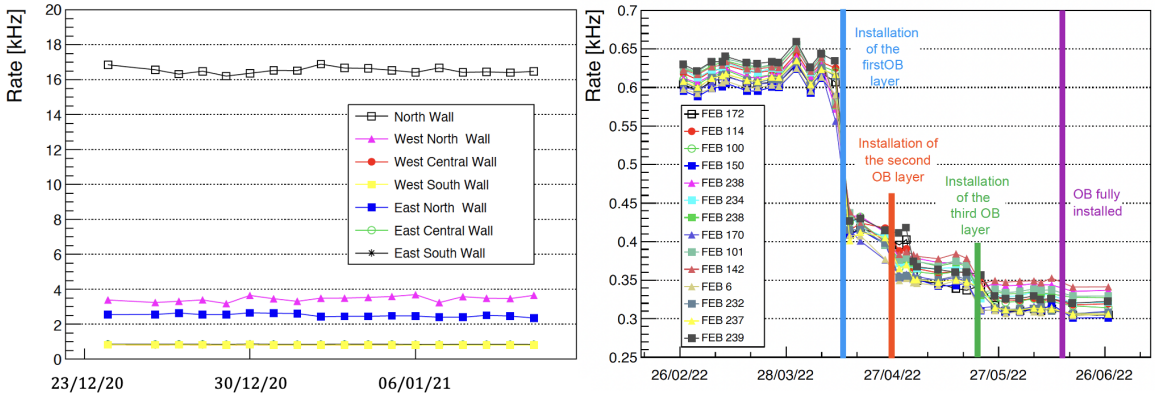


Figure 4.4: Left: Side CRT cosmic event rates as a function of time. Higher values are observed for the north, west north and east north modules due to electrical noise (generated by the cryogenic plant), while the remaining walls are all overlapped at 1 kHz. Right: Cosmic ray rates for a set of Top CRT horizontal modules. The numbers in the legend indicate the module's Front End Board, whereas the vertical lines show the different phases of the 3 m concrete overburden installation. Plots taken from Ref. [145].

ICARUS was first fully operational in June 2021, right before the summer shutdown, when the first neutrinos were collected. After the break, data taking restarted when both beams returned in November 2021. The commissioning phase concluded on June 1st, 2022 with a total proton on target (POT) collected of $2.96 \cdot 10^{20}$ and $5.03 \cdot 10^{20}$ for BNB and NuMI beams respectively. Beam utilization is defined as the amount of POT collected over the delivered one, and considering the commissioning phase, ICARUS achieved a mean value of $\sim$ 88% for both beams. Furthermore, excluding periods when the data acquisition was suspended due to commissioning activities, the average beam utilization per day increases up to 91%. The most frequent causes of operation downtime were related to data acquisition issues, and less frequent to hardware problems. More details about ICARUS' first operation activities can be found in Ref. [145].

### 4.2.1 ICARUS Trigger System

Considering BNB and NuMI beam intensities, spill windows and repetition rates one can evaluate the number of expected events in ICARUS together with its expected physical event rate. BNB has a nominal intensity of $5 \cdot 10^{12}$ POT per spill in a 1.6 $\mu s$ spill window at a 4 Hz repetition rate,

while NuMI has a slightly higher intensity of $6.5 \cdot 10^{13}$ POT per spill, a 9.5 $\mu s$ spill window and a 0.83 Hz repetition rate. Detailed Monte Carlo calculations showed that one neutrino event is expected inside the active volume for every 180 (53) spills in BNB (NuMI). Background events, mainly due to cosmic rays, are expected to happen once every 55 (7) beam spills ("in-time" cosmics) for BNB (NuMI) beam. In general one event is expected every 35 BNB spills and every 6 NuMI spills. Considering also non-physical events, ICARUS T600 foresees 40,000 events per day. With this overwhelming event rate, an online trigger system is mandatory to leverage the data acquisition load and to select potentially interesting physical events. Additional offline data filtering strategies can be developed in order to further reduce the amount of data, without losing any signal event.

The ICARUS trigger system exploits the recognition of the prompt scintillation light signal detected by the PMT system in coincidence with the beam spill windows, for both neutrino beams. The current trigger architecture is based on programmable logic boards, as they provide enough flexibility to the system to be updated and improved as experience is gained and data is collected. In other words, the system initially relied on MC calculations that were later on tuned using real events, ensuring a more accurate description of the current experimental conditions.

As previously mentioned ICARUS' light collection system is composed of 90 PMTs per TPC that are digitized through 6 CAEN V1730B boards (each TPC is equipped with 6 boards). Each module consists of 16 channels, 15 of them are used for the acquisition of PMT pulses, while the remaining channel is reserved for the acquisition of auxiliary signals such as the beam gates and the trigger pulses. Each board is responsible for sampling 15 signals from nearby PMTs, corresponding to the 15 contained PMTs in a 3 m longitudinal region of a TPC, and to write them in a 10 $\mu$s wide circular buffer, to ensure that both the fast and slow components of the scintillation light are correctly collected. For each channel an internal trigger-request logic signal is generated every time the sampled PMT pulse exceeds through a programmable threshold. Trigger requests for each couple of adjacent PMTs are combined with an OR logic and the result set in a low-voltage differential signaling (LVDS) logic output. A schematic drawing of the PMTs read by each digitizer and the PMT pairing geometry are shown in Figure 4.5 left. The LVDS signals from the PMT digitizers are processed by a Field Programmable Gate Array (FPGA) logic board to trigger the activation of the different ICARUS' subsystems read-outs.

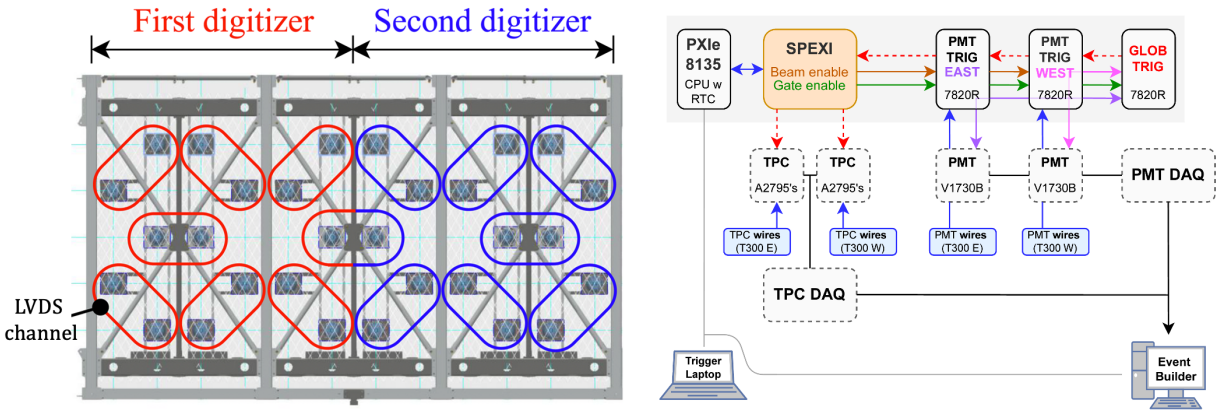


Figure 4.5: Left: 6 m long section of an ICARUS TPC, where the position of the PMTs are shown together with the PMT pairs that provide the LVDS output and the portion of the detector that each digitizer is responsible for. Right: Representation of the trigger layout, including the PXIe Real Time Controller, the SPEXI board and the three FPGAs (7820R) exploited for the trigger handling. Images taken from Ref. [146].

The generation of the beam spill gates starts by receiving dedicated "Early Warning" signals for BNB and NuMI beam, 35 and 730 ms in advance of protons hitting the target, respectively. It is of vital importance to synchronize all detector subsystems' read-outs with the proton

beam spill extraction with precise timing resolution. To that end, an Ethernet-based network known as White Rabbit (WR) [147], was deployed to distribute the beam extraction signals with nanosecond accuracy. When a certain number of LVDS signals are present in the same TPC (PMT trigger) in temporal coincidence with the beam gate window, a global trigger is fired, and the data acquisition system (DAQ) activates the read-out of each detector subsystem, as schematically shown in Figure 4.5 right. The beam gate windows are 2.2 $\mu$s for BNB and 10.1 $\mu$s for NuMI time windows, slightly enlarged with respect to the beam spill to ensure complete containment. The acquisition window for the TPC is 1.5 ms, covering the $\sim$ 1 ms electron drift time. In addition, a 2 ms and 6 ms time window around the global trigger is also recorded acquiring PMT waveforms and CRT signals respectively, to recognize and tag comic rays crossing the detector during the electron drift time in the TPCs.

Considering that around 20,000 photons per MeV are produced in LAr at ICARUS' nominal electric drift field and, in view of the energy range of BNB and NuMI, neutrino interactions are expected to be contained in a $\sim$ 3 m section of the detector along the beam direction. It is then reasonable to implement a trigger logic based on the recognition of fired PMTs inside a limited longitudinal TPC region.

Taking into account the PMT electronic deployment described, each 18 m long TPC wall can be subdivided in 3 consecutive longitudinal slices of 6 m length, including 30 PMTs each, as schematically shown in the inset of Figure 4.6. Front-facing slices in the two adjacent TPCs are combined by taking the sum of triggered LVDS channels in the two slices instead of asking for any coincidence between the two. The logic for processing the PMT LVDS signals as well as the LVDS signal threshold was carefully evaluated with MC calculations. The decision to sum the LVDS signals between the two opposite facing slices was motivated by the observed minimization of the impact of the cathode semi-transparency. In the other hand, a multiplicity threshold of 5 LVDS channels (Majority-5) was chosen as the best trade-off between an acceptable trigger rate to be sustained by the DAQ and a high trigger efficiency.

The trigger event recognition efficiency was evaluated using Monte Carlo simulations; Majority-5 condition showed an average efficiency of $> 99.5\%$ for BNB $\nu_\mu$CC events, as shown in Figure 4.6. Using more stringent conditions led to pronounced inefficiencies near the boundaries of the 6 m slices. However, further lowering the LVDS channel multiplicity threshold was not possible as the DAQ system would overwhelm. The efficiency was also seen to be sensitive to the less instrumented areas in the upstream, but especially in the downstream detector walls.

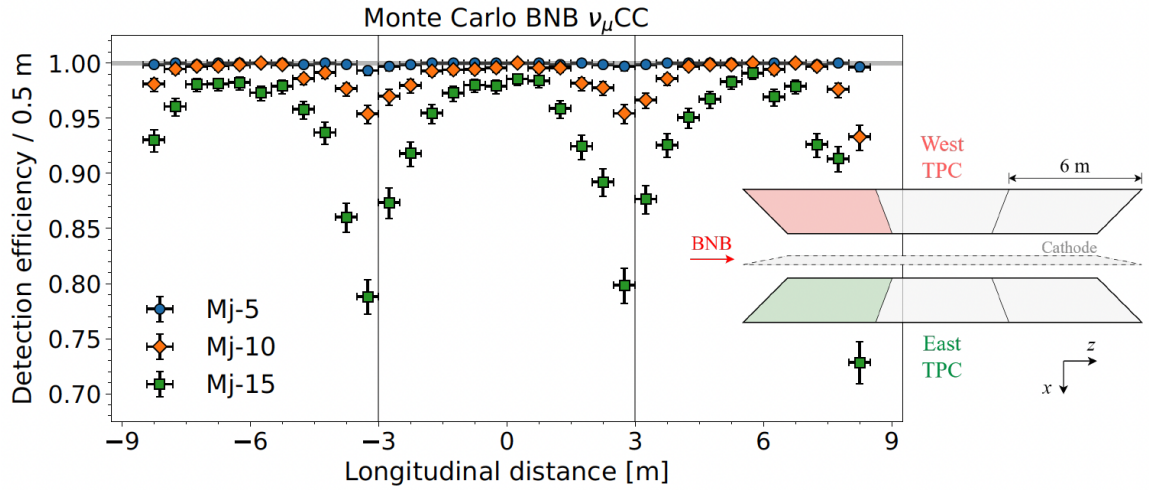


Figure 4.6: Detection efficiency as a function of the neutrino z-vertex position for BNB $\nu_\mu$CC simulated events. Inset: West cryostat of ICARUS detector from a top view, where the cathode is highlighted in the middle. The module is divided into three 6 m long windows, those being the sum of front-facing TPC slices. Taken from Ref. [146].

The described configuration was used during the commissioning phase and the first physics run data taking, while some upgrades where introduce in the trigger system during the second physics run to recover missed events.

## 4.3 ICARUS Physics Operations

As of this writing, ICARUS is on hold to start Run 3 physics data taking after the beam summer shutdown.

Run 1 officially began on June 9 2022 and lasted until July 10, 2022. During Run 1 data was collected from both beams triggering on the scintillation light detected in coincidence with the proton beam extraction signal. The dedicated month of data taking, showed an overall beam data collection efficiency of ∼93% with an excellent stability on long runs. After one of the two argon pumps was repaired during the beginning of May 2022, the cryogenic system performed smoothly guaranteeing an adequate LAr purity for data taking. The free electron lifetime was measured through the attenuation signal of crossing cosmic muons tracks along the drift direction, and the values were found to be stable at $\sim$ 4.5 ms and 3 ms for the East and West cryostats respectively. The collected event statistics for Run 1 are summarized in Table 4.1.

| | Run 1 | Run 2 |
|---|---|---|
| BNB | $4.1 \cdot 10^{19}$ | $2.1 \cdot 10^{20}$ |
| NuMI | $6.8 \cdot 10^{19}$ | $2.8 \cdot 10^{20}$ |

Table 4.1: Collected statistics for Run 1 and Run 2 periods. Values are shown with proton on target (POT) units.

In ICARUS, several data streams are routinely collected for both BNB and NuMI beams.

- Majority triggers: fired by light activity, as previously described, and which are further classified into
  - On-beam trigger: light detected in coincidence with the beam spill. They are the main physics trigger of ICARUS. For this trigger type, PMT scintillation light waveforms are acquired with intervals of 28 $\mu$s, to completely cover the spill region and include some margin aside to study the contribution of late scintillation light on the trigger rates. Both cryostats data are recorded even if triggering light is only visible on one of them. To collect light from out of time activity, but within the 2 ms PMT time window, an additional Majority-10 condition is required to acquire PMT waveforms. In this case a shorter 10 $\mu$s readout is recorded only in the cryostat where the activity was observed; being sufficient to cover the entire scintillation profile in LAr.
  - Off-beam trigger: generated from gates opened away from a beam spill. Thus, only light from cosmic or other sources of not-beam related background can trigger on these gates. Both trigger logic and gate duration are identical to the corresponding on-beam triggers. This allows to evaluate the cosmic background in a more direct way.
- Minimum Bias Trigger: triggers for which the coincidence of light is not required. This avoids any bias introduced by the request of PMT light signals to produce a trigger. Minimum Bias (MinBias) triggers can be collected both synchronous with the beam or not, producing analogous data streams of on-beam or off-beam triggers. MinBias on-beam triggers were used to synchronize the timing with the beam spills at detector activation,

but can also be used for trigger efficiency monitoring studies. Instead, MinBias off-beam can be employed to calibrate the detector and to form data-driven cosmic background to be added on simulated neutrino events for MC studies (overlays).

In normal operations, all triggers described before can operate in parallel, generating 4 different data streams: BNB on-beam, BNB off-beam, NuMI on-beam and NuMI off-beam. The rate between the off-beam and on-beam triggers depends on the detector running configuration. In the commissioning phase of the detector, that ratio was set to 1:3 for BNB and 1:3 for NuMI; however, Run 1 and Run 2 kept a 1:1 ratio for both beams, opening one off-beam gate for each on-beam gate. The ratio chosen for MinBias triggers was in view of the statistics needed to perform calibration and analysis studies. Thus, 1/200 BNB and 1/60 NuMI on-beam triggers were acquired with the MinBias requirement, while the ratio was kept to 1/20 for both beams in the off-beam MinBias configuration.

During the 2022 summer beam shutdown several activities took place in preparation for the upcoming neutrino physics run devoted primarily to improve detector performance and data taking stability. As previously mentioned the standard trigger logic used during the commissioning phase and Run 1, presented some inefficiencies, see Figure 4.6. To address the problem a new overlapping window logic was adopted. It consisted of adding two new 6 m windows partially superposed along the longitudinal direction to the original ones for both in spill and out of spill signals. A schematic drawing of the new configuration can be seen in the inset of Figure 4.7. This resulted in an improved $> 99.9\%$ efficiency for simulated BNB $\nu_\mu$ CC events when considering a Majority-5 trigger. More stringent requirements presented an improved efficiency and detection uniformity across the detector with respect to the standard configuration.

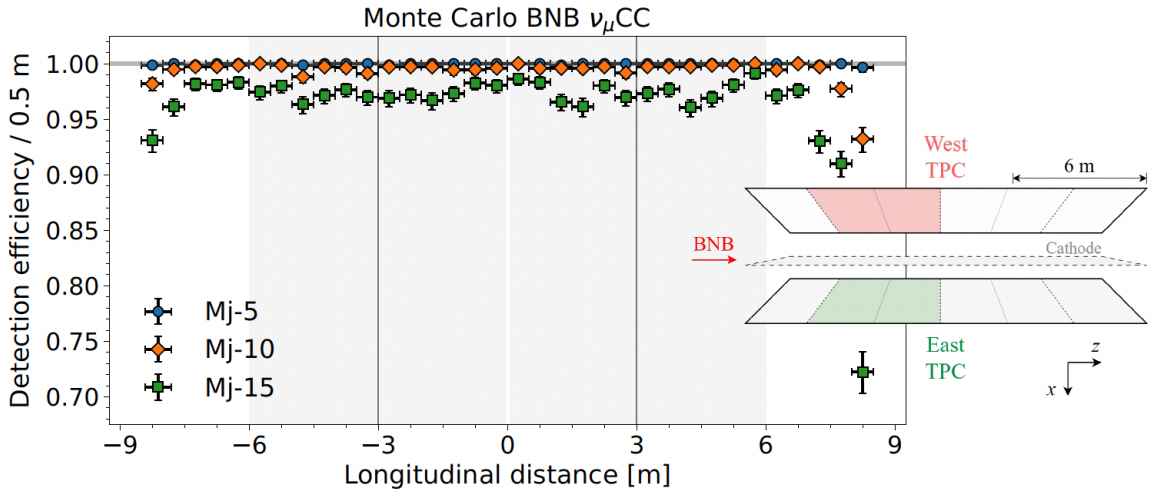


Figure 4.7: Detection efficiency for the new "sliding windows configuration" evaluated with simulated $\nu_\mu$ CC events from the BNB. The module is now divided into the original three 6 m long windows plus two new overlapping slices to overcome the drop of efficiency found in the original design. Image taken from Ref. [146].

In view of the results, it was decided to introduce this new configuration during Run 2 in order to evaluate its performance with real data.

Other summer activities included a campaign to reduce the TPC readout electronic noise evaluating the possibility to install low-pass filters and a new PMT gain and timing calibration effort exploiting cosmic muons. In parallel there were other activities to perform accurate timing measurements, calibrate and finally validate the CRT hit reconstruction algorithms with real data. The goal was to integrate the CRT into the general ICARUS system, equivalently to the PMT and TPC subsystems. At that moment only the Side and Top CRT were fully operational,

as the Bottom panels were damaged by a flood in 2019, and thus the foreseen activities were slightly delayed.

Finally, the work planned at the end of the summer shutdown were interrupted on September 14, 2022 by a fire occurred during the regeneration of the West module LAr recirculation filters. Clean-up task and replacement of damaged hardware took around 4 weeks to conclude, including the completion of filter regeneration works. The detector was brought to normal operation by mid October, were the electron lifetime was at minimum values for both cryostats. A time interval was agreed to recover optimal physics conditions which subsequently gave place to the start of Run 2 physics data taking on December 20, 2022. Run 2 successfully concluded on July 14, 2023 collecting a statistics of $2.05 \cdot 10^{20}$ and $2.74 \cdot 10^{20}$ POT for BNB and NuMI beams respectively, as reported in Table 4.1. It was once again proved that ICARUS is able to collect data steadily, overall beam data collection efficiency exceeded ∼95%, with an excellent performance on long runs at a BNB repetition rate greater than 4 Hz. It is worth mentioning that the conditions during the last months of Run 2 operation, were optimal in terms of free electron lifetime values. East cryostat gradually restored the 4.5 ms that steadily set during the whole commissioning phase and Run 1, whereas the West cryostat after the regeneration of its cryogenic filter experienced a substantial increase of the e-lifetime up to 8.5 ms. The evolution of the free electron lifetime values can be seen in Figure 4.8 through the whole life of ICARUS detector.

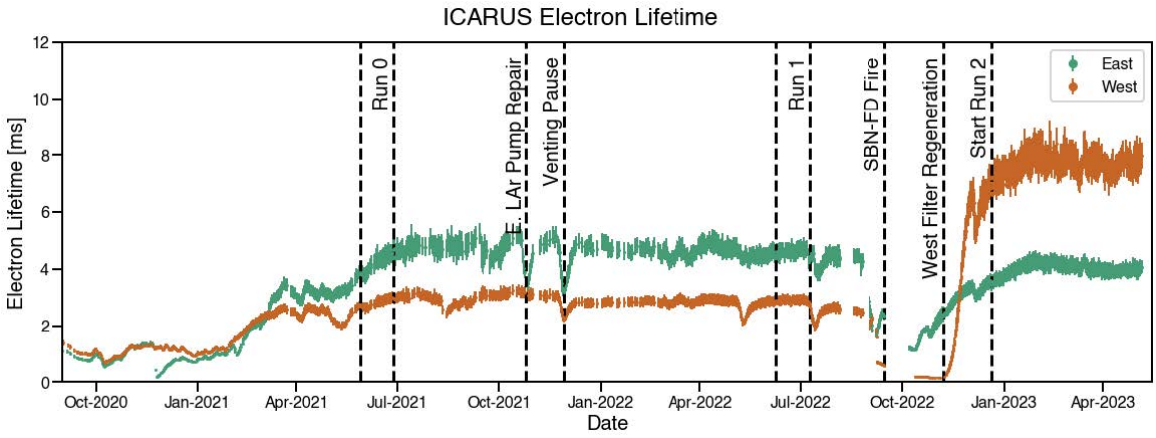


Figure 4.8: Electron lifetime evolution during ICARUS operations, where values for both cryostats are shown, together with indications of relevant events.

The distribution of the trigger times with respect to the beam gate opening for on-beam and off-beam triggers is shown in Figure 4.9, using the whole Run 2 period. It is possible to see the beam related excess in both cases, and the underlying beam structure of NuMI corresponding to the 6 accelerated proton batches, as described in Section 3.2. Several interesting features are present in Figure 4.9. The peak at the beginning of the beam gate ($\sim 0.2$ $\mu$s in the trigger time) is often called "early light" peak and it is originated by the slow light tail of cosmic rays crossing the detector before the beam gate, which produce enough light to meet the global trigger requirement. The fact that no trigger is fired between the peak and the start of trigger time is due to some delay between the PMT signal and the trigger response ($\sim$ 225 ns). The decrease seen in the number of triggers as a function of the trigger time is also related to the late light from cosmic rays (present in both distributions but more noticeable in NuMI due to its longer beam spill). If enough light is collected, a global trigger would be fired vetoing out any further beam-related activity that might have satisfied the triggering conditions, hence decreasing the possibility of a trigger occurring close to the end of the beam gate.

It was also possible to evaluate the trigger efficiency by selecting throughgoing and almost vertical cosmic muons (incident angle $< 20°$ with respect to the vertical direction) which had

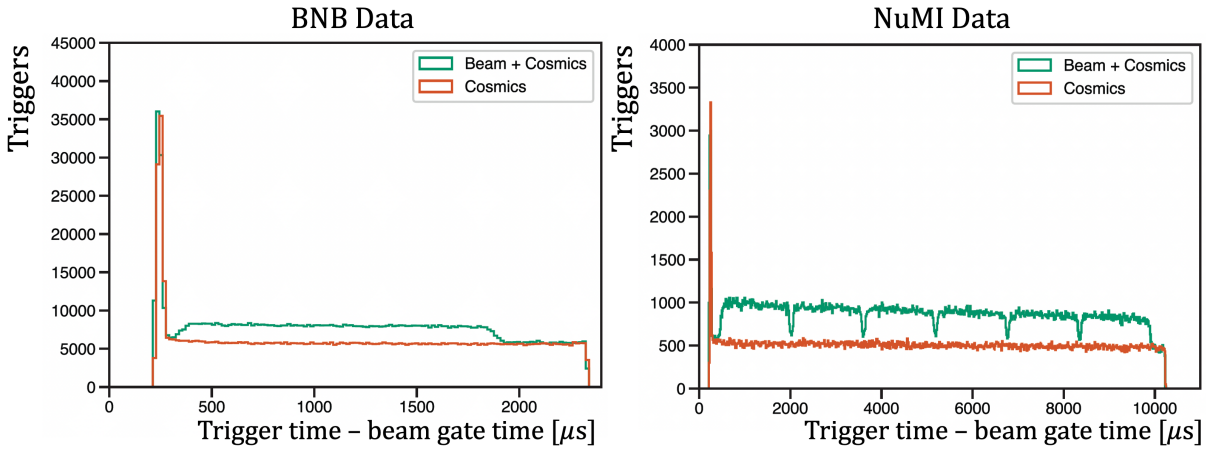


Figure 4.9: Distribution of trigger times with respect to the beam gates opening times for BNB and NuMI beams. PMT majority on-beam and off-beam data streams are shown to identify the beam related activity for data taking of the ICARUS Run 2 period.

a CRT signal in coincidence with the TPC track. The efficiency was measured as a function of the reconstructed length, being a proxy of the deposited energy. Figure 4.10 shows the efficiency for Run 1 and 2 periods in which the standard and sliding windows configuration were tested, respectively. Thanks to the 2 additional overlapping windows present in the Run 2 configuration, a significant improvement in efficiency was observed with respect to Run 1, mainly at low energies; an almost uniform event recognition capability $\geq 90\%$ was reached for $E_{dep} \geq 100$ MeV.

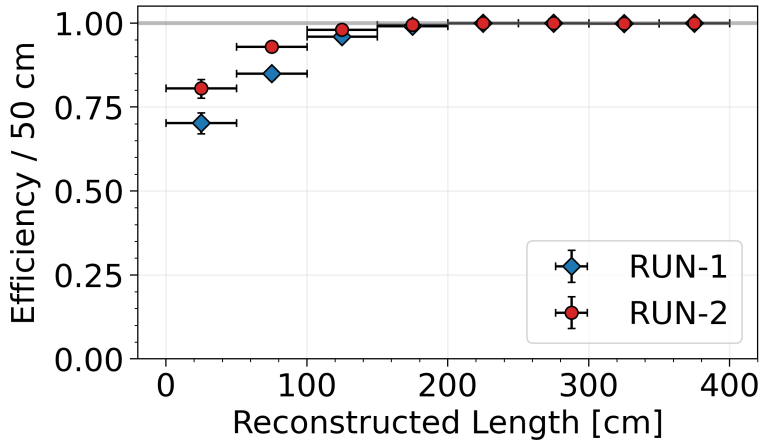


Figure 4.10: Trigger recognition efficiencies measured with almost vertical crossing muons as a function of track length. Run 1 and 2 data are shown with the non-sliding and sliding windows trigger configurations used, respectively. About $\simeq 200$ MeV of energy is deposited for a 1 m long muon track.

Several activities were also planned for the beam summer shutdown of 2023 to continuously improve the detector performance. The filter regeneration of the East module was completed in September, which should allow the module to reach values similar to those of the West cryostat in the near future. Regarding the PMT system, new cables were installed improving the signal transportation and further calibrations allowed to develop a complete timing correction procedure to achieve unprecedented precision. This consisted in three consecutive timing corrections applied at three different stages of the optical data flow. The first one was a hardware-trigger correction, to reduce the internal temporal uncertainty of the digitizers boards. The second

correction was performed exploiting some dedicated data runs taken with 10 Hz laser pulses. This allowed to cancel the PMT transit time differences and readout delays in a PMT-by-PMT basis. Finally, a further improvement was achieved exploiting downward-going cosmic muons, comparing the expected arrival time of photons on the surface of each PMT with observations. The obtained results are shown in Figure 4.11, where the results after each timing correction are presented. The hardware-trigger correction shows a $\sim$ 2 ns resolution, being dominated by the extension delay difference among the PMT channels. The laser correction reduces this time spread to $\sim$ 1 ns, while the final cosmic ray correction allows to achieve a precision better than 1 ns.

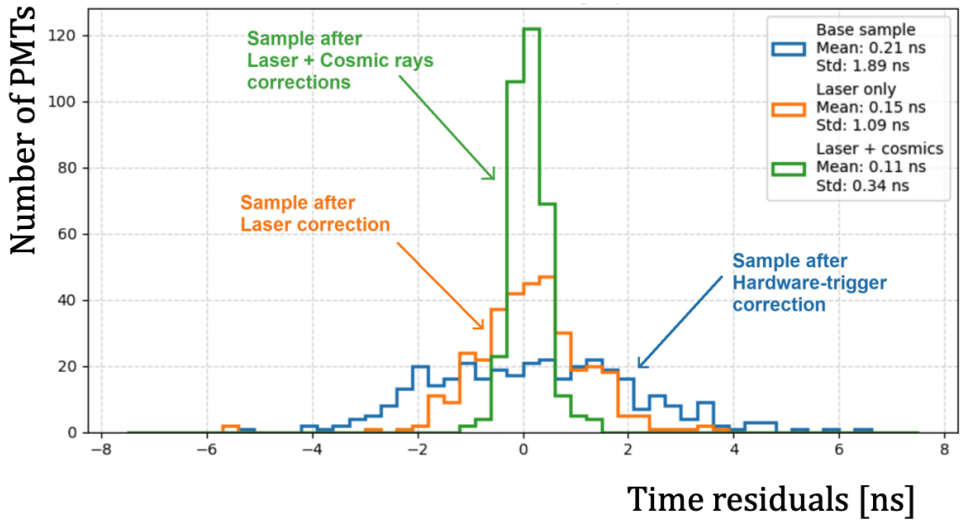


Figure 4.11: Distribution of the residuals resulting after the implementation of each timing correction described on the text. Final timing precision is of the order of $\sigma \approx 300$ ps. Taken from Ref. [148].

In parallel TPC electronic improvements were performed. These included the installation of noise filters in the Induction 1 front end boards, to mitigate the coherent noise, and efforts to finalize a firmware for compression of the TPC data.

Some tests were performed to the Top CRT towards the development of an automated channel-to-channel calibration in terms of pedestals and silicon photomultipliers gain. Simultaneous effort was dedicated to the Bottom CRT to bring the different panels back online.

Finally, the trigger system was reviewed to improve its performance taking advantage of the knowledge acquired during data collection. It was found that non-triggering low-energy events were mainly caused by short tracks crossing near the corners of the detector or close to the PMTs. In these cases, the PMT-majority requirement was not met due to a huge amount of light collected by a small number of PMTs. An additional trigger system based on the scintillation light signal amplitude rather than the multiplicity of fired PMTs, was proposed. The implementation relies on the so-called "adder boards", which are custom-made boards able to divide the PMT signal from 15 adjacent PMTs (corresponding to each group of PMT read by the same board), creating two lines to further evaluate trigger conditions. 24 adder boards summing up 5% of signal were installed within the entire ICARUS light collection system, leaving 95% of the signal amplitude as input to the PMT digitizing boards. The goal is to explore the use of a trigger based on information from the adder boards to recover in spill events missed by the standard PMT Majority-5 condition. To that end, test runs collecting data without any request on PMT signals are being analyzed.

## 4.4 Current status of ICARUS and SBN program

Within SBN program, ICARUS is the only detector currently under data taking phase. As SBND prepares to begin operations, various activities have been carried out at both detectors.

The near detector was assembled and all components inside the cryostat installed, which allowed to close the lid and finalize the cryogenics installation. TPC calibration lasers were set in place and quality control of electronic systems are currently undergoing. The bottom and north panels of the CRT subdetector were already installed and the remaining sides will be placed once stable cryogenic operations are achieved. SBND is expected to be filled with liquid argon at the beginning of 2024, to start the detector commissioning activities right after.

On the other hand, ICARUS is exploiting all the available statistics to characterize detector effects and work towards first physics results.

Detector studies and accurate measurements of physical quantities ( such as the electron drift velocity, the recombination factor or diffusion coefficients, among many others) are essential for calibration and equalization of the detector energy response and to obtain an efficient particle identification. Data-driven approaches are being pursued to achieve a better description of the TPC field response and electron recombination. A good PMT timing is crucial to ensure accurate matching with TPC and CRT information and to resolve the beam bunch structure. Regular calibrations are performed, allowing to achieve a PMT timing equalization with a resolution of $\sim$ 300 ps, which seems to be stable over time. CRT performance has also achieved remarkable improvements, allowing to set an accurate relative synchronization between CRT and PMT subsystems through a global trigger signal to remove most of the external cosmic activity. In addition, CRT is also exploited for vetoing non-contained tracks coming from beam neutrino interactions. Finally, new trigger configurations have been studied to maximize the collection efficiency with plans for future improvements. More details on reconstruction activities will be presented in the upcoming chapters.

During this single phase detector, the Neutrino-4 analysis is the major ongoing investigation by ICARUS with Booster and NuMI beams. To that end, Run 1 and 2 data sets are being actively analysed to understand detector performance and provide robust physics results. The detector behaviour was first investigated by a visual selection of neutrino interaction inside the active LAr. In total $\sim$1500 $\nu_\mu$CC candidates from Run 1 and 2 were visually selected and are being exploited to develop an automated event selection scheme and evaluate its performance (resolution, efficiency, purity, ...), while at the same time addressing the major event reconstruction issues. More details will be given in Chapter 6, where an analysis for a specific event topology using BNB events is presented.

Examples of two visually selected events are shown in Figure 4.12 and 4.13. Both events are shown in a graphical event display for the Collection view only.

Figure 4.12 shows a $\nu_e$CC candidate fully contained in the active LAr collected with the NuMI beam. In the interaction the neutrino produced an electron shower, depositing around 570 MeV of energy, and two additional tracks classified as an upgoing stopping proton candidate with a length of almost 24 cm (labeled as track 1), and a stopping hadron of 33 cm (labeled as track 2). The intensity of the black signal all over the interaction is proportional to the ionization power of each particle, thus darker regions indicate high ionization areas where more energy is deposited.

Instead, Figure 4.13 shows a quasi-elastic $\nu_\mu$CC interaction with two stopping tracks produced at the primary vertex. The longest track, being a muon candidate, is stopping after 2.8 m with a deposited energy $E_{dep} \sim 650$ MeV. The other short, more highly ionizing track, is identified as a possible proton, with a length of 10.9 cm and a $E_{dep}$ of $\sim$ 100 MeV.

The detailed study of neutrino interactions combined with an automatic selection should allow ICARUS to provide first physics results on $\nu$-Ar cross sections and verification of the Neutrino-4 claim, before exploiting full capabilities of the SBN program.

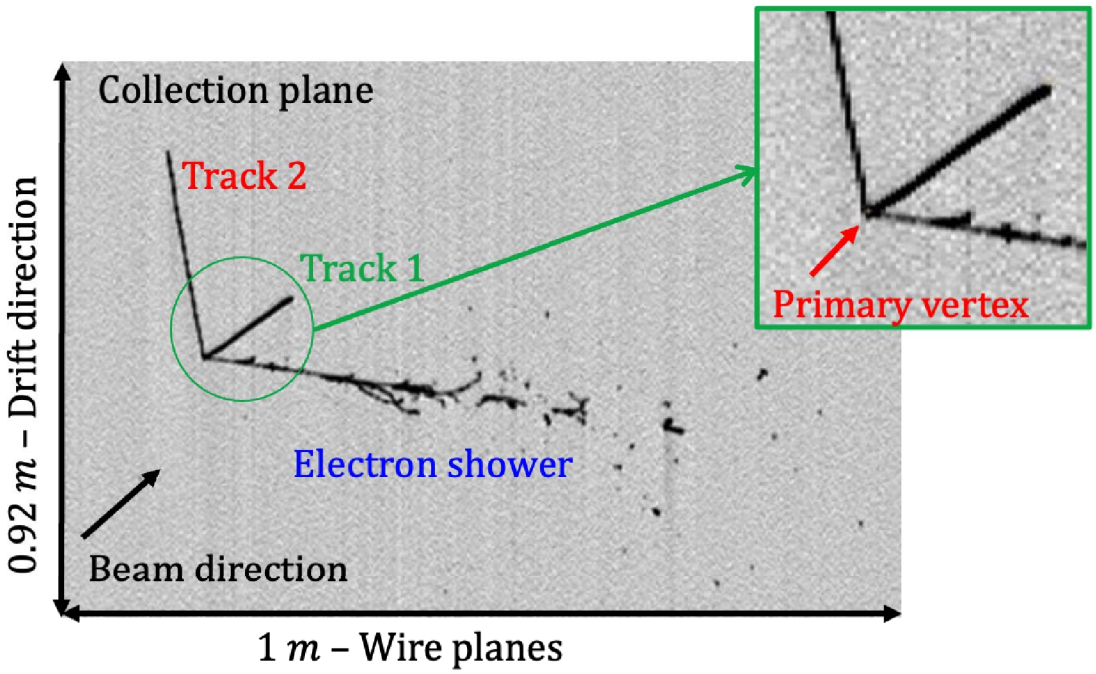


Figure 4.12: $\nu_e$ candidate collected with the NuMI beam, where the neutrino produces an electron shower and two additional track candidates.

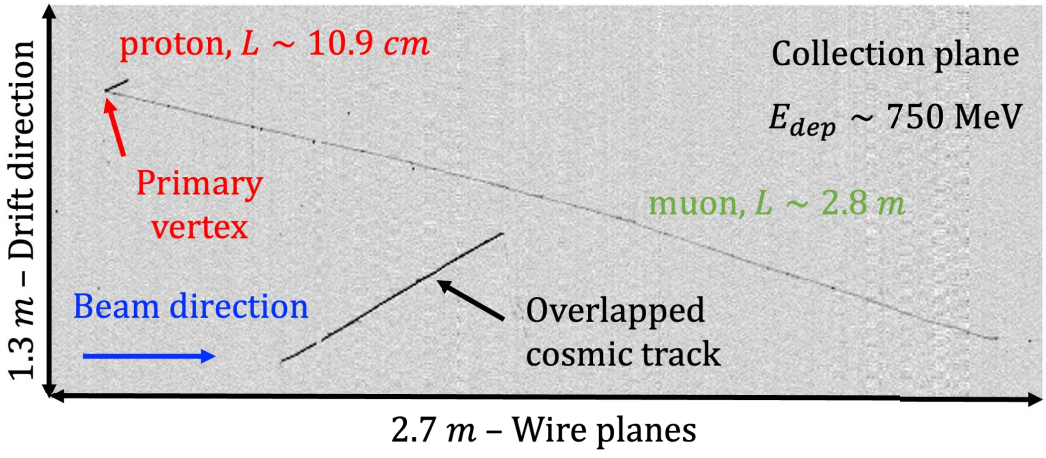


Figure 4.13: Typical BNB $\nu_\mu$CC quasi-elastic candidate visually selected. The total deposited energy $E_{dep} \sim 750$ MeV, coming from a proton and muon candidates that are stopping inside the active LAr.

# Chapter 5

# Event Reconstruction in ICARUS

The ultimate goal of ICARUS is to record neutrino events, however it has already been emphasized that in addition to them, the detector records all any kind of ionizing events, also crossing cosmic rays. To be able to discriminate interesting events, the analysis relies on the information provided by the various detector components: TPC, PMT and CRT sub-systems. Events of interest are not only neutrino interactions, great effort has been devoted to collect well defined samples of cosmic rays crossing the detector for calibration purposes as well as trying to identify smoking gun signals of beyond the standard model physics.

TPC system is in charge of identifying and creating tridimensional track or shower objects exploiting its topological and calorimetric information, in order to reveal the nature of the particles involved. The light detection system (PMT system) leverages the scintillation light to provide the event trigger, to measure with nanosecond precision the event time and to localize the interaction position inside the detector. Finally, the CRT system is responsible for rejecting the cosmic rays, vetoing those which are in coincidence with the neutrino spill, distinguishing incoming from outgoing particles and tagging all activity occurring outside the beam spill associated to the event.

## 5.1 ICARUS Data taking

The ICARUS data acquisition (DAQ) system employs the general *artdaq* data acquisition software development toolkit [149], which provides customizable applications for reading data from detector elements (*BoardReaders*). It also allows to configure applications to perform event building, data logging and data dispatch to downstream online monitors for data quality processes, among many others. The BoardReaders acquire data fragments from the three detector subsystems readout electronics and from the trigger and White Rabbit timing systems (described in Subsection 4.2.1). Event counters and timestamps are assigned appropriately to each data fragment, which are then queued for data transfer to a configurable number of *EventBuilder* applications. When an event is triggered, the corresponding trigger BoardReader sends its data fragment to the EventBuilder, which in turn queries the other subsystems for data. Data is written to separate file streams depending on the trigger type: BNB on-beam, BNB off-beam, NuMI on-beam or NuMI off-beam, and corresponding Minimum Bias.

The BoardReader for the trigger systems sends a single fragment containing different information, among which is the number of beam gates of each type in that specific DAQ run. This information is used offline for proper accounting of the total number of protons on target delivered and detector exposure within a run, being essential for oscillation analysis.

Several tests were performed to evaluate the DAQ performance, successfully demonstrating that the system could stably handle trigger rates up to 5 Hz. However, given the neutrino interaction rate for the BNB and NuMI beams (see Subsection 4.2.1), it was considered more appropriate to use the PMT-based trigger system with the goal of maximizing the collection of

physical events while minimizing the amount of non-physical data collected. Hence, in normal conditions the typical operational trigger rates, taking into account the different data streams, are $\sim$ 1 Hz or below.

## 5.2 ICARUS data processing chain

ICARUS design and acquisition parameters lead to a substantial data rate and volume. To deal with it, several strategies have been introduced in the ICARUS data processing chain. TPC wire signals are digitized by 12 bit ADC with 2 bytes/sample at a 2.5 MHz sampling frequency. This spans over a $\sim$ 1.6 ms time window to record activity before and after the event of interest, corresponding to 4096 samples. Accounting for the $\sim$ 53 k wires of the TPC, it would correspond to $\sim$ 400 MB/event just from TPC raw data. The bulk of the data comes from the four TPCs, which represents the $\sim$ 90% of the total event size. Each event in ICARUS, after a software lossless data compression, is approximately 200 MB. Currently, a further lossless hardware compression similar to the one adopted in the previous Gran Sasso operation [150] is being deployed in ICARUS. This aims to reduce raw data size by a factor $\sim$ 4, prior to the software compression, providing about a factor 2 gain in the TPC raw data. In this situation before any process can take place, it is necessary to decompress the data, however, this measure is mandatory to be able to handle the almost 86,000 events per day that the detector records.

The output data from the detector consists of digitized waveforms from each TPC readout channel, representing the charged induced by the motion of ionization electrons swept by the drift field from the TPC volume. Similarly, the output data from the photomultipliers consists of digitized waveforms giving the signals from detected scintillation photons. This output is common across different LArTPC, which might have slightly different geometries and readout schemes but share the same physics in LAr. LArSoft [141] is a toolkit that provides a software infrastructure and algorithms for the simulation, reconstruction and analysis of events in LArTPCs. It benefits from the experience of multiple experiments and provides the architecture to interface to other packages to facilitate the evolution and improvement of the reconstruction algorithms.

All the collected raw data needs to undergo several software phases before it can be properly analysed; the reconstruction of these events is done in two stages.

The first stage "`Stage0`" translates from raw data format to LArSoft format for offline processing. It also performs signal processing for all three subsystems with the goal of identifying physical signals "`Hits`" to be fed to the pattern recognition and event reconstruction algorithms.

As an example, "`Stage0`" processing for TPC includes:

- Decoding: Decompresses and unpacks raw data into a format that can be used in later steps. Includes electronic noise filtering to remove TPC coherent noise.
- Deconvolution: Removes effect of the electrostatic field around the wires and electronic response.
- Region Of Interest (ROI) finding: Reduces data volume by selection of ROI around candidate signal.
- Hit Finding: Builds `Hit` objects from the ROIs in the previous step. A `Hit` represents the identified signal induced by a charged particle on a wire and are the primary input to the pattern recognition algorithms.

At this point the output of "`Stage0`" is about 10 times smaller than the input raw data, as full waveforms are dropped, and will serve as the input for the next stage. "`Stage1`" processing is mainly focused on the reconstruction of TPC, CRT and PMT signals, and might include calibrations of each subsystem.

To continue the example above, `Stage1` processing of TPC includes:

- Hit filter: Builds tridimensional space points from combination of 2D `Hits` across different wire planes.
- Pattern recognition algorithm: arranges close hits into clusters that are then used to identify track or shower candidates and event topology information, including cosmic ray identification. Inside each defined interaction, the so-called slices, a hierarchy among all reconstructed objects is build to identify parent-daughter relationships.
- Particle fits: Applies detailed algorithms to reconstruct tracks and showers and obtain calorimetric measurements of each particle. It also provides information to allow kinematic reconstruction and to analyze the event.

The output of "`Stage1`" includes Calibration tuples for calibration and detector studies and allows to produce "Common Analysis Framework" (CAF) files for final event selection and analysis. More details of both formats will be given shortly, considering that both files were used to carry out analysis during this thesis. A parallel approach based on machine learning techniques is also available for processing the detector information, however it has not been explored in this work.

## 5.3 CRT Reconstruction

Unlike TPC or PMT systems, for which the digitizers require an external trigger to collect the waveforms, the CRT FEBs are in auto-trigger mode. CRT data from FEBs in a given event are ordered in time and grouped by CRT region; each of which is able to produce a coincidence logic to flag the CRT signals as either related to the triggering event or independent to it. Each region is examined every 80 ms and CRT fragments within the time window of the triggered event are saved for further analysis. The hardware-based coincidence gate width is set to 150 ns; the reason for not making the coincidence too large is to avoid introducing fake coincidences from low energy events, however studies are underway to establish the optimal gate width.

Once CRT data fragments are generated and saved by the DAQ, they are processed through the reconstruction chain. The first step is to format the raw data of each FEB to obtain a CRT Data product suitable for the later stages of the reconstruction. Next step is to construct `CRT Hits`, defined as points in space and time associated to particles crossing the CRT volume. Due to different designs of the side and top CRT systems, `Hit` reconstruction needs to be handle differently in both cases.

First of all, `CRT Hits` are converted from ADC counts to number of photo-electrons (PE) through the following expression:

$$n_{p.e.} = \frac{ADC - Ped}{G} \ , \tag{5.1}$$

where the pedestal (Ped) is the baseline of the signal, and G stands for the gain. A data collection campaign was carried out to estimate the pedestal and gain values of the different CRT modules. In particular two calibration data sets, mainly acquiring through going cosmic muons, were used corresponding to the Run 0 and Run 1, to account for possible differences between the two periods. The pedestal was obtained by fitting with a gaussian distribution the ADC spectrum of a channel when this was not involved in a CRT hit channel coincidence. The gain was computed as the average distance between the quantized photoelectron peaks in the integrated charge spectrum of cosmic muons, after being fitted by multiple gaussian peaks. An example of a channel ADC spectrum for the Top CRT is shown in Figure 5.1, where the pedestal and single PE peaks were fitted.

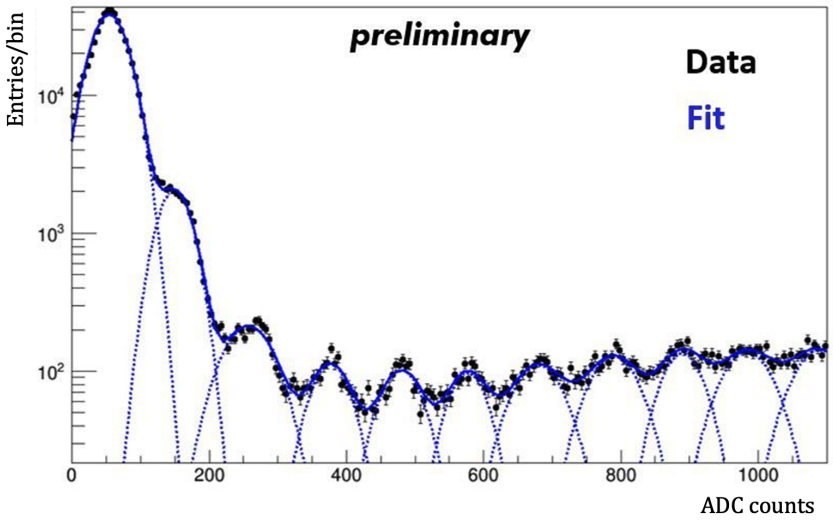


Figure 5.1: ADC spectrum of one channel of the Top CRT showing the fit to data of the pedestal and consecutive photoelectron peaks. Taken from Ref. [140]

Side CRT uses the same configuration for each FEB hence the calibration had to be done on a FEB-base. On the contrary, Top CRT module allows a channel by channel configuration, therefore the calibration was performed in every single channel. For the near future, there are plans to introduce an automatic calibration on a weekly basis to improve its precision.

A first preliminary selection of Side CRT data is performed at this point, where only hits above a threshold of 7.5 PE are kept. Top CRT needs a quadruple coincidence to generate a hit, as explained in p. 72; this robustness allows to select a very pure sample (rarely random coincidences are present) without applying any threshold cut.

In addition to the collected charge, each CRT hits is associated to two different time counters. The first counter, $T_0$ is reset every second by a very precise Pulse Per Second (PPS) generated by the White Rabbit system (based on a GPS timing signal) and provides the global timing of the recorded hit. $T_0$ is used as a reference to compute the time interval between the light generation and its detection on the SiPM. The second counter, $T_1$ is reset by the event trigger signal and is used to determine the relative timing of the hit with respect to the trigger event.

As a second step, the signal that generated the FEB trigger signal needs to be identified; first inside the single module and later on translated into the global coordinate system of the ICARUS building. Hit reconstruction within each module is CRT subsystem specific.

**Position of Top CRT hits** The Top CRT hit reconstruction is performed by selecting the scintillator strip with higher PE in its channel for the top (1 cm thick) and bottom (1.5 cm thick) layers. Due to the orthogonal orientation of the two layers, the position of a Top CRT hit is uniquely identified by the overlapping region of the two scintillator bars, shown in Figure 5.2 left. There are 64 unique 23 cm $\times$ 23 cm crossing strips coincidence regions within each module, due to the orthogonal orientation (XY configuration) of the layers and the width of each strip.

The global coordinates of the CRT module are defined with respect to the center of the module, hence the local coordinates of the CRT hits are reconstructed in relation to the middle position along each scintillator strip.

**Position of Side CRT hits** The coincidence logic of adjacent layers in the Side CRTs is performed offline in the reconstruction stage due to the inner and outer CRT modules being read by multiple FEBs. Hit scintillator strips are identified by selecting in each FEB the channel that generated the FEB trigger signal, which is the one with the highest charge amplitude. Middle

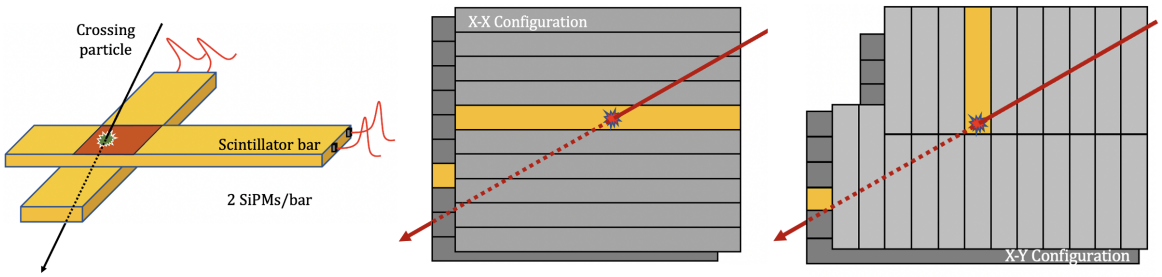


Figure 5.2: Illustration of CRT hit reconstruction position, showing generated overlapping regions for each CRT geometry when a charged particles pass through. Left: Top CRT module coincidence. Middle: East, West and North Walls of the Side CRT, outer and inner layers in an X-X configuration. Right: South Wall, where outer and inner layers are in a X-Y configuration.

and right diagrams of Figure 5.2, show an example of different configuration for Side CRT, where the triggering channels correspond to the yellow strips. Most of the CRT side walls have a XX configuration, which can present different scenarios for hit reconstruction.

1. If the scintillator strip is readout on both ends by two different FEBs and both the corresponding channels are above threshold, the longitudinal position can be reconstructed with respect to the center position of the strip by comparing the timestamps recorded by each FEBs.

$$z = \frac{T_A - T_B}{2} \times v_{WLS} \ , \tag{5.2}$$

where, $T_A$ and $T_B$ are the time stamps recorded by the two FEBs, $z$ is the CRT hit position and $v_{WLS}$ the light group velocity in the wavelength-shifting fibre, estimated to be 0.062 ns/cm. This procedure is performed on both inner and outer layers to obtain the final CRT hit longitudinal location as the average of both reconstructed positions. X and Y coordinates are obtained by averaging the respective transverse coordinates of each strip, given by the CRT geometry.

2. In case only one of the two layers has both channels above threshold, the CRT hit position is reconstructed using only the information of that strip (without considering any information of the strip with a single channel above threshold).

3. In the worst case where none of the layers has two channels above threshold, coincidences with a single channel are considered. In this situation the hit is reconstructed by default in the middle of the scintillator bar and averaged over the two layers.

The South side CRT wall is the only one exploiting a XY configuration: the outer layer has vertical strips while the inner one has the strips horizontally and is read only in one end. To get the most out of this setup the longitudinal position is given by the position of the vertical strip hit in the outer layer. The vertical position is instead obtained by the position of the horizontal strip hit of the inner layer, as shown in Figure 5.2 right.

Following the reconstruction of the CRT hit position, the timestamp of each CRT hit can be further improved by accounting for cable delays and the light propagation inside the scintillator and the WLS fiber.

In addition to the location of the hit it is also interesting to evaluate which is the spatial resolution. Due to the different geometries, the resolution will not be the same for all regions.

Top CRT allocates a hit into a volume of 23 cm $\times$ 23 cm $\times$ 2.5 cm, which are the crossing scintillator area times the thickness of the two layers (1 cm + 1.5 cm). Hence the standard

deviation for each coordinate, considering the hits are uniformly distributed along each strip, is $\sigma = \text{width}/\sqrt{12}$, where $\text{width}_{x,y} = 23$ cm and $\text{width}_z = 2.5$ cm. These results into the following upper limits

$$[\sigma_x, \sigma_y, \sigma_z] = (< 7, < 7, < 1) \text{ cm} .$$

Side CRT resolution needs to be addressed more carefully, considering that the spatial precision strongly depends on the timing resolution. Generally the error along the transverse direction of the scintillator strip is $\sigma_z \sim 1$ cm, while the resolution along the other two directions has only been evaluated using simulation.

Currently a lot of effort is being dedicated to implementing and improving the matching between CRT and PMT information. The goal is to reject out-of-time activity using a completely timing-based algorithm between the CRT and PMT subsystems, which for the CRT boards the internal timing resolution if of the order of $\sim 2.3$ ns. The CRT-PMT matching will be later on exploited to automatically select events of interest.

## 5.4 PMT Reconstruction

The reconstruction of the scintillation light associated to a specific event, is based on the recorded PMTs waveforms of that event, which are sampled at 500 MHz. Events in coincidence with the beam spill have all 360 PMTs digitized signals recorded in 28 $\mu$s in the beam window. Out of time activity within $\pm$ 1 ms around the beam gate and satisfying the trigger logic (at least 9 PMT pairs fired) are also recorded in a 10 $\mu$s window, but only considering the cryostat where the cosmic activity took place.

In the first step a threshold-based algorithm is applied to each recorded signal to identify fired PMTs and reconstruct the characteristics of the detected light to be further analysed.

Light hits are defined as signal above threshold, hence a reference value needs to be established for the baseline, the so-called pedestal. ICARUS uses as a pedestal a rolling mean[1] of the waveform over consecutive 2 ns samples (1 tick or t-samples equals to 2 ns) corresponding to a 80 ns interval. Pedestal of i-th tick is then computed as the mean of all values between the (i-20)th tick and the (i+19)th tick. This allows pedestal subtraction which is needed to evaluate the threshold requirement of the waveform. In addition to the averaged pedestal the root mean squared (RMS) is also computed for each sample, allowing to estimate the significance of the signal. If in one sample the RMS is unusually high (more than 5 ADC counts) or the baseline is outside an expected range (between 14 kADC and 16 kADC) the pedestal is replaced with a constant value or an interpolation between the pedestals of the adjacent samples. This is a prevention against biases due to noisy regions or regions where signal is present, as it is not sensible to evaluate the pedestal in a signal region. Typical value of PMT baseline in ICARUS is 15 kADC counts with an average RMS of 3 ADC counts.

A hit finding algorithm (SlidingWindow) is applied to each waveform afterwards to determine the time extent of hits and extract their parameters. Three thresholds define the start of a hit, the tail and the end points. Each one can be specified in units of RMS or in absolute ADC counts, and the largest between the two is used each time. The current values used in the ICARUS optical hit reconstruction algorithm are summarized in Table 5.1, all of them being tunable variables within the algorithm. PMT signal polarity is negative as was shown in Figure 4.2, however the SlidingWindow algorithm operates on a pedestal-subtracted waveform like the one shown in Figure 5.3 top, where the different regions of a hit in the reconstruction algorithm are shown.

The algorithm has the following principle: a hit is created when the signal crosses a start threshold, the object is called `OpHit` ("Optical Hit"). As signal decreases over time, it might

[1] The rolling mean is first computed in the 20th digitized sample, as a window of 40 ticks is needed around. In the same way the last value is computed 20 ticks before the end of the waveform.

reach a tail threshold where if the signal goes above the start threshold, a new `OpHit` would be created truncating the previous one. Instead, if the signal keeps decreasing and reaches the end threshold, the `OpHit` ends after 20 ns. Again this is only true if no other signal above the start threshold is found in the meantime.

| Region | Threshold |
|---|---|
| Hit start | 10 ADC or 3 × local RMS |
| Hit tail | 6 ADC or 2 × local RMS |
| Hit end | 2 ADC or 1 × local RMS |

Table 5.1: Hit thresholds implemented in the current version of the SlidingWindow algorithm for optical reconstruction.

Each `OpHit` is characterized by: the start time, the hit width (time interval for the signal to end), maximal amplitude, integral above baseline and PMT information, as illustrated in Figure 5.3 bottom. In addition, there is also a relative hit time, with respect to the trigger time, which will be essential to associate light activity with triggering events.

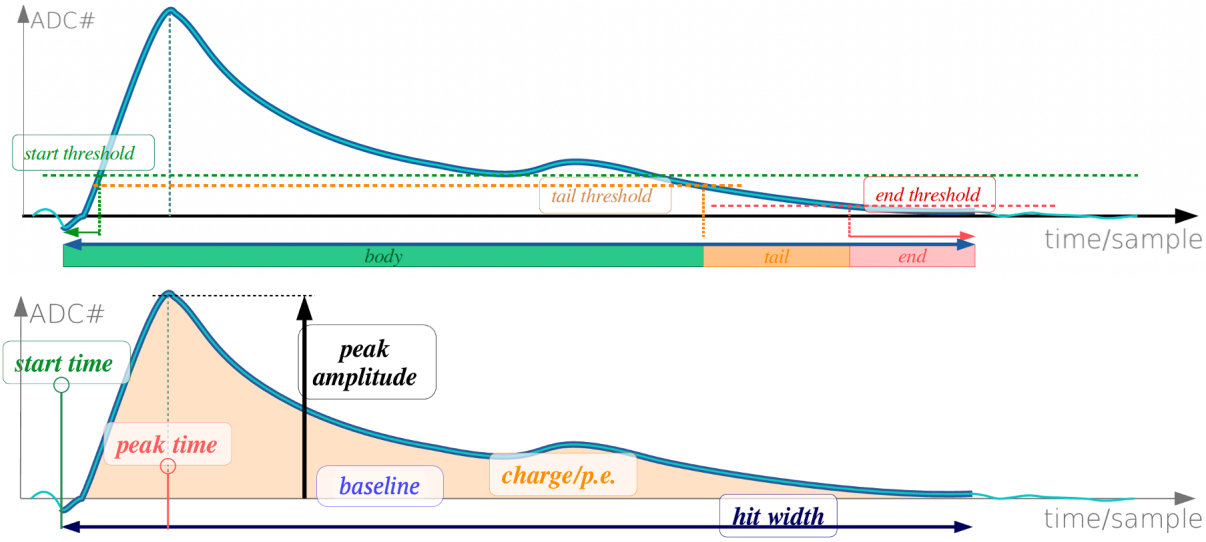


Figure 5.3: PMT waveform illustration, showing the regions of a hit in the SlidingWindow reconstruction algorithm (top) and the definition of some variables contained in an `OpHit` object (bottom).

Photons arriving simultaneously are expected to create a single `OpHit`. The timing resolution depends on the hardware (detector+readout electronics) and reconstruction algorithm. Current ICARUS software reconstructs a single photo-electron (SPE) pulse the order of ns resolution.

After optical hits are reconstructed, they are clustered together into higher-level objects called `OpFlash` ("Optical Flash"). To that end, the time scale is sampled in 10 ns bins, and each `OpHit` is placed in the corresponding time bin according to its peak time. Time bins with less than 5 `OpHit` or below 100 PE are discarded as possible `OpFlashes`. Each time bin is considered a possible candidate to become a flash in the order of the amount of PE they have. All candidates within 1 $\mu$s to an already defined `OpFlash` are not suitable to become a new `OpFlash`, where the time proximity is calculated as the peak time of the `OpFlash` - start time of the flash candidate (candidate peak time - 20 ns). Instead, the `OpFlash` is expanded to include all `OpHit` within 1 $\mu$s after the start time of the `OpFlash` (start time = peak time - 20 ns).

An Optical flash produced by another interaction can be identified if it occurs after 1 $\mu$s

from the previous one. It is expected that each `OpFlash` should correspond to the total detected light associated to an interaction, either coming from a neutrino or a cosmic ray.

The timing resolution is subject to that of `OpHit` and additional smearing due to `OpFlash` reconstruction algorithm. In ICARUS that resolution is below 1 ns.

## 5.5 TPC Reconstruction

TPC Reconstruction begins as soon as the ionization electrons are detected and collected by the anode wire planes, as described in Section 3.4.1. Each wire in each plane of the detector records a waveform in ADC/tick units, where the amplitude of the signal is expressed in ADC and the tick correspond to the t-sample of 0.4 $\mu$s in the ICARUS TPC timing. The anode consists of 3 wire planes with specific bias voltages so that 100% of the ionization electrons should be transported to the collection plane[2]. These produce a bipolar signal while coming to the two induction planes, and are finally collected by the collection plane where a unipolar signal is created, as shown in Figure 5.4.

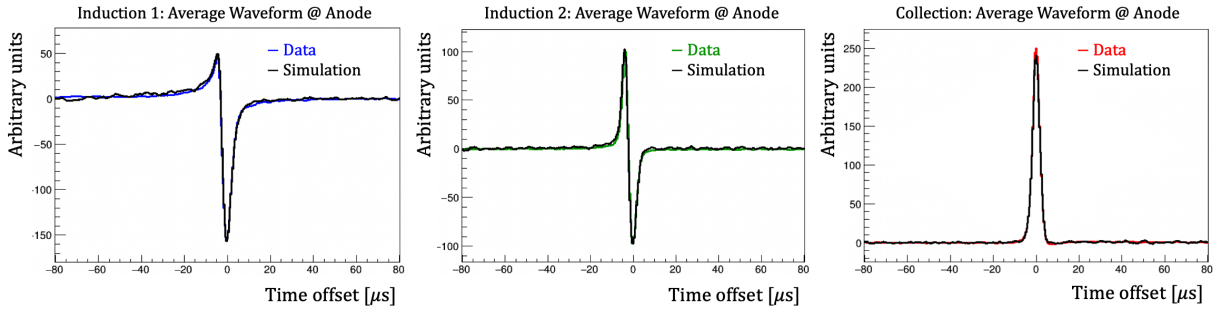


Figure 5.4: Measured signal shape at the anode plane averaged across one TPCs. Data and simulated responses are reported for the three wire planes, showing the characteristic unipolar and bipolar shape.

### 5.5.1 Signal processing

The first step in the reconstruction is to obtain the distribution of ionization electrons arriving at the anode plane. However, the recorded signal not only depends on the ionization charge but also on a number of different factors. The resulting signal on the wires is a convolution of the serial effects of signal formation, electron propagation through the LArTPC, electrostatic field around the wires and process by the readout chain. This can be schematically factorized as: Ionization $\otimes$ Recombination $\otimes$ Diffusion and Attachment $\otimes$ Field Response $\otimes$ Electronic Response plus the additional contribution of the electronic noise. These effects must be unfolded from the TPC waveforms in order to recover the desired information about the deposited charge per wire as a function of time. Specific noise filters are applied to remove the noise, both random noise from the electronics and correlated noise (coherent[3]) from other detector components, which in theory should preserve the signal unaltered. Coherent TPC noise most commonly originates from the readout electronics and the high voltage supply. However, as explained in Section 4.2, the latter was seen to introduce a negligible amount of noise, while the coherent component was effectively filtered out by a dedicated software noise filter.

[2]The precise wire plane bias voltage to achieve full transparency of electrons to the collection plane is a function of the wire diameter, wire spacing and plane spacing.

[3]The so-called coherent noise, finds its origin in the low voltage regulator that supplies the cold readout electronics. Its name comes from the fact that it causes correlated fluctuation between channels of the same front-end board.

A rather poor performance of the noise filter algorithm is found when dealing with isochronous track, which are tracks traveling nearly parallel to the wire planes. In that case the noise filter can mistake the signal as part of the coherent noise and distort the waveforms from a group of channels. Nevertheless, this effect is greatly reduced as the angle of the track increases with respect to the wire plane.

The ICARUS wire signal processing chain follows a logic similar to other LArTPC experiments, exploiting the deconvolution of the wire signal waveform. Ideally, after deconvolution, the signal pulse produced by a charged track on a wire would be gaussian-like (if no charge diffusion was present, the expected signal would be a $\delta$ function) with mean and integral determined by the drift coordinate and ionization charge of the corresponding track segment. In that case, the area under the deconvolved waveform will be proportional to the number of deposited electrons. The general concept of deconvolution technique is as follows.

The measured signal $M(t')$ is modeled as a convolution integral over the original ionization charge signal $S(t)$ and the detector response function $R(t, t')$. This latter, gives the instantaneous portion of the measured signal at some time $t'$ due to an element of the original signal at time $t$. This can be mathematically expressed as

$$M(t') = \int_{-\infty}^{\infty} R(t' - t) \cdot S(t) dt \, . \tag{5.3}$$

Where $R(t', t) = R(t' - t)$ when assuming the detector response function is time-invariant. This function includes both the wire field and electronics response. Eq. 5.3 can be transformed into the frequency domain by applying a Fourier transformation, yielding $M(\omega) = R(\omega) \cdot S(\omega)$, where $\omega$ is in units of angular frequency. The naive implementation of this approach suffers from high-frequency noise which is amplified by the deconvolution procedure (division of noise by the response function at high frequencies where the signal response is very small). Hence, the previous solution in the frequency space is extended through the introduction of a low-pass filter function $F(\omega)$, such as:

$$S(\omega) = \frac{M(\omega)}{R(\omega) \cdot F(\omega)} \, . \tag{5.4}$$

This is essentially equivalent to replacing the real detector response function with an effective response function. The original signal can then be retrieved by applying the inverse Fourier transform to $S(\omega)$.

This deconvolution prescription is known as the "one-dimensional deconvolution", in the sense that a Fast Fourier transform is carried out as a function of time only. Thus, this procedure assumes the induced current on each sense wire is independent of the charge distribution in its vicinity. However, as described in [151, 152], the induced current on the sense wire receives contributions not only from ionization charge passing by the sense wire, but also from ionization charge drifting in nearby wire regions at roughly the same time. While these contributions are generally small they can produce destructive interference particularly on the induction planes and for isochronous tracks. To take into account charge over nearby effects, a 2D deconvolution involving both the time and the wire direction can be performed. A complete description of this technique can be found in Ref. [151], along with some data evaluation performance done by MicroBooNE, proving that the 2D deconvolution provides a robust and computationally efficient method to extract the distribution of ionization electrons. Currently ICARUS uses a 1D deconvolution technique, but is finishing some validation tests to transition to 2D deconvolution. An example of the result of the TPC signal processing at different stages is shown in Figure 5.5.

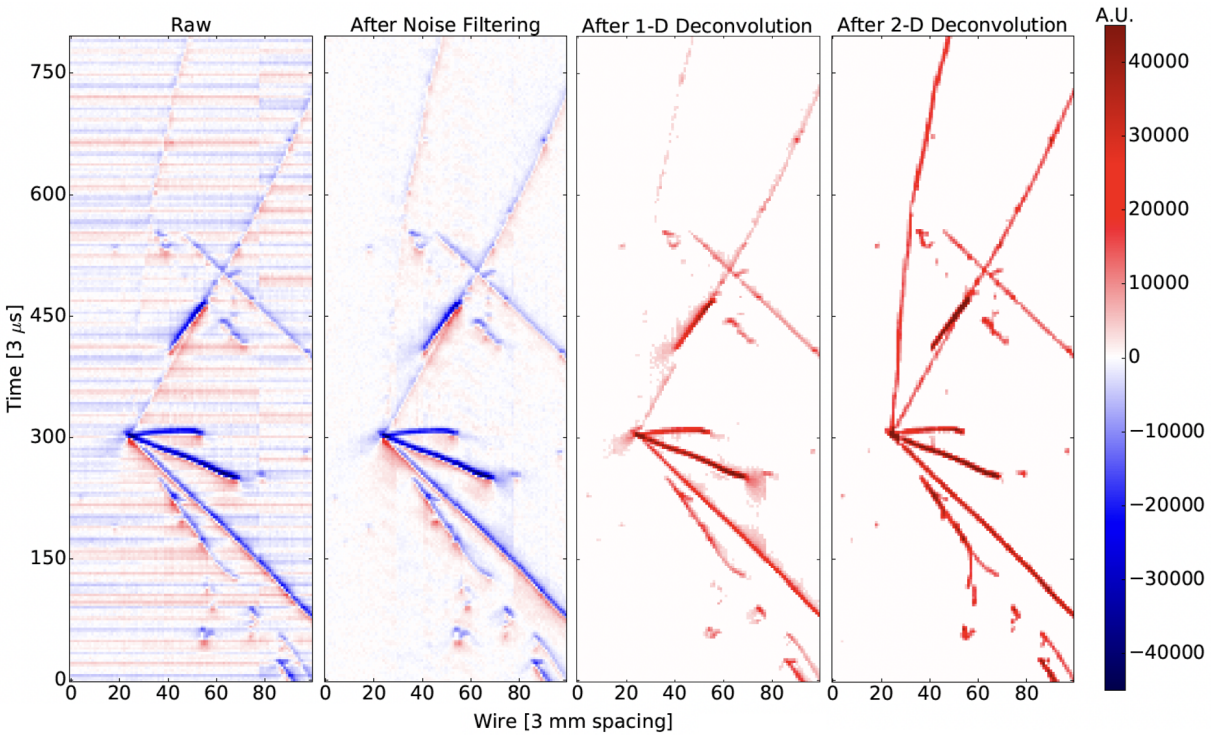


Figure 5.5: Event displays of the Induction 1 plane, from a neutrino interaction candidate recorded by MicroBooNE. From left to right: Raw waveform image in units of average baseline subtracted ADC. Same raw waveform after software noise-filtering. Last two images show the charge spectrum in units of electrons after signal processing with 1D and 2D deconvolution techniques. The bipolar shape with red (blue) colour representing positive (negative) signals is converted to the unipolar shape after the deconvolution. Figure adapted from Ref. [151, 152].

Prolonged signals associated with near-vertical tracks, such as the one at the top left of each event display window, are recovered after the deconvolution step. In addition, the image quality near the neutrino interaction vertex is enhanced after 2D deconvolution, which is expected to improve neutrino reconstruction efficiencies and estimation of physics observables. Ionization electrons pass between the induction wires of the anode plane on their way to the collection wires. While approaching the induction planes, they generate a positive signal, whereas this change to a negative signal once they have cross the plane and are moving away from it. This bipolar signal is converted into a unipolar signal similar to the one in collection plane at the end of the deconvolution process. This difference between induction and collection planes, makes the 1D deconvolution technique successful for the collection plane but not quite optimal for induction planes. Compared to the collection plane, the induction planes suffer from wire response suppression at low frequencies due to its bipolar signal nature, which is problematic for the deconvolution procedure. Without mitigation, the amplification of low frequency noise would lead to large uncertainties in the estimation of charge induced on the waveforms. This can be address considering only regions of interest (ROIs) in the time domain. The idea is to limit the deconvolution to a small time window, slightly bigger than the extent of the signal it contains, and replace the entire event readout window with a set of ROIs, as shown in Figure 5.6. On induction planes, the portions of waveforms inside the ROIs are baseline subtracted in order to remove the residual effects of the low frequency noise. The ROI technique is also performed for the collection plane, as it helps reduce the overall data size and speed up the deconvolution process. The deconvolution filters applied all along the process are chosen such that the signal due to an individual element of charge is Gaussian-shaped, which is convenient for the downstream reconstruction steps.

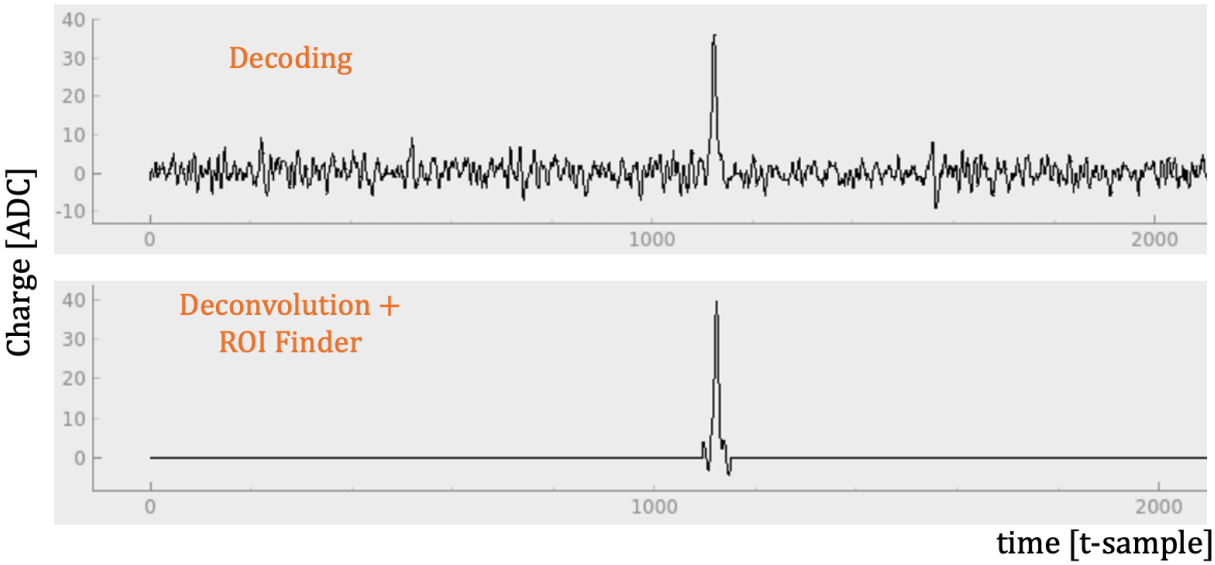


Figure 5.6: Collection plane waveform with signal processing. Top: example of measured waveform in collection plane. Middle: Waveform after 1D deconvolution and selection of the region of interest (ROI). Note that a t-sample corresponds to 0.4 $\mu$s.

### 5.5.2 Hit finding

The segments of waveforms left over after deconvolution are considered to have a high signal-to-noise ratio however, they need to be further manipulated to provide meaningful physical information. A `Hit` is a two-dimensional object representing a cluster of electric charge arriving at a given wire at a given time. The reconstruction algorithms currently employed are based on finding `Hits` (over a certain threshold) on the deconvolved waveforms for each plane. Under the assumption that the output of the deconvolution process will be Gaussian-shaped charge deposits, the hit finder module is called *gaushit* as it captures the waveform shape into a series of Gaussian distributions. Generally the module loops over the input ROIs from the deconvolved waveforms and handles each in two main steps: first it searches for candidate pulses with the idea that a ROI can contain more than one hit and secondly, it fits these candidates to a Gaussian shape. When the hit shape is not a simple Gaussian but instead multiple charge is seen by the same wire in a short time, the pulse is divided into a certain number of hits under the assumption that the entire pulse can be described accurately with overlapping Gaussian peaks. The number of gaussians used to fit the pulse is often called multiplicity. The extracted properties of the hits are the parameters of the Gaussian fit: the area represents the total charge (with the appropriate calibration constant to convert ADC×t-sample to Coulombs), the mean gives the hit peak time, the amplitude represents the height of the hit and the gaussian width corresponds to the RMS of the hit. Figure 5.7 visually shows the performance of the Hit Finder algorithm.

At this point, a collection of 2D hits for each wire plane has been created, representing a signal detected on a specific wire at a specific time. These three 2D views are used as the input to pattern recognition algorithms.

The method aims to create all possible space points with the goal of maximizing efficiency at the possible expense of purity, assuming that a 3D level algorithm (such as the pattern recognition employed afterwards) will resolved the allowed ambiguities. The collection of all 2D hits used to create space points, sometimes called "list of reconstructed and disambiguated 2D hits", will be passed as the input to the pattern recognition algorithm. With this approach, the pattern recognition algorithm will be able to run more efficiently on the reduced set of hits.

The candidate 3D points are found by performing combinations of 2D hits on neighboring

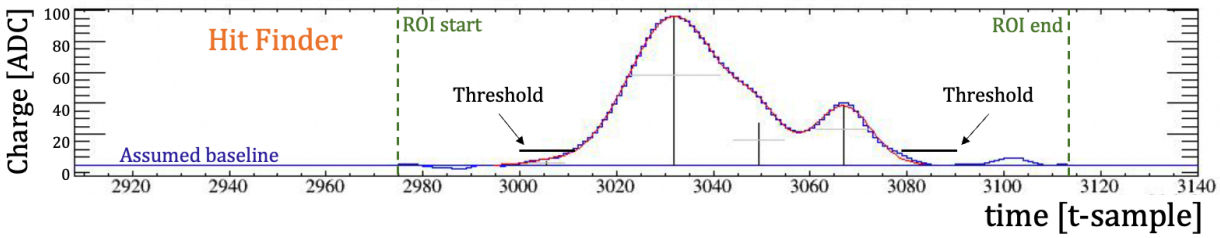


Figure 5.7: Collection plane waveform showing the Hit Finder algorithm performance. A Gaussian fit is carried out each time a certain threshold is exceeded. In this example the Hit Finder chooses to fit the hit with three Gaussian shapes (red line), the crosses represent the center of the fit peaks, the pulse heights above the baseline and their fit widths.

planes using the so-called `Cluster3D`, an algorithm combining compatible hits. Compatible hits must coincide in time, which means that the difference in the peak times of the Gaussian pulses should be within a predefined interval. In addition, their wires also need to intersect in the Y-Z projection. Once a pair of compatible signals has been identified, a 3D candidate space point can be form using both 2D hit information.

ICARUS Hit Finder algorithm is optimized to keep hit finding efficiency high, however high levels of noise might cause the creation of hits due to non physical signals or the loss of real signal. These will cause problems in the pattern recognition performance, yielding poorly reconstructed track and shower candidates or very long reconstruction times. To solve this problem one can exploit the fact that physical hits are expected to have correlated matches across the three planes. Conversely, pure noise hits will be mostly uncorrelated and will not have matches on the other planes. In addition, the horizontal wires on the first induction plane are split into two 9 m long wires at $z = 0$ m; this might produce ambiguous hit combinations and could also benefit from the triple coincidence.

Thus, taking advantage that the x coordinate is common to all three views for correlated hits, a search is done to the third plane to look for a compatible hit with the preliminary extracted 3D position. If a compatible hit is found, a 3D space point is formed and saved.

It is clear that creating space points is critically dependent on the 2D hit finding efficiency and quality, which ultimately relies on the whole signal processing chain. The requirement of having a triple match will introduce inefficiencies if a set of hits is missing in one plane.

An alternative could be to rely on hits with matches on just two planes, to recover some signal, these are the so-called `Mythical points`. However, given the typical width of a hit (some tens of t-samples) there might be a non negligible number of combinations satisfying the time overlap criteria and thus, creating an abundant number of spacepoints if all of them are used.

Regardless of the strategy chosen, it is important to treat both cases carefully and be aware of their limitations. More details will be given in the following sections, including the most common problems and the strategy adopted to overcome them.

### 5.5.3 Pandora Pattern Recognition

Pattern recognition is the identification of structures or regularities in data. The Pandora software development kit [153] was created to ease the process of designing, implementing and running pattern recognition algorithms. Pandora aims to address the problem of identifying energy deposits from individual particles in fine granularity detectors using a multi-algorithm approach. Complex and varied topologies in particle interactions, especially with the level of detail provided by LArTPCs, are unlikely to be solved successfully by a single clustering algorithm. Instead, the Pandora approach is to break the pattern recognition into over 100 algorithms to develop the reconstruction from the input hits to a hierarchy of fully reconstructed particles. Each algorithm is designed to address a specific aspect of event reconstruction, and collectively

provide robust and sophisticated patter recognition. The final goal is for each particle, to be reconstructed as a single object particle, that is both pure (containing only hits from that particle) and complete (containing all hits from that particle). The Pandora event reconstruction can be run standalone and has been interfaced with LArSoft. Several LArTPC experiments, such as MicroBooNE and ProtoDUNE-SP, have successfully used Pandora to automatically reconstruct cosmic ray muons and neutrino interactions [154, 155].

As previously mentioned, the input to Pandora is a list of reconstructed and disambiguated 2D hits, alongside detector information (detector geometry and unresponsive or dead wire regions), to which the entire pattern recognition chain is applied. Note that Pandora ignores previously created space points and instead builds its own 3D space points based on individual cluster topology.

The major Pandora output is a list of reconstructed 3D particles, named particle flow particles (PFParticles, or PFPs for short) in Pandora nomenclature. Each PFParticle corresponds to a distinct track or shower in the event, and has associated objects such as collections of 2D hits for each view (Clusters), 3D positions (SpacePoints) and a reconstructed Vertex position that defines its interaction point or first energy deposit. The PFParticles are placed in a hierarchy, which identifies parent-daughter relationships and describes the particle flow in the observed interactions. Pandora does not reconstruct the identity of each particle, but rather identifies the PFP as track-like or shower-like based on their topological features. Track and Shower objects carry additional information, such as position and momentum values for tracks or principal-axis information for showers.

#### Reconstruction chain

The current chain of Pandora algorithms has largely been tuned for neutrino interactions from the Fermilab Booster Neutrino Beam, however the algorithms are designed to be generic and easily reusable for other experiments. Pandora has two main chain algorithms for event reconstruction in neutrino detectors[4], PandoraCosmic and PandoraNu, targeting the reconstruction of interactions under cosmic ray and neutrino hypothesis, respectively. Many algorithms are shared between these two reconstruction paths, but the overall algorithm selection results in the following key features:

- **PandoraCosmic**: Strongly track-oriented reconstruction, producing primary particles that represent cosmic ray muons. Showers are assumed to be delta rays and are added as daughter particles of the most appropriate cosmic ray muon. The reconstructed start point for a cosmic ray muon is chosen to be the highest vertical coordinate of the muon track.
- **PandoraNu**: Focus on the identification of a neutrino interaction vertex, which becomes the pivot to reconstruct all particles emerging from it. Vertex identification algorithms are PandoraNu specific and there is a more sophisticated treatment of track and electromagnetic showers. The chain concludes building a hierarchy, where a parent neutrino particle is created and the reconstructed visible particles are added as daughters of the neutrino (which in turn, have their internal hierarchy).

Each algorithm chain works well on the type of interactions it was designed for. Surface detectors need to deal with events both containing neutrino and cosmic rays interactions. In order to optimize the pattern recognition performance a consolidated reconstruction approach is often adopted. A flow diagram illustrating this approach is shown in Figure 5.8. This starts by running the PandoraCosmic reconstruction on the entire collection of identified hits during the readout window.

[4] ProtoDUNE-SP modified the neutrino oriented Pandora chain to represent the interactions of charged particles in a test beam, see Ref. [155].

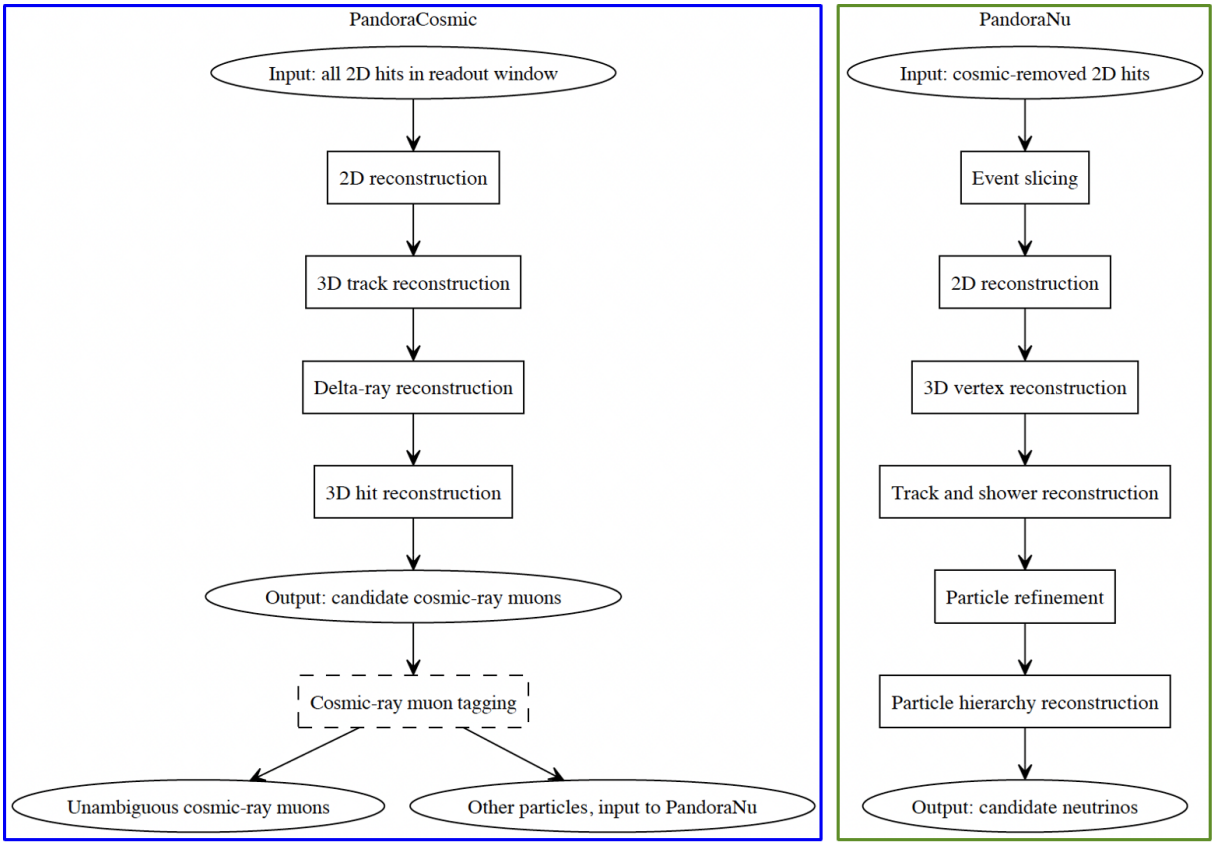


Figure 5.8: Outline of the Pandora consolidated reconstruction used in ICARUS. Particles output by the PandoraCosmic are examined by an external module to tag and reject *clear cosmic* interactions. 2D hits unambiguously associated to a cosmic ray muon are removed from the initial hit collection and generate the new input to the PandoraNu chain algorithm. Picture taken from Ref. [154].

### PandoraCosmic

In the first step a two-dimensional clustering of hits is performed for each read-out plane independently, producing a list of clusters that represent continuous and unambiguous lines of hits. As a first approach separate clusters are created whenever a bifurcation or ambiguity is found, providing high purity clusters. Still within 2D reconstruction, a cluster merging algorithm is applied to identify associations between multiple 2D clusters trying to grow the clusters to improve completeness, without compromising purity. The typical approach used is based on close clusters proximity or respectively pointing clusters. Finally, to improve purity, the hit selection is refined by breaking single clusters into two parts if topological features indicate a possible inclusion of hits from multiple particles. The generated 2D clusters are used as an input to the next step.

The aim of the 3D track reconstruction stage is to identify consistent groups of 2D clusters from the three readout planes that describe a single track-like particle. A dedicated algorithm considers the suitability of all combinations of clusters from the three readout planes and stores the results for further analysis. For each combination, a number of sampling points are defined in the common x region, exploiting the existing redundancy provided by the three independent views. For a given sample point located at a certain x coordinate, the sliding-fit position can be extracted for a pair of cluster (corresponding to two different positions for each of the two wire views). These positions can be used to predict the location of the third cluster, at that fixed x coordinate, to be compared with the standalone sliding fit position of the third cluster. By

consider all combination of wire plane pairs a sort of $\chi^2$ is computed, providing information about the consistency of 3D clusters, the connection between multiple clusters and their matching ambiguities. If a given 3D cluster contains more than one cluster from any single view, an ambiguity is defined. A set of specific algorithms with the ability to create new particles or modify the 2D clusters are available to address this problem.

Following the 3D track reconstruction, the Delta-ray reconstruction step dissolves any 2D clusters that have not been included in a reconstructed object, under the assumption that these are likely to be fragments of delta-ray showers, which are used to seed and grow shower particles. At this point, 2D hits have been assigned to different particles containing clusters from one, two or usually three readout planes and new 3D hits, also called space points, are created.

PandoraCosmic last task is to place the start position of the cosmic ray muon at their highest reconstructed vertical coordinate, as they are assumed to always be downward going. Secondary shower particles are joined to the parent muon track through a hierarchical parent-daughter dependency, representing Michel electrons and delta rays.

In this first step, hits from the different drift volumes are processed separately. Before applying the PandoraNu chain, a stitching algorithm is performed to fully reconstruct particles crossing neighbouring drift volumes. In addition, a cosmic ray tagging filter is applied to distinguish hits unambiguously associated with cosmic ray muons from the remaining ambiguous hits. Unambiguous cosmic-ray associated hits are removed from the input hit collection that was first given to PandoraCosmic, providing a new cosmic-removed hit collection which will serve as the initial point for PandoraNu path.

**Track timing and cosmic ray muon tagging**

As previously stated, the x coordinate is computed relying solely on temporal information, see Eq 3.1. Hence, a precise and robust assignation of the interaction time to each reconstructed object inside the TPC is crucial to correctly locate the interaction position along the drift coordinate.

The time at which the charge was collected on the wires ($t_m$) is a function of the time at which the particle entered the detector ($t_0$) relative to the global trigger time and the distance in the drift coordinate from the anode plane where the energy was deposited (x): $t_m = t_0 + x/v_d$. It is straight forward to see that there is an ambiguity in this equation between $t_0$ and x for a given $t_m$ unless $t_0$ is known.

The track time can be accurately measured with the PMTs if an optical flash is matched to a reconstructed object in the TPC, exploiting the so-called "PMT-TPC matching". In spite of this, the high number of cosmic tracks crossing each TPC during the readout window makes it challenging to unambiguously assign a unique $t_0$ to each track. For in-time interactions $t_0 = 0$ by definition and no ambiguity arises. In all other cases, the $t_0$ is initially unknown and Pandora reconstruction assumes by default, that the track arrived at the trigger time; hence assigning a preliminary value of $t_0 = 0$. For this reason, the exact position in the drift coordinate where charge was physically deposited, is only well determined for in-time interactions. For out-of-time particles, the intrinsic ambiguity in x makes it, a priory, impossible to distinguish between charge deposited by a particle arriving before the trigger time but far from the anode plane from a charge deposition that happened after the trigger time but was much closer to the anode ($t_m$ would be the same in both cases).

Each cryostat of ICARUS detector has two adjacent volumes, separated by a central common cathode, which can be traversed by tracks. Light-independent methods can be implemented to measure the correct $t_0$, taking advantage of the additional information provided by those tracks that have crossed the cathode plane.

As previously seen, reconstruction initially processes each drift volume independently, resulting in separately reconstructed 3D objects in each volume. For tracks at $t_0 \neq 0$ and crossing

the cathode, the reconstruction will in general, produce two separate segments characterized by the same displacement from the cathode. However, these will be shifted in opposite directions as the drift field direction alternates between adjacent TPCs. That distance will be proportional to the real $t_0$ track time and inversely proportional to the drift velocity. The direction of the shift depends on weather the physical track occurred before (*early track*) or after (*late track*) the trigger time, see Figure 5.9 for graphical representation of all three possible situations.

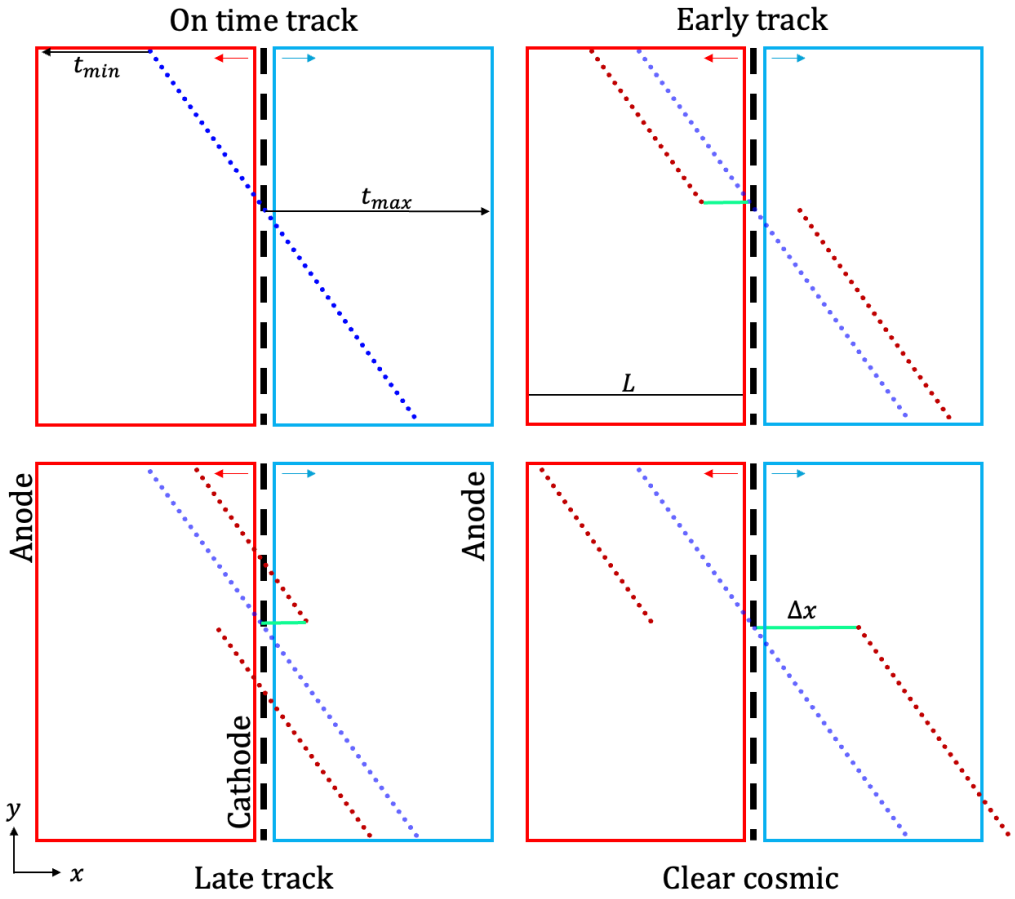


Figure 5.9: Example of possible situations for a cosmic ray crossing the detector from top to bottom and passing through the cathode. Blue dots represent the true trajectory of the cosmic, while red segments are the reconstructed Pandora tracks under the initial assumption of $t_0 = 0$. Some of the key variables for performing the stitching between the split tracks are also shown. Red and blue arrows indicate the drift field direction in each TPC.

This characteristic geometry is exploited by Pandora to search for two 3D clusters that are reconstructed in two different drift volumes and are consistent with creating a single continuous trajectory both in its position and direction across the cathode boundary. If such a match is found, the separate components can be stitched together by shifting the two clusters to the x coordinate of the cathode plane. The $t_0$ corrections identified by this stitching process allow to estimate the track time as

$$t_0 = t_{\text{max}} - (L - \Delta x)/v_d \, . \tag{5.5}$$

Where $t_{\text{max}}$ is the time of the closest hit to the cathode, $L$ is the maximum drift length and $\Delta x$ is the distance between the cathode and x position of the hit with $t_{\text{max}}$ before any correction. ICARUS have $L = 1.5$ m and $v_d \sim 1.6$ $mm/\mu s$ at the nominal electric field, 500 $V/cm$. During the stitching algorithm a tolerance factor in the shifts between the two tracks segments was introduced to account for possible asymmetries due to space charge effects or inefficiencies during the track reconstruction. Taking into account the readout characteristics for ICARUS TPC

subsystem, a track would be fully visible only if both the time of the first and last hit are inside the delimited time window. A total of 4096 t-samples are recorded (t-sample = 0.4 $\mu$s), of which $\sim$ 850 are recorded before the trigger. Therefore, the first hit should be recorded no earlier than $\sim$ 340 $\mu$s before the trigger time, and the last hit no later than 1300 $\mu$s.

Once the stitching algorithm is done, a clear cosmic ray candidate is identified if it satisfies at least one of the following criteria:

- The reconstructed particle crosses the top and bottom boundaries of the detector ("through-going particle")
- Any hit in the reconstructed particle (assuming $t_0 = 0$) fall outside of the physical drift volume, clearly indicating that the object is not compatible with the beam spill gate (an example is shown in the last diagram of Figure 5.9)
- The $t_0$ correction found during the stitching algorithm is too large to be compatible with a particle coming from the beam

The reconstructed particle hierarchies tagged as clear cosmic ray muons constitute the first output of the consolidated reconstruction. Note that this sample of clear cosmics tracks, in particular those whose $t_0$ was assigned, form a critical component to study any detector calibration in detail. Their hits are removed from the event record before the Pandora reconstruction chain continues to further process the data, easing neutrino-induced particle reconstruction.

**PandoraNu**

In order to avoid possible inefficiencies during the PandoraCosmic chain, PandoraNu reconstruction path must be able to cope with the presence of cosmic ray remnants within its input (cosmic removed hit collection). The strategy is to run the previously described algorithms up to the 3D hit creation, where the 3D hits are subsequently divided into *slices*. These are separated list of hits, which have been created on the basis of proximity and direction, and are intended to isolate neutrino interactions and cosmic ray remnants in different slices. Each slice is processed in isolation through dedicated neutrino reconstruction algorithms and results in one neutrino candidate.

The first step of PandoraNu reuses the track oriented clustering and topological association previously described, where now the algorithms need to handle more complex topologies, in terms of detailed interactions and number of possible reinteractions. The list of 2D clusters for the different readout planes are used to produce a list of possible 3D vertex candidates. Once all the candidate vertex positions are identified, it is necessary to select one as the most likely neutrino interaction vertex. All candidates must pass a quality cut before being accepted as a valid vertex: they are required to be located on or near a hit in all three views. After this filter, an algorithm assigns a score to each remaining candidate and the vertex with the highest score is selected. This algorithm takes three main inputs; the first one reflects the fact that primary particles produced in the interaction should point back towards the true interaction vertex, hence candidates are disadvantaged if the sum of the transverse energy over all cluster is not compensated. Downstream secondary particles might cause some imbalance, however they are expected to be less energetic and thus of minor impact. The second factor is an asymmetry check, true vertex are expected to have a large asymmetry between the number of upstream and downstream hits; symmetric candidates are severely penalized. Last input comes from the knowledge of the beam direction, benefiting those candidates with low z positions (in ICARUS the beam direction is along the positive z axis). When the highest score candidate is chosen, any 2D cluster crossing the vertex is split into two pieces, creating new cluster on either side of the projected vertex position.

Next step is 3D track reconstruction which proceeds almost exactly as in PandoraCosmic. The only difference is that now PandoraNu also attempts to reconstruct primary electromagnetic showers from electrons and photons, by adding branches to any long cluster that might represent the central structure of a shower. The obtained 2D shower-like clusters are matched between readout planes in order to form 3D shower particles, reusing the ideas from 3D track reconstruction. After 3D shower reconstruction, a second iteration of 3D track reconstruction is applied, in order to recover any inefficiencies associated with dissolving track particles to examine their potential as showers[5]. The final output of this phase is an independent classification of each particle as either track-like or shower-like, where a boosted decision tree (BDT) algorithm is used. Successive steps are particle refinement, trying to improve particle completeness by picking up small, unassociated cluster remnants, and particle hierarchy reconstruction. This latter is in charge of organising the reconstructed particles into a parent-daughter structure. The strategy is to start building the interaction from 3D neutrino vertex, and proceed adding branches and leaves to those. The branches would be all primary particles, which are directly related to the neutrino particle, whereas the leaves represent all particles produced by its primary parent, being either new interactions or decays. The interaction will grow as much as necessary, until all particles of the slice are correctly associated. The final output from the reconstruction chain is a single reconstructed neutrino particle for each slice with internal particle hierarchy, which provides the flow of the neutrino interaction. Figure 5.10 shows different reconstruction stages for a simulated neutrino. Pandora also allows to simulate dead or malfunctioning channels, which gives the program additional information to prevent cluster splitting in that specific signal-less region.

[5]In order to asses the available clusters as shower candidates, the 2D shower reconstruction includes an algorithm that dissolves any existing track particles if it is claimed to be shower-like.

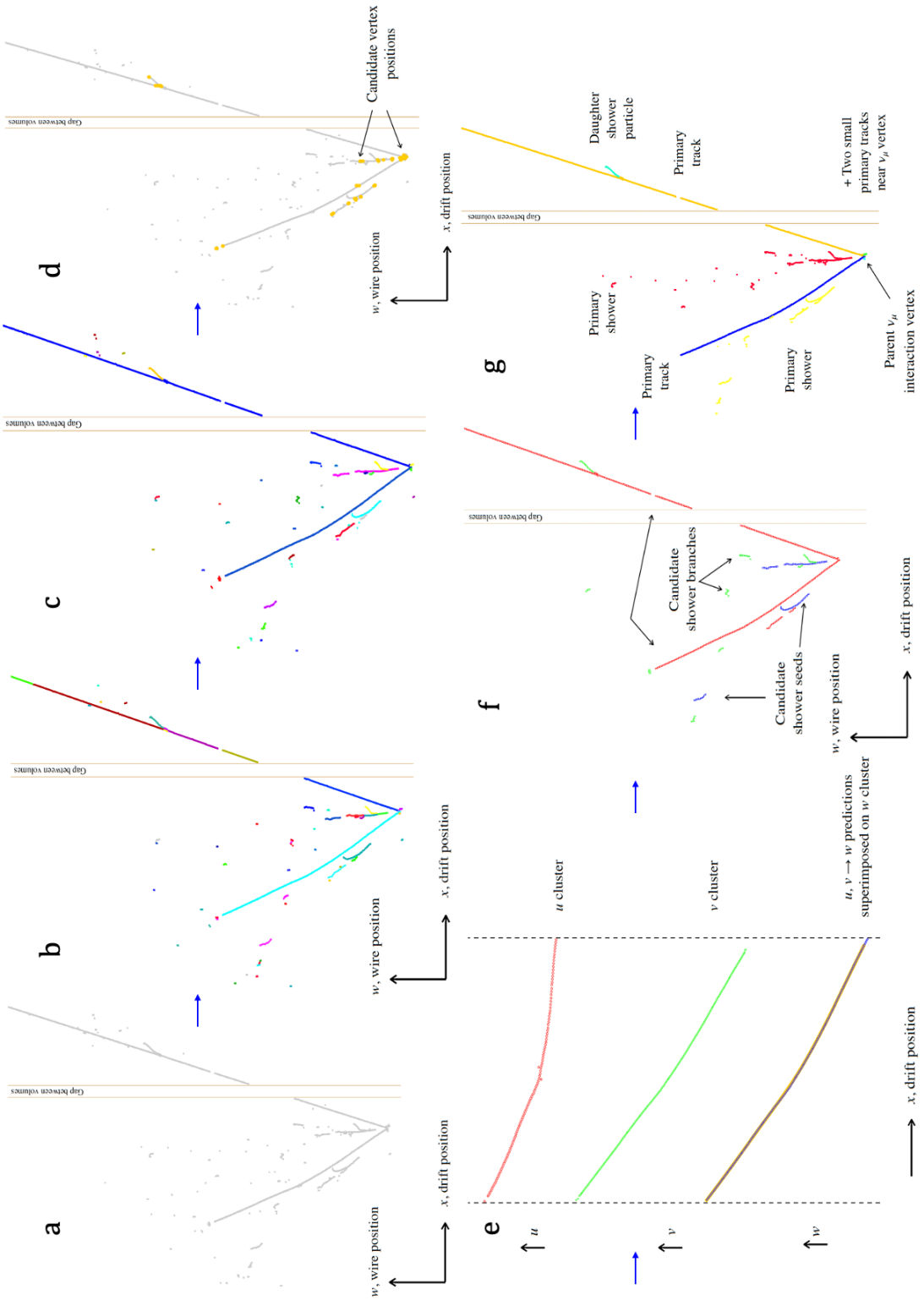


Figure 5.10: Illustration of the main stages of Pandora pattern recognition chain. Input hits (a), 2D track-like cluster creation (b) and refinement (c), 3D vertex reconstruction (d), 3D track reconstruction (e) where the yellow band on top of the blue hits (w plane) indicate the cluster prediction using the clusters in the other two views. Track and shower separation is shown in (f) panel, while (g) shows the particle refinement and event building, including the internal hierarchy structure. Figure taken from Ref. [119]

### 5.5.4 Calorimetric energy reconstruction and particle identification

Precision calorimetry measurements are one of the reasons why LArTPC detectors were proposed for neutrino experiments. As charged particles pass through a LAr volume, they deposit energy through ionization and scintillation. It is then crucial to measure this energy deposition, as it provides not only information about the energy of the particle, but also allows to identify its specie.

Neutrinos themselves are not electrically charged and thus, leave no ionization trace, but their products often do, and it is by these that the original neutrino flavour might be identified. The energy loss of charged particles traveling through a material can be described as the sum of the energy lost due to interaction with the material's electrons and the energy dissipated through radiative processes. Muon and proton energy loss in the kinematic regime relevant to ICARUS is primarily by ionization. The mean energy loss is accurately described by the Bethe equation and corrections to it [33].

$$\left\langle \frac{dE}{dx} \right\rangle = \zeta T_{max} \left[ \ln \frac{2m_e c^2 \beta^2 \gamma^2 T_{max}}{I_0^2} - 2\beta^2 - \delta(\beta\gamma) \right] , \tag{5.6}$$

where

$$T_{max} = \frac{2m_e c^2 \beta^2 \gamma^2}{1 + 2\gamma m_e/M + (m_e/M)^2} \quad \text{and} \quad \zeta = \rho \frac{KZ}{2AT_{max}\beta^2} .$$

Relevant parameters in these expressions are: the traveling particle (M) and electron ($m_e$) masses, the mean excitation energy ($I_0$), the argon charge (Z) and mass (A) number, the argon mass density ($\rho$) and a physical constant (K), with units of $MeV \times cm^2/\text{mol}$. $\gamma$ and $\beta$ are given by the particle velocity and $T_{max}$ is the maximum energy transfer to a single electron. Finally $\zeta$ encapsulates the scattering rate, with units of inverse length, and $\delta$ is a density effect correction to ionization energy loss. This equation is valid only in the region $0.1 \leq \beta\gamma \leq 1000$, with an accuracy of a few percent.

There are two situations worth noticing from the Bethe equation, see Figure 5.11; the first is the presence of a minimum around $\beta\gamma \approx 3$. This is referred as the minimum ionizing region, and a particle with an energy close to the minimum of $\langle dE/dx \rangle$ is said to be a minimum ionizing particle (MIP). In liquid argon this value is 2.12 MeV/cm [120]. It is possible to see that the variation of $dE/dx$ from $\beta\gamma \approx 3$ to $\beta\gamma \approx 100$ is rather small, allowing to assume a MIP like behaviour between these two values.

Going from $\beta\gamma \approx 3$ towards lower kinetic energies, the $\langle dE/dx \rangle$ shape presents a sharp rise known as "Bragg peak", indicating an increase in energy deposition, and therefore ionization, towards the end of the track. It will be seen that this ionization rise is characteristic of each type of particle, providing a good method to discriminate between species.

The description of charged particle energy loss is complicated by the presence of delta rays. These are secondary electrons to which a significant amount of energy is transferred by the ionizing particle, allowing them to produce further ionization along the primary track trajectory. This produces a long tail on the distribution of particle energy loss, significantly perturbing the measurement of the mean energy loss. To overcome this problem it is recommended to use the most probable value (MPV) of the energy loss distribution, rather than its mean, as the MPV only depends on the peak of the distribution. Due to the typical deposited energy intervals ($\sim$ 0.3 - 0.4 cm) and the precise sampling of calorimetric information in ICARUS, it is possible to achieve an excellent measurement of the energy loss distribution. In the Landau limit, which is applicable to energy depositions far from the stopping point of a particle, the corresponding most probable energy loss is given by

$$\left. \frac{dE}{dx} \right|_{MPV} = \left\langle \frac{dE}{dx} \right\rangle + \zeta T_{max} \left( \log[\zeta p] + 0.2 + \beta^2 \right) , \tag{5.7}$$

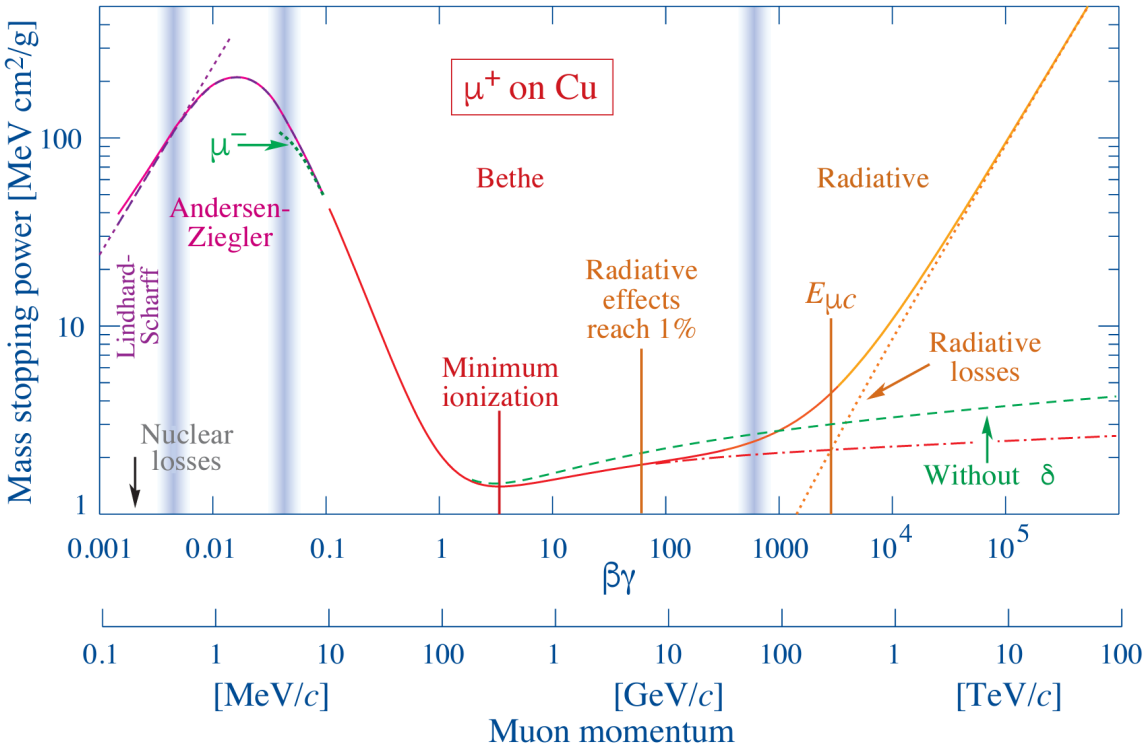


Figure 5.11: Mean rate of energy loss for positive muons in copper as a function of $\beta\gamma$ and kinetic energy. Solid curves indicate the total stopping power. Although the figure describes the energy loss of muons in copper, it is qualitatively identical for other target materials such as LAr. Figure taken from Ref. [33]

where $p$ is the length of the track observed by a sense wire. All work presented in this thesis is currently using the track pitch ($dx$) as the value of $p$. However, it is expected that a more precise treatment will be soon introduced in the software analysis modules of ICARUS, exploiting the track angle and transverse diffusion dependency of $p$ as shown in Ref. [156].

### dQ/dx Calorimetry

At this point of the event reconstruction, 3D trajectories, with its 3D spacepoints, have been reconstructed and categorized as track or shower. The relevant quantities from calorimetry are the hit area, the hit time coordinate and the track pitch length associated to the hit wire, for all hits belonging to the track.

The $dE/dx$ (MeV/cm) for track-like particles, is calculated for each hit separately from the $dQ/dx$ (ADC/cm), which in turn is obtained as the ratio between the area under the hit ($dQ$) and the track pitch. The track pitch ($dx$) defines the distance the particle travels within the wire pitch (3 mm for ICARUS) and is calculated from the direction of the track at the energy deposition using the `TrajectoryPoint`[6]. In particular,

$$dx = 3 \text{ mm}/\cos\gamma \,, \tag{5.8}$$

[6]In order to link all spacepoints produced by Pandora, two 2D sliding fits are applied to the projected 3d points orthogonal to the principal axis. A 2D sliding fit is a series of linear regression fits performed at each segment in 2D space. The linear regression fit at a particular segment (straight line between a spacepoint and the following one) uses ten segments before and after as additional fitting points. The direction of the track uses the local gradients of the linear fits, while the 3D position is reconstructed using both the gradients and intercepts obtained in the fit. In the LArSoft framework this information is stored in a `TrajectoryPoint` object.

where here $\gamma$ is the three dimensional angle between the local direction of the track and the vector that connects adjacent wires, as shown in Figure 5.12. $\gamma$ in general ranges from 0 to 90 degrees, while in ICARUS $dx$ is close to the 3 mm wire spacing for tracks parallel to the beam direction and increases for tracks at large angle from the beam.

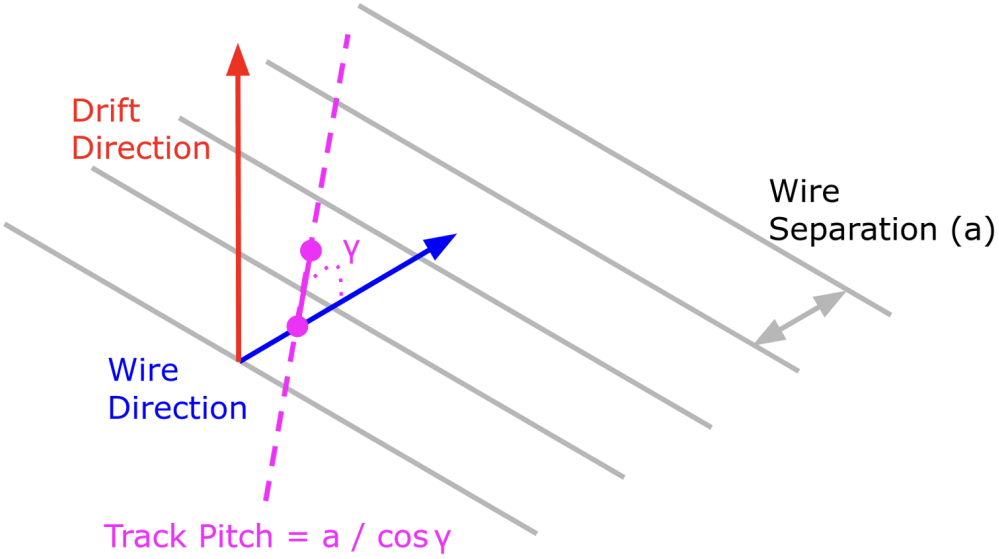


Figure 5.12: Sketch of the relevant directions and angle in the calorimetric reconstruction, showing the relation between the track orientation and the track pitch in a general LArTPC. Figure taken from Ref. [156]

### Charge equalization

Calorimetry measurements require a good understanding of the charge response of the wires inside a LArTPC. The $dQ/dx$ obtained might substantially differ from the original $dQ/dx$ at the location where the ionization occurred hence, it needs to be corrected before charge deposition is converted into the energy loss ($dE/dx$) for further studies. A number of effects perturb the charge response in ICARUS, thus a charge equalization procedure with the goal of making the detector response to charge uniform in space and time was put in place. The strategy adopted to equalize the charge response was separated in three main steps: a first equalization in the drift direction ($\hat{x}$), a second equalization in the two wire plane directions ($\hat{y}$ and $\hat{z}$), and a third and final TPC equalization.

Being at shallow depth, ICARUS has access to a huge number of cosmic muon tracks ideal to perform this type of detector calibrations. Cosmic rays are the standard candle for uniform energy deposition throughout the detector, as they cross the detector as nearly minimum ionizing particles. However, only the subset of muon tracks crossing the cathode was used. As previously seen, tracks that cross the cathode are stitched by Pandora, enabling the identification of the arrival time of the track ($t_0$). This requirement comes from the need to know the proper time a particle crossed the detector, to apply a precise drift time correction.

In ICARUS the $dQ/dx$ is affected by:

- Argon impurities: when ionization electrons drift towards the anode, they can be captured by electronegative impurities (primarily $O_2$ and $H_2O$) contained in the liquid argon volume. The electron attachment is modeled as an exponential decay, hence the name of "electron lifetime". This latter one is inversely proportional to the concentration of impurities, and

the measured $dQ/dx$ can be corrected using the following formula

$$\left.\frac{dQ}{dx}\right|_{corr} = \left.\frac{dQ}{dx}\right|_{meas} \cdot e^{\frac{t_{hit}-t_0}{\tau}} \ . \tag{5.9}$$

The subscripts *corr* and *meas* correspond to the initially deposited charged (before the drift, corrected) and the collected charge on the wires (measured), respectively. $t_{hit}$ is the time at which the charge was collected and $\tau$ the measured electron lifetime. As seen in Figure 4.8, ICARUS electron lifetime ranged from 3 to 8 ms, which corresponds to a $\sim$ 5-15% average charge signal attenuation across the full drift time.

- Drift field distortions: as a surface detector, ICARUS experiences a large flux of cosmic rays that results in a substantial amount of ionization produced in the detector per unit of time. Along with ionization electrons, argon ions are also produces in the detector by the cosmic rays. Argon ions have drift velocities 2-4 $\times 10^5$ times slower than $e^-$ at the same electric drift field. These ions, which slowly drift towards the cathode, remain long enough to create substantial electric field distortions [157]. In addition, ICARUS cathode plane is not perfectly flat. This effect was previously observed during the ICARUS run at Gran Sasso [135] nonetheless, after the refurbishment at CERN, the effect is still present although to a lesser extent. The last known distortion comes from the East TPC of the East cryostat, where a failure in the field cage induces a large but localized deflection to the drift field. Drift field distortions affect the charge scale in two ways: first, through the amount of charge that recombine with argon ions at the ionization point; and secondly, distorting the trajectory of the ionizing tracks.

- Induction wire plane transparency: Each plane is biased at a different potential to guarantee transparency to the drift electrons in induction wires. After some studies, ICARUS found that the induction wire planes (especially the middle induction plane) absorb charge in a position dependent way across the detector. The non fully transparency affects all three planes; a reduced charged is seen by collection plane, while the signal shape in induction planes are deformed, impacting the performance of signal processing and deconvolution.

- Gain variations: charge signals are amplified and digitized by individual readout boards, each of which handles a set of 64 readout channels. Gain variations across different readout boards create spatial variation in the amplitude of signals that need to be properly accounted for.

- Diffusion: Diffusion causes electrons to slightly spread apart, effectively making the signal fuzzier as they travel; the impact increases with the drift time. Diffusion can happen in both the longitudinal (drift) and the transverse direction, impacting the timing and transverse spatial resolution, respectively. Measurements in ICARUS have shown a percentage-level impact on $dE/dx$, leading to a bias in particle identification.

Drift direction equalization corrects the measured charge for effects that vary with ionization drift time, with the largest impact coming from argon impurities. Because the electron lifetime is not constant throughout the ICARUS data taking, this correction needs to be done on a run-by-run basis. Data acquisition runs in ICARUS last from a few hours to a few days, where this period is short enough to safely assume that the electron lifetime is constant.

To guarantee a uniform and non biased sample, this step of the calibration was done using through going tracks crossing both the cathode and the anode planes. Cathode crossers are identified by asking a defined $t_0$ time of the track, while a cut on the drift direction length was imposed to ensure the track was also crossing the anode. In order to mitigate the impact of diffusion, $dQ/dx$ was summed together across 10 wires to form a broad $dQ/dx$, being 3 cm much

larger than the smearing width of transverse diffusion. This 10-wire $dQ/dx$ is binned in terms of the drift time (every 50 $\mu$s) and fitted with a Landau convolved with a Gaussian distribution to extract the most probable value of the $dQ/dx$ distribution. The Landau function models the physical $dQ/dx$ behaviour, while the Gaussian part accounts for all the smearing factors, such as electronic noise contribution to the signal, different inclination of the tracks or its wide range of energies. The collection of all MPV as a function of the drift time is fit to an exponential to obtain an effective electron lifetime that encapsulates the non-uniformities. With this general procedure, the obtained electron lifetime should be understood as an effective value. It does not only includes effects from argon impurities, but it is also sensitive to electric field distortions and imperfections during the signal processing.

Next step, is the wire plane equalization, which corrects charge reconstruction for detector effects that vary across the plane of the readout wires (vertical and beam directions). The procedure is similar to the drift direction equalization one, however now the analysis is done in small area bins and the MPV obtained from the Landau $\circledast$ Gaussian fit is used to compute a scale factor to keep the mean MPV fixed across the TPC. The scale factors need to be computed individually for each TPC in each wire plane, and also for each Run time period (Run 1 and Run 2), since it is important to monitor time dependent changes in detector operation.

The final step is the equalization and measurement of the gains in the four TPCs. This equalization is applied to the 10-wire $dQ/dx$ distributions, once the drift and wire plane direction equalizations are applied. Instead of using through going muons as has been done until now, it is more appropriate to use stopping muons, since these will be used to measure the absolute gain equalization in ICARUS. Nonetheless, to avoid non uniform distributions of energy loss, muons are only analyzed far from their stopping point, in particular only the region from 2 to 3 m of end point is considered. Distributions of broad $dQ/dx$ after the first two equalizations are binned in terms of distance to the end point and as a function of drift time. These are once again fitted to a Landau $\circledast$ Gaussian distribution to obtain the MPV. A single value is computed for each drift time averaging over distance, obtaining a final distribution of MPVs as a function of drift time for each TPC. Arbitrarily choosing one TPC of a specific run period to be the reference value, the scale factors are computed for each drift time bin of each TPC, so that the reference TPC has a scale factor equal to 1.

These corrections enter the reconstruction chain through a calibration database, which are retrieved when producing the files for high level analysis.

#### dE/dx Calorimetry

Last step in the calorimetry reconstruction is to calculate $dE/dx$ from the previously corrected $dQ/dx$, measured in ADC/cm, which are related through [158]:

$$\frac{dE}{dx} = \frac{W_{ion}}{\mathcal{R} \cdot \mathcal{G}} \frac{dQ}{dx} \, . \tag{5.10}$$

Where $\mathcal{R}$ is the fraction of electrons that survive the recombination with ions, $W_{ion} = 23.6$ eV is the amount of energy required to ionize an argon atom. $\mathcal{G}$ is the electronic gain that converts ADC in number of electrons and accounts for any perturbation induced by signal processing and charge corrections.

Before reaching the anode plane, ionization electrons have the chance to recombine either with their parent atom or another ion in the ionization cloud. The fraction of electrons which recombine depends on the electric field strength and the amount of localized ionization. Therefore the recombination also depends on the $dE/dx$ of the passing particle. Several models exist to describe electron recombination, such as the Birks' law [159]:

$$\frac{dQ}{dx} = \frac{\mathcal{R}}{W_{ion}} \frac{dE}{dx} = \frac{1}{W_{ion}} \frac{A}{1 + k \frac{dE}{dx} / (\mathcal{E}\rho)} \frac{dE}{dx} \, , \tag{5.11}$$

where $\mathcal{E}$ is the electric drift field, A and k are fit parameters, and $dQ/dx$ is assumed to be in electrons per unit length just for simplicity. This model was previously used to measure the electron recombination in ICARUS during the Gran Sasso Run [123]. An alternative approach is the modified Box model, proposed by ArgoNeuT [158]:

$$\frac{dQ}{dx} = \frac{\ln\left(\alpha + \mathcal{B}\frac{dE}{dx}\right)}{\mathcal{B}W_{ion}} \quad \text{where} \quad \mathcal{B} = \frac{\beta}{\mathcal{E}\rho} \,. \tag{5.12}$$

With $\alpha$ and $\beta$ being the fit parameters, and $\mathcal{R} = [\mathcal{B}dE/dx]^{-1} \ln(\alpha + \mathcal{B}dE/dx)$.

Note that both models contain one fit parameter (A or $\alpha$) uncoupled to the electric field, which control the amount of recombination, and one coupled parameter (k or $\beta$) that determines the non-linearity of recombination with respect to $dE/dx$. Figure 5.13 shows the expected recombination factor as a function of the energy deposition in liquid argon for both models.


Figure 5.13: Recombination factors for different models: Birks equation using ICARUS Gran Sasso parameters in blue, the Box model (with $\alpha = 1$ and $\beta = 0.3$ (kV/MeV)(g/mL)) shown in red, while the red dotted line presents the modified Box model ($\alpha = 0.93$ and $\beta = 0.3$ (kV/MeV)(g/mL)). Figure taken from Ref. [158]

It was seen after calibration studies in ICARUS, that the modified Box model of recombination had a better performance when fitting the data than the Birks' model. It was then decided to use the modified box fit to perform the energy scale calibration. The obtained parameters which are currently used in the determination of a hit $dE/dx$ in ICARUS are:

$$\begin{aligned} \mathcal{G} &= 75.1 \pm 1.1 \; e^-/ADC \\ \alpha &= 0.906 \pm 0.008 \\ \beta &= 0.203 \pm 0.008 \; \text{(kV/MeV)(g/mL)} \,. \end{aligned}$$

Where the electronics gain has been include in the fit as a free parameter via the following equation

$$\left.\frac{dQ}{dx}\right|_{ADC} = \frac{1}{\mathcal{G}} \left.\frac{dQ}{dx}\right|_{e^-} . \tag{5.13}$$

The gain in the fit should be understood as an effective parameter that encodes any perturbation induced by signal processing and charge corrections.

The total energy deposition from a track like particle is obtained by summing the $dE/dx$ multiplied by the track pitch at its deposition point, that is

$$\sum_{i}^{\text{all hits}} (dE/dx)_i \cdot dx_i \, . \tag{5.14}$$

Besides this calorimetry approach, the energy of a track particle can also be computed from its range, as will be shown later on.

The measurements of energy scale calibrations performed in ICARUS have pointed to a clear angular dependence in recombination for highly-ionizing particles in LAr. Thus new recombination models, such as the ellipsoid modified box [160], are being investigated to achieve a better description of data across different incident angles. A detailed review of these measurements is in preparation and will be published in the near future.

**Particle identification**

Typical particle identification methods condense spatial and calorimetric information into a score used to distinguish different particle species. If the incident particle stops in the LArTPC active volume, the energy loss $dE/dx$ as a function of the residual range ($rr$) is used as a powerful method for particle identification. Here residual range is defined as the distance of a given energy deposition, within the track it belongs to, from the endpoint of the track itself. Charged particles of different mass (or charge) have different increasing stopping power at decreasing distance from the track end, in particular this separation is maximal few centimeters before the end of the tracks between the typical particles involved in ICARUS's interactions (muons, protons, pions and kaons).

The particle identification method used in ICARUS is based on a so-called "$\chi^2$" calculation[7] between the measured response and a predicted particle hypothesis, including the proton, charged kaon, charged pion and muon. These theoretical profiles of $dE/dx$ versus residual range are computed using the mean $dE/dx$ from the Bethe formula under the hypothesis of different particles. For each selected track the reconstructed $dE/dx$ per hit is computed following the aforementioned procedure and compared hit by hit to the theoretical mean of $dE/dx$. To extract the total $\chi^2$ the contribution of all hits on the selected track are summed, excluding the first and last hits of the track. This is due to the fact that residual range calculation for these two points might be wrong, since the exact position of the hit between the wires is unknown. On average, a track stops half-way through the last wire cell, leading to an uncertainty in the stopping point position equal to the space point separation/$\sqrt{12}$ [8], where the space point separation has values of $\geq$ 3mm depending on the incident angle of the track. Removing these two points also avoid complications from particle activity effects (f.i. scattering) and energy deposition overlap at the interaction vertex. The $\chi^2$ value is finally normalized by the number of degrees of freedom ($ndof$), which corresponds to the number of hits present in the wire plane the $\chi^2$ is being computed.

$$\text{PID} = \chi^2/ndof = \sum_{hit} \left[ \frac{dE/dx_{meas} - dE/dx_{theory}}{\sigma_{dE/dx}} \right]^2 /ndof \tag{5.15}$$

[7] Note that the "$\chi^2$" is not a proper $\chi^2$ but rather a score due to the non gaussian tails of $dE/dx$.
[8] Considering the hits are uniformly distributed along the two wires.

$\sigma_{dE/dx}$ is the estimated resolution of the $dE/dx$ per hit defined in studies performed by ArgoNeuT and is of the order of $\sim 3\%$ [161]. A $\chi^2$ value is computed for each wire plane, where redundancy plays a crucial role for these tracks crossing few wires in a specific plane.

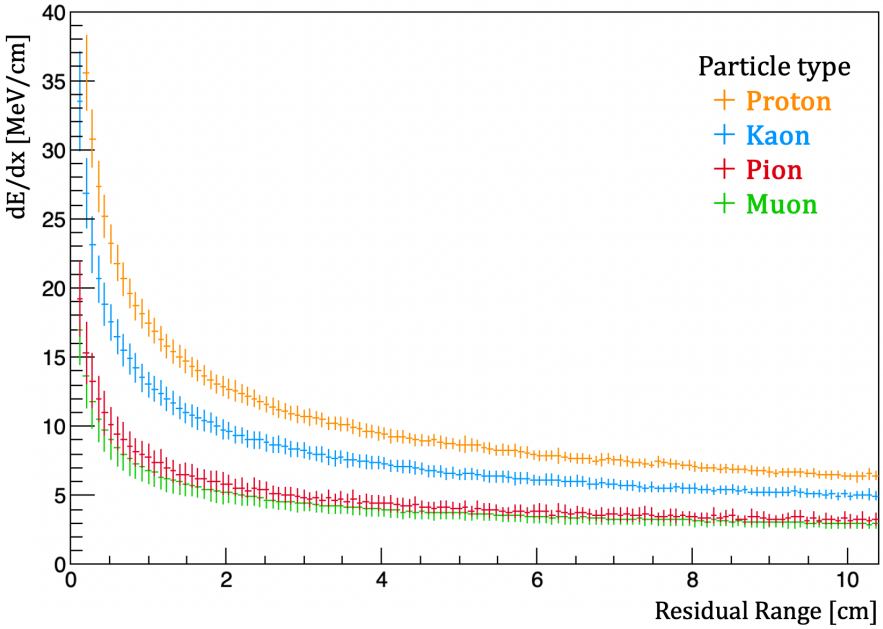


Figure 5.14: Theoretical distributions of the mean $dE/dx$ values with respect to the residual ranges for different types of particles. The estimated resolution for each residual range bin is also shown as an error band. These curves are the ones used to compute the $\chi^2$ for particle identification in ICARUS.

Figure 5.14 shows the theoretical curves representing the mean values of $dE/dx$ with respect to the residual range of different particle types in argon. Even if only the last 10 cm are shown, ICARUS uses the last 25 cm to compute the $\chi^2$, or the full length if the track is shorter. It is important to notice that this procedure relies on the characteristic Bragg peak of each particle, thus if a particle scatters, instead of stopping, it does not produce the Bragg peak and the identification power is lost. This discrimination power is also reduced when the reconstruction fails to identify the entire track, losing some hits, especially at its end point.

### 5.5.5 Particle momentum from range

Eq. 5.6 describes the relation between particle momentum and mean energy loss. The equation might be integrated to find the total (or partial) continuous slowing down approximation (CSDA) range $R$ for a particle which losses energy only through ionization and atomic excitation [162].

$$\Delta R = \int_{E_0}^{E_f} \left[\frac{dE}{dx}\right]^{-1} dE \,, \tag{5.16}$$

where $E_0$ is sufficiently small that the result is insensitive to its exact value. The CSDA range is a useful quantity as it relates the distance traveled by a particle in a medium with its momentum ($p$), or kinetic energy ($K$). Tables of stopping power contributions and CSDA ranges can be found in Ref. [162] for a selection of elements and kinetic energies in the range of 10 MeV to 100 TeV. In particular the muon range-momentum in LAr is taken from there. To interpolate the kinetic energy for all ranges, a cubic spline[9] is used. On the other hand, proton range-momentum tables are taken from NIST Standard Reference Database [163]. In this case, the

[9] A spline interpolation is a form of interpolation where the interpolant is a special type of piecewise polynomial called a spline. That is, instead of fitting a single, high-degree polynomial to all of the values at once, spline

proton interpolation is done using a $a + x^b$ function for proton ranges below 80 cm and a sixth order polynomial for bigger ranges. Muon calculation is valid up to $1.91 \times 10^4$ cm range, corresponding to a muon of kinetic energy $K \sim 40$ GeV. The calculation for protons is accurate up to $3.02 \times 10^3$ cm range, corresponding to $K \sim 5$ GeV.

To summarize, when a particle stops inside the detector, the range is measured and converted to kinetic energy using the lookup tables. Finally the momentum is obtained through the following expression $p = \sqrt{K^2 + 2KM}$. The equivalence between range and momentum for muons and protons is shown in Figure 5.15. For exiting particles, the most common approach is the momentum measurement via the Multiple Coulomb Scattering. Nevertheless, all studies that will be presented in this work use contained particles and range based momentum calculations from the CSDA approximation.

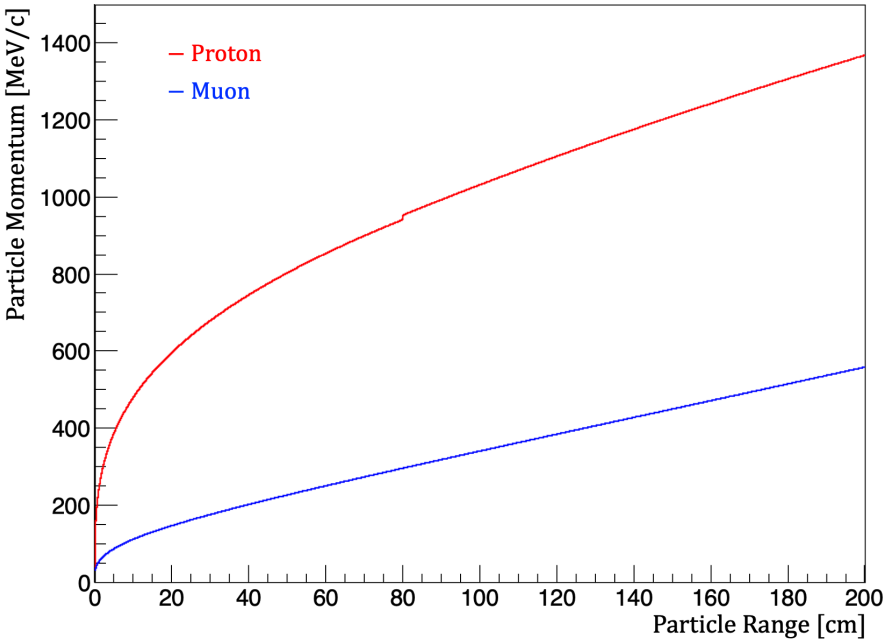


Figure 5.15: Track momentum values for protons and muons as a function of their range. Values extrapolated from different lookup tables.

## 5.6 ICARUS Monte Carlo Simulation

The event simulation in ICARUS is performed with LArSoft, a set of software tools for simulating, reconstructing and analysing events in liquid argon neutrino experiments. This approach is shared across the SBN program, where each detector has a configurable geometry allowing detector-independent developments at every stage of event processing. The simulation in LArSoft can be divided in few consecutive steps. First, particle fluxes are simulated to produce the expected distribution on desired species such as cosmic rays, neutrinos or individual particles, for instance the creation of only muons. These are usually based on Monte Carlo (MC) generators which use random numbers to sample from the expected interaction kinematic distributions and final state particles according to cross section models. Then, the generated particles are propagated to the detector and their interactions with argon nuclei simulated to obtain an expectation for the final state particles and their kinematics. The propagation of these particles and their secondaries through the different materials that make up the detector follows.

interpolation fits low-degree polynomials to small subsets of the values. In this case polynomials of exactly degree 3 are used.

Note that neutrino simulation is different from the rest generated particles in terms of flux and cross section. External particles entering the detector and the products of a neutrino interaction share the same propagation and detection simulation phases.

The final step that brings the simulation to the same point as the collected raw data is the detector simulation response, in terms of the CRT, PMT and TPC signals. After this stage, the same reconstruction algorithms that were applied to the data, are used to process simulated events. This is shown schematically in Figure 5.16.

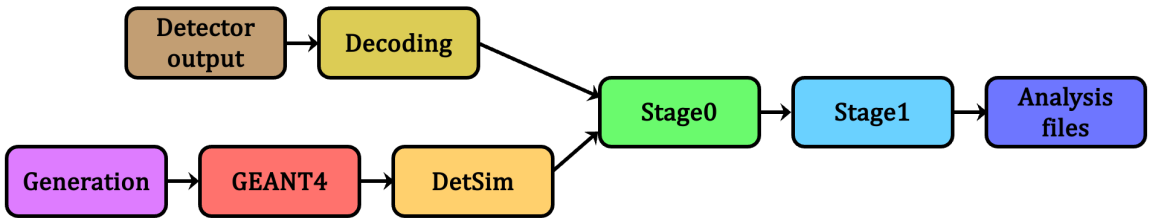


Figure 5.16: Complete reconstruction workflow of data and simulated events in ICARUS.

Only BNB neutrinos and cosmic rays simulations have been used in this work, thus the description of how ICARUS produces simulated samples will focus on them. However, the procedure is analogous to simulating NuMI samples, since the only difference lies in the simulation of the neutrino flux.

### Cosmic Flux Modeling

As a surface detector, an accurate prediction of the cosmic ray background present in the detector volume is crucial. Even though there are plans to exploit cosmic ray data to subtract the cosmogenic background activity, simulated cosmic rays have been used throughout this work. As briefly described in p. 74, ICARUS uses CORSIKA to generate cosmogenic events, which simulates air showers created from high-energy cosmic particles based on the magnetic field components for a given geographic location. ICARUS utilizes the proton-only model, where only primary cosmic protons are assumed to contribute to the Earth's cosmic ray flux. Cosmic primaries are sampled from a pregenerated CORSIKA library uniformly distributed on top of the cryostats, covering an extended surface of 12 m on each cryostat side (for a total of $\sim$ 1400 $m^2$). Only particles whose trajectory crosses the "buffer box", encapsulating the cryostats with some buffer around each side of the cryostat (3 m, 6 m and 5 m in the vertical, beam and drift direction respectively) are considered for simulation. Each particle with kinetic $E_K \geq 50$ MeV is then extrapolated back to a surface placed 20 m above the center of the TPCs and fed as input to the MC simulation, which will propagate the particles and its secondaries through the experimental setup.

### Neutrino Flux Modeling

SBN neutrino flux predictions are modelled using a data-driven MC, tuned to the characteristics of the BNB beam and external hadron-production measurements (see Section 3).

The flux simulation begins with a detailed beam line geometry description and a simulation of the protons produced by the Linac. The interactions between the protons and the Beryllium target are modeled using a combination of existing GEANT4 [142] models and those tuned to external data to describe all possible scattering processes. These generate hadronic interactions in the target and surrounding area, where the proton beam first interact and produces the majority of secondary particles. All secondary particles produced in the collision, including the scattered primary protons, are propagated using GEANT4 until they decay producing neutrinos or are stopped, in particular at the beam dump. Neutrino trajectories are extrapolated to the

ICARUS detector position to obtain the predicted neutrino fluxes and energy spectra, as it was shown in Figure 3.5.

Flux simulation is not repeated at every MC production, but rather fluxes shown in Figure 3.5 are stored in files that are used as input to the next stage, and are regenerated only when neutrino fluxes need some modifications.

### Neutrino Interaction Simulation

Once the simulated neutrinos travel toward the detector, it is necessary to determine which of them will interact within the active volume of ICARUS to successively characterize the $\nu$-Ar interactions. In ICARUS these are simulated using the GENIE[10] neutrino event generator [164], which has been broadly used inside the neutrino experiment community. GENIE is an open-source product, primarily built for MC generation of neutrino interactions with varying nuclear structures over a wide spectrum of energies ranging from 1 MeV to 1 PeV. This provides an state-of-the-art modeling of neutrino-nucleus interactions using a combination of nuclear physics, cross section, hadronization and hadron transport models tuned to neutrino scattering data available[11].

To precise infer oscillation parameters in a neutrino experiment, it is mandatory to measure the neutrino energy on an event-by-event basis. Hence it is worth mentioning few important aspects of how MC simulations deal with nuclear physics relevant to neutrino-nucleus scattering at few-GeV energies. In most experimental contexts, such as LAr experiments, the struck nucleon resides inside a nucleus and therefore cannot be modelled as a free particle. In these cases, especially when the struck nucleon lives in a crowded nucleus, the so-called "nuclear effects" need to be accounted for when modeling neutrino interactions. These include Fermi motion, nuclear binding, Pauli blocking and many-body scattering mechanisms including long- and short-range nucleon-nucleon correlations, among others.

The starting point for many nuclear models is the Global Fermi Gas (GFG) model [165], in which nucleons are allowed to move freely in a constant binding potential while obeying the Pauli exclusion principle. As a result, nucleons might reside in energy levels in which they have non-zero momentum even at 0 $K$ temperatures. This is known as the *Fermi motion* of nucleons and the energy of the last occupied level at $T = 0$ $K$ defines the so-called *Fermi momentum*, $p_F$. In view of this, the possible states that an excited nucleon may occupy following an interaction are limited to those with $p > p_F$. This is known as *Pauli blocking* and has an impact on the interaction cross-section.

This simple mean field model is able to give reasonable prediction at QE kinematics, but it only contains statistical correlations between nucleons from the exclusion principle. At present, nuclear ground state is represented by a spectral function which describes the probability that a nucleon involved in a neutrino-nucleus interaction will have a certain initial momentum and removal energy. GENIE v2 had the initial nucleon momentum sampled according to the Relativistic Fermi Gas (RFG) treatment of Bodek and Ritchie [166]. This version has non-interacting nucleons up to the Fermi momentum, determined from inclusive electron scattering. In addition, an isotope-specific removal energy is used and the Pauli blocking is implemented by requiring the final-state nucleon momentum to exceed $p_F$. An alternative nuclear physics model introduced in GENIE v3, is the Local Fermi Gas (LFG) model [167], which defines the Fermi momentum as a function of radius, obtained from the nucleon number density: $p_F = (3\pi^2\rho(r)/2)^{1/3}$. A further variation of the LFG model is the so called Correlated Fermi Gas (CFG) which accounts for nucleon-nucleon interactions inside the medium, introducing a high-momentum tail above $p_F$. The momentum distribution predicted by each of the three models of the nuclear ground state

[10] GENIE stands for Generates Events for Neutrino Interaction Experiments.

[11] The hadronization model describes particle production from free targets. Hadrons produced in the nuclear environment might rescatter on their way out of the nucleus (hadron transport), and these reinteractions significantly modify the observable distributions in most detectors.

is shown in Figure 5.17 left. Last GENIE version v3.4, which is the one used to produce the simulated samples used in this work, introduces a further improvement, allowing the binding energy to be a function of the nucleon momentum, as shown in Figure 5.17 right.

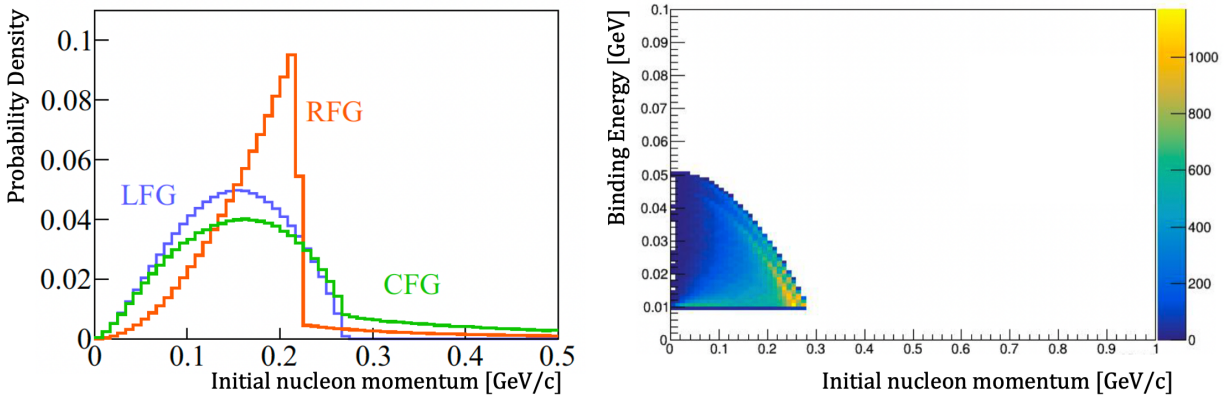


Figure 5.17: Left: Initial nucleon momentum distributions according to GENIE implementation of relativistic, local and correlated Fermi Gas models, from Ref. [168]. Right: Nucleon removal energy as a function of the initial nucleon momentum, currently used in GENIE v3.4, from Ref. [169].

The result of this step of the simulation is a neutrino interaction in the ICARUS detector that produces a set of final state particles with their corresponding kinematics, creating a `MCNeutrino` object in LArSoft. These particles are input into the next step for particle propagation.

### Particle Propagation Simulation

The particle propagation step relies on GEANT4 to fully simulate the chain of daughter particles resulting from the interaction with liquid argon[12], either of neutrino or cosmic origin. Each daughter particle is tracked when traversing the LAr and their energy deposits at each step recorded. The simulated geometry of detector is described by GDML files (Geometry Description Markup Language). These include the full description of the detector and its surroundings, such as the internal composition of the TPC, the cryostat, the field cage, the CRT and the experimental hall.

The energy deposition of each particle is converted to ionization electrons and scintillation photons. A fraction of ionization electrons undergo recombination[13], while the remaining ones are drifted towards the wire planes. The number of ionization charge is further reduced due to impurities in the LAr, which is commonly parameterized as the electron lifetime. Diffusion smearing, either transverse or longitudinal, can also be implemented to smear the arrival time or detection location of the electrons, respectively. A `SimChannel` object is created to store the information about the electrons deposited on one TPC readout channel with all the previous mitigations, as function of time, and connected to the generated particle which produced them.

A minimum ionising particle has an approximate average energy loss of 2.12 MeV/cm. It takes 23.6 eV to create an electron-ion pair and 19.5 eV to emit a photon in LAr at nominal 500 V/cm drift field. This implies that tens of thousands of electrons and photons need to be tracked in the simulation for each cm of charged-particle track. Each photon undergoes simulation of Rayleigh scattering with the argon and reflections on the surfaces within the

[12]The detector simulation propagates particles through the detector in intervals of "steps". In GEANT4, a step is normally defined by $\sim$ 1/10th of the wire spacing in the planes of the TPC in order to process the energy deposited by each step into electron clusters.

[13]The recombination model can be chosen during the set up of the simulation, at the moment ICARUS uses the modified Box model presented in Subsection 5.5.4

detector, eventually being absorbed either by the active surface of an optical detector or by any other inactive surface. The "full" simulation, by means of GEANT4, tracks the path of every photon until their absorption. This method is extremely computationally expensive, hence an alternative procedure called "fast" optical simulation uses a photon visibility library that preserves the accuracy of signal prediction while maintaining a reasonable computation time. The parametrization used gives the probability for a scintillation photon produced at a certain location, to reach the sensitive surface of the optical detector assuming an isotropic emission. Photons reaching the optical detector surface are reduced by a conversion efficiency, which in ICARUS corresponds to the PMT quantum efficiency and was measured to be 12.1 ± 1.0% [170]. Figure 5.18 shows an example of the scintillation photon visibility in ICARUS for points 5 cm away from the anode plane. At each location, the total visibility is computed, that being the fraction of scintillation photons isotropically generated at that point which reaches any of the 180 PMTs of the cryostat. Obviously, the total visibility decreases as position moves towards the cathode.

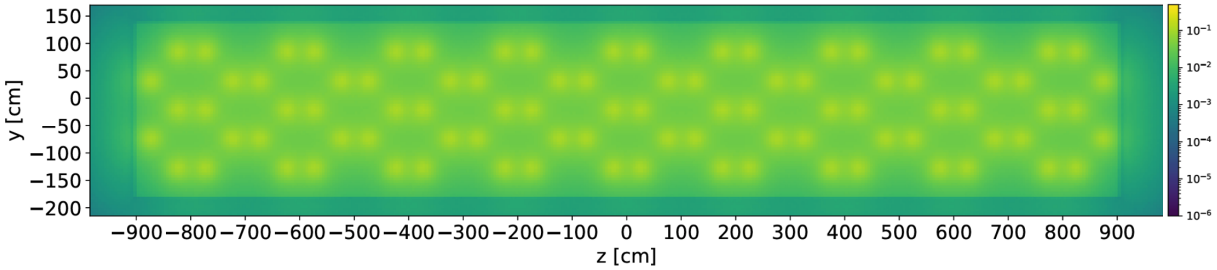


Figure 5.18: Visibility map for points located in a parallel plane 5 cm away from the anode wires. The maximum visibility spots match the locations of the PMTs. The total visibility ranges from 0 to 10%, where the decrease in photons observed outside the active volume is due to the presence of the field cage. Image courtesy of A. Manegolli and G. Petrillo.

With each energy deposition of a specific particle, the amount of light from that position can be read from the photon library and converted into the number of photons produced at the deposition point, without the need of tracking all of them. The photon visibility library takes into account the characteristic time profile of the scintillation light, dividing the photons into two components, one decaying with the "fast" process ($\tau_{fast} \approx 6$ ns) and the other one with the "slow" process ($\tau_{slow} \approx 1.6$ $\mu$s). It also considers the light propagation time from the generation point to the optical detector surface, accounting for possible Rayleigh scattering and reflections with surrounding materials. At this point, the optical detector has a time distribution of the scintillation photons that would produce a signal in it. A `SimPhoton` object is generated containing the information of all photons reaching one optical detector readout channel.

CRT panels are external to the TPC, hence they need a special treatment as simulated light and charge is only run within the TPC volume. LArSoft supports the creation of auxiliary detectors if properly included in the GDML geometry, allowing an extension of the GEANT4 simulation. GEANT4 determines the positions and energy deposits of charged particles in each piece of plastic scintillator which are stored in an `AuxDetSimChannel` object.

The final output of the particle propagation step is a list of particles created either by an event generator (GENIE, Corsika) or by the detector simulation (GEANT4), which includes their timing information, complete trajectories and energy deposits along them.

`SimChannel`, `SimPhotons` and `AuxDetSimChannel` objects will be convoluted with electronic and detector effects or input to the optical detector and readout simulation, to produce the predicted signal that the detector would see if the reconstruction were perfect.

### Detector Response Simulation

The simulation of the detector response has to be properly addressed for each detector subsystem. All of them use simulation packages interfaced with LArSoft.

The ionization charge amount and arrival time at each wire (`SimChannels`) is used as the input to the TPC detector response simulation. The true charge arrival times are convoluted with the field response simulated via the GARFIELD program [171] to obtain TPC wire waveforms. The simulation considers the nominal ICARUS wire plane configuration. The field response describes the shaping of the signal generated by a sense wire due to a drifting charge, being upstream of any electronic effect. The current field responses are calculated using a 1D simulation, that is considering a single wire and without taking into account the induced charge effects of electrons traveling in regions close to the sense wire. At the time of writing ICARUS is working to implement a 2D field response with a range of 10 wires on either side of a given wire. Even though it is independent of the position along the wire direction itself, it is meant to serve as a good approximation of a more realistic 3D field response. The application of the electronic response (modeling the shaping and amplification of the front-end electronics) and simulated noise follow. The noise waveform is simulated for each TPC channel using a data-driven approach and is the sum of intrinsic and coherent noise, individually. Finally, the resulting waveform is quantized according to a given sampling rate, resolution and dynamic voltage range to mimic electronic digitization and obtain an ADC waveform. This simulation output is then appropriate for use in event reconstruction.

For the light collection system, the information on the number and timing of photons (`SimPhotons`) is used to build the simulated waveform at each PMT channel. The PMT simulation includes digitization of light signals, which selects photoelectrons (PE) arriving in a simulated window of 2 ms, to collect light produced during the electrons drift time. The PEs are binned in arrival time (2 ns) and the digitized single photoelectron response (SPR) computed. This is done by associating a SPR to each simulated photon (converted to PE), shifted in time according to its corresponding arrival time. The obtained SPR are progressively added to the total response. The initial modeling of PMT signal formation and digitization was build upon experience from CERN test stand data [172], and has evolved to a more data-driven approach. The total response is smeared to account for gain fluctuations and superimposed to a baseline of 14999.5 ADC. The electronic and dark noise are added to the final waveform before being stored in 14 bit. An example of how the final PMT waveform is progressively built by adding incoming PE is shown in Figure 5.19. As described in Subsection 4.2.1 there is a discrimination threshold to activate the trigger logic request, previous studies showed that a $\sim 390$ ADC threshold was effective in rejecting background events, thus the black line represents this discrimination threshold corresponding to 13 PE or $\sim 49$ mV. Nonetheless, it is worth pointing out that this is just for illustration and that no trigger emulation is presently implemented in the ICARUS simulation chain.

The task of the CRT detector simulation is to convert the deposited energy in the scintillator strips (`AuxDetSimChannel`) into an analog SiPM signal. The light production in the scintillator implemented in ICARUS follows an empirical model developed from measurements of the detector response, which involves the intrinsic light yield and light attenuations. This signal is then injected into the detector readout simulation, reproducing the front-end electronics, which include the subdetector gain and minimum thresholds, charge resolution, time stamp generation and trigger logic. When a trigger occurs, the number of detected PEs is output along with a single timestamp corresponding to the moment the trigger pulse crosses the discrimination threshold. More details can be found in Ref. [173]

Gathering together the output of the three subsystems, it is possible to run the same reconstruction algorithms that were described for real data.

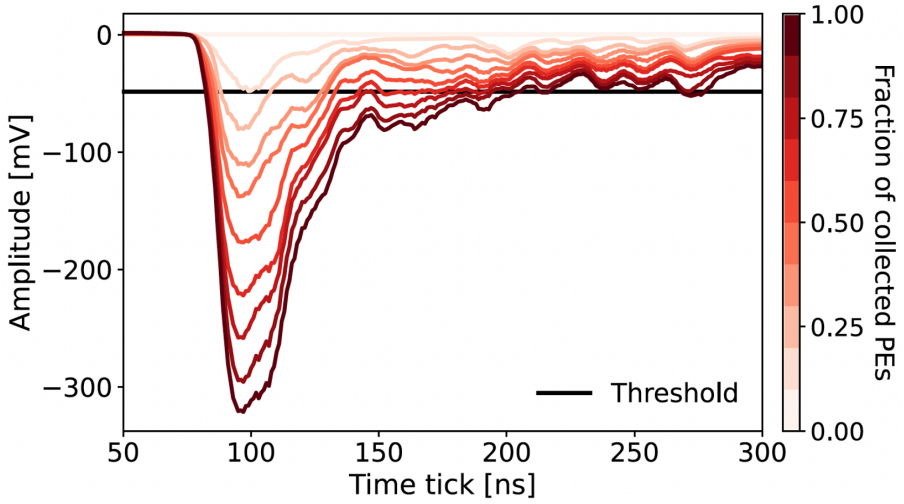


Figure 5.19: Example of how the final waveform of a single PMT is build as photoelectrons are considered. Waveforms below threshold are not considered in the simulation. Image from Ref. [146]

#### Reconstruction - Truth matching

In order to assess the performance of the TPC reconstruction algorithms used in this thesis, the association between the truth information on the generated particles and the corresponding reconstructed objects was exploited. These associations are based on the amount of hits shared between the generated and reconstructed particles[14]. Each reconstructed 2D hit is matched to a simulated particle responsible for the largest deposit of energy in the region of space and time covered by the hit. From the hit level it is therefore possible to connect reconstructed objects with a known purity and completeness back to simulated neutrino interaction products. If *nShared* is the number of shared hits between a simulated and a reconstructed particle, the purity for each object is defined as the ratio between *nShared* and the total number of reconstructed hits, while the completeness is computed as *nShared* divided by the total number of simulated hits. Single reconstructed particles might contain hits from multiple true particles, either because a few hits are incorrectly assign in regions where several true particles meet, or due to poor reconstruction performance merging together pieces of two independent interactions. Each reconstructed particle has a list of associations to true particles ordered from highest to lowest energy contribution. However, for the validation of the analysis carried out in this work, the best match corresponding to the first entry in that list has always been used.

## 5.7 Neutrino energy reconstruction

Several approaches can be employed to obtain the reconstructed neutrino energy, such as calorimetry or momentum based methods. Two different momentum based methods have been used here to reconstruct the neutrino energy, with special attention to events with a single muon and a single proton as final state particles.

In a neutrino-nuclei collision, if the momentum and energy transferred to the hadronic system is large enough the impulse approximation can be used. This assumes an interaction with an individual (bound and moving) nucleon, and the QE hypothesis remains valid. The notion of charged-current QE-like events was introduced to define primary interactions on a bound nucleon followed by hadron rescattering (final-state interactions, FSI). Thus, CCQE-like samples

[14] Here reconstructed does not involve real data at all, it just means the reconstructed variables after the pattern recognition algorithms are applied to simulated charge depositions.

of events contain also those in which a real pion is first produced and then absorbed, or those arising from a two-nucleon knockout. In view of this, true CCQE events might occasionally produce pions through FSI and thus not be classified as CCQE-like.

The first method to estimate the neutrino energy of CCQE-like $1\mu 1$p events is based on the reconstructed momentum of the final particles. In such case, the energy is defined as

$$E_\nu = E_\mu + E_p - M_{\text{nucleon}} \ , \tag{5.17}$$

where the $E_\mu$ and $E_p$ are calculated from the measured range based momentum through the following formula: $E = \sqrt{p^2 + M^2}$. This assumes a quasi-elastic interaction and a struck nucleon ($M_{\text{nucleon}}$) at rest.

If a CCQE-like interaction has no final-state interactions a more accurate description is possible. Energy and momentum conservation allow to resolve the kinematics of the process completely and calculate the initial neutrino and neutron momenta, as presented in Ref. [174].

The model assumes a CCQE interaction on a nucleon inside a nucleus, where only one nucleon is knocked out and detected together with a final state muon. If the target nucleus is at rest, the energy and momentum conservation read:

$$E_\nu = M(A) + E'_\mu + E'_p + E'_{A-1} \ , \tag{5.18}$$

$$\vec{k}_\nu = \vec{k'}_\mu + \vec{k'}_p + \vec{p'}_{A-1} \ , \tag{5.19}$$

where $(E_\nu, \vec{k}_\nu)$ and $(E'_\mu, \vec{k'}_\mu)$ are the neutrino and muon four-momenta, $M(A)$ is the mass of the target nucleus of atomic number A, and $(E'_{A-1}, \vec{p'}_{A-1})$ and $(E'_p, \vec{k'}_p)$ the final state nucleus and nucleon four-momenta, respectively. Everything related to final particles of the interaction will be marked with an apostrophe for clarification. In the impulse approximation picture, the interaction occurs on a nucleon with initial momentum $\vec{p}$, which should cancel out with the final state nucleus momentum $\vec{p}_{A-1}$, if no final interactions took place. Decomposing the momentum into parallel (L) and perpendicular (T) components with respect to the neutrino direction, Eq. 5.19 can be rewritten as:

$$E_\nu = {k'}_{\mu_L} + {k'}_{p_L} - p_{p_L} \ , \tag{5.20}$$

$$0 = {k'}_{\mu_T} + {k'}_{p_T} - p_{p_T} \ , \tag{5.21}$$

where now the initial nucleon momentum is also present. The final state nucleus is in general an excited state of invariant mass $M^*(A-1)$.

If final state muon and proton momenta are measured, the transverse momenta of the struck nucleon ($p_{p_T}$) can be straight forward computed from the last equation. The remaining two expressions form a system of two equations with two unknowns, which can be easily solved. The results are:

$$p_{p_L} = \frac{R}{2} - \frac{[M^*(A-1)]^2 + p_{pT}^2}{2R} \ , \tag{5.22}$$

where

$$R = M(A) + {k'}_{\mu_L} + {k'}_{p_L} - E'_\mu - E'_p \ .$$

Allowing to compute the neutrino energy with Eq. 5.20. The mass of the initial nucleus can be calculated from

$$M(A) = 22 M_{\text{neutron}} + 18 M_{\text{proton}} - 343.81 MeV \ ,$$

where the last term corresponds to the binding energy of argon in the ground state. The final excited state invariant mass is given by

$$M^*(A-1) = M(A) - M_{\text{neutron}} + E_b \ ,$$

where $E_b$ is the neutron separation energy. This can be modeled by a probability distribution function using information about neutron occupancy in Ar nucleus. However, and given the present MC neutrino generators implementations, it was chosen to use the mean excitation energy in the Bodek-Ritchie formalism reported in Ref. [175]. This corresponds to 21.8 MeV in case of neutrino-neutron interaction.

## 5.8 CAF files and Calibration Ntuples

At the end of `Stage1`, events are ultimately reconstructed and output into `ROOT TTree` files suitable as input to analysis.

ICARUS has adopted two different approaches, producing two different formats of analysis files from the `Stage1` output. The first one is created automatically after the `Stage1` and are the so called `Calibration Ntuples`. These are regular ROOT files containing useful information from the detector reconstruction, for all the CRT, PMT and TPC subsystems. `Calibration Ntuples` were envisioned as the main input for all types of calibration studies, hence none of the aforementioned charge scale corrections are applied at their production, nor correction to the CRT or PMT subsystems. In addition since most of the calibration studies are performed exploiting track like events, only certain tracks from the reconstruction are saved in the `Calibration Ntuples`. These are the subsample of tracks with a defined $t_0$, namely tracks crossing the cathode. The TTree that deals with all the available information contains an entry for each reconstructed track with track-level, hit-level and truth-level (only for simulated MC events) information. Hit-level variables are stored for each plane containing information about all hits on each track, allowing an in-depth study of TPC events. The PMT stored information contains all `OpHits` recorded and all `OpFlashes` created, where the defined TTree structure allows to obtain global information of the `OpFlashes` while at the same time providing a list of its constituent `OpHits`. CRT information is analogously saved for all CRT `Hits`, including their geometrical and temporal details about the fired CRT slab.

The information stored for the three subsystems contains all the necessary input to perform all types of calibration studies.

On the other hand, the second analysis file is in the form of `CAF` files, which stands for "Common Analysis Framework". These are created with the `Stage1` output and are reduced analysis ROOT TTree files. They retain all the useful information required to do a high-level analysis while dropping the heavy data products like raw digits, wire responses or all hit information to make the files small and fast to process. Another big difference with the `Calibration Ntuples` is that `CAFs` preserve the hierarchical structure that is inherited from Pandora (f.i. the slice object). `CAFs` consist of a series of branches containing different type of information as defined in Ref. [176], including the three detector subsystems, where each entry in the branch corresponds to one detector readout. The `CAF` data files include the charge scale corrections, as well as the energy scale calibration. Each of the three equalizations are derived from separate calibration database files, which are continually updated based on detector conditions.

The main analysis performed in this thesis has been carried out using `CAF` files. They were used to perform event selection analysis and to develop an automatic selection procedure to identify events containing a single muon and a single proton, as will be detailed in Chapter 6.

Nonetheless, `Calibration Ntuples` were employed for additional calibration studies to address a first phase of TPC wire equalization, to study the planarity of the cathode in each cryostat and lastly, to define containment conditions taking into account the present space charge effects seen in ICARUS, as described in Appendix A.

# Chapter 6

# Neutrino event selection

The Short Baseline Neutrino program should clarify the question of sterile neutrinos exploiting the Booster Neutrino Beam by comparing the neutrino interactions observed at different distances along the beam by ICARUS and SBND. As seen in Chapter 3, both $\nu_e$ appearance and $\nu_\mu$ disappearance channels can be observed at the same time, with the same neutrino beam and detectors. While the near detector of SBN is getting ready to be online and join the common effort, ICARUS-standalone phase is addressed to test the exciting and recent results of the Neutrino-4 experiment [77]. ICARUS has been taking data with both BNB and NuMI beams with the goal of assessing the Neutrino-4 oscillation hypothesis in the same baseline over energy range (L/E $\sim$ 1-3 m/MeV), but collecting $\sim$ hundred times more energetic events.

Presently, the $\nu_e$ disappearance channel is being addressed with neutrino events collected by the NuMI beam, in particular selecting contained electro-magnetic showers (EM) from quasi-elastic $\nu_e$CC interactions. An example of $\nu_e$CC QE candidate fully contained in the active LAr and collected with NuMI beam is shown in Figure 6.1. There is an electron shower (along the direction of the wires) with a deposited energy around 600 MeV and an upward-going hadron track of 43 cm length.

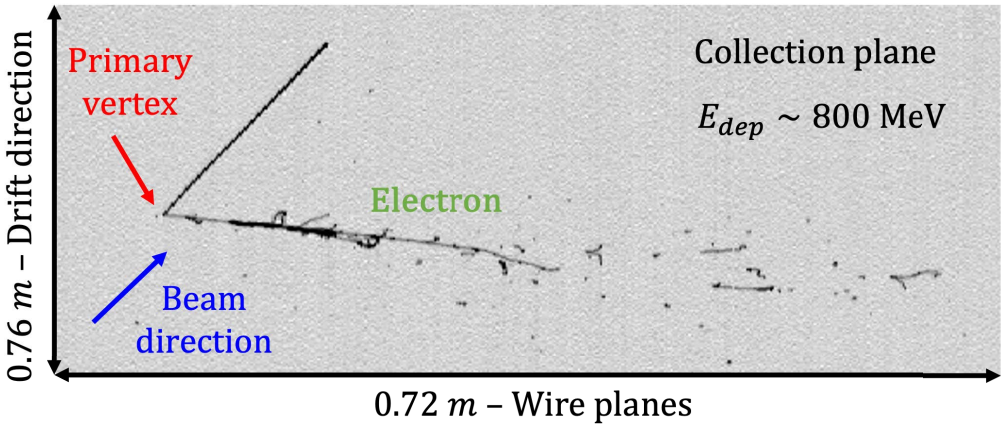


Figure 6.1: A visually selected $\nu_e$CC candidate collected with the NuMI beam. There is an electron shower and an hadron candidate, with a total $E_{dep}$ around 800 MeV.

The LArTPC technology presents a unique electron-photon discrimination, hence the $\nu_e$ CC candidates are required to have a clearly connected EM shower to the primary vertex and initial $dE/dx$ of the shower compatible with a mip, to remove $\pi^0$ backgrounds.

On the other hand, the $\nu_\mu$ disappearance channel is being studied with neutrino events collected with the BNB, focusing on quasi-elastic $\nu_\mu$CC interactions fully contained. These are required to have a single muon and at least a proton existing from the same interaction vertex

and with all tracks stopping inside the active LAr. An example of $\nu_\mu$CC QE candidate collected with BNB beam is shown in Figure 6.2, where there is a 2.3 m long muon crossing the cathode and stopping inside the adjacent TPC, and a proton track of almost 8 cm. The whole event deposits around 620 MeV of energy.

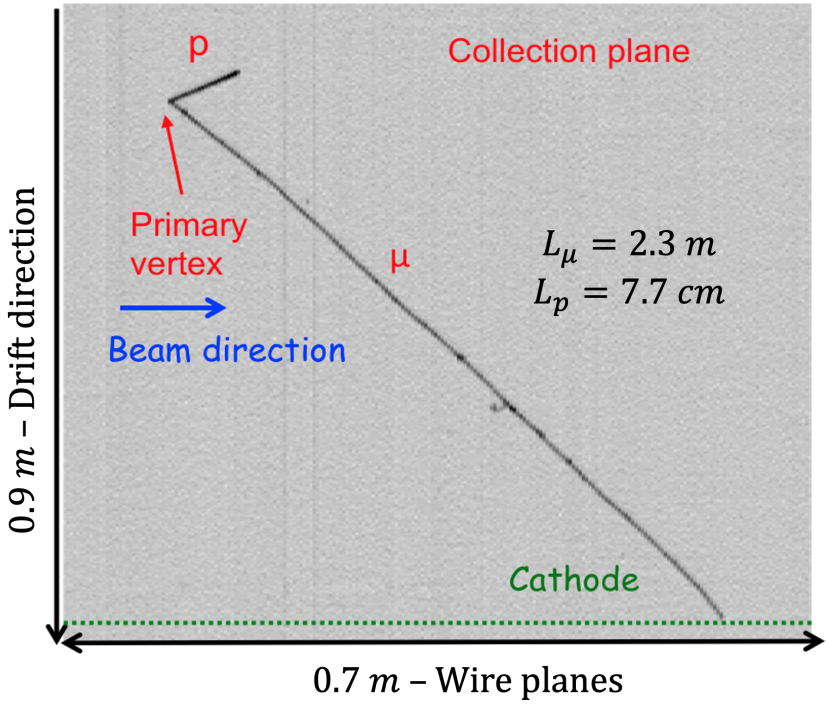


Figure 6.2: $\nu_\mu$CC QE candidate collected with the BNB beam. The event has a muon and proton candidates, which can be distinguish based on their ionization and length. Along the muon track it is possible to see some delta rays as small blobs or ramifications.

The goals of the analysis, and hence also of this work, are three. The first one is to validate the performance of event reconstruction and particle identification tools as these should allow to correctly reconstruct the events and unambiguously recognize stopping muons and protons. The second one focuses on the evaluation of the kinematic reconstruction capability of the events in the transverse plane, as transverse variables are used as proxy variables for event interpretation and energy resolution. Last but not least, and due to the amount of data to analyze, an automatic procedure to select signal events while rejecting cosmic rays is mandatory to handle the large statistics.

## 6.1 Visual scanning effort

A dedicated visual study of events was perform to select a sample of $\nu_\mu$CC interactions from BNB in the active liquid argon, to allow validating the performance of the Pandora reconstruction.

A group of approximately 30 people, of which I was part of, was trained to identify and classify neutrino interactions. Scanners identified the neutrino vertex, the end of the muon and when present, the end proton positions. To minimize possible errors, around 30% of the events were checked twice by different people, and all of them were validated by experts. A description was added for each event, including how many primary tracks were present in the interaction, if the event was contained or if there were signs of other particles, such as $\pi^0$.

It was shown in Ref. [97], that the most important background contribution to the $\nu_\mu$CC selection is due to neutral current charged pion production, where the $\pi^\pm$ can be mistaken for a $\mu^\pm$. Simulations showed that charged pion tracks produced in the BNB were in average short,

with most pions traveling less than half a meter in the liquid argon. It was then chosen to apply a simple cut requiring the muon candidates to be longer than 50 cm, to minimize the neutral current contamination in the $\nu_\mu$CC selection. Figure 6.3 left shows the small contribution ($\sim$ 2%) of neutral events after the length requirement towards an inclusive $\nu_\mu$CC selection, for simulated interactions. For this reason, the scan event effort was restricted to events with at least a track longer than 50 cm, the neutrino vertex inside the fiducial volume and only selecting fully contained interactions. The fiducial volume is defined as a restricted volume in terms of the ICARUS geometry (see Figure 6.3 right), where the detector performance is not affected by electric field distortions or these have a minimal impact. Hence, primary vertices inside the fiducial volume are required to be at least 25 cm apart from the lateral TPC active walls and 30/50 cm from the upstream/downstream active walls[1]. Instead, an event is fully contained if both the start and end points of the track are more than 5 cm away of the LAr active volume boundaries.

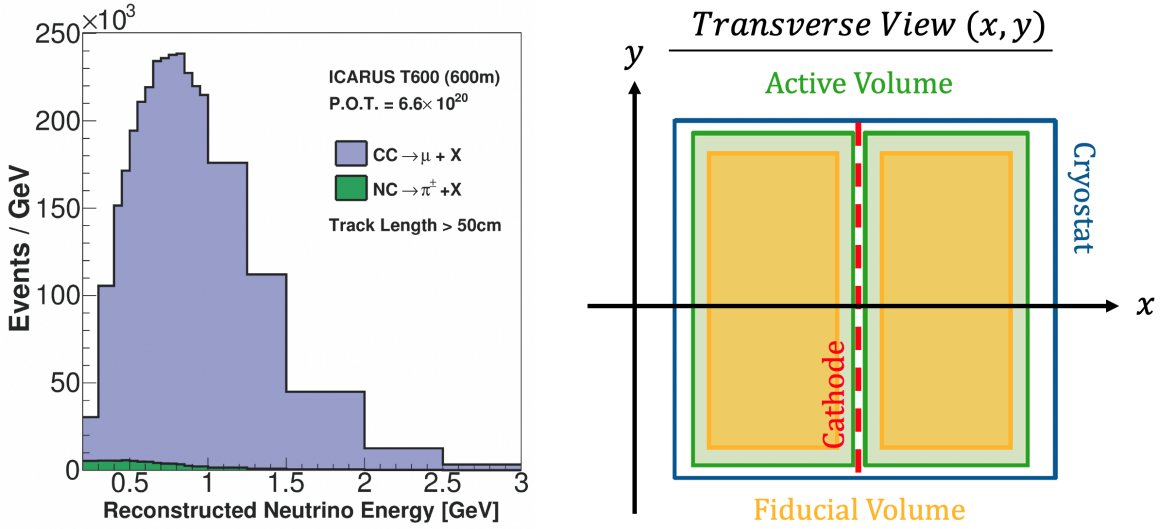


Figure 6.3: Left: Selected muon neutrino charged-current inclusive candidate events in ICARUS, as obtained in a Monte Carlo simulation. Final state muon tracks are required to have a length of at least 50 cm to minimize the neutral current contamination. Plot taken from Ref. [97]. Right: Sketch of ICARUS geometry for one cryostat, showing the active and fiducial volumes in the transverse plane.

With previous conditions, a sample of 518 $\nu_\mu$CC BNB events from a couple of runs lasting 85 h in total and without the overburden, were used to compare some manually and automatically selected variables. For this scanning effort, all the events associated to the trigger light and containing a track of at least 50 cm were checked. For each visually scanned event the 3D positions of the vertex, end muon and when present, the end proton were measured by the scanners and saved. Scanned values of each position were compared to the automatic reconstruction outputs and the events were classified accordingly. The scanning precision is of the order of mm, since the presence of signal at wire-per-wire level can be clearly distinguished.

A compatible events is defined as an event that has its reconstructed vertex within 15 cm from the scanned vertex position, and similarly for the end muon position, always within the 15 cm tolerance. 450 events were found with a compatible vertex, while 396 of them had also a good match in terms of the end muon position. Figure 6.4 shows the difference between the scanned and reconstructed vertex position in the drift direction (x axis), while the mean and

[1]Recall ICARUS has two identical modules with internal dimensions of 3.6×3.9×19.6 $m^3$ and containing $\sim$ 760 tons of LAr. Instead, the active volume, has a total mass of 476 tons and internal dimensions of 3.2×2.96×18.0 $m^3$ for each cryostat.

the standard deviation of the distribution are reported in Table 6.1, together with the obtained values for the other coordinates and end muon positions. It can be noticed that the more precise coordinate is the x, directly related to the drift time, while y and z are determined from the combination of the different projection with slightly worse resolution. For a general evaluation, the 3D distance between the automatic and scanned positions of the vertex and the end muon were also calculated, showing that in both cases almost 70% of the events coincide within 5 cm with the scanned values. The fraction of events decreases to 45% if a tighter cut is placed at 2 cm tolerance. Possible failures when identifying the neutrino vertex positions are its misplacement, either in the middle of a track or at the end of it or, less frequently, the total loss of the event.

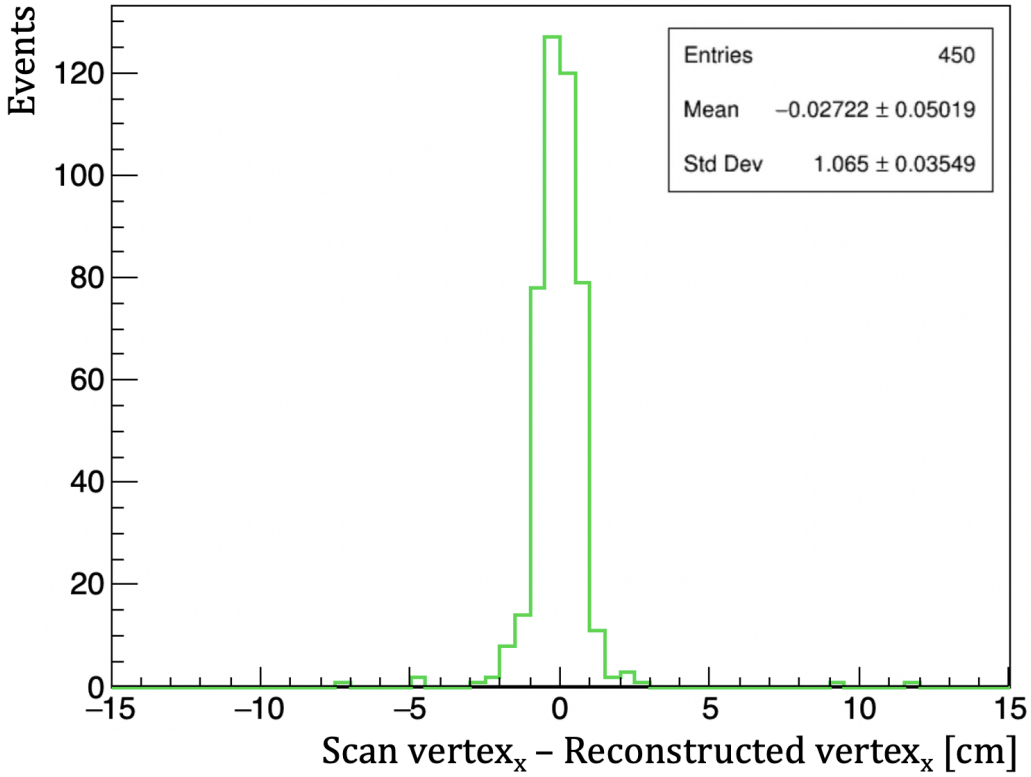


Figure 6.4: Distribution of the difference between the scanned and automatically reconstructed neutrino vertex x positions for the available scanned events. It was possible to identify 450 neutrinos events with a compatible vertex.

Another important quantity to check is the difference between the scanned and automatically reconstructed length of the muon, which gives a further evaluation of the quality of the reconstruction. Note that the scanned length is computed as the minimum distance between the scanned vertex and end muon positions, while the reconstructed one takes into account all the scattering and kinks that the particle might suffer. Even though it is expected that in most of the cases the muon track is essentially straight, for this comparison it was decided to define the reconstructed length as the straight distance between the reconstructed start and end points of a track. This definition allows both magnitudes to be compared in a sensible way.

In order to identify the muon candidate it was chosen to select the longest track whose reconstructed end muon position was within 15 cm from the scanned value. The events selected with this requirement were 396 and are shown in Figure 6.5 left. The figure shows in black the scanned muon length of each event, while the reconstructed length of the identified muon candidate is shown in red. Note that on average the red distribution is shifted towards smaller values due to different reconstruction problems, and even if all hand scanned events had a muon of at least 50 cm, there are some reconstructed values below that threshold. The most common

| Variable | Mean value [cm] | Standard deviation [cm] |
|---|---|---|
| $\Delta$Vertex$_x$ | -0.03±0.05 | 1.06±0.04 |
| $\Delta$Vertex$_y$ | -0.09±0.09 | 1.93±0.06 |
| $\Delta$Vertex$_z$ | -0.20±0.09 | 1.85±0.06 |
| $\Delta$End $\mu_x$ | 0.04±0.06 | 1.23±0.05 |
| $\Delta$End $\mu_y$ | -0.06±0.11 | 2.13±0.08 |
| $\Delta$End $\mu_z$ | -0.01±0.11 | 2.17±0.08 |

Table 6.1: Mean value and standard deviation for neutrino vertex and end muon positions of a sample of hand scanned neutrinos, providing an estimate precision of the reconstruction algorithms in real data events.

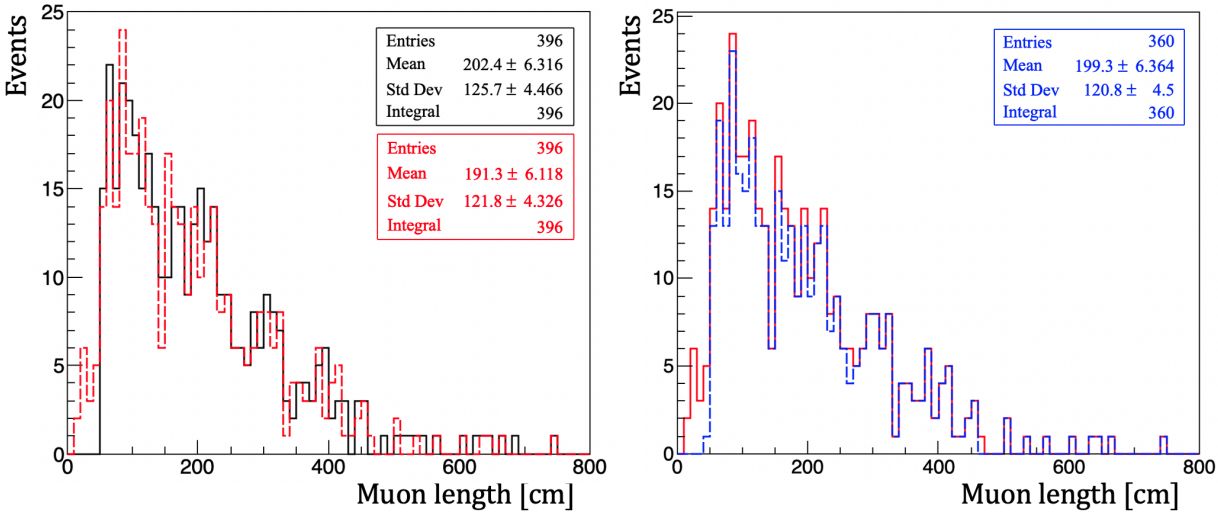


Figure 6.5: Muon length distribution for all events with a compatible vertex and end muon positions. Black histogram shows the muon scan length (left), while red histogram shows the longest track inside a certain slice whose end position is within 15 cm from the scanned value. To ensure the muon candidate is well reconstructed, the track is asked to start within 15 cm from the scanned vertex position. This further requirement identifies 360 events, which are shown in the blue histogram (right).

problem is related to long tracks that Pandora has reconstructed into more than one piece, for instance generating the loss of events at large muon lengths seen in Figure 6.5 left. This can happen under certain circumstances:

- A track crosses the cathode, Pandora needs to stitch the two adjacent segments to properly reconstruct the track. If no merging occurs, the entire track is split or not even assigned to the same interaction. As seen in Section A.3, the non planarity of the cathode might also reduce the efficiency of the stitching procedure.

- Induction 1 wires consist of two $\sim$ 9 m long segments, with few cm wide region around z=0 not read out and affected by a slight electric field distortion, causing further splitting if a track crosses that region.

- Kinks along the track due to particle scattering or reinteracting along its trajectory, for instance, at low energies, it is more probable that a particle scatters. If the reconstruction

interprets the change in direction is due to some new interaction, the track is broken, even though it could just be a scatter.

- Hit finding inefficiencies in one or more wire planes causing gaps on the reconstructed tracks. This could led to split tracks if the gap is large enough according to Pandora.

Another problem is when the reconstruction fails to associate some hits at the beginning or the end of a track, and hence it reconstructs a smaller object, contributing to the accumulation at low muon lengths as well. It was noticed that, with the solely requirements of compatible vertex and end muon positions, the selected muon candidate might be far away from the vertex. In order to avoid these cases, a further requirement was introduced. Figure 6.5 right, shows the same events, now with the requirement that its start muon position needs to be within 15 cm from the scanned vertex. This condition indirectly guarantees that the muon candidate has a length similar to the scanned one, since both the start and end reconstructed positions are bound within 15 cm from each reference point. This latter consequence is shown in Figure 6.6 left, where the reconstructed and scanned muon length are shown for the final selection of 360 events. Figure 6.6 right, shows the difference of these two quantities, where $\sim 96\%$ of the events have a discrepancy below 10 cm. The distribution shows two different populations: the ones with $L_{scan} > L_{reco}$ where the second piece of muon is missed by the reconstruction and hence the start or end positions are wrongly identified (within the 15 cm tolerance), and the ones with $L_{scan} < L_{reco}$ where the reconstruction adds a piece of some other particle, either a Michel electron or a track crossing the muon (f.i. a cosmic).

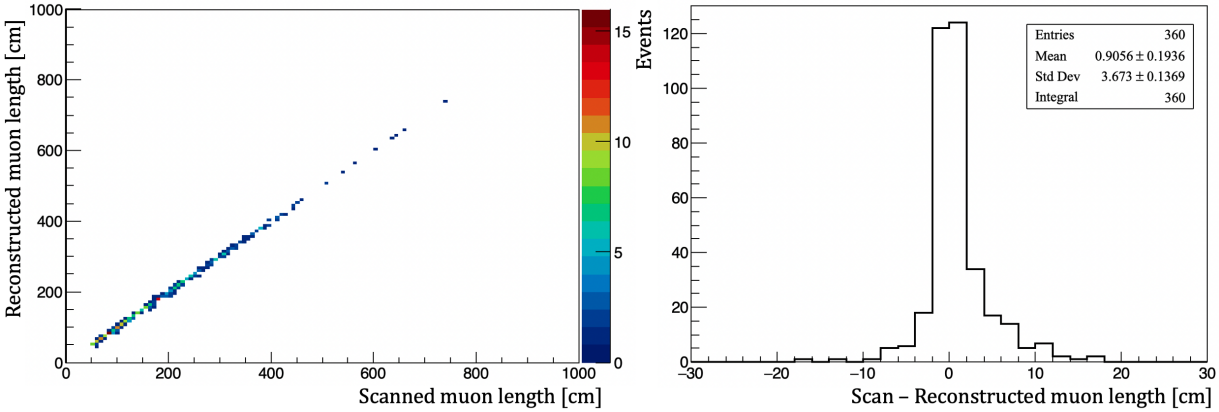


Figure 6.6: Length distributions for well reconstructed events, where all the neutrino vertex, end and start muon positions are within 15 cm from the scanned values (360 events). The left scatter plot, shows good agreement across all muon lengths, while the difference between scanned and reconstructed muon length is shown in the right, where $\sim 96\%$ of the events have a $|\Delta L| < 10$ cm.

ICARUS has different event displays available, allowing to visualize the raw digits or the reconstructed objects, which are especially useful when trying to identify the sources of reconstruction failures. Two pathological events, reflecting two of the most frequent problems in Pandora reconstruction, are shown below. In the first one both the vertex and end muon positions were identified within the 15 cm tolerance, however the scanned and reconstructed muon length differed by more than a meter, $\Delta L_{scan-reco} = 108$ cm. The event is a $\nu_\mu$CC interaction, producing a short proton and a muon, crossing the cathode and stopping inside the adjacent TPC (Figure 6.7 left). Pandora's event display is presented in Figure 6.7 right, where the reconstruction of the event is shown in the three-wire plane views. Collection plane is displayed on top, while Induction 2 and Induction 1 are shown in the middle and bottom panels, respectively. Horizontal axis always represent the direction of the wire planes, instead the drift time

is shown in the vertical direction. The event display has different colour options, the one being showed here sets a colour for each slice; where the green slice contains the event under study. In addition, each coloured hit is a 2D hit that has been used to create a 3D space point.

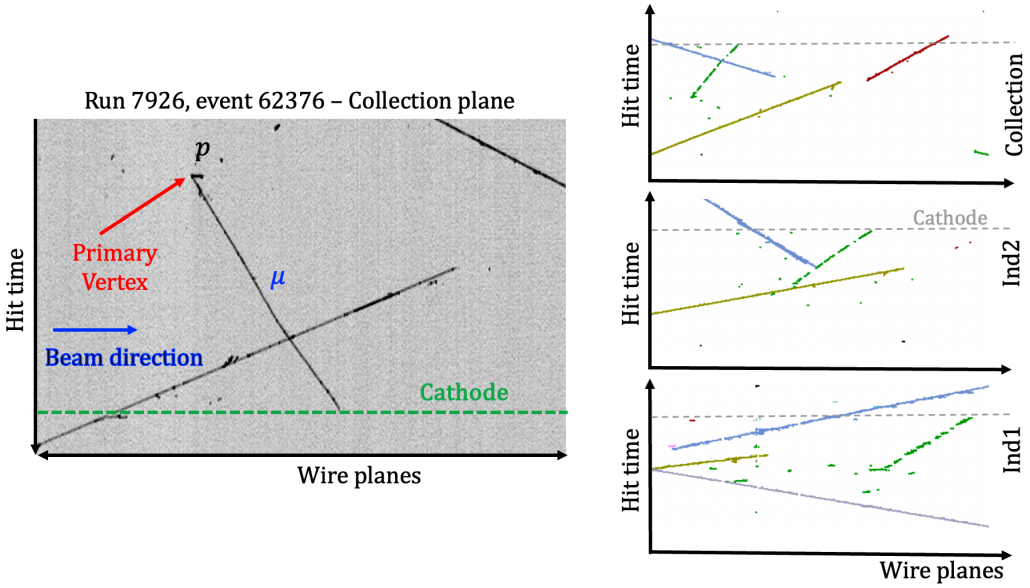


Figure 6.7: Left: TPC picture of a pathological $\nu_\mu$ event, producing a short proton and a muon crossing the cathode. Right: Pandora's event display, showing some of the reconstructed slices inside the spill readout. Part of the slice under study is shown in green, as the other half of it is reconstructed in the adjacent TPC.

Contrary to the other reconstructed tracks visible in the event display, the neutrino slice presents several gaps along the longest track. In order to see what is causing the gaps one can enable the option to draw all the gaussian hits to identify which of them were left out in `Cluster3D`, and hence not assigned to any reconstructed object, which are illustrated in black. Figure 6.8 left shows that gaps are related to Induction 1 plane. Both Collection and Induction 2 planes have hits all along the track (either green or black), contrary to the Induction 1 plane where empty spaces are present. Pandora was unable to find consistent hits across the three planes breaking the muon track in 3 pieces with triple matches. Split tracks were not a problem when checking the agreement between the scanned and reconstructed end muon positions. Still, the length of the segment containing the compatible end muon position and the total muon length are completely different, being a potential issue for further analysis. It was noted that the selected muon track crossed a noisy region of Induction 1 which was affecting the hit finding algorithm due to some signal removal during the noise subtraction process. Space point inefficiencies can be driven by small pulses height that are indistinguishable from background noise, specially in Induction 1 plane, where the signal to noise ratio is the lowest.

To improve Pandora's reconstruction, it was decided to modify the `Cluster3D` algorithm, which is responsible of finding compatible hits across the planes (see Section 5.5.2) and feeding them to Pandora. The change allowed `Cluster3D` to create space points from hits matched across two planes, rather than requiring match with all of them. With this modification, the output from `Cluster3D` contains more hits as more combinations are allowed to form spacepoints ($\sim$ 16% of increase), the latter ones being renamed `Mythical points`. Pandora's output using the `Mythical points` for the studied neutrino event is shown on the right hand side of Figure 6.8. The candidate muon track is shown in purple, where now a continuous track is visible in all three planes. Note that with this modification no new 2D hits were created, but only a larger portion of the existing ones were used.

This modification was validated with a larger statistics showing an improvement in recon-

struction performance, and therefore was introduced as the default option in the reconstruction chain. The algorithm to input hits to Pandora was updated accordingly to remove possible duplicates due to the modified `Cluster3D`.

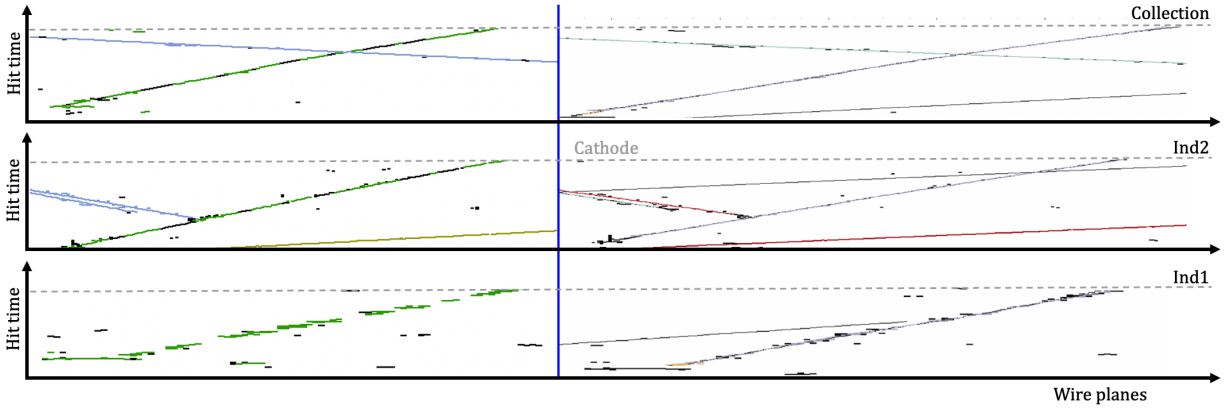


Figure 6.8: Zoomed event display showing all gaussian hits found for a specific neutrino interaction (left side of the blue vertical line). Coloured hits are associated with some reconstructed track or shower, whereas black hits are those unable to generate a 3D space point. The event display on the right side of the blue line, shows the same event as before, but using the `Mythical points` where now the `Cluster3D` algorithm is allowed to create 3D points even if a match is found only across two of the three wire planes.

The second event that was studied in detailed was a misclassified event; the visual scanning claimed it was a $\nu_\mu$CC candidate with a 2.1 m long muon and two shorter proton candidates, while the automatic reconstruction was able to identify the muon track and only one of the two protons. Figure 6.9 top shows the neutrino candidate in the collection plane, while the bottom figure shows Pandora's reconstructed output in the same view.

Two aspects are worth mentioning: the first proton is classified as a shower instead of a track, while the second one is not reconstructed at all. Pandora is not able to identify the second proton as a different particle, which might be influenced by the fact that it is close and alongside the muon track. This second issue needs a sophisticated and challenging fix to improve Pandora's ability to identify tracks in crowded regions. On the contrary, and in order to benefit from all track and shower specific handling of particles, it was decided to perform both track and shower fits to all reconstructed objects regardless of Pandora's intrinsic classification. The change turned out to be of great benefit allowing to study all reconstructed objects, even if their track-shower topology was wrongly identified by Pandora, and to leave to the analysis stage the possibility to overturn that classification.

A full analysis using reconstructed variables was performed on several hand scanned events, to demonstrate the ability to fully reconstruct neutrino interactions. The effort was concentrated on $\nu_\mu$CC QE events, contained and with a single proton at the primary vertex. Full kinematic reconstruction was done for the interaction in Figure 6.2, which produces a proton and a muon crossing the cathode and decaying into a Michel electron. The total deposited energy can be obtained by integrating the energy loss along the track as: $\sum_{i}^{\text{all hits}} (dE/dx)_i \cdot dx_i$, which for this event results in $E_{dep} \sim 620$ MeV. The $dE/dx$ distribution for the muon track was also computed, showing the expected behaviour for a minimum ionizing particle. This preliminary identification check was done excluding the last 50 cm of the muon track, to avoid any increase in ionization, and reporting a mean value of $2.14 \pm 0.79$ MeV/cm compatible with the MIP expectations of 2.12 MeV/cm. The final identification of the muon and proton candidates was done overlapping the $dE/dx$ values along its residual range to the theoretical distributions shown in 5.14, individually.

A good agreement was found in both cases, even though a small modification was needed.

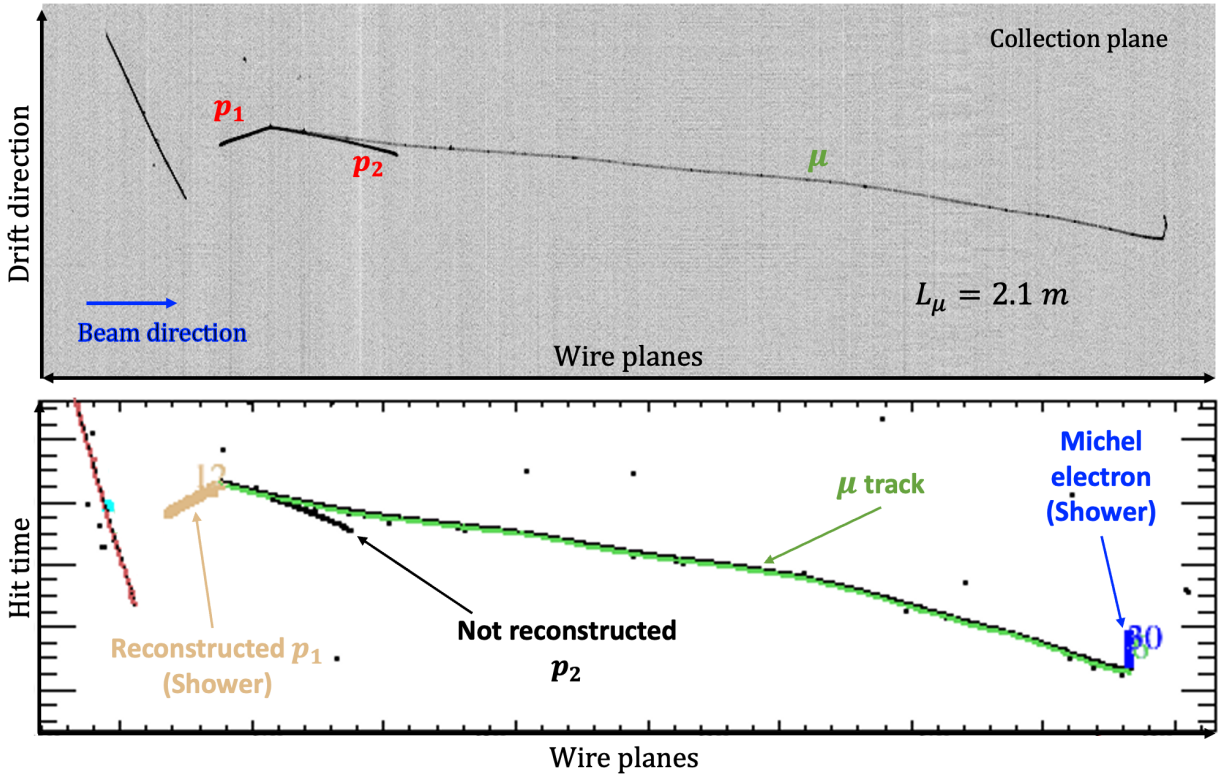


Figure 6.9: $\nu_\mu$ visually scanned event shown in collection view, producing a muon and 2 proton candidates. Top image shows the raw signal induced by the event, instead bottom figure shows Pandora's event display with its reconstructed objects. The muon candidates is well reconstructed as a complete track, while only one of the two protons is reconstructed and classified as a shower-like candidate. It is possible to see that the Michel electron attached at the end of the muon is also reconstructed as a shower candidate.

Figure 6.10 left shows all hits associated to the muon track, which clearly present an anomalous behaviour at very low residual ranges. The Bragg peak reconstruction was spoiled by a $\sim$ 7.3 MeV Michel electron, that was wrongly merged with the muon track. After removing all the hits from the decay electron, the reconstructed $dE/dx$ vs residual range was within the expectations for both proton and muon candidates, as shown in Figure 6.10 right. This proves that with the present signal calibration the Bragg peak for both species are correctly reproduced. There are some outlying hits along the muon track, which were identified as delta rays and can be seen in the inset image of Figure 6.10 as darker dots along the muon track.

Lastly, the muon and proton momenta were computed based on their range, as explained in Subsection 5.5.5. The total momentum is obtained by summing the reconstructed momenta of each particle, namely $\vec{p}_{tot} = \vec{p}_\mu + \vec{p}_p$, which for this event resulted in a vector pointing 16° from the beam axis. Genuine $\nu_\mu$CC QE interactions from the BNB beam are recognized to be balanced in the plane perpendicular to the beam direction, with the total transverse momentum generated by the Fermi momentum of the struck neutron in argon nuclei. The transverse momentum of the event was computed summing the transverse components of both particles, as shown in Figure 6.11, obtaining a $p_T \sim 218$ MeV/c in agreement with the Fermi momentum.

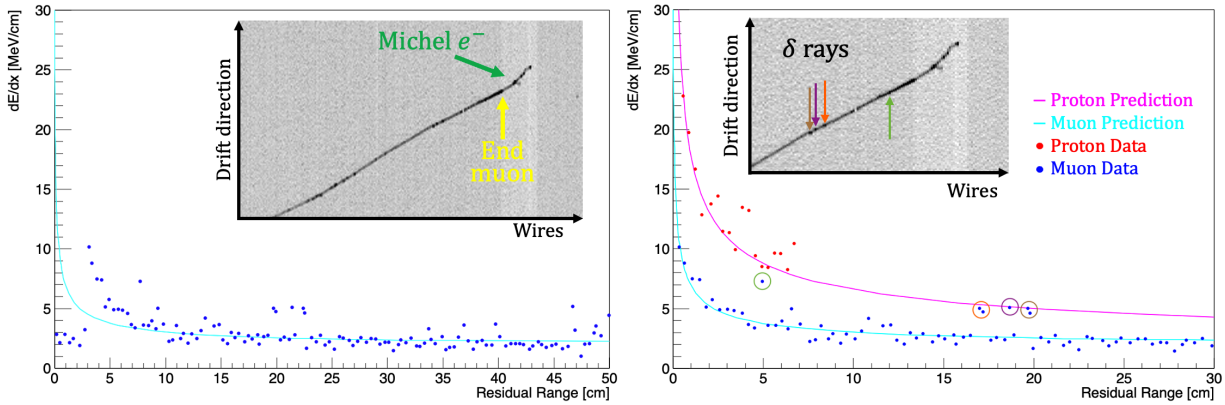


Figure 6.10: Particle identification of both tracks involved in the neutrino interaction. Left plot shows the hits associated with the muon track, where the Michel electron is visible as a MIP particle at residual range below 3 cm. Right plot shows the hits associated to the proton and the muon after the modification of the latter one. Circled hits correspond to the delta rays along the muon indicated by the arrows in the top right inset image.

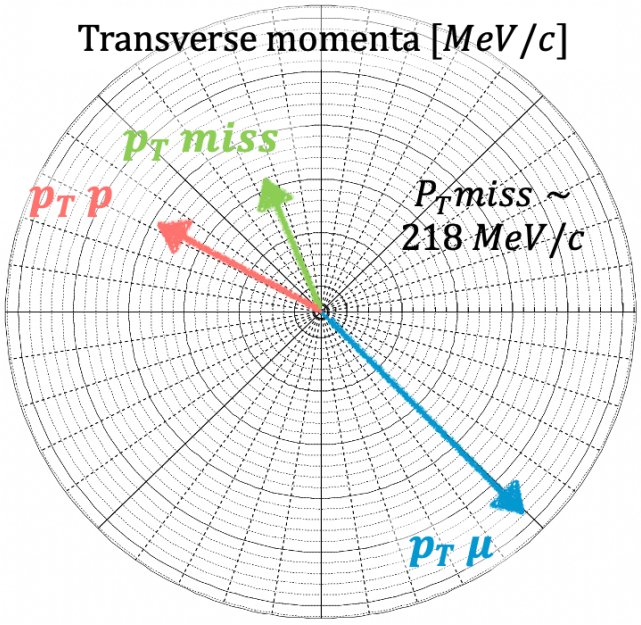


Figure 6.11: Reconstruction of the momentum in the plane perpendicular to the beam direction for the event shown in Figure 6.2. Muon and proton transverse momenta are shown with blue and pink arrows respectively, whereas the total missing transverse momentum is shown in green.

## 6.2 1$\mu$1p studies with visually selected events

The current focus of ICARUS oscillation analysis is on BNB $\nu_\mu$ disappearance, using $\nu_\mu$CC fully contained events with a muon track longer than 50 cm and a single proton at the primary vertex (1$\mu$1p events). This first simplified approach requires good performance of only track reconstruction, muon and proton particle identification and range-based momentum estimation which are in an advanced state of development. In addition, the requirement to have one proton forming a vertex with the muon track strongly reduces the background from cosmics. For this reason, the entire analysis that will be presented below focuses on the study of the 1$\mu$1p typology, investigating the performance of Pandora's reconstruction, the development of methods to automatically select 1$\mu$1p events and their optimization.

A first study to evaluate the quality of reconstructed events was carried out exploiting the reference sample of hand scanned events. An enlarged statistics of 520 events, containing only 1$\mu$1p topology was available. The candidates were selected by requiring the same conditions as before (neutrino vertex inside the fiducial volume, fully contained interaction and stopping muon of at least 50 cm length), with an additional requisite regarding the proton candidate. Only events with one proton produced at the primary vertex and of at least 1 cm length corresponding to $\geq$ 30 MeV of deposited energy were considered. The greatest vantage of using hand scanned events is the possibility of exploiting the visually obtained information as true values, with 3D points measured with few mm accuracy, while at the same time analyzing real data. This last point is of utmost importance, since real events are affected by all problems that reconstruction might encounter, which could not be well modeled in Monte Carlo simulated events.

To evaluate the performance of Pandora's reconstruction algorithms a set of quality requirements were defined. For this analysis two assumptions were done. First, slices which had been tagged as clear cosmics (as defined in *Cosmic ray muon tagging*, Subsection 5.5.3) were rejected and not considered as valid neutrino candidates. Secondly, the muon candidate was chosen to be the longest reconstructed track inside the interaction. Therefore, after the removal of all clear cosmic slices, a set of requirements were applied to guarantee an excellent automatic reconstruction and interpretation of the event in the following order.

1. Reconstructed vertex in agreement with the scanning information inside the limit of 2 cm
2. Muon track candidate tagged as primary particle by Pandora and with a reconstructed length of at least 50 cm
3. Muon start position within 2 cm from the scanned vertex position
4. End point of the muon track in agreement with the scanning information not beyond 2 cm
5. Particle identification algorithm should correctly classify the muon track as a muon candidate
6. Proton track candidate chosen as the longest remaining track (excluding the muon) with well reconstructed start and end point positions. Conditions analogous to those of the muon track apply.
7. Particle identification algorithm should correctly classify the proton track as a proton candidate

During the analysis it was decided to apply a rather stringent cut-off at 2 cm, to enhance the selection of well-reconstructed events at the expenses of losing some efficiency.

The particle identification tool defines 4 parameters for each analyzed track. These are $\chi^2_k(j)$, which gives the $\chi^2$ value computed as Eq 5.15, for particle $j$ under the hypothesis of being a

$k$ particle, where $k$ can be a muon, proton, pion or kaon[2]. Particles with $\chi^2_\mu < 30$ and $\chi^2_p > 60$ were identified as muon track, while protons were required to have $\chi^2_p < 90$ and $\chi^2_\mu > 30$. The upper and lower limits of all these variables were chosen on the basis of a study carried out using simulated events, trying to obtain the best trade-off between efficiency and purity of the selected events. The result of the analysis is shown in the two normalized distributions of Figure 6.12, where the reconstructed $\chi^2$ value under the hypothesis of being a muon or a proton for several tracks associated to different particles are shown. It is possible to see two different peaks for the muon, pion and proton distributions. The lower peak of muons and pions in the left hand side plot, represents well reconstructed contained tracks, including the Bragg peak and therefore well described by the theoretical curve of the stopping muon used to compute the $\chi^2_\mu$. In contrast, the higher peaks are due to MIP-like particles, either split or uncontained tracks for which the increase in ionization is not present, slightly worsening the agreement with the stopping muon prediction. For the proton the explanation is the other way around, the highest peak is due to well reconstructed protons, which should have a rather high $\chi^2_\mu$ score. Instead, the lowest peak is generated by events that have lost some hits at the end of the track or are very short, and therefore the $\chi^2$ method performs poorly. The logic can be applied analogously to the other variables, changing the roles between the muon/pion and the proton.

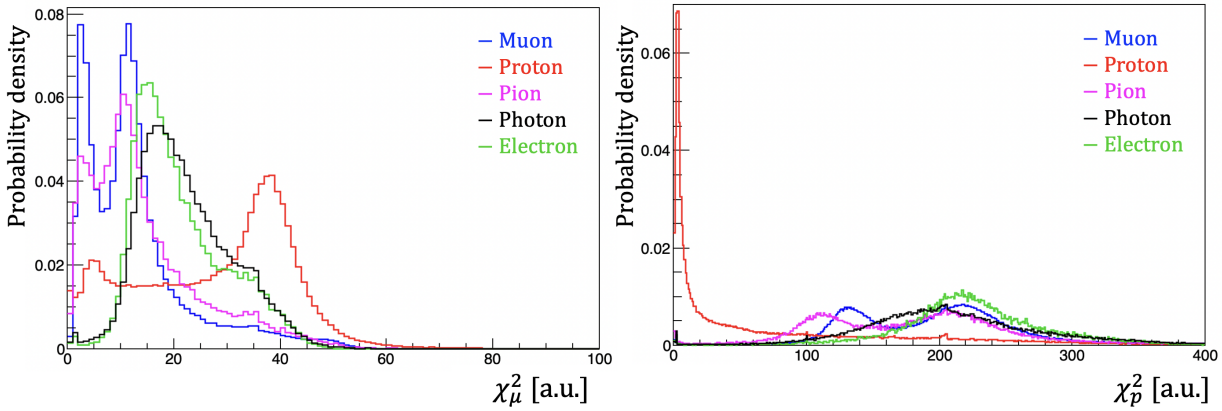


Figure 6.12: $\chi^2$ distributions under the hypothesis of being a muon (left) or a proton (right) for different particles. The distributions were made with simulated events associated to any neutrino interaction and normalized to 1.

Table 6.2 shows the effect of the different quality cuts applied, where 120 events out of 520 1$\mu$1p candidates were selected as well reconstructed interactions.

The reduction of events is mostly related to three reconstruction problems: misidentification of the primary vertex, incomplete or missing reconstruction of the muon and poor reconstruction of the proton.

The interaction vertex is in some cases not properly reconstructed or sometimes placed in the middle/end of the muon track causing the loss of events in the first quality cut. Secondly, due to the capability to fully recognize and reconstruct the muon track: split or reverted tracks, problems related to noisy regions in the detector or affected by the passage through the cathode. In addition, isochronous tracks traveling close to parallel to the wire planes, such that all TPC activity is recorded at approximately the same time, are a particularly challenging sample to reconstruct. While this might not be a problem for reconstruction within a single view, it is certainly an issue when trying to match clusters between views, as the common x coordinate (directly related to the drift time) is used to relate the 2D clusters, as explained in Subsection 5.5.3. On top of that, the noise filter can mistake the signal as part of the coherent noise and

[2]Note that the so-called "$\chi^2$" is not a proper $\chi^2$ but rather a score, due to the Landau component in the $dE/dx$ distribution.

| Quality cuts | Selected events |
|---|---|
| Total events | 520 - 100% |
| 1. Well reconstructed vertex | 405 - 78% |
| 2. Primary muon track and of $L_\mu$ >50 cm | 400 - 77% |
| 3. Well reconstructed start muon | 353 - 68% |
| 4. Well reconstructed end muon | 247 - 48% |
| 5. Correct identification of muon | 246 - 47% |
| 6. Proton track candidate | 183 - 35% |
| 7. Correct identification of proton | 120 - 23% |

Table 6.2: Effect of all quality cuts applied to hand scanned data.

filter out some charge along the isochronous tracks. Consequently, the 2D cluster could have gaps along the track leading to poorly reconstructed events or simply a failure of the entire interaction.

The last justification for the loss of events was fount to be related to the poor reconstruction of some proton tracks. A minimum length threshold was introduced when defining the 1$\mu$1p scanned signal, the proton candidate was required to have a path length of at least 1 cm, which translates into approximately 30 MeV of deposited energy in Ar. However, this might not be enough to obtain higher identification efficiency.

Figure 6.13 shows the $dE/dx$ values as a function of the residual range for particles selected as muon and protons candidates in the collection plane. In particular, 247 muon tracks are shown in the left hand side plot (all selected events up to the well reconstructed end muon quality cut), while 120 protons are displayed on the right hand side plot, containing the remaining proton candidates after all the selection requirements. Good agreement in shown in both cases confirming the correct classification of these tracks.

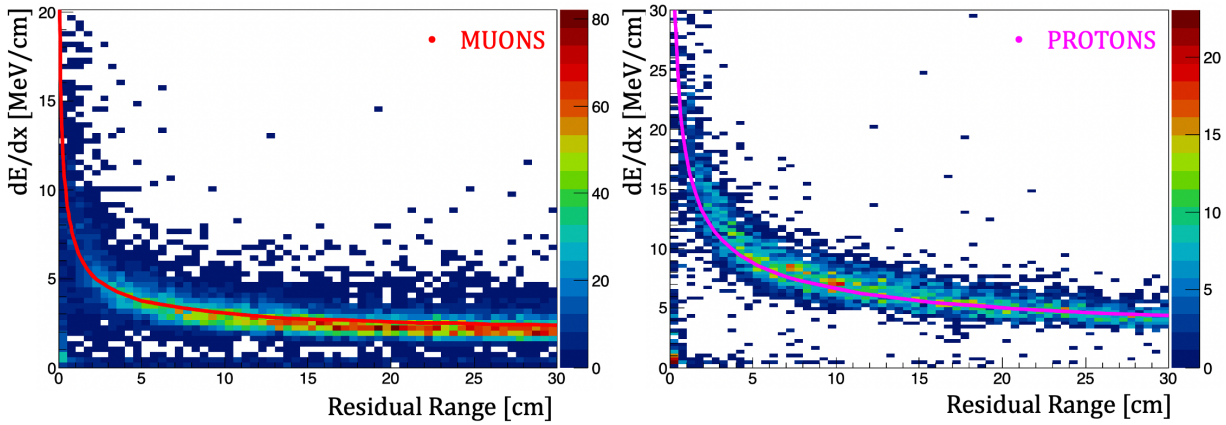


Figure 6.13: Deposited energy along the trajectory for muon and proton candidates. The theoretical mean stopping power predictions used in the particle identification algorithm are overlapped for each specie.

Some disagreement is visible at very low residual range in both distributions. This is because the $dE/dx$ estimation is unreliable for the last hit on a track due to the uncertainty on the exact stopping point of the particle. The second interesting feature present in both plots as well, is the amount of hits at very low $dE/dx$ values. This is most evident in the muon distribution simply because it contains twice as many statistics as the proton distribution and the fact that

muons contribute to the whole 30 cm residual range, whereas protons can be shorter. This effect is caused by particles traveling parallel to the drift direction and inducing long signals in time, for which the Gaussian fit performed by the hit-finding process is not adequate (see Subsection 5.5.2). The total deposited charge is therefore segmented into multiple hits, leading to an underestimation of the hit charge and resulting in smaller $dE/dx$ values. These small values of $dE/dx$ encountered at large pitches negatively affects the particle identification performance.

To further confirm that the track is stopping inside the detector and not misreconstructed as contained when truly exiting the LAr, the integrated energy over a certain residual range can be exploited. The sum of $dE/dx$ times the pitch for all hits associated to the muon track in the last 12.5 cm of the track was computed. Unlike muons, which are all more than 50 cm long, protons have a broader variety of lengths, making it impossible to establish a fixed integration range suitable for all proton tracks. The muon integration range was chosen to maximize the impact of the ionization rise without masking the effect due to excessive contribution of MIP-like particle relative to the segment distant from the Bragg peak. The values obtained can be compared with the expected ones for each type of particle, from an analogous integration of Eq. 5.6. This method is able to distinguish tracks producing a Bragg peak from those that do not present a rise in ionization in its final part, either because they are exiting or due to the loss of some hits in the final part of the track. Figure 6.14 left shows the expected deposited energy for different particles as a function of traveled length, while the right hand side distribution shows the integrated energy of well reconstructed muon tracks (as defined by the above quality cuts) for their last 12.5 cm.

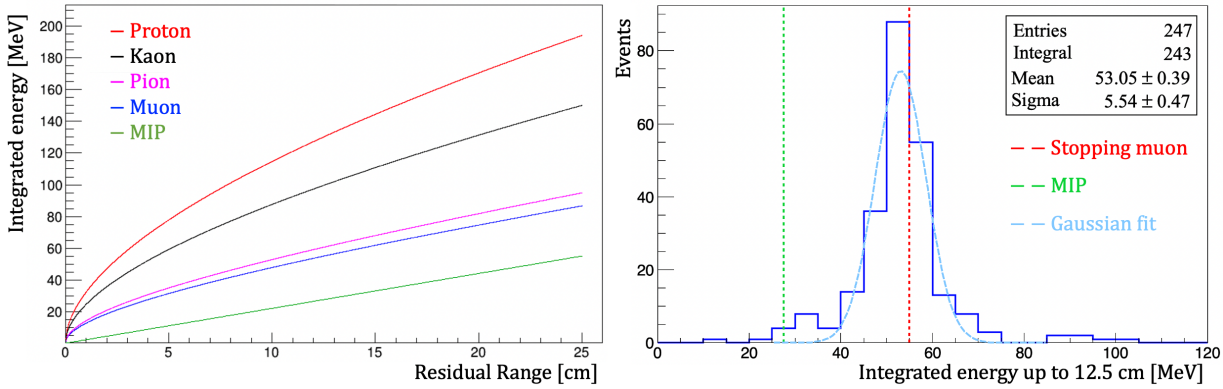


Figure 6.14: Left: reference values of integrated energy as a function of their traveled length for different particles. Right: Integrated energy deposited by the well reconstructed muon tracks selected with the quality cuts described in the text. The integration is done considering all hits associated to the muon track with residual range below 12.5 cm. The expected values for a stopping muon and a minimum ionizing particle are also shown as red and green vertical lines, respectively. In addition a gaussian fit is overlapped, reporting the obtained mean and sigma values of the fit.

A stopping muon is expected to deposit on average $\sim$ 55 MeV in the last 12.5 cm of the track, while the predicted value for a minimum ionizing particle is of $E_{dep} \sim 28$ MeV.

Even if the distribution peaks around the expected value for stopping muons, confirming the nature of the selected tracks, it is far from being a narrow distribution. This can derive from the dispersion seen in Figure 6.13, where several hits have really small values while others are well above the average curve. To overcome these poorly reconstructed tracks, a gaussian fit was performed to the bulk of the distribution. The fit of the integrated energy distribution resulted in a mean value of $\sim$ 53 MeV and a standard deviation of $\sim$ 6 MeV. This value is in good agreement with the stopping muon hypothesis, while falls outside the errors for the MIP assumption.

The compatibility with the stopping muon hypothesis was expected having required the precise identification of the end muon position within 2 cm. This guarantees that the Bragg peak is partially, if not entirely, included in the reconstruction, provided that the $dE/dx$ and pitch are correctly evaluated.

To get an insight of the hand scanned events, the transverse momentum for each one of them was computed, following the procedure shown in Figure 6.11. Considering all the well reconstructed 1$\mu$1p candidates, which comply with the quality selection requirements, the transverse momentum distribution shown in Figure 6.15 was obtained. $P_T$ is of great interest, as it can be used as a proxy for the event interpretation and energy resolution. The obtained distribution is centered at low transverse momenta, below 250 MeV/c, compatible with the Fermi momentum of the struck nucleon, however it presents a long tail up to 700 MeV/c.

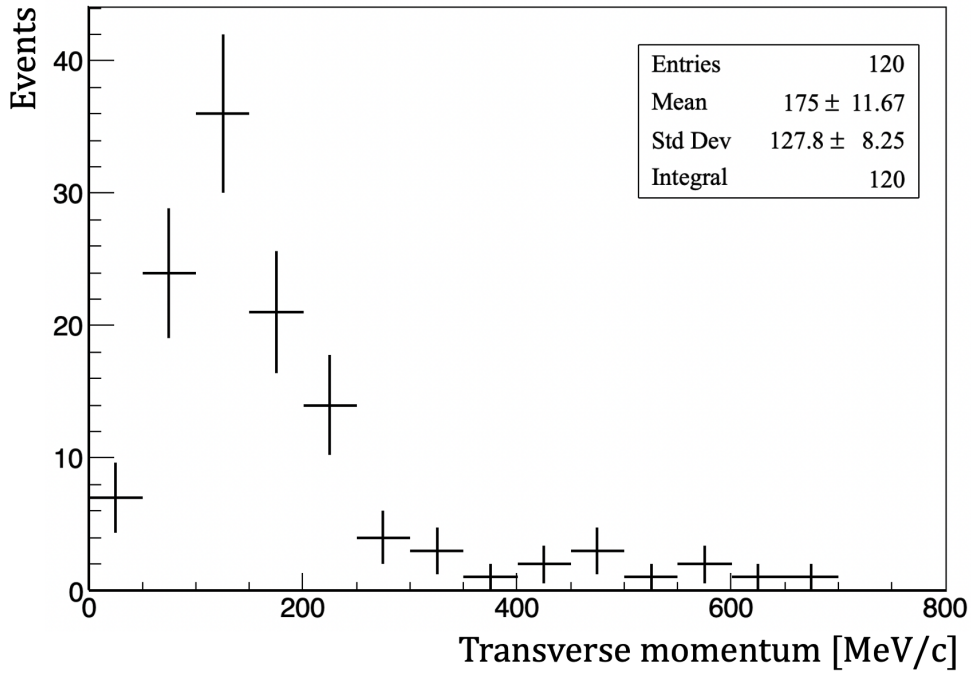


Figure 6.15: Transverse momenta distribution for all well reconstructed scanned events.

## 6.3 1$\mu$1p Monte Carlo studies

Further studies were performed on simulated interactions to understand the features of the selected events, especially of the transverse momentum distribution shown in Figure 6.15.

A small sample of BNB neutrino interactions was simulated with the goal of examining and reproducing the analysis performed on the visually selected 1$\mu$1p real events (Table 6.2).

The definition of `True 1μ1p` MC events was applied requiring the following conditions at true level.

- $\nu_\mu$CC events with the interaction vertex inside the fiducial volume
- Only 2 primary track, corresponding to one muon and one proton
- Both particles fully contained within 5 cm from the active borders
- Muon and proton length of at least 50 cm and 1 cm, respectively.

The true information was used to apply the quality cuts on the reconstructed MC quantities. As a result 771 `True 1μ1p` over $\sim$ 9300 $\nu_\mu$CC simulated interactions were selected ($\sim$ 8%).

| Quality cuts | True 1$\mu$1p | Scanned events |
|---|---|---|
| Total events | 771 - 100% | 520 - 100% |
| 1. Well reconstructed vertex | 579 - 76% | 405 - 78% |
| 2. Primary muon track and of $L_\mu$ >50 cm | 574 - 75% | 400 - 77% |
| 3. Well reconstructed start muon | 506 - 66% | 353 - 68% |
| 4. Well reconstructed end muon | 344 - 45% | 247 - 48% |
| 5. Correct identification of muon | 336 - 44% | 246 - 47% |
| 6. Proton track candidate | 234 - 30% | 183 - 35% |
| 7. Correct identification of proton | 156 - 20% | 120 - 23% |

Table 6.3: Effect of all quality cuts applied to a sample of 1$\mu$1p simulated events. The results obtained with scanned data events are also shown for comparison.

The efficiency of the quality cuts for MC events agrees with what observed with real data within the statistical errors as shown in Table 6.3.

Figure 6.16 shows the true and reconstructed transverse momenta for the 156 well reconstructed 1$\mu$1p events after applying the quality cuts, with the true distribution scaled down to the same number of reconstructed events for the sake of comparison. Even if good agreement is found between the true and reconstructed values of transverse momenta, the obtained distribution is only partially describing the results seen with real data (see Figure 6.15).

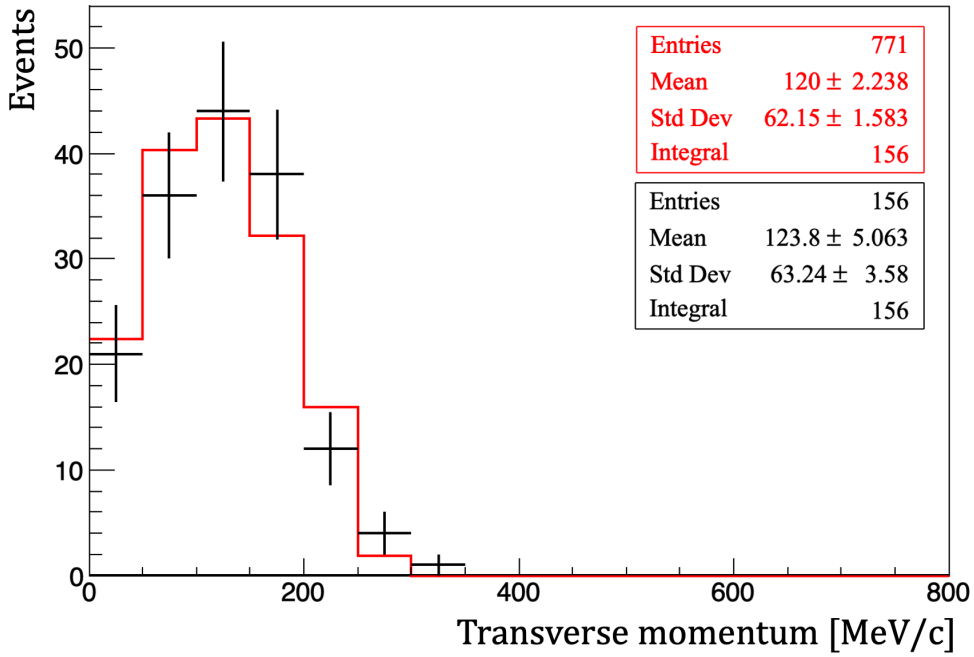


Figure 6.16: Transverse momenta distribution for simulated events. Red histogram shows the $p_T$ evaluated for all `True 1$\mu$1p` events using true information. Black points indicate the reconstructed transverse momentum of selected events satisfying all quality cuts.

While data events have a long tail at higher transverse momentum, none of the simulated events have a $p_T$ greater than 350 MeV/c. Although visual scanning is a valuable tool to evaluate the performance of selection and reconstruction algorithms, it also has some limitations. For instance all particles are identified based on their ionization, hence it is possible that different hadrons are wrongly classified as protons, being an important source of errors. In the scanning,

very short protons are not visible, thus events with tiny protons can be easily misidentified as $1\mu 1$p candidates. Finally, neutrons and low energy photons produced at the primary vertex are very difficult to recognize, unless they do some interaction. The introduction of a visibility threshold of protons, namely that a proton is visible only if its range is long enough, and similarly for neutrons and photons, based on their deposited energy, should be considered to have a more accurate comparison between simulated and data events.

To get some insight of the discrepancy, two data events at high transverse momentum were studied in more detail. The first one (see Figure 6.17 top) has a muon of 215 cm, a 5 cm proton and a reconstructed transverse momentum of $p_T = 638.8$ MeV/c. From the collection view image, it is possible to recognize the Bragg peak, characterized by increased ionization at the end of the muon, which is represented in the image with a shift towards darker colours. Near the vertex some black dots suggest a possible interaction of neutral particles produced at the primary vertex, which could explain the high transverse momentum value. These neutral particles carry away part of the total momentum, causing an imbalance in the transverse momentum if not taken into account. The problem could be solved by introducing an energy threshold to eliminate events with some interaction activity unrelated to the proton or muon tracks. Visibility thresholds need to be tuned appropriately to account for the energy resolution of the reconstruction algorithms.

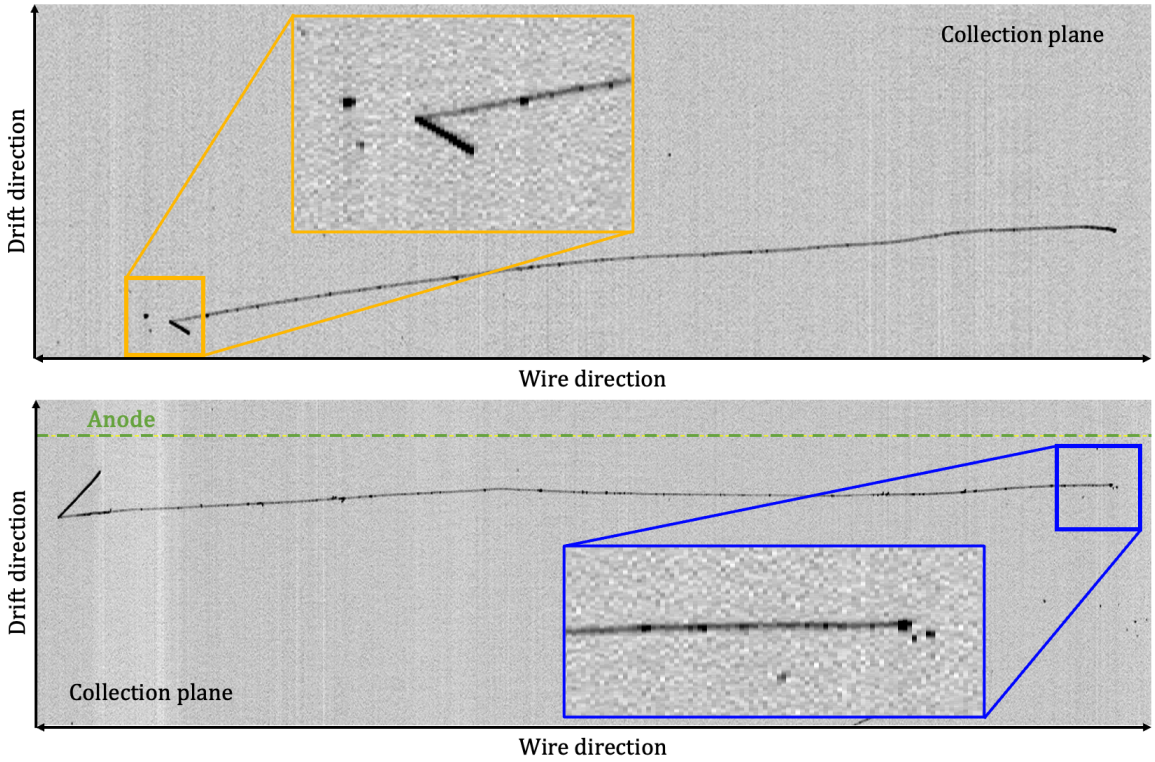


Figure 6.17: Example of high transverse momentum events from the hand scanned sample, passing all the selection quality requirements.

The second event (see Figure 6.17 bottom) has a slightly smaller transverse momentum, $p_T = 453.6$ MeV/c, calculated from a 296 cm long muon and a 32 cm long proton. In this case, no additional activity is detected at the primary vertex, but rather a sudden deposition of energy at the end of the muon candidate. This could be a sign that the particle reinteracts before stopping or is simply absorbed, making discrimination between a muon and a proton track impossible. Track momentum measurement via its range will report an underestimation in both cases, resulting in an unbalance in the total transverse momentum.

To address the visibility threshold issue and find the optimal values allowing the most accurate comparison between simulated and data events, a scanning of Monte Carlo events was

performed.

A sample of 142 simulated events was visually examined, of which there were 18 events producing only the muon and the proton at the primary vertex. The scanning result claimed 68 visually selected 1$\mu$1p candidates, identifying all 18 true 1$\mu$1p but also 40 other events. Significantly more events than expected were recognized as 1$\mu$1p due to the presence of photons and neutrons, whose secondaries deposited a small amount of energy in the detector. Besides the 18 true 1$\mu$1p, 51 events were found producing photons and neutrons together with a single muon and a single proton. The distribution of the deposited energies associated with these neutrons and photons produced in the primary vertex are shown in Figure 6.18. The deposited energy of the neutron has been defined as the energy deposited by itself plus the deposited energy of all its secondary particles. In the case of more than one neutron or photon produced at the primary vertex, the highest energy deposited is shown.

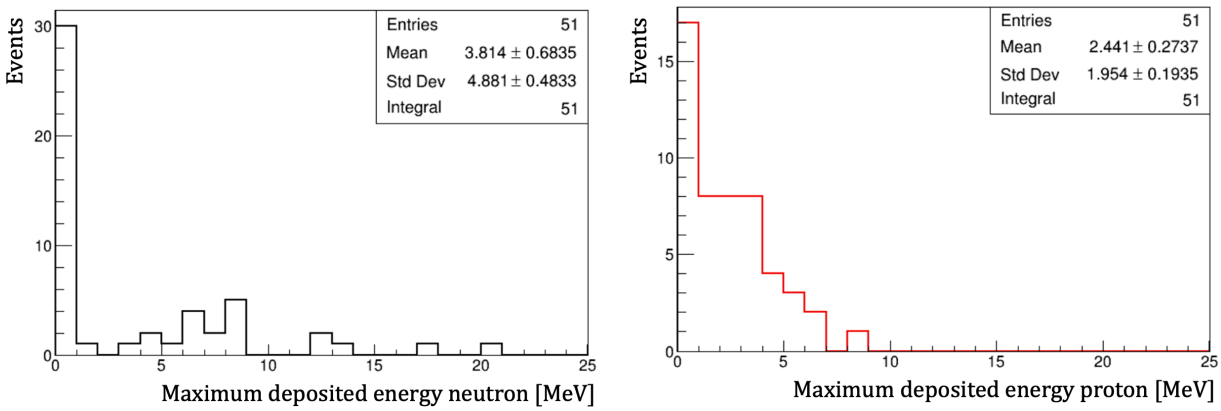


Figure 6.18: Deposited energy associated to neutrons and photons in neutrino events, where one muon, one proton and neutrons or photons are produced at the primary vertex.

It was decided to include all of these events in a so-called `Visible 1μ1p` sample, which at true level translates into the following requirements: in addition to the previous conditions only two visible tracks are allowed at the primary vertex (corresponding to a muon and a proton), assuming that:

- A primary proton is considered visible if its kinetic energy is above 25 MeV ($\sim$ 6 mm)
- A primary neutron is considered visible if the sum of the deposited energy of the neutron and its daughters is above 25 MeV
- A primary photon is considered visible if its deposited energy is above 10 MeV

The proton energy threshold was set according to the visual scanning experience, since 25 MeV of proton approximately corresponds to having a two-wire wide signal, which can be visually identified without problems. This `Visible 1μ1p` sample, includes also the `True 1μ1p` events, where nothing but the muon and the proton are produced at the primary vertex.

With this new definition, the classification of visually studied events was revised. At true level, from the available sample of 142 events, 69 of them were visible 1$\mu$1p events, while the remaining 73 were other neutrino topologies. In the MC visual scanning 68 events were selected, 63 of which were correctly classified as visible 1$\mu$1p, while only 5 of them corresponded to other interactions. In particular these were (at true level): two neutral currents events, one interaction with a too short proton and two cases with more than one visible proton. The 6 visible 1$\mu$1p events that were misclassified as background had either big kinks, rare in short proton tracks, or some black dots close to the primary vertex indicating some neutral activity, which were within the defined visibility thresholds. In conclusion, 63 out of the total 69 visible 1$\mu$1p MC events

were found and only 5 of the 68 visually claimed events were misclassified as 1$\mu$1p candidates. A good performance of $\sim$ 90% efficiency and purity was reported demonstrating the correct choice of the energy thresholds.

Just for completeness, and with energy thresholds properly determined, the previously defined selection was applied to the `Visible 1`$\mu$`1p` sample, selected with the aforementioned requirements at true level. The impact of each quality requirement is shown in Table 6.4 in comparison with previous results.

| Quality cuts | Visible 1$\mu$1p | True 1$\mu$1p | Scanned events |
|---|---|---|---|
| Total events | 1293 - 100% | 771 - 100% | 520 - 100% |
| 1. Well reconstructed vertex | 926 - 72% | 579 - 76% | 405 - 78% |
| 2. Primary muon track and of $L_\mu$ >50 cm | 916 - 71% | 574 - 75% | 400 - 77% |
| 3. Well reconstructed start muon | 792 - 61% | 506 - 66% | 353 - 68% |
| 4. Well reconstructed end muon | 537 - 42% | 344 - 45% | 247 - 48% |
| 5. Correct identification of muon | 527 - 41% | 336 - 44% | 246 - 47% |
| 6. Proton track candidate | 373 - 29% | 234 - 30% | 183 - 35% |
| 7. Correct identification of proton | 222 - 17% | 156 - 20% | 120 - 23% |

Table 6.4: Impact of quality cuts applied to a sample of `Visible 1`$\mu$`1p` simulated events. The results obtained with the `True 1`$\mu$`1p` and scanned data events are also shown for comparison.

Finally, all well reconstructed `Visible 1`$\mu$`1p` events were considered to compute the transverse momentum, which is shown in Figure 6.19. This distribution is much more alike to the one obtained with real data, reproducing both the low $p_T$ peak and the long tail at higher transverse momenta up to 750 MeV/c.

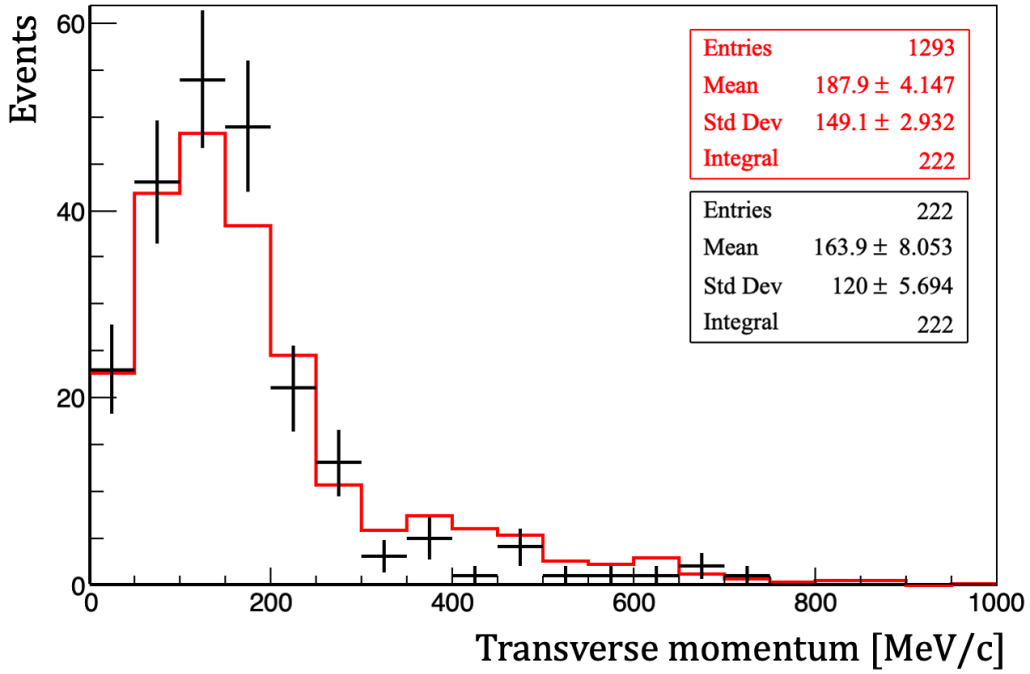


Figure 6.19: Left: Transverse momentum distribution for `Visible 1`$\mu$`1p` simulated events. Red histogram shows the true information, scaled down to the number of well reconstructed `Visible 1`$\mu$`1p` events, which is represented by the black dots.

To emphasize the effect introduced by the new definition of signal, the true transverse momenta of all `Visible 1`$\mu$`1p` events is shown in Figure 6.20, where `True 1`$\mu$`1p` events and interactions which contain 1$\mu$1p plus low energetic protons, neutrons or photons, within the defined thresholds, are also shown separately. It is clear from there that these low energetic particles are the only ones producing the long tail visible in the distribution, which need to be treated appropriately for an accurate comparison with real data.

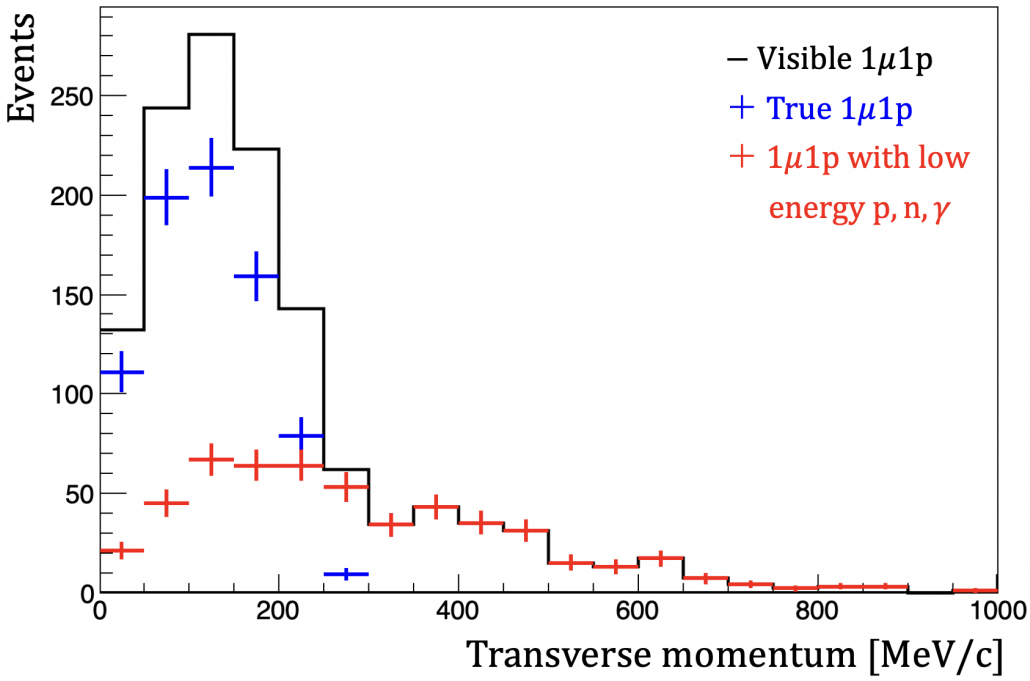


Figure 6.20: Transverse momentum distribution for `Visible 1`$\mu$`1p` simulated events using the true momenta of the visible muon and proton (black). `Visible 1`$\mu$`1p` events are made up of: `True 1`$\mu$`1p` events, which have nothing but the muon and proton at the primary vertex (blue) and events which in addition to the 1$\mu$1p produce low energetic protons, neutrons or photons at the interaction vertex (red), always within the thresholds defined in the text. Both contributions are shown separately to illustrate their different transverse momentum distributions.

At this point, it is possible to retrieve the reconstructed transverse momenta for data events, and compare it to MC expectations, corresponding to the reconstructed transverse momenta of well reconstructed `Visible 1`$\mu$`1p` events, as shown in Figure 6.21. As a result, the transverse momentum distribution of data and MC agrees within the available event statistics.

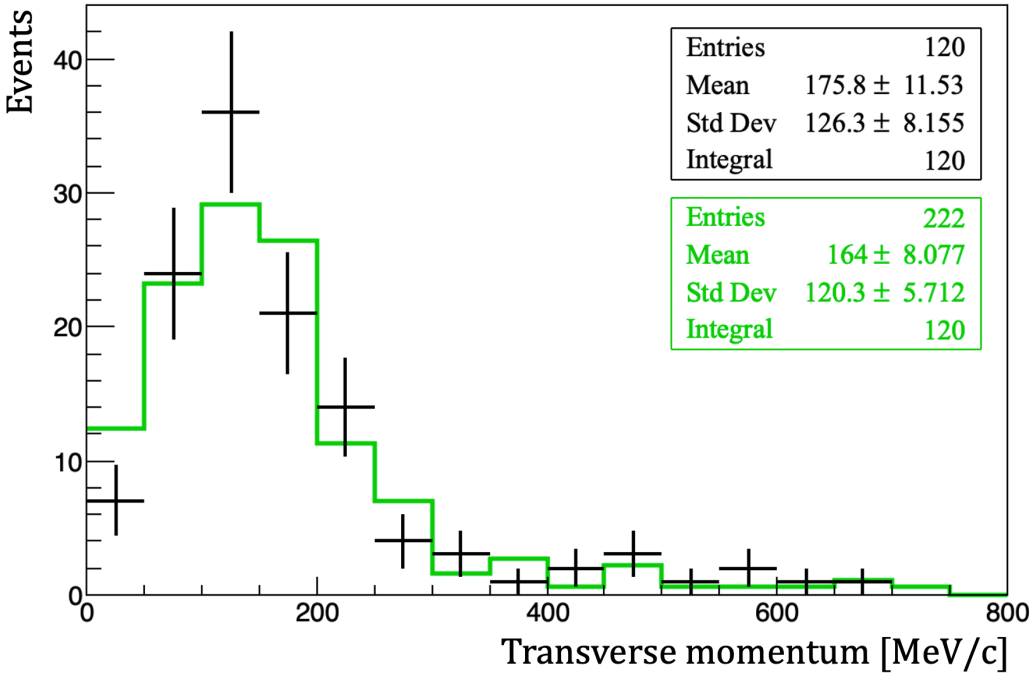


Figure 6.21: Transverse momentum distribution for well reconstructed 1$\mu$1p hand scanned events (black). The simulated expectations are also shown as the green histogram, corresponding to the `Visible 1`$\mu$`1p` simulated events selected analogously to the data. Both distributions show the reconstructed transverse momentum of data and simulated events.

## 6.4 Automatic selection of 1$\mu$1p contained events (MC)

Until now, visually scanned events have been exploited to study neutrino interactions and in particular the 1$\mu$1p topology. However the oscillation analysis requires a robust and automatic procedure to efficiently identify 1$\mu$1p events. Thanks to the experience gained during the previous analysis, it is possible to develop a method to automatically identify these events. A first test was done to simulated events to verify and optimize the automatic procedure. All calculations shown below were performed with a MC production of $\sim 3.2\times 10^{20}$ protons on target (POT), but have been normalized to an exposure of $2.5\times 10^{20}$ POT, unless otherwise mentioned, corresponding to the data collected during the Run 1 and 2 period.

The definition of the sought 1$\mu$1p signal events at true level was based on the previous definition of `Visible 1μ1p` with minimal changes, requiring:

- $\nu_\mu$CC events with its vertex inside the fiducial volume
- 1 muon of at least 50 cm length
- 1 proton with deposited energy greater than 50 MeV in the collection plane, which corresponds to ∼2.3 cm of range
- All primary particles contained within 5 cm from the active TPC borders
- 0 pions, neutrons or photons with more than 25 MeV of deposited energy

The changes introduced were related to the energy threshold of the photons and to the energy requirement of the leading proton. The first threshold was increased as no modification was observed in the visual classification of MC events. The second change was motivated by seeking greater efficiency when correctly reconstructing the proton. Note that with this threshold definition subleading protons might deposit up to 50 MeV, which could worsen the neutrino energy resolution but their inclusion is mandatory to have an accurate description of real data.

The energy spectrum of all simulated events that constitute the signal defined with previous requirements is reported in Figure 6.22 with the single contributions from the different interactions. The labels stand for Quasi-Elastic interactions (QE), RESonance production (RES), Deep Inelastic Scattering (DIS), Coherent pion production (Coh) and Meson Exchange Current (MEC). A total of 22,808 neutrinos were found, whose separate contribution by interaction is shown in Table 6.5 and which constituted the 16.3% of the total $\nu_\mu$CC with vertex inside the fiducial volume.

| Interaction | $\nu_\mu$CC QE | $\nu_\mu$CC Res | $\nu_\mu$CC MEC | $\nu_\mu$CC DIS |
|---|---|---|---|---|
| Contribution | 70.9% | 15.6% | 12.2% | 1.3% |

Table 6.5: Contribution of different interaction types to the 1$\mu$1p signal at true level.

The correct determination of the incoming neutrino energy is required in oscillation experiments, for this purpose, two different methods described in Section 5.7 were applied to all interactions using the true information for both muon and leading proton tracks.

For genuine charged current quasi-elastic (CCQE) events with no proton final-state interactions, energy and momentum conservation allow to resolve the kinematics of the process completely and calculate the initial neutrino energy.

The first method (labeled as 1) considers a free neutron at rest, and computes the neutrino energy as $E_\nu = E_\mu + E_p - M_n$, where $M_n$ is the mass of the struck neutron, while the second approach assumes a nucleon bound and moving within the target nucleus (labeled as 2). The energy resolution is defined as the ratio $R = (E_{comp} - E_\nu)/E_\nu$, where $E_{comp}$ is the calculated neutrino energy with any of the two methods. Figure 6.23 shows the resolution obtained using

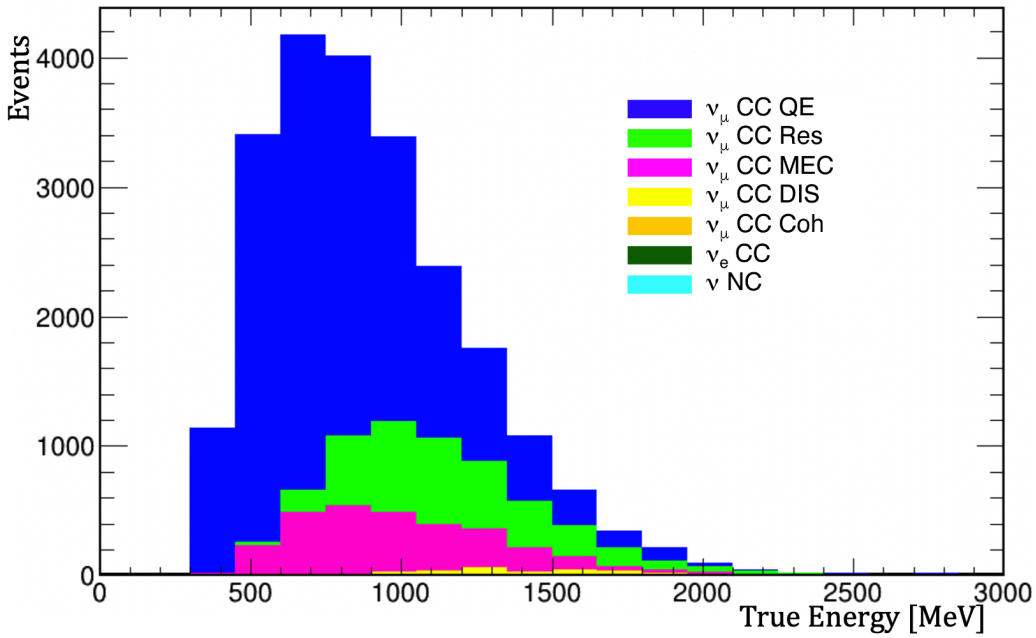


Figure 6.22: Stacked energy spectrum of the events contributing to the 1$\mu$1p signal definition for different neutrino interactions.

both methods, separately for events with only 1 muon and 1 proton in the primary vertex (left) and for events containing some other low energy primary particles (right).

The second method presents more accurate results in both subsamples, with smaller full width at half maximum values in the bulk of the distribution and less negative skewed profiles. The first approach produces distributions shifted towards negative values, indicating a systematic underestimation of the neutrino energy, while the second method is peaked at 0. Unlike the first one, the second method presents also positive values of R. This is related to the fact that simulated nucleons have a non constant value of the binding energy ($E_b$), being a function of the nucleon momentum, as described by the correlated Fermi Gas Model [167]. The second method uses a fixed value of binding energy, set to the mean value of $\langle E_b \rangle = 21.8$ MeV [175], overestimating (R>0) or underestimating (R<0) the energy of the neutrino, depending on the precise $E_b$ value in the interaction compared to the average binding energy.

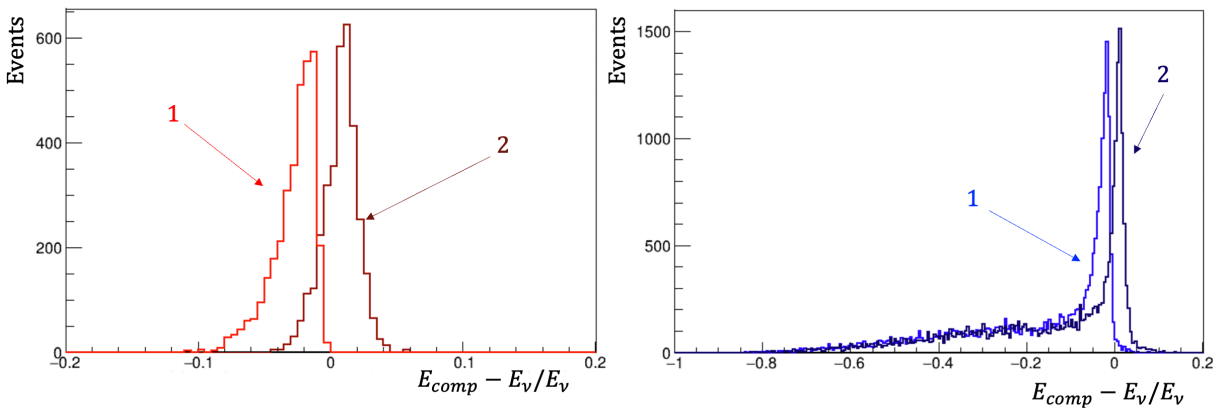


Figure 6.23: Energy resolution of 1$\mu$1p events using true information computed for both methods described in the text. The left plots shows the genuine 1$\mu$1p, while the right distributions represent the 1$\mu$1p containing some additional low energy particles. The horizontal scale is normalized such that 0.1 represents a 10% discrepancy.

A huge difference was seen between the genuine 1$\mu$1p events and those containing low energy particles in both methods. While genuine 1$\mu$1p events have an energy resolution of ∼4%, the remaining ones can reach an underestimation of ∼70%. Figure 6.24 shows that the long tails are populated primarily by non-QE interactions, although QE events can reach such high discrepancies on rare occasions. This is due to neutral particles produced at the primary vertex or charged particles quickly reinteracting and producing several daughters. Neutral particles, by definition, deposit tiny amounts of energy, so it was considered more appropriate to compute their energy as their deposited energy plus that of their secondaries.

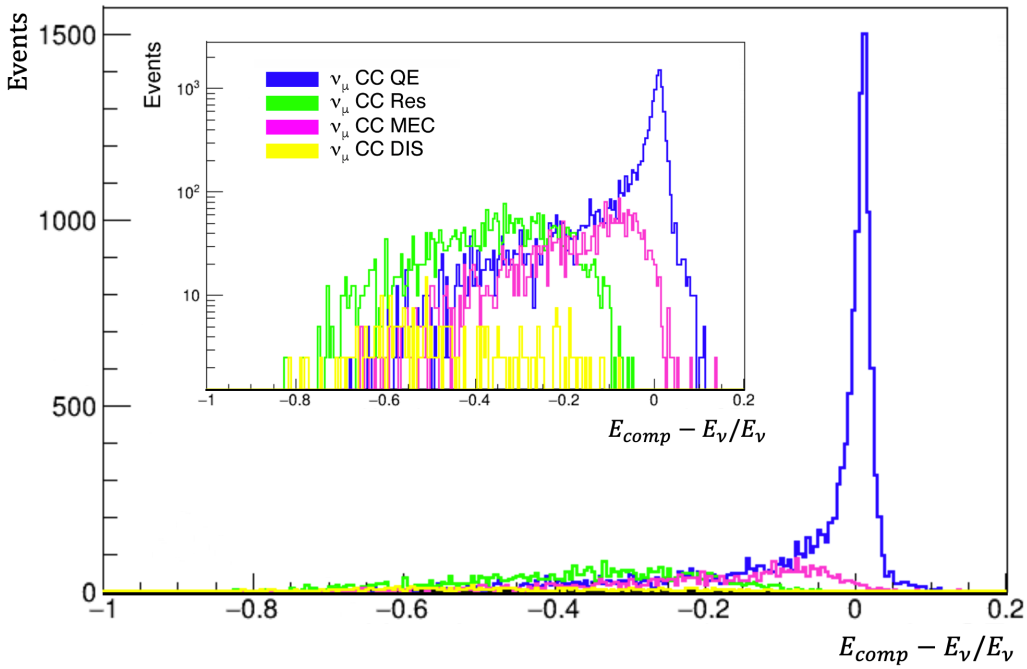


Figure 6.24: Energy resolution of `Visible 1$\mu$1p` events (excluding genuine 1$\mu$1p) showing the contribution of each neutrino interaction type. Note that the inset image has a logarithmic vertical axis to have better resolution of the negative tails.

The second method was adopted as the standard procedure to reconstruct the neutrino energy for the present analysis.

### 6.4.1 Automatic selection of 1$\mu$1p QE simulated events

Fewer additional requirements were introduced in the original signal definition at true level quantities targeting the best sample that could be obtained. This allowed to optimize the neutrino energy resolution and to perform some test to validate an automatic selection procedure with QE events.

- $\nu_\mu$CC events with its vertex inside the fiducial volume
- Only quasi-elastic neutrino interactions
- 1 muon of at least 50 cm length
- 1 proton with deposited energy greater than 50 MeV in the collection plane, which corresponds to ∼2.3 cm of range
- All visible primary particles contained within 5 cm from the active TPC borders
- No neutral pions allowed and 0 charged pions with $E_{dep} > 25$ MeV

- 0 neutrons with $E_{dep} = E_{dep}(n) + \sum E_{dep}(\text{daughters}) > 25$ MeV
- No photons with more than 25 MeV of deposited energy

The number of signal events was 17036 for a simulated statistics of $2.5\times 10^{20}$ POT, which provided a neutrino energy resolution essentially identical to the blue curve in Figure 6.24.

All the information available after the pattern recognition and event reconstruction phases, described in Chapter 5, was exploited to build an automatic selection procedure to identify $1\mu 1$p events.

The first selection cut was based on the temporal coincidence between a hit in the CRT system and an optical flash, from the PMTs, inside the 150 ns coincidence gate to reject not contained neutrino interactions or entering cosmic rays. The applied cut checked all the optical flashes happening between 0 and 1.6 $\mu$s from the beam gate opening time, and kept all the spills containing one or more flashes with no associated CRT hit (CRT offline Veto[3]).

Once each spill had been accepted or rejected by the CRT Veto, only slices whose reconstructed interaction vertex was inside the fiducial volume were selected.

Then a region of interest around the triggering PMT flash, being the first one to happen inside the beam spill window, was identified. Optical flashes are characterized by different magnitudes but the region of interest was based on its light barycenter, which was computed as the weighted mean of optical hit positions.

$$\vec{x} = \frac{\sum_i \vec{x}_i \cdot \mathrm{PE}_i}{\sum_i \mathrm{PE}_i} \,, \tag{6.1}$$

where $\vec{x}_i$ represents the coordinate of the PMT detecting the i-th optical hit in the studied flash, and $\mathrm{PE}_i$ is the signal integral in photo-electrons of the i-th optical hit. To identify if an interaction was compatible with an optical flash, the charge barycenter[4] of the reconstructed slice was required to be within a certain distance from the light barycenter. A detailed study on simulated events, showed that a 98% efficiency was achieved when considering a distance of 1 m in all neutrino interactions, rising to almost 99% when only $\nu_\mu$CC QE events, fully contained and with a muon of at least 50 cm (Figure 6.25) were present. Two main sources of inefficiencies were identified: poor reconstruction of the event, either due to lost hits or tracks split into two slices, or because of the inclusion of unrelated tracks from cosmic rays overlapping the slice. It was also proven that considering only the beam direction coordinate to compute the distance between both barycenters, a $\sim$10% more signal was selected without significantly introducing background events ($< 2.5\%$), with respect to including also the vertical direction in the calculation. Therefore, the cut was set to find the triggering flash and reject all slices whose charged z-barycenter was more than 1 m away from the light z-barycenter.

The next sequence of selection cuts used only the information from the TPC reconstruction. An important variable that was used throughout the selection is the so-called track score, contained between 0 and 1. This is obtained during the Pandora reconstruction chain, which uses a Boosted Decision Tree (BDT) algorithm to classify an event as a track or as a shower according to the values of a set of reconstructed quantities associated to it, describing the geometrical and charge distribution of the hits. The track score distribution for a set of different particles is shown in Figure 6.26. Track-like objects like muon, pion and proton have larger track scores while shower like particles have generally smaller score values. Due to the non-negligible overlap between the different species, it was decided to consider a track only if its track score was greater or equal than 0.5. Since the vast majority of protons are concentrated at values around 0.5, it was decided to lower their track score threshold to 0.4 for the identification of a proton candidate.

[3]Preliminary results of the CRT-PMT matching for cosmic rejection implemented in ICARUS can be seen in Ref. [177].

[4]The charge barycenter is calculated in an analogous way from the light barycenter, changing only the integral of the optical hit by the integral of the gaussian hit recorded in the collection plane.

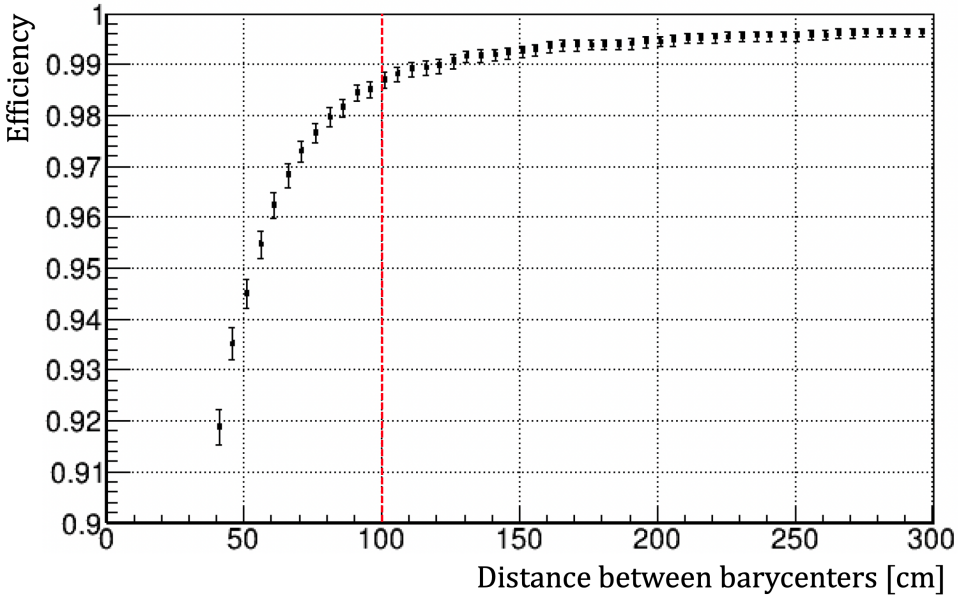


Figure 6.25: Efficiency curve as a function of the cut placed between the distance of the light and charge barycenters in the z coordinate, for simulated $\nu_\mu$CC QE fully contained interactions, with a muon of at least 50 cm. The red line indicates the chosen cut at 1 m, with an efficiency of almost 99%. Plot taken from Ref. [178].

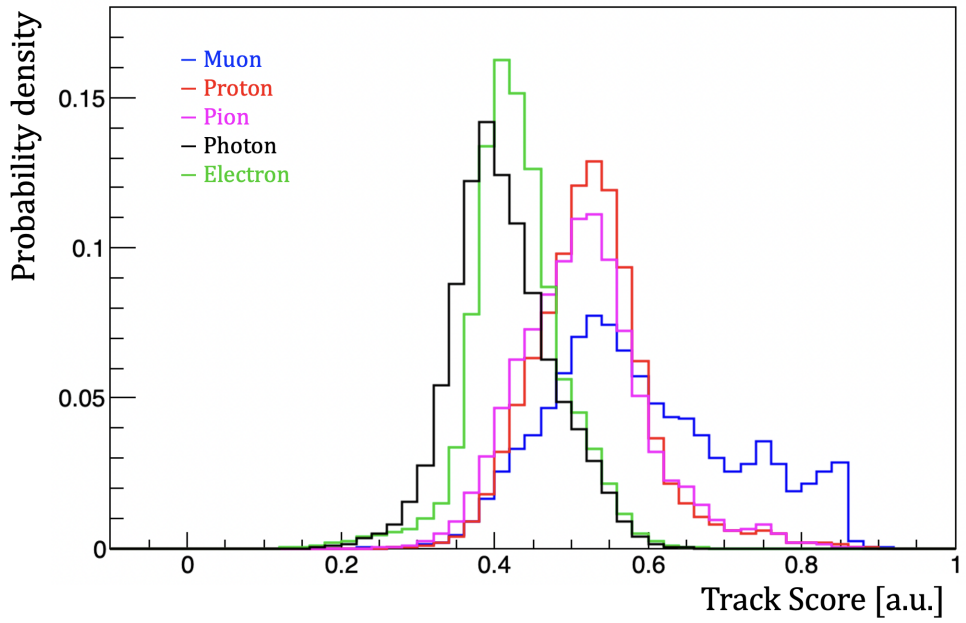


Figure 6.26: Track score values for different simulated particles obtained with a BDT algorithm within Pandora. Values towards 1 indicate track-like objects, while smaller scores are sign of a more shower-like behaviour.

Figure 6.27 shows the previous track score as a function of the true kinetic energy for different particles. Higher scores are obtained for higher kinetic energies in the case of track-like particles, opposite to the behaviour observed for photons.

Great efforts are being made within the collaboration to train a new BDT that has better discrimination performance, since the one currently used was produced years ago and does not benefit from all the improvements that have occurred at the reconstruction level.

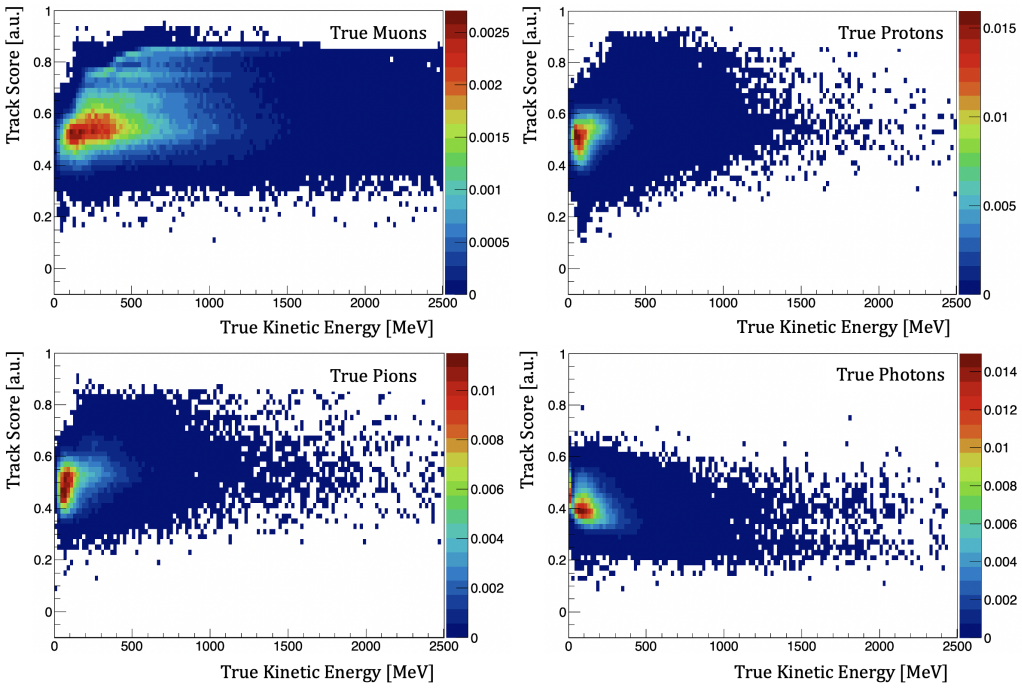


Figure 6.27: Track score values for muons, protons, pions and photons as a function of their true kinetic energy. Entries have been normalized to have a unitary integral.

The muon track was identified as the longest track in the slice fulfilling all the following criteria to reproduce the conditions imposed during the visual analysis:

- Tagged as primary particle by the reconstruction code
- Identified as track-like object, track score $\geq 0.5$
- Length of the track greater than 50 cm
- Reconstructed start of the track within 10 cm from the interaction vertex
- Tagged as a muon, namely $\chi^2_\mu < 30$ and $\chi^2_p > 60$

To be noted the introduction of the track score and the requirement to have a track attached to the vertex, reinforcing the condition to be a primary particle, and in addition well reconstructed.

Once the muon was identified, the containment of all reconstructed primary tracks was checked by requiring them to be within 5 cm from the active TPC boundaries.

Finally, two additional conditions were applied: no visible pions present in the event and only one additional primary reconstructed object compatible with a proton. The $\chi^2_\mu$ and $\chi^2_p$ were exploited to reject charged pion events without affecting the genuine signal. The scatter plots of these variables are shown for true muons, protons and charged pions in Figure 6.28, where pions present a very similar behaviour to the muons. Pions were rejected by requiring that, excluding the muon, there was no primary track (track score $\geq$0.5) in the slice with a $\chi^2_p > 100$ and kinetic energy greater than 25 MeV, where the kinetic energy was calculated by the track range under the pion hypothesis.

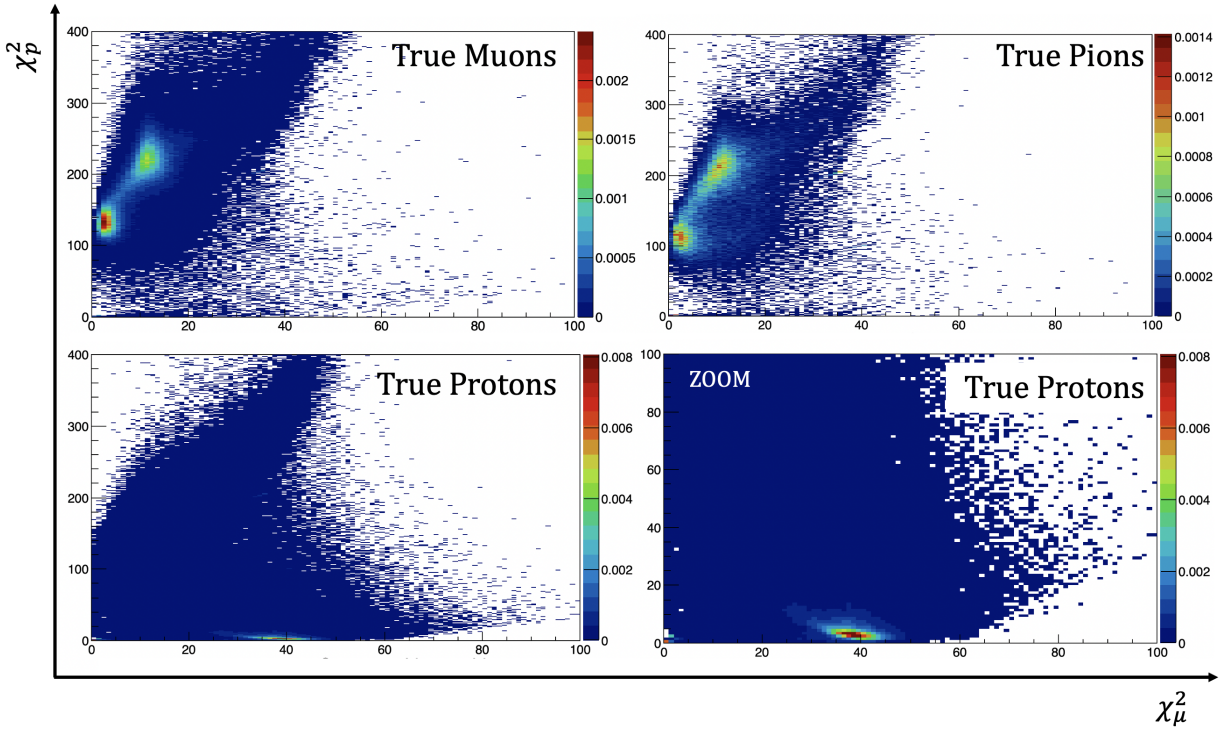


Figure 6.28: $\chi^2_p$ values as a function of $\chi^2_\mu$ for different particles. Top left and right plots show true muons and pions respectively, while protons are shown in the bottom. The bottom right is just a zoom of the left image, to better visualize the bulk of the distribution. All plots have been normalized to 1 to ease the comparison among them.

The check on the Particle-Flow Particles reconstructed objects (PFPs) was done to all tagged primary particles excluding the already identified muon and using exclusively information from the TPC collection wire signal. The primary PFPs were divided in those with the track score greater or equal to 0.5 and those below 0.5. The kinetic energy of all track-like objects was evaluated from the range under the pion hypothesis if $\chi^2_p > 100$ and assuming a proton track if $\chi^2_p < 100$. Tracks and showers with energy greater than 25 MeV were accounted as visible objects.

For a 1$\mu$1p event two visible PFPs are expected, regardless of whether they are classified as tracks or showers. Hence, all slices with more than two visible and primary PFPs were rejected.

Finally, the second visible PFP was examined to identify if it was a possible proton candidate; requiring a track score $\geq 0.4$, a loose $\chi^2_p < 100$ (see Figure 6.12 right) and a kinetic energy greater than 50 MeV. Slices fulfilling all these cuts, were considered 1$\mu$1p interactions.

The efficiency and the purity of this event selection were evaluated with a sample of simulated BNB neutrino interactions including the out of time cosmics and using the 1$\mu$1p true signal definition at the beginning of this section. The results obtained are shown in Table 6.6, which indicates the number of remaining slices for each cut applied, and normalized to $2.5 \times 10^{20}$ POT. The number of events selected in each step has been divided into three categories based on their associated true interaction. The first column shows the events associated to the signal, the second one to background neutrino interactions and the last one to cosmic related activity.

All automatically selected events are shown in Figure 6.29 as a function of the reconstructed neutrino energy and separately for the different interaction channels. The relative contribution of each interaction is shown in Table 6.7.

| Cut | Signal | $\nu$ Background | Cosmic Background |
|---|---|---|---|
| All reco slices | 17298 - 100% | 257350 - 100% | $8.86{\cdot}10^6$ - 100% |
| CRT-PMT spill cut | 16966 - 98.1% | 227856 - 88.5% | $7.73{\cdot}10^6$ - 87.3% |
| $\nu_\mu$ Fiducial Volume | 16458 - 95.1% | 150182 - 58.4% | $2.35{\cdot}10^6$ - 26.6% |
| Barycenter cut | 16064 - 92.9% | 143864 - 55.9% | 144787 - 1.6% |
| Muon Track id. | 12221 - 70.6% | 40557 - 15.8% | 3254 - 0.04% |
| Containment primaries | 12042 - 69.9% | 36587 - 14.2% | 2606 - 0.03% |
| No pions cut | 10402 - 60.1% | 27465 - 10.7% | 2214 - 0.02% |
| 2 visible PFP | 8125 - 47.0% | 9127 - 3.5% | 594 - 0.01% |
| 1$\mu$1p candidates | 7262 - 42.0% | 5890 - 2.3% | 129 - <0.01% |
| Total selected | | 13281 | |

Table 6.6: Number of events after the application of each selection cut, depending on whether they belong to the signal, the neutrino background or the cosmic interaction.

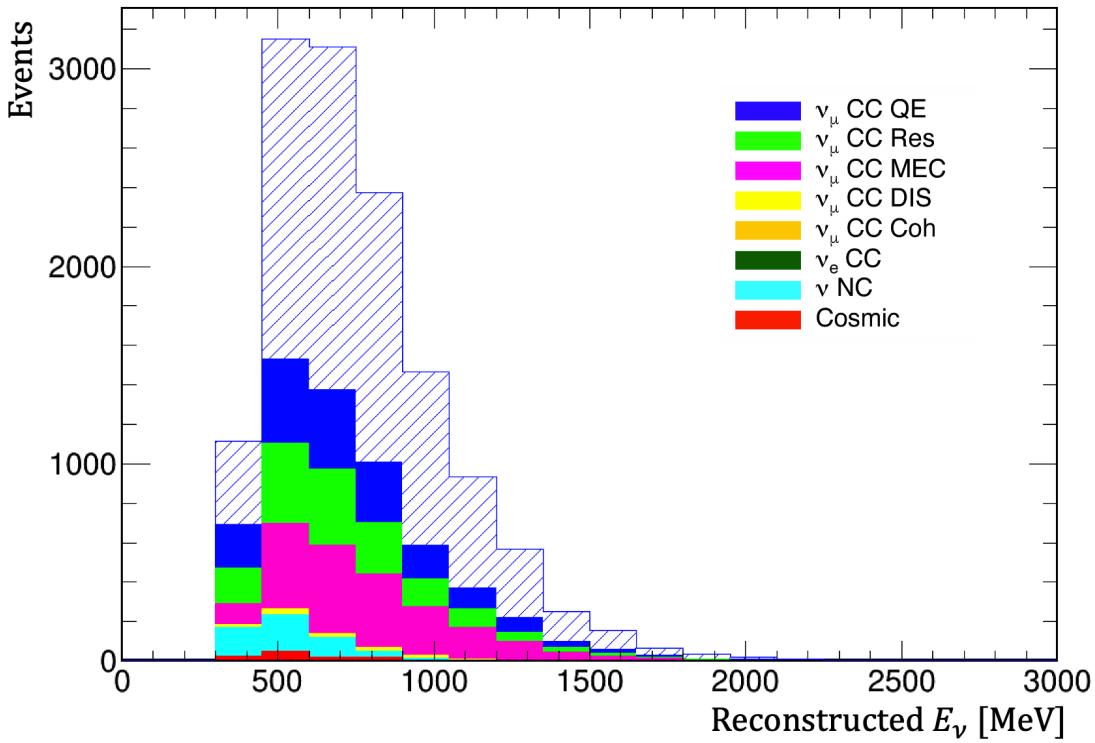


Figure 6.29: Energy spectrum of all events automatically selected with the cuts described in the text. The signal selected is shown in dashed blue, while the backgrounds have been divided based on their neutrino interaction or cosmic origin. Histograms are stacked and the number of entries have been normalized to an exposure of $2.5 \times 10^{20}$ POT.

| Signal QE | $\nu_\mu$CC QE Bkg | $\nu_\mu$CC Res | $\nu_\mu$CC MEC | $\nu_\mu$CC DIS | $\nu_\mu$CC Coh | $\nu_e$CC | $\nu$NC | Cosmic |
|---|---|---|---|---|---|---|---|---|
| 54.7% | 13.4% | 11.9% | 14.7% | 0.7% | 0.1% | <0.1% | 3.6% | 1.0% |

Table 6.7: Contribution of different interaction types to the 1$\mu$1p signal.

Taking into account that the total number of true simulated 1$\mu$1p contained QE events was 17036, the purity and efficiency of the automatic selection was computed.

$$\text{Efficiency} = \frac{\text{Selected signal}}{\text{True signal}} = 42.6\%$$

$$\text{Purity} = \frac{\text{Selected signal}}{\text{All selected events}} = 54.7\%$$

Further studies were carried out to understand the typology of the 13.4% of $\nu_\mu$CC QE events classified as background. It was found that in ∼22% of the cases, the muon or the leading proton was not contained at true level while being reconstructed as contained. The remaining ones were identified as events with no proton over threshold or containing more than 2 visible particles. There were a handful of events containing also a pion at true level which was not reconstructed or properly identified by the reconstruction[5].

The energy resolution obtained using all the automatically selected events is shown in Figure 6.30, where the contribution of signal and background has been explicitly divided. Figure 6.31 shows how energy is reconstructed as a function of the neutrino true energy, to better visualize the dispersion in each category.

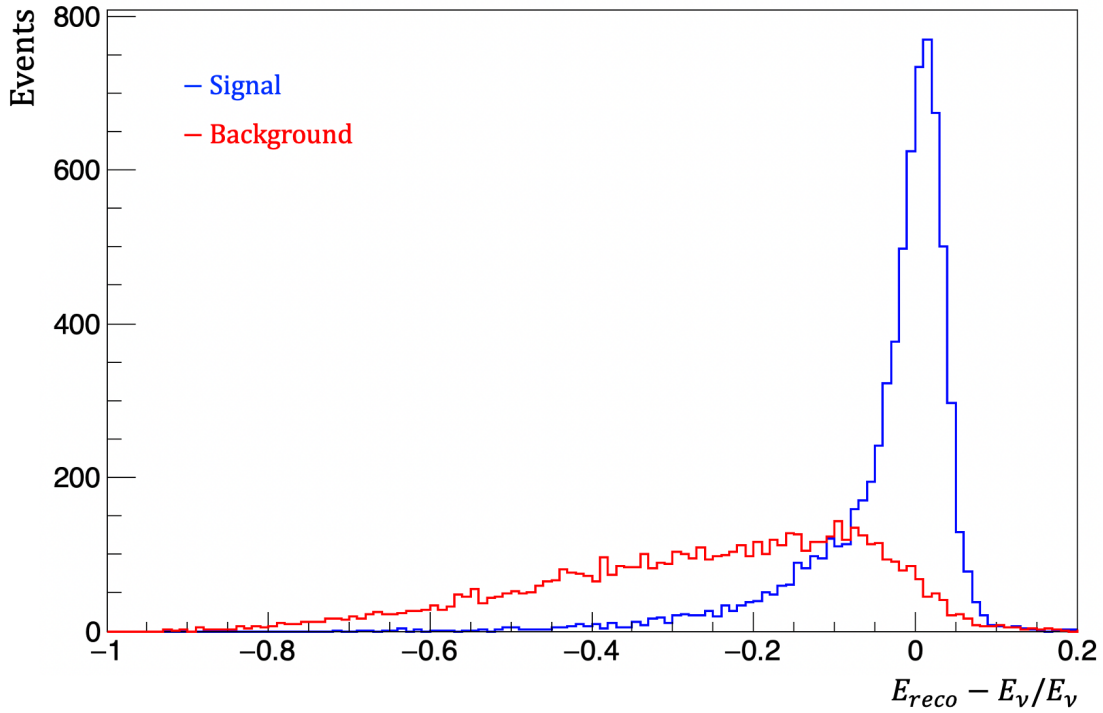


Figure 6.30: Energy resolution for all automatically selected events, computed as the difference between the reconstructed and the true neutrino energy over the last one. Signal and background events have been explicitly separated to evidence their different distributions.

It is important to notice that the simulated events used so far, contained only neutrinos and out of time cosmics. A similar analysis was applied to a low statistic sample of simulated in-time cosmic events, showing that the contribution of in-time cosmic alone to the total number of selected events was ∼ 0.5%.

[5] A QE interaction can produce a pion exiting the nuclei due to the presence of final state interactions. These might arise during the passage of final state particles through the nucleus when a neutrino interacts with a heavy nucleus, such as the argon. Additional processes can occur before the initial neutrino interaction products are able to leave the nucleus, altering the contents and the kinematics of the observed final state in the detector [164].

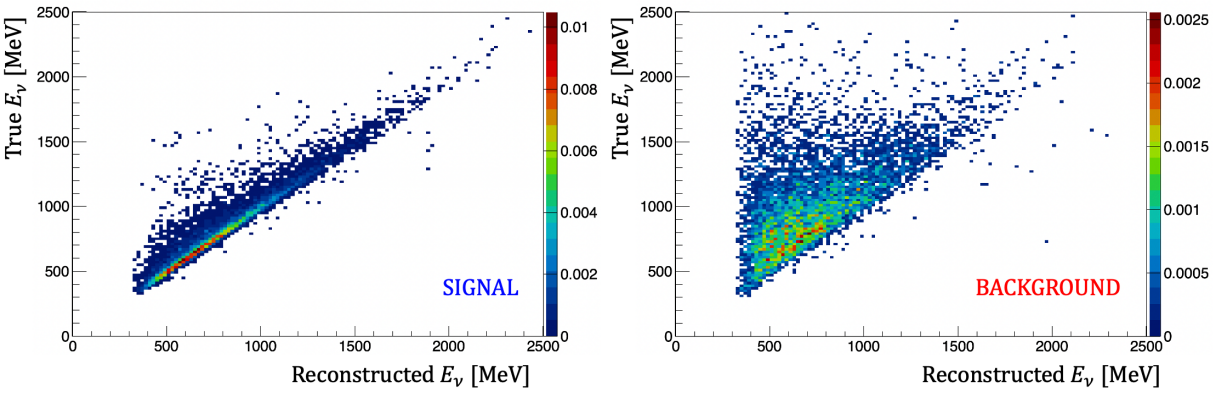


Figure 6.31: Reconstructed neutrino energy as a function of the true value, for all automatically selected events. Left shows the dispersion for signal events, while the background scatter is shown on the right hand side. Both plots have been normalized to 1.

A large production of neutrino only events was simulated to quantify the impact on the event selection and reconstruction quality due to the out of time cosmics randomly overlapping the neutrino events. The total statistics was $5.6{\cdot}10^{20}$ POT, almost twice the available statistics for the neutrino plus cosmics sample. After applying the selection procedure, the results of Table 6.8 were obtained.

| Cut | Signal | $\nu$ Background |
|---|---|---|
| All reco slices | 17817 - 100% | 271497 - 100% |
| CRT-PMT spill cut | 17742 - 99.6% | 240240 - 88.5% |
| $\nu_\mu$ Fiducial Volume | 17331 - 97.3% | 158711 - 585% |
| Barycenter cut | 17089 - 95.9% | 154356 - 56.9% |
| Muon Track id. | 13207 - 74.1% | 42480 - 15.6% |
| Containment primaries | 13171 - 73.9% | 38969 - 14.4% |
| No pions cut | 11476 - 64.4% | 29345 - 10.8% |
| 2 visible PFP | 9157 - 51.4% | 9678 - 3.6% |
| 1$\mu$1p candidates | 8334 - 46.8% | 6468 - 2.4% |
| Total selected | 14802 | |

Table 6.8: Events selected at each step of the selection procedure, for a sample of neutrino only simulated events. As before, the events have been divided as a function of the association to their true interaction.

As a conclusion, by comparing Table 6.8 and Table 6.6, the presence of overlapping out of time cosmic rays reduces by $\sim$ 11% the number of selected neutrino events and by $\sim$ 13% the signal efficiency.

In order to improve the efficiency and purity of the selection, several events from two different categories were studied in detail. First, signal events that did not pass the cuts were analyzed to find possible causes of inefficiency. Second, selected background events were studied to improve the purity.

The main source of inefficiency were identified as failures on creating a PFP containing the proton, due to true muons or protons failing their $\chi^2$ particle id cut or events containing more than 2 PFPs. The first problem is related to Pandora's performance which would require a

sophisticated modification of its algorithms.

The other two issues were addressed modifying the selection. First of all, unphysical reconstructed hits with $dE/dx$ signals below 0.5 MeV/cm or above 100 MeV/cm were excluded from the $\chi^2$ calculation algorithm, increasing by ~3% the purity of the sample without impacting the efficiency.

The second modification was applied to primary tagged particles, since as shown in Figure 6.32, some tracks were labeled as primary even if they were more than 5 m away from the interaction vertex. To avoid this, primary tracks were required to have either the start or end position within 50 cm from the reconstructed vertex. In addition, and to ensure a well proton reconstruction, the leading protons were further required to start not more than 10 cm away from the vertex.

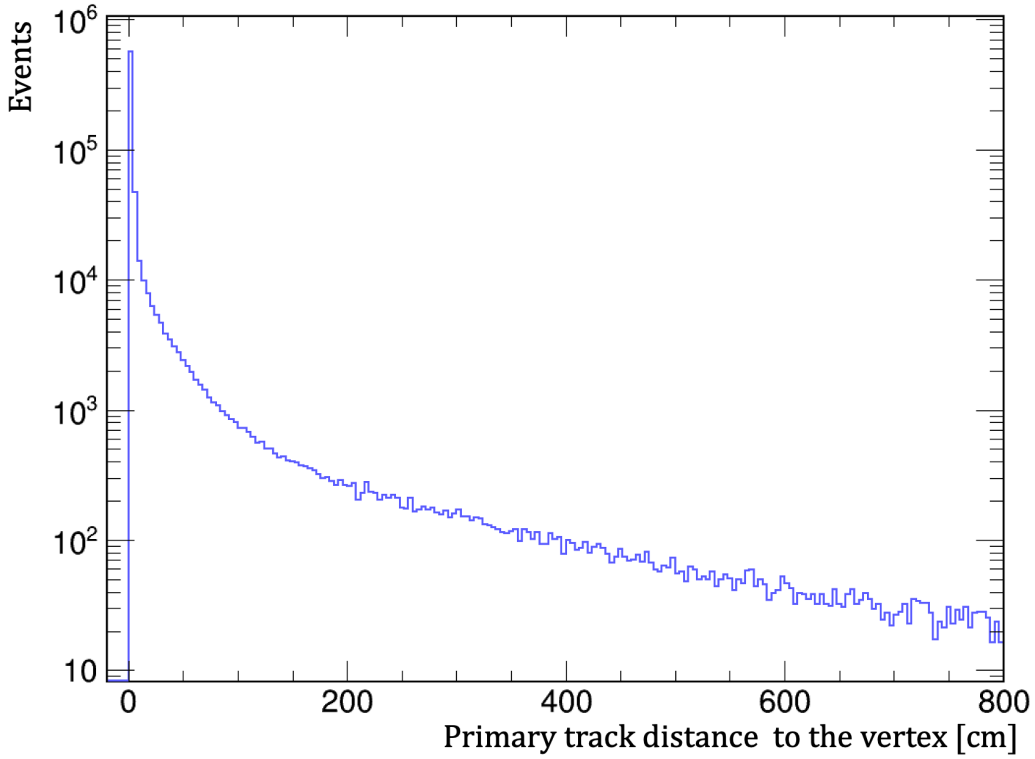


Figure 6.32: Distance between the closest start or end point of a primary track to the reconstructed vertex. All primary tracks within a reconstructed slice associated to a neutrino background interaction are shown.

The backgrounds were observed to be mainly driven by events in which an additional primary particle was not identified, by extra PFP with $\chi^2 = 0$ in the collection plane, or by events that were not actually contained. Two solutions were implemented: to identify exiting particles, the containment condition was extended to both primary and secondary reconstructed objects inside each slice. $\chi^2 = 0$ is caused by tracks without hits in the delimited $dE/dx$ range used in the calculation of $\chi^2$. To solve this problem it was chosen to use the plane with most reconstructed hits between Induction 2 and Collection planes with the aim of maximizing both sample purity and selection efficiency.

To reflect these changes, the definition of the MC signal was modified accordingly. Containment was checked for all charged primary and secondary particles, to reject events with secondary tracks exiting the detector. On the other hand, it was noted that tracks quickly interacting and producing secondaries, were not included in the signal definition if the primary was too short or its energy deposition below threshold. Therefore, the deposited energy of each primary particle was redefined to include also the deposited energy of its associated secondaries.

Hence the final true signal definition and automatic selection procedure were implemented as follows.

**Automatic selection of 1$\mu$1p CC events**

The studies performed on well selected clean QE 1$\mu$1p contained events were extended to the analysis of $\nu_\mu$CC interactions with 1$\mu$1p reconstructed topology. The signal definition was modified accordingly to also benefit from all previous results from the QE MC subsample:

- $\nu_\mu$CC events with its vertex inside the fiducial volume
- 1 muon of at least 50 cm length
- 1 proton with deposited energy $E_{\text{dep}} > 50$ MeV
- All charged primary and secondary particles contained within 5 cm from the active TPC borders
- No other particles with $E_{\text{dep}} > 25$ MeV

where $E_{\text{dep}}(\text{primary}) = E_{\text{dep}}(\text{primary}) + E_{\text{dep}}(\text{secondaries})$. The deposited energy of all tracks was computed using the TPC plane with higher number of reconstructed hits between Induction 2 and Collection; which turned out to be used in approximately equal proportions. 19,373 MC events satisfying the above criteria were found considering $2.5 \times 10^{20}$ POT, with the energy spectrum shown in Figure 6.33. The vast majority of events were found to be QE interactions (88.7%), while the other channels had a smaller contribution: 8.8% of MEC, 2.4% of Res and 0.1% of DIS.

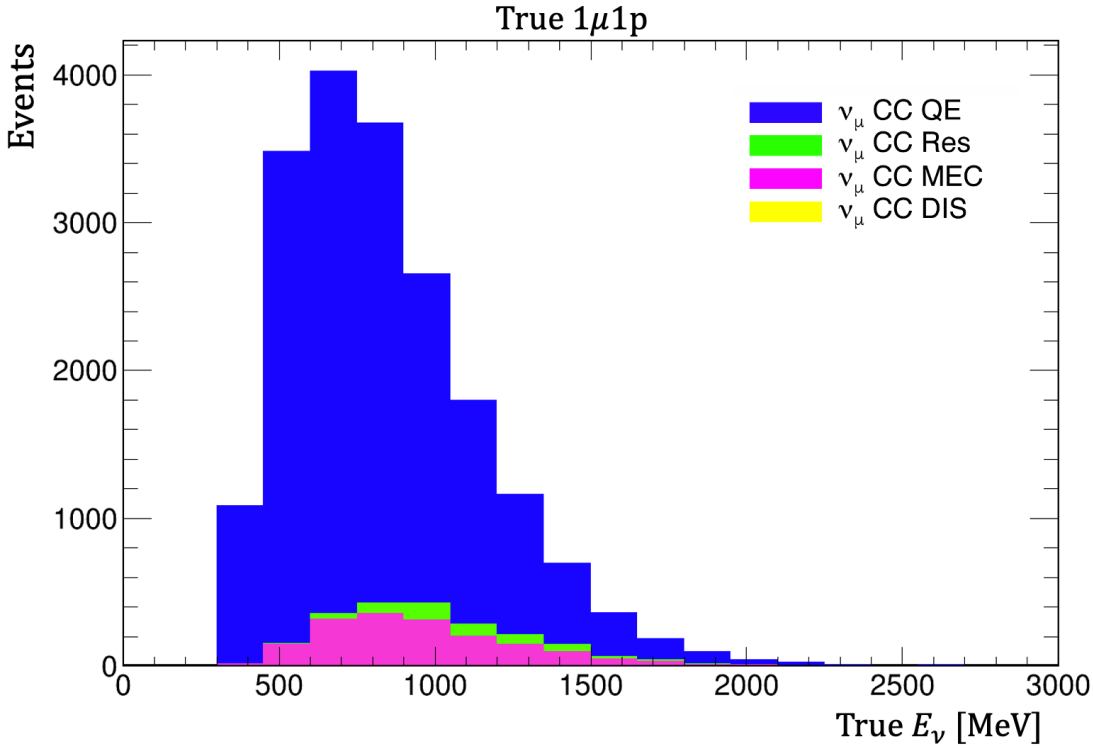


Figure 6.33: Energy spectrum of 1$\mu$1p events as a function of their neutrino interaction mode. Histograms are stacked and normalized to a $2.5 \times 10^{20}$ POT.

To select this 1$\mu$1p signal the following automatic procedure was implemented:

1. $\nu_\mu$CC events with reconstructed vertex inside the fiducial volume
2. CRT Veto: no CRT - PMT in-time matching inside the 1.6 $\mu$s beam spill
3. TPC - PMT matching: require z-barycenter of interaction to be within 1 m from the light z-barycenter of the triggering flash
4. All reconstructed objects contained within 5 cm from the active TPC borders
5. Muon identification corresponding to longest track in the slice satisfying
   - Start point within 10 cm from the reconstructed vertex
   - Length of at least 50 cm
   - Tagged as primary track
   - Track score $\geq 0.5$
   - $\chi^2_\mu < 30$ and $\chi^2_p > 60$
6. 0 reconstructed pions: excluding the already identified muon, no reconstructed primary tracks fulfilling all the following requirements
   - track score $\geq 0.5$
   - 50 cm from the interaction vertex, either the start or end point
   - $\chi^2_p \geq 100$
   - Kinetic energy greater than 25 MeV, from track range under the pion hypothesis
7. Only 2 visible primary PFPs: exactly 2 primary PFPs with more than 25 MeV of kinetic energy. Only primary tracks within 50 cm from the reconstructed vertex are considered and one of the two PFPs needs to be the muon candidate
8. Proton identification: the non-muon PFP identified in the previous step needs to fulfill the following conditions to be tagged as a proton candidate.
   - Start point within 10 cm from the reconstructed vertex
   - Tagged as primary track
   - Track score $\geq 0.4$
   - At least 50 MeV of kinetic energy, range based measurement
   - $\chi^2_p < 100$

Where all calorimetric quantities were computed by the TPC wire signals in the most populated view. The procedure selected 12,916 events, whose energy spectrum is shown with the contribution of each interaction channel in Figure 6.34 and Table 6.9.

| | $\nu_\mu$CC QE | $\nu_\mu$CC Res | $\nu_\mu$CC MEC | $\nu_\mu$CC DIS | $\nu_\mu$CC Coh | $\nu_e$CC | $\nu$NC | Cosmic |
|---|---|---|---|---|---|---|---|---|
| Signal | 60.3% | 1.4% | 5.4% | <0.1% | | | | |
| Bkg | 10.3% | 8.8% | 8.8% | 0.6% | 0.1% | <0.1% | 3.6% | 0.6% |

Table 6.9: Interaction classification of all events identified with the automatic 1$\mu$1p selection. Percentages are computed with respect to the total number of selected events (12916).

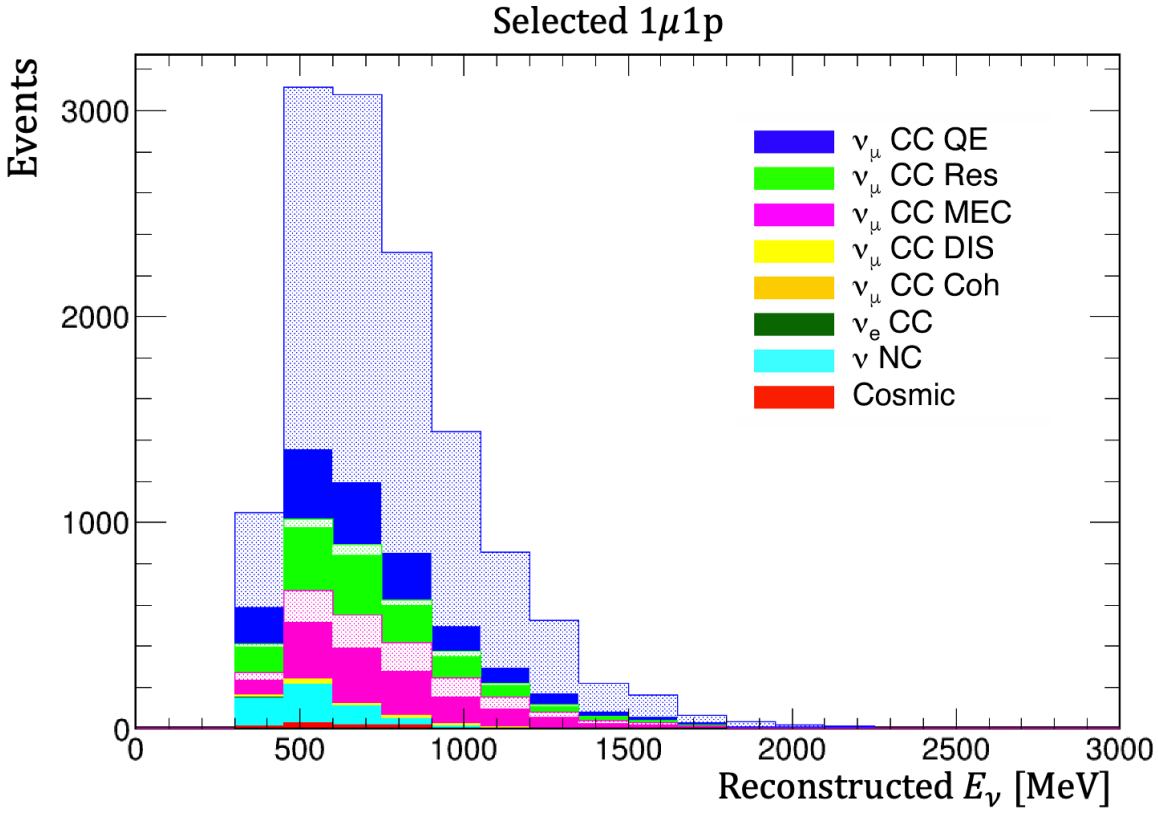


Figure 6.34: Energy spectrum of all events identified with the automatic 1$\mu$1p final selection. The signal selected is shown in dotted pattern, while the backgrounds are represented with filled histograms. All contributions have been identified according to their neutrino interaction or cosmic origin. As before, histograms are stacked and the number of entries have been normalized to an exposure of $2.5 \times 10^{20}$ POT.

The particle identification performance was assessed for all automatically selected muon and proton candidates. $\sim$ 95% of the muon candidates were associated to a true muon, and analogously for the proton candidate, showing a robust particle identification. The largest background contributions to the muon were due to misidentified $\pi^{\pm}$, while muons and pions were the main sources of the proton identification failures.

The progress of the selection with each cut applied is shown in Table 6.10.

The biggest background contribution comes from other type of neutrino interaction, misclassified as 1$\mu$1p events. Notice that only $\sim$ 1% of selected events have a cosmogenic origin, when the in-time cosmics are included. This suppose a big improvement given the large cosmic flux to which ICARUS is exposed.

The purity and efficiency of the 1$\mu$1p selection were found to be:

$$\text{Efficiency} = \frac{\text{Selected signal}}{\text{True signal}} = 44.7\% \ ,$$

$$\text{Purity} = \frac{\text{Selected signal}}{\text{All selected events}} = 67.1\% \ .$$

| Cut | Signal | $\nu$ Background | Cosmic Background |
|---|---|---|---|
| All reco slices | 19752 - 100% | 254896 - 100% | $8.86{\cdot}10^6$ - 100% |
| CRT-PMT spill cut | 19383 - 98.1% | 225439 - 88.4% | $7.73{\cdot}10^6$ - 87.3% |
| $\nu_\mu$ Fiducial Volume | 18824 - 95.3% | 147816 - 58.0% | $2.36{\cdot}10^6$ - 26.6% |
| Barycenter cut | 18318 - 92.7% | 141610 - 55.6% | 144787 - 1.6% |
| Slice containment | 17585 - 89.0% | 87757 - 34.4% | 90771 - 1.0% |
| Muon Track id. | 14071 - 71.2% | 34229 - 13.4% | 2651 - 0.03% |
| No pions cut | 12255 - 62.0% | 25659 - 10.1% | 2260 - 0.03% |
| 2 visible PFP | 9837 - 49.8% | 7843 - 3.1% | 478 - 0.01% |
| 1$\mu$1p candidates | 8662 - 43.9% | 4175 - 1.6% | 79 - <0.01% |
| Total selected | | 12916 | |

Table 6.10: Survival events after each cut of the final 1$\mu$1p automatic selection depending on whether they belong to the signal, the neutrino background or generated by cosmic interactions (in-spill contribution not included).

The neutrino energy resolution is shown in Figure 6.35 left for the selected signal and neutrino background events, separately. On the other hand, the reconstructed transverse momentum was computed for all selected events, as shown in Figure 6.35 right.

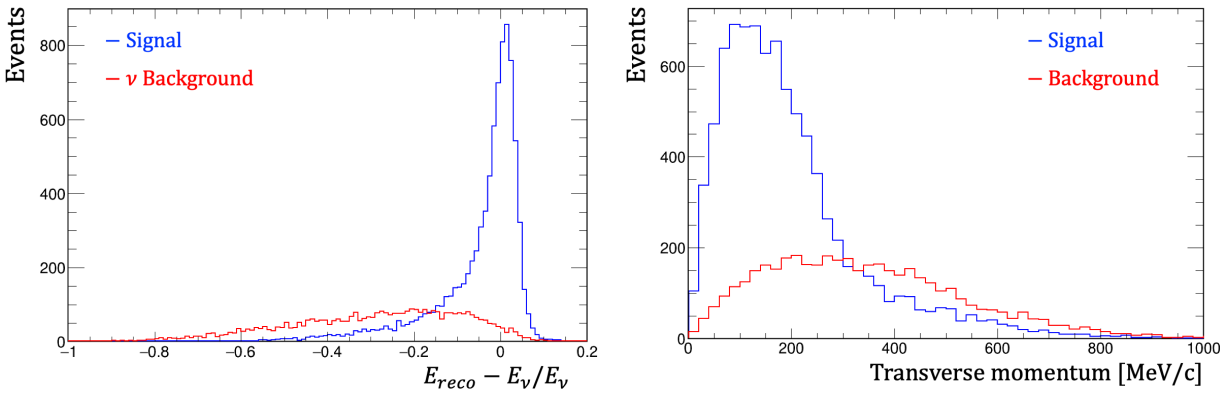


Figure 6.35: Left: Energy resolution for automatically selected events, where the blue curve shows the resolution for signal events, while the red curve represents the neutrino background contribution. Right: Reconstructed transverse momentum for all automatically selected events, showing the values of signal and all background separately.

Figure 6.36 shows the correlation between the energy resolution and the transverse momentum, indicating that events with large reconstructed transverse momentum are associated with worse neutrino energy measurements

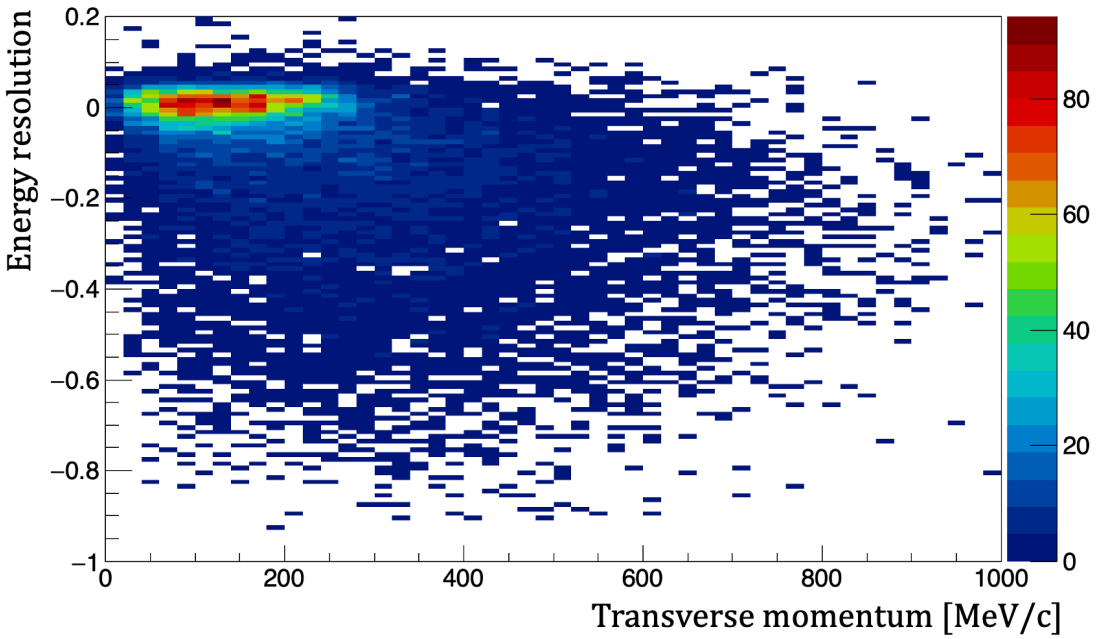


Figure 6.36: Energy resolution as a function of the transverse momenta for all selected events associated to neutrino interactions, either signal or background.

To better understand the impact of each single step during the automatic selection, the effect of each cuts was plotted as a function of the true neutrino energy, as shown in Figure 6.37. Each line represents the fraction of events passing a specific cut with respect to the initial sample. Error bands indicate statistical binomial errors, which are upper limited when reaching 100% efficiency. The last energy bin was expanded to account for the lack of statistics at energies above 2.25 GeV.

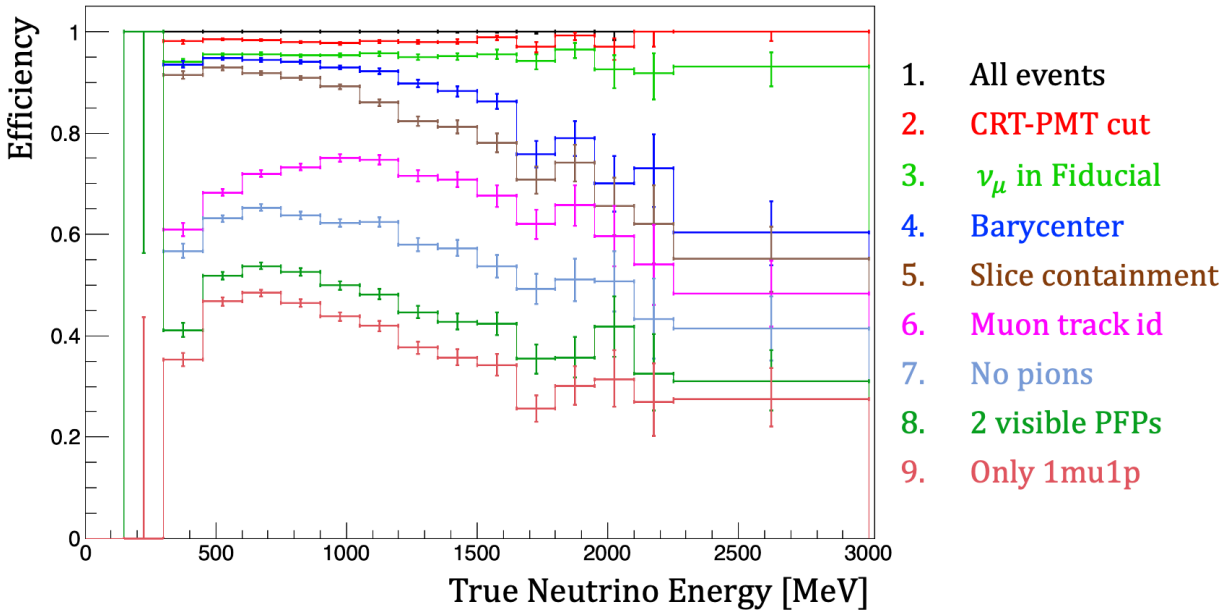


Figure 6.37: Selection efficiency of each cut with respect to the initial sample of events, shown over the entire range of true neutrino energy. The graph contains only signal events and error bands just indicate statistical errors.

The selection applied is not uniform across all energies, but rather some cuts have a stronger impact at higher energies, while others reject more events at lower energies. To quantify this effect, each cut was plotted with respect to the previous one, as shown in Figure 6.38, where any deviation from an horizontal line indicates some energy dependency.

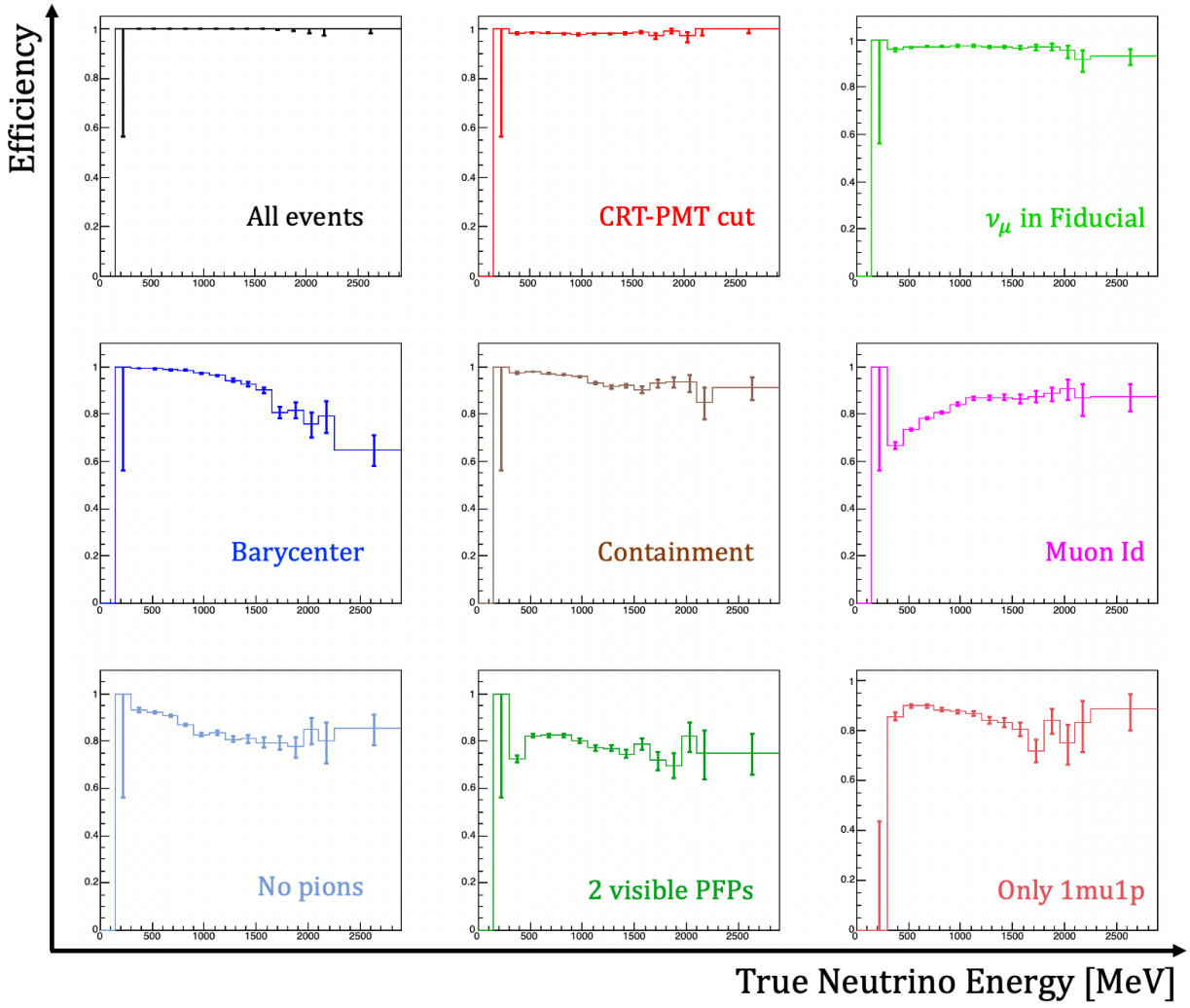


Figure 6.38: Selection efficiency of each cut with respect to the previous one for signal events as a function of true neutrino energy. Only statistical errors are shown.

The first feature appears in the TPC-PMT matching becoming more inefficient at higher energies, where the probability of splitting long tracks is greater spoiling the charge barycenter calculation. On the contrary, the muon identification is less efficient at low energies, which might be related to the 50 cm length requirement. Short muons might have a reconstructed length $L_\mu < 50$ cm or suffer more scattering resulting in a split track, that fails the 50 cm muon requirement. Misplacement of the interaction vertex might also play a role, enhancing the problem when short tracks are present. Last three cuts have a less straight forward explanation and will be further studied in the near future to optimize their performance.

The ultimate goal of the event selection is to provide an oscillation measurement, in particular a BNB $\nu_\mu$ disappearance analysis. Just for the sake of illustration, it is possible to compute the survival probability of the selected events, under an oscillated hypothesis. Even though the Neutrino-4 claim [76] can only be directly tested with $\nu_e$ samples, the $\nu_\mu$ disappearance channel is sensitive to the $\sin^2(2\theta_{\mu\mu})$ and the same $\Delta m^2_{14}$ in the 3+1 sterile model, as shown in Eq. 2.62. A consistent theory model requires signals in all three oscillation modes, $P(\nu_\mu \longrightarrow \nu_\mu)$, $P(\nu_\mu \longrightarrow \nu_e)$ and $P(\nu_e \longrightarrow \nu_e)$, which can be rewritten in the following form [179]:

$$P_{\mu\mu} \equiv P(\nu_\mu \longrightarrow \nu_\mu) \simeq 1 - \sin^2(2\theta_{24}) \sin^2\left(1.27\Delta m^2_{41} L/E_\nu\right) \ , \tag{6.2}$$

$$P(\nu_\mu \longrightarrow \nu_e) \simeq \frac{1}{4} \sin^2(2\theta_{14}) \sin^2(2\theta_{24}) \sin^2\left(1.27\Delta m^2_{41} L/E_\nu\right) \ , \tag{6.3}$$

$$P(\nu_e \longrightarrow \nu_e) \simeq 1 - \sin^2(2\theta_{14}) \sin^2\left(1.27\Delta m^2_{41} L/E_\nu\right) \ . \tag{6.4}$$

Assuming the Neutrino-4 $\bar{\nu}_e$ amplitude and $\Delta m^2$ to perform an example of a $\nu_\mu$ analysis

$$\sin^2(2\theta_{14}) = 0.36 \pm 0.12(stat) \quad \text{and} \quad \Delta m^2_{14} = 7.3 \pm 0.13(stat) \pm 1.16(syst)\ eV^2 \ ,$$

it is possible to define

$$P(\nu_\mu \longrightarrow \nu_\mu) \simeq 1 - 0.36 \sin^2\left(1.27 \cdot 7.3 \cdot L/E_{\nu_\mu}\right) \ ,$$

where $L$ and $E_{\nu_\mu}$ were taken to be the true values of simulated events. The true energy spectrum of all neutrino-induced interactions selected with the automatic procedure is shown in Figure 6.39 left. Instead, Figure 6.39 right shows the reconstructed energy spectrum for all selected events, including the cosmic contribution. The oscillated spectrum was obtained by weighing the initial distribution by a factor $P_{\mu\mu}$ to reproduce the spectrum that should be observed in the presence of sterile neutrinos, where cosmic events were left unoscillated.

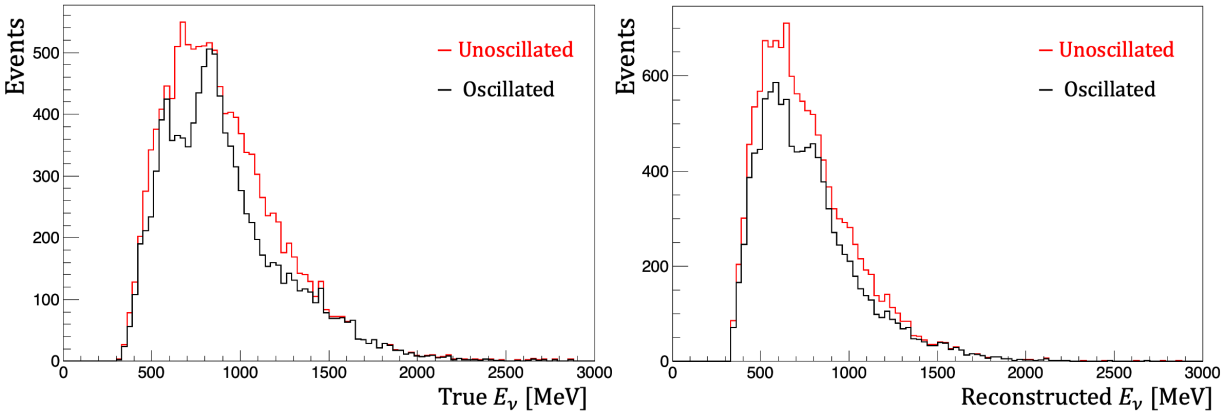


Figure 6.39: Left: True energy spectrum for all neutrino induced interaction that have been automatically selected. Right: Reconstructed energy spectrum including all selected events, using the true neutrino baseline (L). The oscillated spectrum is weighted with respect to the original one by $P_{\mu\mu}$, to simulate the sterile neutrino impact. $P_{\mu\mu} = 1$ for cosmic events.

The survival probability shown in Figure 6.40 was obtained by dividing the oscillated energy spectrum with respect to the unoscillated one. The amplitude smearing present in the left distribution, is due to the different precise location of neutrino generation inside the decay pipe, resulting into an overlap of slightly different $L/E$ oscillations. The baseline distribution for all true $1\mu1$p events is plotted in Figure 6.41, showing a peak at around 580 m, but also proving that interactions occur from baselines of $\sim$ 540 m to $\sim$ 600 m.

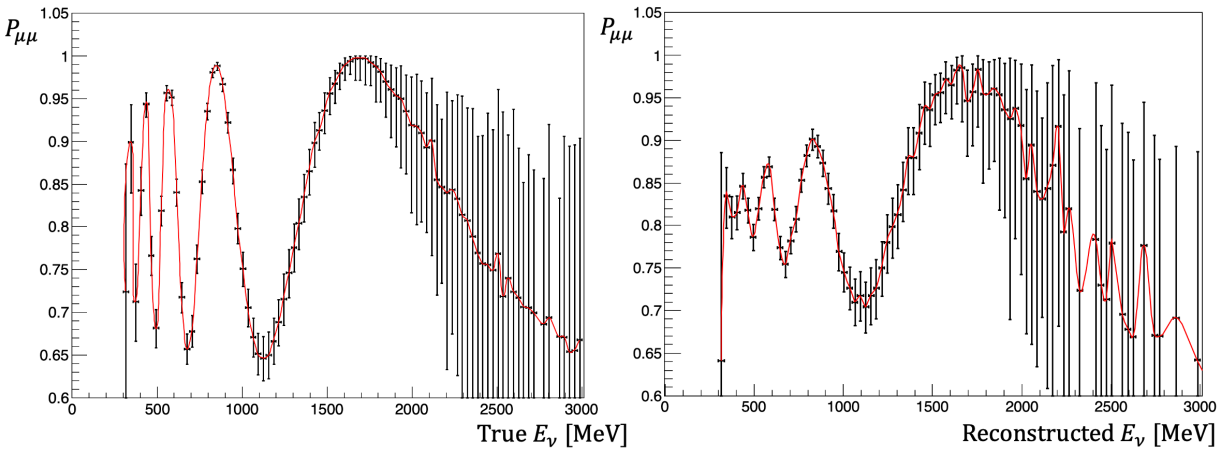


Figure 6.40: Survival probability of selected neutrino candidates. Left plot shows the theoretical behaviour, while on the right the expected shape taking into account the reconstruction effects is presented.

The right plot of Figure 6.40 has the additional reconstruction effect, blurring the oscillatory behaviour but not spoiling the patter present under the hypothesis of sterile neutrinos. It is important to perform a precise evaluation of all systematic uncertainties affecting the 1$\mu$1p measurement to determine the final sensitivity of the $\nu_\mu$CC analysis, thus ICARUS is working to achieve a precise characterization of detector systematics, new measurements of $\nu$-Ar cross sections and a better BNB flux description.

Analogous procedure was applied to the transverse momentum, considering all automatically selected events. The ratio between the reconstructed transverse momentum oscillated to the unoscilated one is shown in Figure 6.41 right. Neutrino-4 $\bar{\nu}_e$ values were used to obtain the oscillated distribution and both histograms were first normalized to 1 to perform a shape only comparison. A linear fit was performed to the ratio, reporting a value compatible with the unit, thereby demonstrating that the transverse momentum is not affected by the mixing of sterile-active neutrinos and can be exploited without inferring any neutrino oscillation properties. The fit was limited to the high statistics region, namely up to $\sim$ 800 MeV/c.

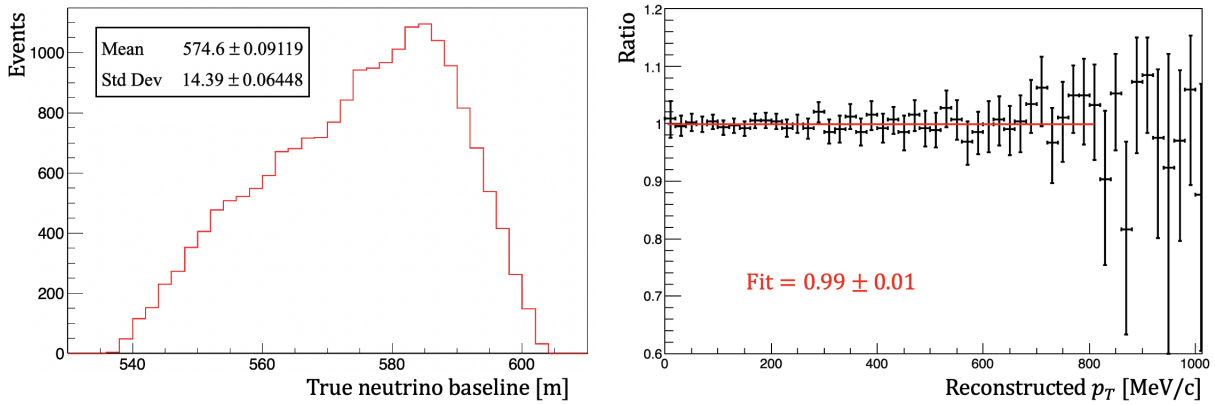


Figure 6.41: Left: Baseline distribution at ICARUS for all true 1$\mu$1p simulated events. Right: Ratio between the oscillated and unoscillated reconstructed transverse momentum, for all automatically selected events. The oscillated histogram was obtained with the following parameters: $\sin^2(2\theta_{14}) = 0.36$ and $\Delta m^2_{14} = 7.3$; and using the entire MC sample scaled to an exposure of $2.5{\times}10^{20}$.

## 6.5 Cross checks with test datasets

The automatic procedure previously described was applied to a small sample of collected data, corresponding to $1.025 \times 10^{18}$ POT, which identified 123 $1\mu1p$ candidates.

A 41% efficiency was evaluated for the selection procedure applied to a sample of 100 events visually identified in a flat scan and certified to satisfy the adopted signal definition. This value should be compared with the $\sim$ 45% efficiency estimated by MC studies, showing agreement given the available statistics. The number of selected events after the application of each cut is reported in Table 6.11.

| Cut | Selected |
|---|---|
| All events | 100 |
| CRT-PMT spill cut | 100 |
| $\nu_\mu$ Fiducial Volume | 100 |
| Barycenter cut | 100 |
| Slice containment | 94 |
| Muon Track id. | 76 |
| No pions cut | 69 |
| 2 visible PFP | 53 |
| $1\mu1p$ candidates | 41 |

Table 6.11: Survival events after each cut of the flat scan data sample, used to evaluate the efficiency of the selection.

All 123 selected events were visually scanned to confirm the topology of the event:

- 87/123 were confirmed to be $1\mu1p$
- 20/123 $1\mu2p$, presented a visually identified additional proton of more than 6 mm length
- 1/123 was a cosmic interaction
- 5/123 were not contained events
- 10/123 resulted to be other interactions, containing more than 3 tracks in the primary vertex, with showers or identified as neutral currents

As a result, the purity of the automatic selection was found to be 70.7%, in agreement with the MC expectations of $\sim$ 67%.

$$\text{Purity} = \frac{\text{Confirmed } 1\mu1p}{\text{All selected events}} = 70.7\%$$

It is important to recall that no trigger emulation has been used so far to select simulated events. As a first approximation it was decided to use the reported values presented in Figure 4.10, and apply an efficiency factor to the MC events based on the true deposited energy of each interaction. Figure 6.42 left shows the reconstructed neutrino energy spectrum for all automatically selected events before and after the introduction of the trigger efficiency, considering only simulated events. A $\sim$ 0.2% modification was observed, with impact restricted to low energy values. Note that the requirement of having a 50 cm muon and a $\sim$ 2.3 cm proton restricts the deposited energy spectrum to values where the trigger efficiency is optimal, and thus its impact is almost negligible.

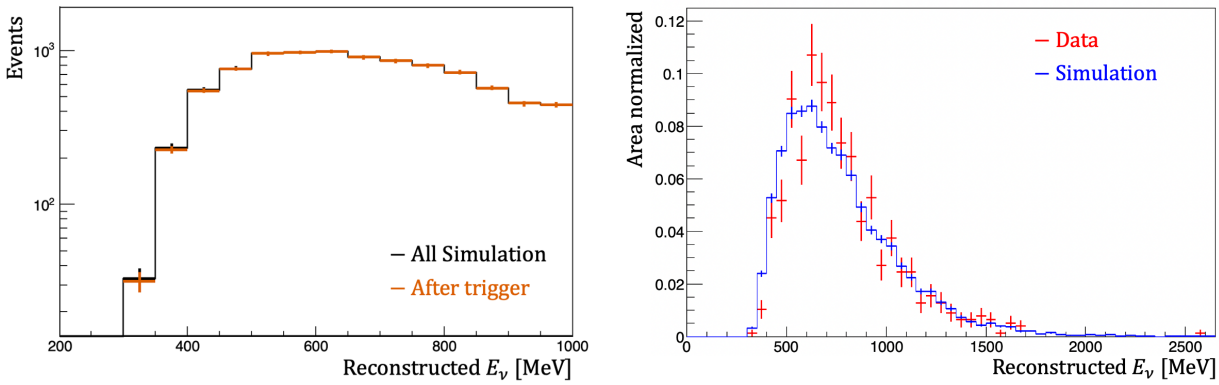


Figure 6.42: Reconstructed neutrino energy for automatically selected events. Left plot shows a MC comparison between all events (black) and the remaining ones after the trigger efficiency factor is applied (also simulated events, in brown), where the vertical axis is set to a logarithmic scale to appreciate the difference. On the right, a data (red) - simulation (blue) comparison is shown using the $\sim 5\%$ of the total collected data and the simulated events after the trigger efficiency. Only statistical errors are shown.

To compare the results from data and simulated events, some reconstructed quantities were analyzed using a $\sim 5\%$ of the total collected data. Even though larger statistics are available, a blinding policy within the ICARUS Collaboration restricts the amount of on-beam data that can be studied to avoid biases in the development of the automatic selection. In addition, only a shape analysis is presented here, all distributions have been normalized to 1, and no systematic uncertainties are included in all these comparisons.

Figure 6.42 right shows the reconstructed energy of the incoming neutrino for data and MC events, illustrating a good agreement in almost all energy values, despite the limited statistics. This MC distribution and all those that will be shown below have the trigger efficiency factor applied.

Figure 6.43 presents the muon and proton reconstructed lengths for all automatically selected events, where data and MC results are reported.

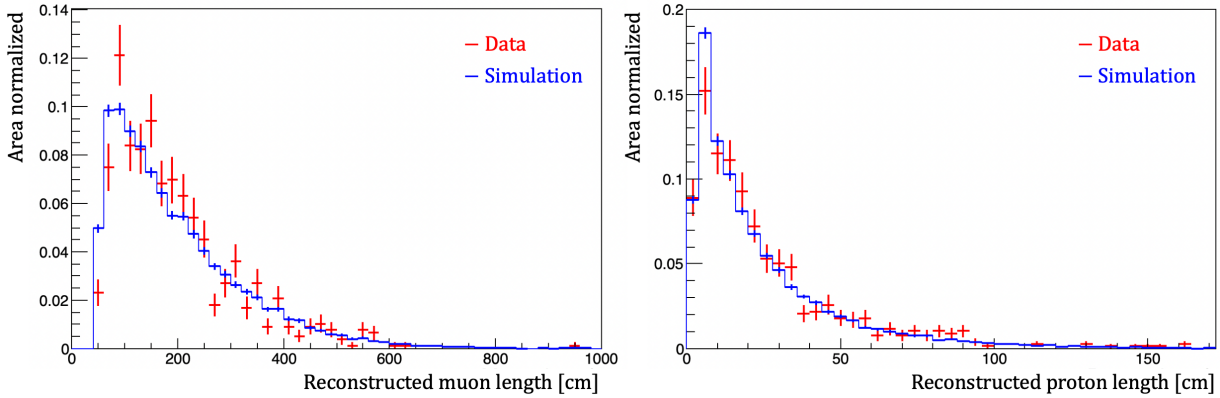


Figure 6.43: Reconstructed muon (left) and proton (right) lengths for automatically selected data and simulated events shown in red and blue respectively. Only statistical errors are shown.

The muon distribution seems to have a reasonable agreement above 1 m long tracks, but some discrepancies are present below that value. This could be related to a poorer reconstruction of short tracks or the more frequent presence of split events in the data than in the simulation. Problems might arise due to length underestimations or because tracks are split into several pieces (scattering is more frequent at low energies), resulting into reconstructed objects not

satisfying the 50 cm length requirement. More studies will follow to understand the origin of this discrepancy, including also a verification of the trigger efficiency values. Even though, the reconstructed proton length shows a better agreement the follow up studies will be extended to the proton as well.

Given the recurrent presence of split tracks a more in depth investigation is planned to mitigate the problem, either modifying the reconstruction code to improve its performance or developing a stitching algorithm to merge the tracks at downstream level.

Figure 6.44 presents the track score for both identified particles of the interaction, where muon and proton track scores show agreement within the errors with MC expectations. It is possible to see that both distributions are shifted towards 0.5-0.6 scores, indicating that track and shower topologies are not robustly distinguished. It is expected that with the new BDT training, a better discrimination will be obtained, which in turn should have a positive impact on the automatic selection.

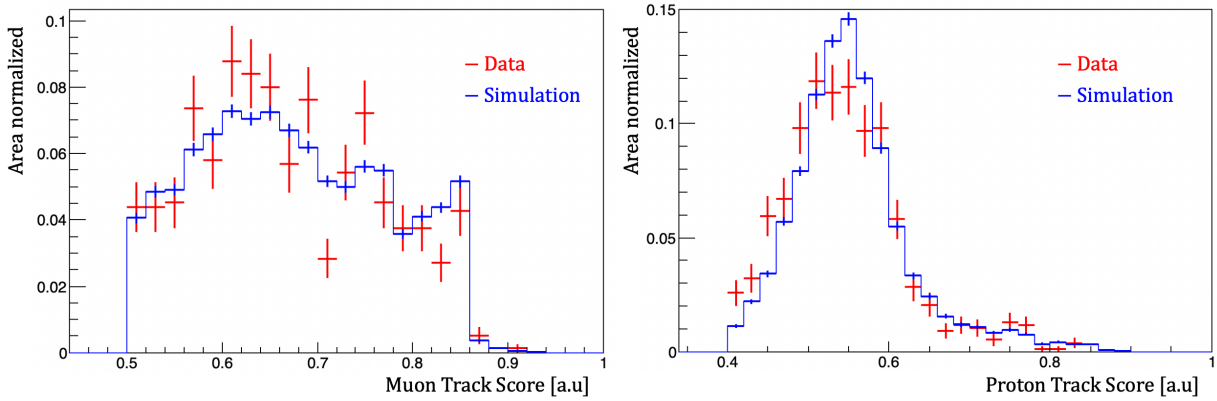


Figure 6.44: Data (red) and MC (blue) comparison of the particle track scores for the muon and proton candidates, where only statistical errors are shown.

The reconstructed total and muon momenta in the transverse plane are shown in Figure 6.45 left and middle, respectively. The total $p_T$ presents the expected behaviour, where the distribution is peaked below $\sim$ 250 MeV/c, compatible with the Fermi momentum of the struck nucleon, and presents a long tail due to the additional non visible activity in the interaction vertex. Good agreement with expectations is also seen for the reconstructed muon $p_T$. The transverse angle between the muon candidate and the total momentum direction is reported in Figure 6.45 right. It seems to indicate a slightly underestimation of events when both vectors are perpendicular in the transverse plane, while good agreement is observed in the other angles.

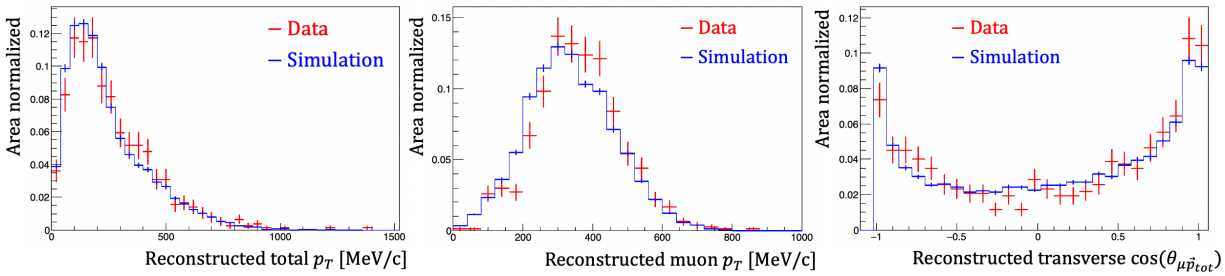


Figure 6.45: Reconstructed transverse momentum of the total event (left) and the muon candidate (middle). The cosine of the angle between the muon and total momentum directions is shown in the right hand side plot. Data events are shown in red, while MC are illustrated in blue. Only statistical errors are shown in both cases.

In addition, the angle between the muon and proton tracks (cos$\theta_{\mu p}$) is shown in the transverse

plane and in 3D in Figure 6.46. While the left distribution shows good agreement and indicates that both particles have in general opposite directions in the transverse plane, the right plot presents an underestimation for values $\theta_{\mu p} \lesssim 100°$, and an overestimation elsewhere. More studies are needed to disentangle the sources of these discrepancies, although it could be related to an angular dependence not modeled in the current calibration.

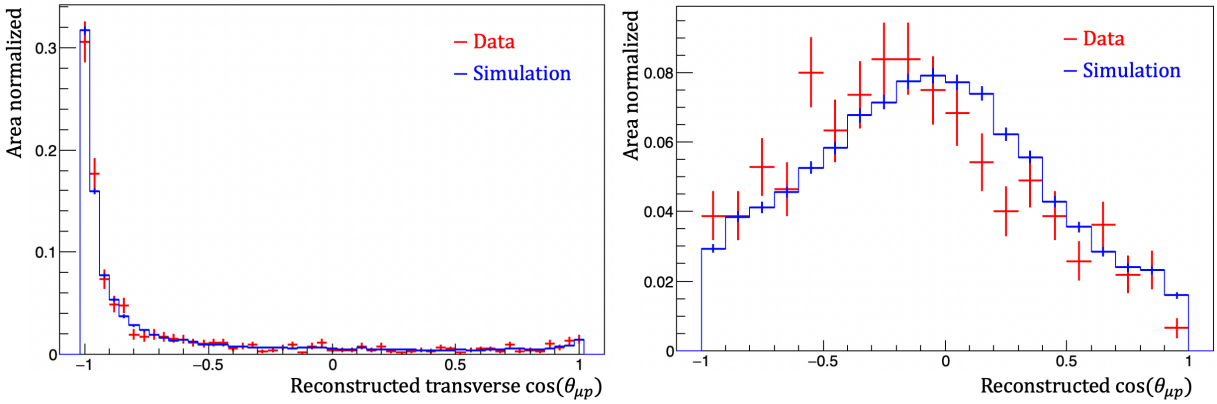


Figure 6.46: Angle between the muon and proton candidates shown in the transverse plane (left) and in 3D (right). Data events are shown in red, while MC interactions are illustrated in blue. Only statistical errors are shown in both cases.

Finally, the integrated energy of muon candidates was measured for their last 12.5 cm of track, to further evaluate their reconstruction. The results for data and MC events are shown in Figure 6.47, where two populations are clearly visible.

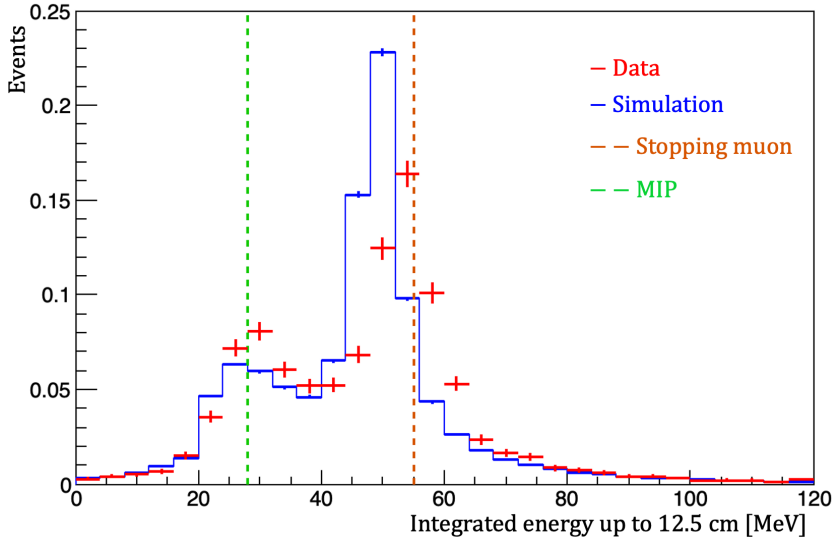


Figure 6.47: Integrated energy deposition by automatically selected muon candidates when the last 12.5 cm of track are considered. Data (red) and MC (blue) distributions are shown together with two vertical lines indicating the expected deposited energy for a MIP-like particle or a stopping muon, in the same integrated range. Statistical errors are shown in both cases.

The peak at $\sim$ 30 MeV is caused by reconstructed tracks without increased ionization in their final part, while the highest peak corresponds to those producing a Bragg peak. Given the integration range, a MIP-like particle is expected to deposit on average $\sim$ 28 MeV, whereas the predicted value for a stopping muon is around $\sim$ 55 MeV (see Figure 6.14). Data distribution has both peaks centered on the MIP and stopping muon expected values, respectively, while a global shift is observed in the MC distribution. A gaussian fit was performed in each peak

to evaluate the displacement, reporting a $\sim$ 8% underestimation of MC values with respect to the data. After further investigation, it was discovered that some calibration constants were modified in the present MC simulation, introducing a miscalibration of the global energy scale. Efforts are underway to find the right MC calibration values and fix this discrepancy, as they might have some impact on the selection procedure.

All presented variables, are continuously being investigated, in particular those in the transverse plane which are not affected by the presence of anomalous oscillation and can probe the initial and final state nuclear effects. The goal is to improve the performance of the automatic selection with further cuts that remove background events with minimal impact on the signal.

An additional cross check was performed using 50% of the Run 1 data collected with the off-beam trigger configuration, which is equivalent to an $\sim$ 8% of the total on-beam statistics. The automatic selection was applied identifying 5 candidates, so a total of $\sim$ 60 background events due to cosmics in-time (given the trigger configuration) could be expected for a total $2.5\times10^{20}$ POT exposure. The MC expectation of 0.5% background from in-time cosmics, corresponding to 67 events for the same exposure, is then confirmed even if with large statistical uncertainty by this first measurement. The full off-beam data sample should be studied, together with a larger sample of simulated cosmic to confirm this first order conclusion. Nonetheless, it is sufficient to demonstrate that cosmic contributions are effectively suppressed and do not represent the main source of backgrounds.

Even though limited statistics were analyzed, the presented work demonstrates the ability to automatically select $1\mu1$p events and the capability to fully reconstruct neutrino interactions, paving the way towards a final BNB disappearance analysis with all the available statistics.

# Chapter 7

# Conclusions

Since eV-mass neutrinos were first proposed as a consistent explanation for short baseline anomalies, many efforts have been made to either confirm or rule out this hypothesis. The Short-Baseline Neutrino (SBN) program located at Fermilab is one of them, designed to carry out precision searches for eV mass-scale sterile neutrinos and provide definitive clarification of the long-standing puzzle generated by the observed neutrino anomalies.

ICARUS is the far detector of the SBN program and, while the near detector is getting ready to join the common effort, is addressing in a standalone phase the test of the Neutrino-4 $\bar{\nu}_e$ oscillation hypothesis studying the $\nu_\mu$ disappearance channel with BNB events. After the successful completion of the second physics run of ICARUS, reconstructed neutrino event candidates and cosmic ray interactions were available and have been exploited to perform several studies.

The work of this thesis was dedicated to validating the ICARUS detector and reconstruction algorithms' performance and developing an automatic selection to identify a simple event topology ($1\mu 1$p) as a first step towards a final BNB $\nu_\mu$ disappearance analysis.

A visual scanning campaign turned out to be extremely valuable to directly assess the reconstruction performance currently in place and to identify recurrent pathologies. The introduction of less stringent constraints when merging the collected charge signals in the three wire planes allowed to recover some of the previously lost events. This visually scanned sample enabled to prove ICARUS' capability to perform calorimetric studies, particle identification and complete kinematic reconstruction of contained $\nu_\mu$ CC quasi-elastic interactions. With the additional input of simulated events, visibility thresholds into low-energy particles were established, with the goal of introducing a robust definition of the sought signal and determine a sensible strategy to perform data - Monte Carlo (MC) comparison.

Using all the knowledge acquired in the preceding studies, an automatic selection targeting the identification of fully contained $\nu_\mu$ CC quasi-elastic interactions on argon leading to final states containing one muon and one proton was developed. MC events were exploited to test the performance of the selection and modify the criteria until optimal performance was achieved. First tests were performed using QE interactions as the only events present in the signal definition, targeting the best possible sample. An efficiency of 43% was reported with a purity of 55%, where an improved method to define the neutrino location was presented involving the charge and light barycenters of the interaction. Due to the shallow depth operation of the detector, the reconstruction of the neutrino events is affected by the presence of the abundant flux of cosmic rays crossing the detector. A reduction of $\sim$ 11% of selected neutrino candidates and $\sim$ 13% loss of signal efficiency with the present automatic event reconstruction was estimated from MC studies.

The automatic selection was afterwards enlarged to the whole variety of neutrino interactions, taking advantage of the QE results. A total of 12,916 events were automatically selected in a simulated sample corresponding to $2.5\times10^{20}$ protons on target (POT) exposure, with an ef-

ficiency and purity of 45% and 67%, respectively. The neutrino energy resolution and transverse momentum of each event were evaluated, together with the total efficiency of each applied cut, showing some energy dependency that will be addressed in the future. The survival probability of $\nu_\mu$ was presented as an illustrative example, showing that the oscillation pattern due to the neutrino active-sterile mixing is not spoiled when the precision of reconstructed neutrino energy is accounted for.

It was also noted that the total transverse momentum $p_T$ of the interaction is a proxy for the kinematic reconstruction, energy resolution and interpretation of the event. Furthermore, it represents a valuable tool to test the robustness of the analysis and provides an insight into the physical model of neutrino interaction. In general, the kinematic variables reconstructed in the plane transverse to the neutrino beam are not affected by the presence of anomalous oscillation. For this reason, they can be effectively exploited in a blind analysis scheme to study, tune, and validate the event reconstruction and interaction model before "opening the box" and studying the oscillation signal.

Finally, a data - simulation comparison was performed with a small statistics dataset, showing overall a reasonable description of both sample purity ($\sim 71\%$) and selection efficiency ($\sim 41\%$). It is planned to increased the statistics, within the allowed limits of the blinding policy, to further analyze the obtained results. A study performed with $\sim 5\%$ of the total collected data shows, to first approximation, that the simulation reasonably reproduces the distribution of several event reconstructed physical quantities. A more detailed and quantitative comparison of these variables, including also an estimate of the detector, flux and interaction model systematic uncertainties will be fundamental in the final BNB $\nu_\mu$ disappearance analysis.

As a conclusion, this work has provided a proof of concept of a $1\mu1$p automatic selection, which will be further improved to overcome the flaws presented. A complete analysis is expected before the end of 2024, with more statistics and a full description of systematic uncertainties.

# Appendix A

# Calibration studies

ICARUS LArTPC provides rich information for events occurring in the active volume, with $\sim$ mm 3D geometrical reconstruction and accurate calorimetric measurements. To take advantage of such information, it is mandatory to have a precise knowledge of the detector performance and study possible effects impacting the reconstruction and selection of desired events. Before having the well established charge equalization method described in Subsection 5.5.4, several studies were performed to address this problem, and are reported here. Due to the shallow depth at which ICARUS operates, large statistics of cosmic rays crossing the detector are available, offering a gold sample to carry out calibration studies. These were used to investigate the equalization response of the $\sim$ 54,000 electronic channels and to assess the flatness of the central cathode. Given the interest on $\nu_\mu$CC contained events, the capability to correctly identify contained tracks was also quantified with cosmics. All calibration studies presented in this Chapter were performed using Calibration Ntuples files with data collected during the end of 2021, where the amount of data analyzed in each section might vary depending on when the analysis was performed.

## A.1 Containment conditions and space charge effects

The main goal of calibration studies is to optimize the detector response in order to perform high-quality analysis for neutrino events. In particular, this work focuses attention on contained events, ensuring that all calorimetric variables can be fully reconstructed. It is then mandatory, to quantify how well the reconstruction chain is able to correctly identify the entry and exit points of each event. In addition, containment conditions are very effective in rejecting background events associated to charged cosmic rays, of uttermost importance given ICARUS location. The Calibration Ntuples contain cathode-crossing cosmic muons that can be further classified as being anode-cathode crossing, throughgoing or stopping tracks.

Stopping tracks (see Figure A.1) were identified as those stopping inside a reduced active volume (corresponding to 10, 20 and 45 cm from the detector walls in the drift, vertical and beam directions, respectively) and with a median $dQ/dx$ in the last 5 cm greater than 1000 ADC/cm, i.e. $\sim$ 75,000 $e^-$/cm or $\approx$ 2.9 MeV/cm. For this study tracks not labeled as stopping and with $t_0 \in (-300, 300)$ $\mu$s were used, where the last condition ensured the collection of all associated ionization electrons, and thus the full visibility of the track. This selection was motivated by the possibility to determine with few mm precision the start and end positions inside the detector of the analyzed sample.

Figure A.2 shows the start and end positions for all selected tracks, using around 300,000 tracks collected before the Run 1 phase. Despite having removed all tracks tagged as stopping particles, there was still a non negligible amount of them starting or ending in the bulk of liquid argon. This might be due to broken tracks or stopping particles whose Bragg peak is not properly reconstructed.

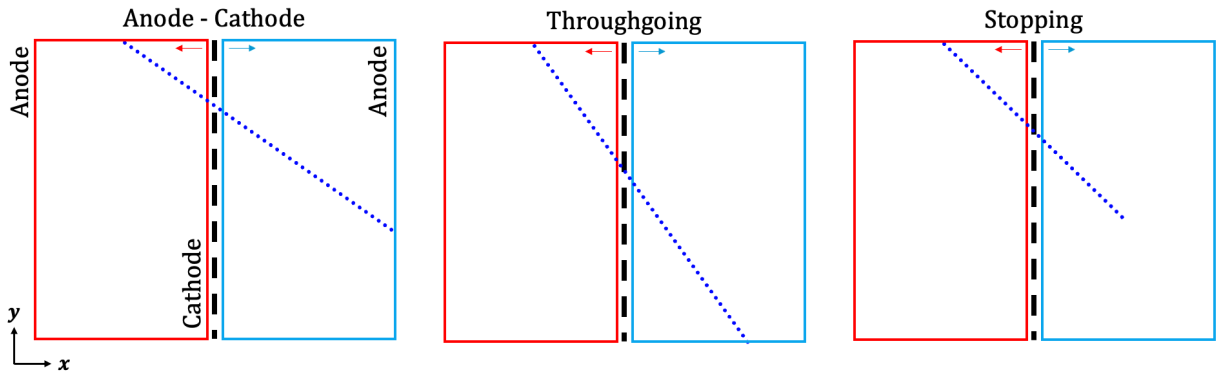


Figure A.1: Possible classification of cathode crossing tracks within the Calibration Ntuples for a track entering from the top face of the detector. Tracks entering from other faces are classified similarly.

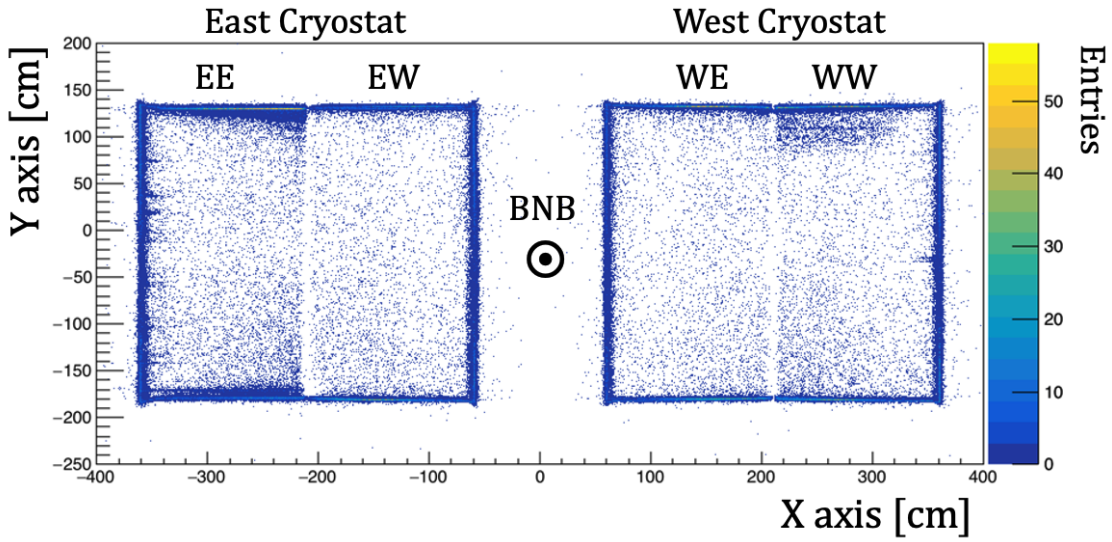


Figure A.2: Start end exit points of muons crossing the detector, where both cryostats are shown together with the BNB beam direction.

For simplicity TPCs are labeled with two letters, the first indicating the cryostat and the second the chamber inside the cryostat, for instance WE TPC is the East TPC of the West cryostat.

A number of features showed up in the 4 TPCs, which are presented in Figure A.3 for the upper and lower regions of the detector. A "$v$" shape centered on the cathode position ($\sim \pm$ 210 cm) was present in both cryostats for each top and bottom boundaries, with the $y$ coordinate inflecting around 2 cm inwards as expected from space charge effects (SCE). The effects occur due to the accumulation in the active volume of positive argon ions. When charged particles cross the detector they ionize the argon atoms producing electron-ion pairs. Electrons and positive ions drift along the same electric drift field lines, however their drift velocities are quite different: $v_{d_{Ar}} \sim 5 \times 10^{-6}$ mm/$\mu$s while $v_{d_{e^-}} = 1.6$ mm/$\mu$s, considering the ICARUS nominal electric field. Due to the reduced mobility of Ar ions with respect to the electrons, positive charge survives in the drift region of the TPC several minutes before being neutralized on the cathode or the field shaping electrodes. On top of that, ICARUS is continuously crossed by cosmic muons, enhancing the accumulation of positive charge. As a consequence, a not negligible distortion in the electric drift field arises affecting the reconstruction of the TPC tracks. The electric field distortion is of the order of few percent, and more significant at the TPC borders and near the

cathode plane, resulting in a displacement towards the center of the detector, as previously seen in Ref. [180].

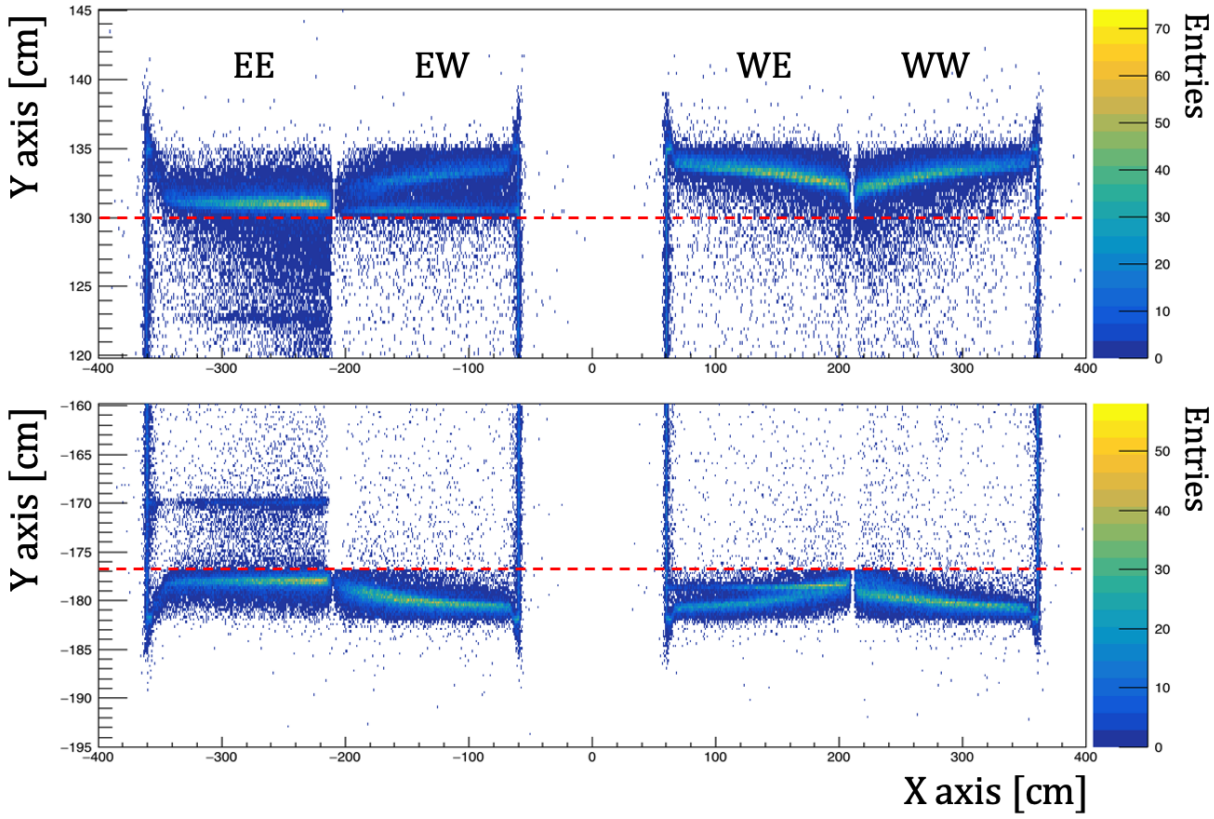


Figure A.3: Enlarged view of the upper and lower part of the detector, showing the entry and exit points in all 4 TPCs. Red lines indicate 5 cm from the top and bottom active volume boundaries.

In addition to this characteristic shape, several horizontal bars were seen at more internal positions. The WE bottom and EW upper horizontal lines were identified to be related to 7 and 15 problematic wires in Induction 1 causing a cut off on the track reconstruction. This is a drawback of requiring charge matching across the three wire planes to create space points, resulting in an increase of split tracks in the vicinity of the malfunctioning wires. Possible mitigation strategies were investigated and are be presented in Chapter 6.

The inner horizontal lines in the EE TPC were vanished after an onsite intervention to achieve some noise reduction, during September 2021. However, it is clear that the EE TPC presents some further problem, as both upper and lower regions have field uniformity issues that are not consistent with SCE.

The problem seems to have emerged on the $9^{th}$ of October, 2020 where a high voltage issue was reported. There was a change in the resistor configuration on the circuit diagram corresponding to the EE TPC, which was spotted due to a rise in the voltage divider (from -7.3 V to -7.6 V) and the total current (from 393.3 $\mu$s to 396.6 $\mu$s). The most likely hypothesis is that the change was caused by a field cage short between two electrodes in that specific TPC causing significant non uniformities in the electric drift field.

Analogous studies were performed with simulated cosmic muons, to confirm the previous hypothesis. Start and end positions of crossing muons were identified and the results are shown in Figure A.4. It is possible to see that MC generally presents the same features but with higher resolution, even though low statistics were available at the time. The track points were more clearly distributed along the detector walls and only a reduced fraction of them was found in the

interior of the LAr. Since SCE were simulated in the MC sample used, the $v$ shape was present in all 4 TPCs. Similar effect sizes were observed, allowing to confirm that the analogous behaviour seen in data was caused by the SCE. By averaging the entry and exit points in the x axis with finite bins, it was possible to compute an effective y top and bottom detector boundaries, by fitting the data to the sum of two gaussian plus a vertical offset.

The peaks near the anode planes observed in Figure A.3 cannot be attributed to SCE as they are not present in the simulated results. However, they could be explained by boundary effects in the vicinity of the electrodes generating the electric drift field, as indicated by more recent detailed electrostatic calculations.

Considering that no other peculiarities were present in the simulation, it was concluded that additional features observed in the data had to be necessarily related to the detector operations.

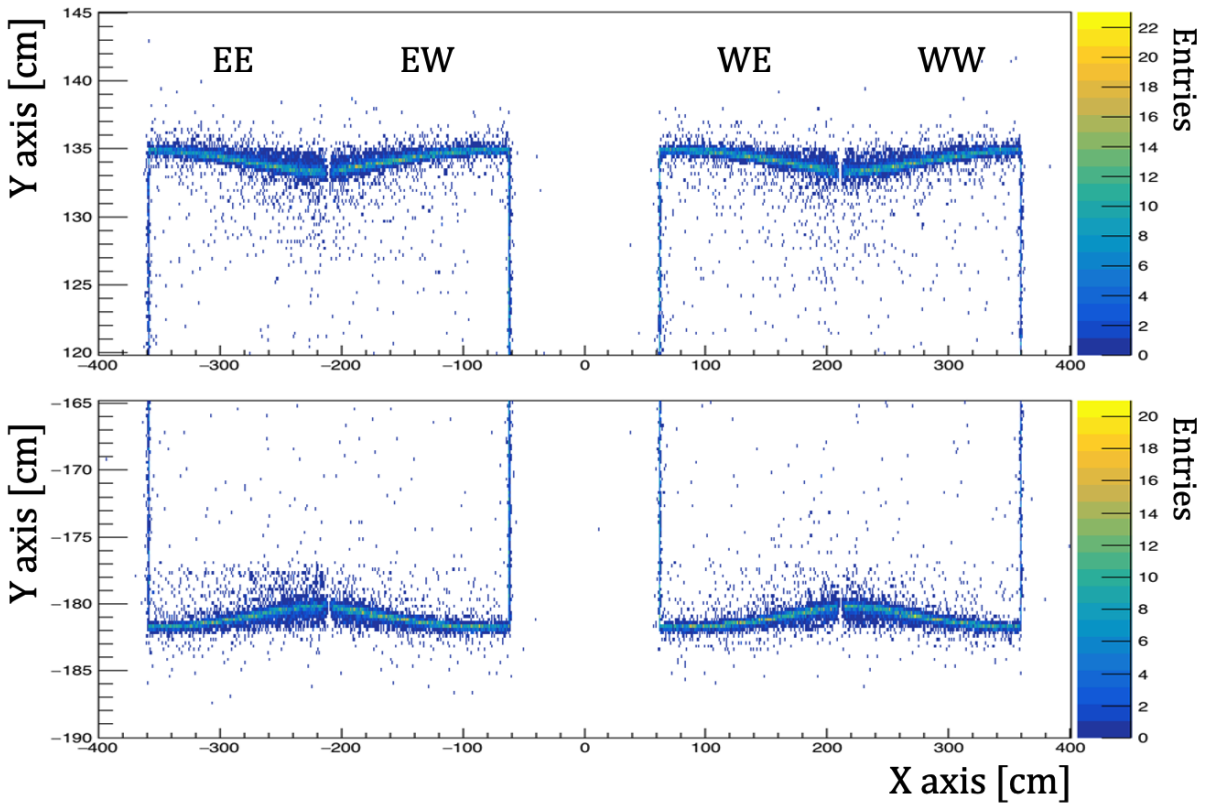


Figure A.4: Start and end positions of simulated cathode crossing cosmic rays for the 4 TPCs. The upper and lower TPC boundaries are shown in the top and bottom plots, respectively.

In view of the results, it was decided to define the containment of tracks within 5 cm from the active volume to avoid the field distortions in the aforementioned regions, as illustrated in Figure A.3 with a red horizontal line for the Y axis. Therefore, all reconstructed tracks with the start and end point positions more than 5 cm away from the TPC walls were considered to be contained.

Finally, the minimal distance distribution between the entry point and the closest TPC wall was computed in the XY plane for data events in each TPC. Considering that only throughgoing muon tracks were present, contained start points using the previous definition indicate a poor reconstruction of the event. The fraction of contained entry points is reported in Table A.1, where only tracks fulfilling $y_{\text{entry}} > y_{\text{exit}}$ were considered. Results showed a dependency as a function of the considered TPC, but indicating some anomaly in the EE TPC and a minor discrepancy in the WW TPC.

An in depth analysis of the WW TPC, revealed that there is an object hanging from the top of the detector into the active TPC volume, causing an electric field distortion and a huge

| EE TPC | EW TPC | WE TPC | WW TPC |
|---|---|---|---|
| 12.2% | 5.64% | 5.73% | 8.81% |

Table A.1: Fraction of events with respect the total points in each TPC located more than 5 cm away from any TPC wall.

deformation of tracks crossing that region. This finding, could explain the increase of contained start points seen in WW TPC with respect to the value obtained in the WE, as more points are seen in the upper boundary of WW than in the bottom face (see Figure A.3).

The EE behaviour is expected given the electric field problem previously reported, however a follow up study on more recent data events of Run 2, showed a significant change after the East cryostat filter regeneration work in which the high voltage system was turned off. The cryogenic maintenance took place on the $3^{rd}$ of October 2023, and the drift high voltage was ramped up the day after. It was noticed that the readback current and the EE voltage divider measurements were roughly back to the nominal values seen before the EE TPC short. Thus it appears that the EE field cage short is reversed. At the time of writing, more detailed studies are being carried out to understand the actual situation and find the best approach to address it. Nonetheless, all data analyzed in this section is prior to that change, and hence affected by the field cage short.

## A.2 TPC wire equalization

The aim of the TPC wire equalization is to make the wire response to charge uniform in space and time. To that end a careful treatment of each wire is needed to achieve a uniform behaviour among all wires. Once all TPC wires are calibrated it is possible to find a global calibration to set the absolute energy scale of the detector.

As a first approximation, it is possible to assume that cosmics have a small variation of $dE/dx$ all over the track. This implies a constant recombination along the muon trajectory and $dQ/dx$ is expected to behave as $dE/dx$. The ionization signal generated by a cosmic muon on a wire depends on its momentum and the track segment contributing to the signal on the wire itself. However, it is reasonable to consider that each wire should see the same $dQ/dx$ on average, regardless of the specific wire number. In order to validate these hypothesis, the standard deviation of the most probable value (MPV) for $dQ/dx$ with respect to the TPC wire number was studied. This was done selecting anode to cathode crossing tracks and rejecting stopping particles, to avoid biases and to have a uniform coverage on the wire planes. Anode to cathode tracks have a projected length along the drift direction within a TPC equal to the maximum drift distance, hence they were selected by requiring a drift time between $\Delta t \in (936, 952)$ $\mu$s. 200,000 tracks were considered for the study using data taken between August and November of 2021. It was decided to perform the study using collection plane only and focusing on the West cryostat, due to the problems seen in the EE TPC. As previously mentioned, Calibration Ntuples do not have any type of charge scale corrections, hence $dQ/dx$ needs to be corrected for the electron lifetime to account for signal attenuation due to electronegative impurities through Eq. 5.9. The electron lifetime for the set of runs employed were $\tau \sim 3.2$ ms. An example of the magnitude of the this correction factor for an electron lifetime of 3 ms and 4 ms is shown in Figure A.5 left.

The $dQ/dx$ distribution as a function of the drift time is shown in the middle plot of Figure A.5, while the same distribution is reported in the right after the lifetime correction. It is possible to see that after the purity correction the $dQ/dx$ distribution is almost flat.

To quantify the flatness of the distribution the MPV was computed with a Landau convoluted with a Gaussian function every 48 ticks or 19.2 $\mu$s. The obtained results are shown with the red

line of Figure A.5 left. Drift times greater than 500 ticks (200 $\mu$s) were seen to have an almost constant MPV around $\mu \pm \sigma = (620.5 \pm 1.1)$ ADC/cm, while values below 500 ticks presented an increase of $dQ/dx$ up to 4% with respect to the computed mean. These distortions were found to be mainly due to space charge effects near the anode or the cathode and the lack of statistics in these regions. However the effect showed to be more important at low drift times, where some additional reconstruction distortions are present because of tracks crossing the wire planes.

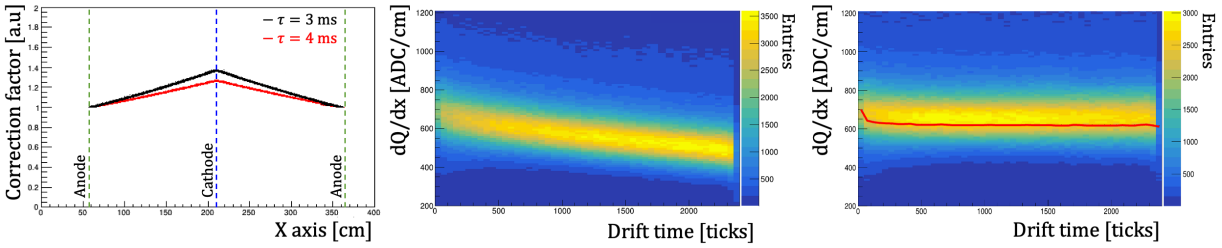


Figure A.5: Left: electron lifetime correction factor for two different values of $\tau$. Vertical lines indicate the anode and cathode positions, coinciding with the maximum and minimum achieved values. Middle: $dQ/dx$ distribution as a function of the electron drift time before the purity correction for the WE TPC. Right: same distribution as before with the lifetime correction applied. The red line indicates the MPV computed with a Landau convoluted with a Gaussian distribution. In the drift time axis scale the anode is located at drift time equal 0, while the cathode is placed at maximum drift time. Note that 1 tick = 0.4 $\mu$s $\sim$ 0.6 mm.

The length distribution of the selected tracks, together with the incident angle and the drift time distributions as a function of the wire number were proven to have a uniform behaviour indicating that no further correction was needed. The distribution of the corrected $dQ/dx$ was plotted for each channel considering only hits at least 5 ticks ($\sim$ 3 mm) away from the TPC borders and with multiplicity[1] 1. These two conditions were required to avoid biases due to space charge effects or low $dQ/dx$ values because of charge being split in several hits, respectively. The distribution of $dQ/dx$ for all channels of the WE TPC is shown in Figure A.6 left, where a non uniform behaviour was clearly seen. Each $dQ/dx$ distribution was fitted with a Landau convoluted with a Gaussian function. The Landau contribution models the physical $dQ/dx$ distribution for each wire, while the Gaussian part accounts for all the smearing introduced by electronic noise, different inclination of the tracks and wide range of energies, among others. An example of the fit for a specific wire is shown in Figure A.6 right, where before any equalization the distribution showed a channel MPV = 588.7 $\pm$ 3.1.

To mitigate the contribution to $dQ/dx$ of unresolved delta rays or noise hits, the fit was limited to the range $dQ/dx \in (400, 1200)$ ADC/cm, which was found to provide the best $\chi^2$ per degree of freedom on the fit. The MPV of each convergent fit was extracted, while those that failed were flagged so that no correction was applied afterwards. Around 5500 channels out of the 5648 present in the collection plane were found to have a convergent fit. To equalize all the wires, it was chosen to compute the median of all converging wires and apply the following correction factor channel by channel

$$\left.\frac{dQ}{dx}\right|_{cal} = \left.\frac{dQ}{dx}\right|_{corr} \times \frac{\mathrm{MPV}_{\mathrm{median}}}{\mathrm{MPV}_{\mathrm{channel}}} , \tag{A.1}$$

where *cal* stands for calibrated, the corrected $dQ/dx$ is extracted from 5.9 and the median was used to avoid biases due to poorly calibrated channels. The obtained correction factors are

[1] As seen in Subsection 5.5.2, the multiplicity is defined as the number of gaussian fits used to fit a recorded charge deposition for a specific wire.

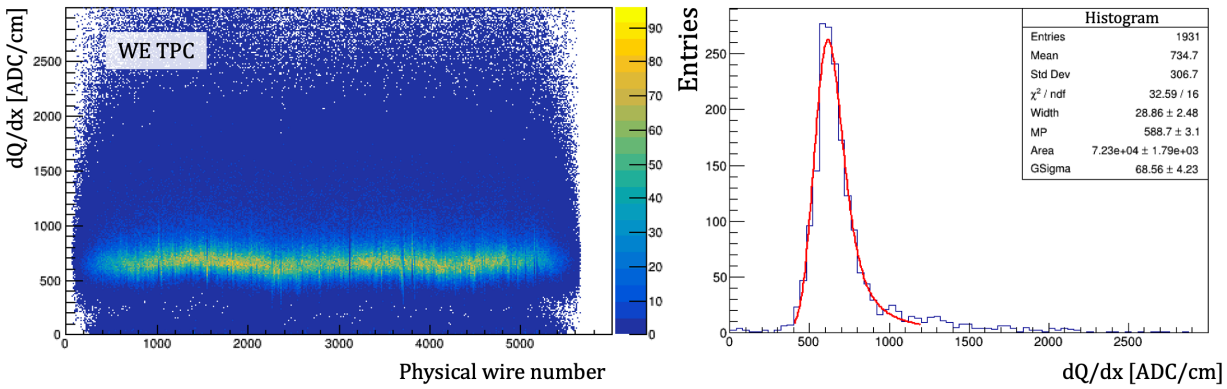


Figure A.6: Left: Distribution of $dQ/dx$ for each channel of the WE TPC, using collection plane only. Right: Example of $dQ/dx$ distribution of a single wire before equalization, where the Landau ⊛ Gaussian fit is superimposed.

shown in Figure A.7 left for each channel, where the total average value was compatible with 1 at the level of 1‰; indicating that no additional offset was introduced to the average response.

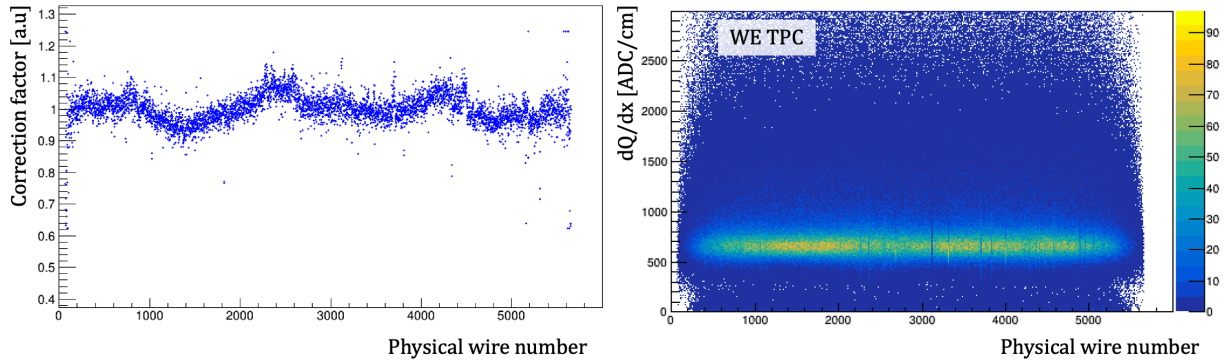


Figure A.7: Left: Correction factor as a function of wire number computed as the ratio between the median of all channel MPV and the MPV of each channel. Right: $dQ/dx$ equalized distribution after applying the correction factor channel by channel, as described in the text.

The distribution of the $dQ/dx$ for each wire after applying the equalization is shown in Figure A.7 right. To obtain an estimate of the accuracy of the method, the distribution of all MPVs for converging channels was fitted to a Gaussian function before and after the equalization, as shown in Figure A.8 left and right, respectively. Table A.2 reports the results of the Gaussian fits and shows the median MPV values used for equalization. It is possible to see the drastic reduction in the dispersion of the MPV distribution after calibration, demonstrating the effectiveness of the method. The equalization was stable over the analyzed period of time, showing only a slight discrepancy between the two adjacent TPCs.

With this method it was also possible to identify malfunctioning channels since these had atypical values in their MPVs, allowing to tag them in view of future studies.

The developed strategy is applicable to all 4 different TPC, being a first proof of concept towards a more sophisticated charge equalization (as explained in Subsection 5.5.4).

## A.3 Cathode planarity

In order to determine the position of tracks along the drift coordinate, it is essential to measure the absolute time $t_0$ at which the particle crossed the detector. While the interaction time for tracks not associated to the event trigger is in general unknown, cathode crossing tracks are

| Fit values | WE TPC Before | WE TPC After | WW TPC Before | WW TPC After |
|---|---|---|---|---|
| $MPV_{median}$ | 626.6 | 625.9 | 638.6 | 638.2 |
| Mean MPV | 626.5 ± 0.4 | 623.9 ± 0.1 | 638.8 ± 0.4 | 638.1 ± 0.1 |
| Sigma MPV | 25.4 ± 0.3 | 1.1 ± 0.1 | 28.1 ± 0.3 | 1.1 ± 0.1 |
| Sigma/Mean | 4.05% | 0.18% | 4.4% | 0.17% |

Table A.2: Results of the Gaussian fit for the MPVs before and after calibration. The two TPC in the West cryostat are reported.

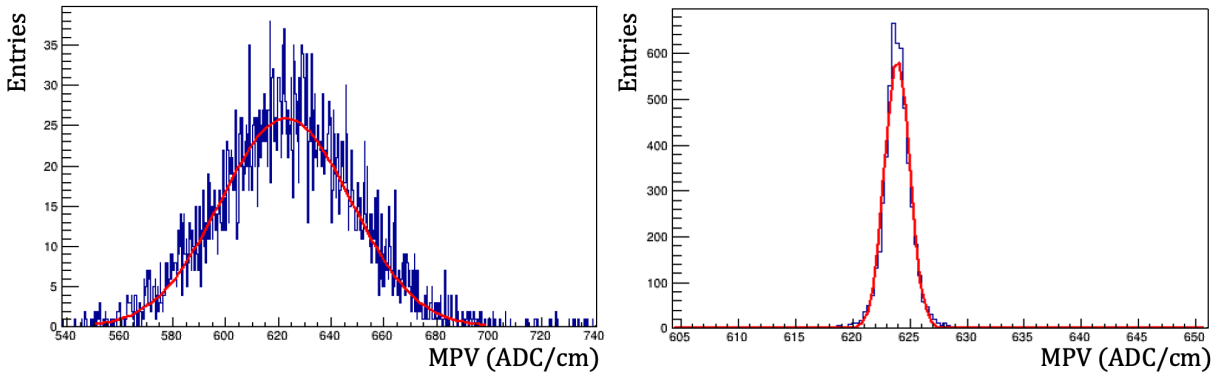


Figure A.8: Distribution of MPV for each converging channel before (left) and after (right) applying the equalization procedure, for the WE TPC.

a special subsample for which $t_0$ might be computed by the reconstruction algorithm taking advantage of the cathode position (see Subsection 5.5.3). Local deviations from planarity in the central cathode, could affect the uniformity of the electric field causing poorly reconstructed drift times, and thus distortions in the spatial reconstruction. As a result the stitching algorithm in charge of identifying the segments of a track crossing the cathode might not have an optimal performance, splitting the tracks more frequently. Another consequence is the loss of precision when measuring the momentum of exiting tracks via the multiple coulomb scattering (MCS). Local deviations of the drift velocity might introduce additional track deviation mimicking the MCS effect, and since the method exploits the track deflection angles, which are inversely proportional to momentum, bias measurements might arise. This effect was already observed and quantified as an underestimation at high muon momentum during ICARUS underground operations [135].

In this study the cathode planarity was investigated exploiting cathode crossing cosmic muons reconstructed in the Calibration Ntuples. The method relied on the difference between the maximum drift times of the tracks in the two adjacent chambers to estimate the cathode distortion at the crossing point. By design, the two TPC on the left and right side of the cathode are symmetrical. Hence, each cryostat should have an identical maximum drift distance and electric field intensity, in particular the nominal values are

$$d_L = d_R = d_D = 148.2 \text{ cm} \qquad E_L = E_R = E_0 = 500 \text{ V/cm} ,$$

where all the variables are defined according to the magnitudes shown in Figure A.9 left. For tracks crossing the cathode, the maximum drift time should also be identical on the left and right chambers, namely $t_L = t_R = t_D$.

A global displacement of the cathode $\Delta$, such that $\Delta << d_D$, would break the left-right symmetry by changing both the drift distance and electric field intensity by the following amount:

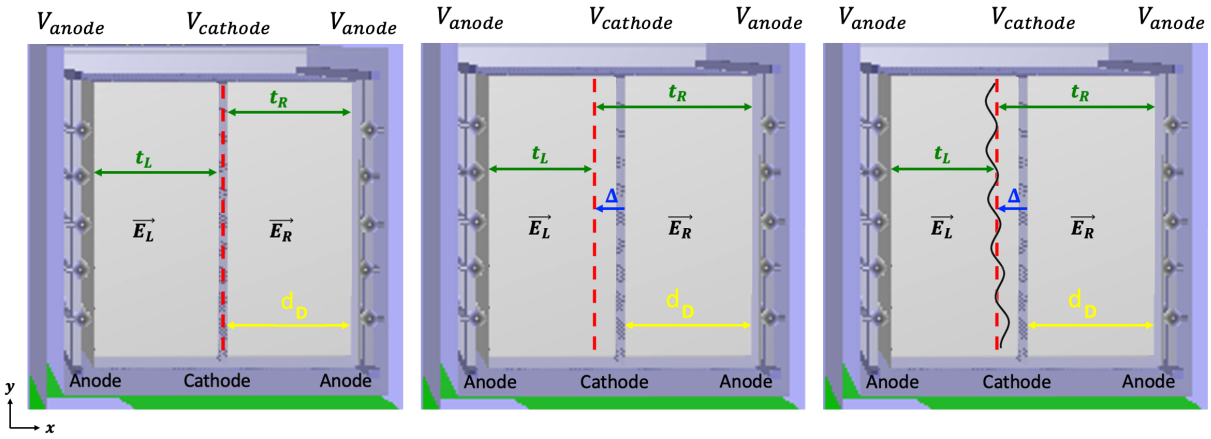


Figure A.9: Schematic drawing of all magnitudes involved in the calculation of $\Delta$ variation. Ideal scenario is shown in left, middle picture illustrates a global cathode displacement, while right pictures a cathode with local displacements.

$$d_L = d_D - \Delta \qquad E_L = \frac{HV}{d_L} \approx E_0 \left(1 + \frac{\Delta}{d_D}\right) , \tag{A.2}$$

$$d_R = d_D + \Delta \qquad E_R = \frac{HV}{d_R} \approx E_0 \left(1 - \frac{\Delta}{d_D}\right) , \tag{A.3}$$

where $HV$ is the fixed cathode potential. For small variations of the electric field around $E_0$, the drift velocity scales approximately as $v_\mathrm{d} \propto \sqrt{E}$, resulting in the following effective drift velocities for each TPC,

$$v_j = v_d \sqrt{\frac{E_j}{E_0}} \simeq v_d \left(1 \pm \frac{\Delta}{2d_D}\right) , \tag{A.4}$$

where $j = L, R$, and the positive sign corresponds to $j = L$. The maximum drift time in this case would be

$$v_j = \frac{d_j}{v_j} = t_D \left(1 \mp \frac{3}{2}\frac{\Delta}{d_D}\right) , \tag{A.5}$$

with the same $j$ definition, but now the negative sign is obtained for $j = L$. This allows to define

$$t_R - t_L \simeq 3 t_D \frac{\Delta}{d_D} , \tag{A.6}$$

which can be used to compute the global displacement $\Delta$ as

$$\Delta\,[\mathrm{mm}] = \frac{t_R - t_L}{3} v_d = \frac{1.6\ \mathrm{mm}/\mu s}{3} (t_R - t_L)\,\mathrm{ticks} \times \frac{0.4\ \mu s}{1\ \mathrm{tick}} , \tag{A.7}$$

where an approximate drift value of 1.6 mm/$\mu s$ was employed and the ticks to time conversion factor used to obtain $\Delta$ in units of length. Even if the procedure is valid in any of the three wire planes, the study was performed using collection plane. However, similar results are expected if the other two planes are used.

Even if the entire derivation considered a global displacement, as a first approximation it can be assumed that this relation remains valid even for local cathode displacements. This approach was used during the ICARUS data taking at Gran Sasso, which was tested and validated during its operation [135]. At that time, local cathode distortions were first measured at LAr temperature during underground operations, exploiting muons crossing the cathode as previously described (indirect method). The cathode distortions were also measured using a

laser meter during the CERN overhaul of the detector, which allowed to inspect the inside of the module at room temperature (direct method). The two methods are clearly independent and use information collected under very different conditions, such as full of liquid argon at cryogenic temperature and at room temperature with an empty detector. Their correlation for the majority of the cathode panels as shown in Figure A.10 left demonstrated the compatibility of both methods and the reliability of using the indirect one during detector operations, where the direct approach cannot be used. After ICARUS underground operations, a mechanical intervention allowed to restore the cathode planarity within few mm from the initial deviation of 2.5 cm. It is therefore important to perform the measurement again to quantify the current flatness of the cathode.

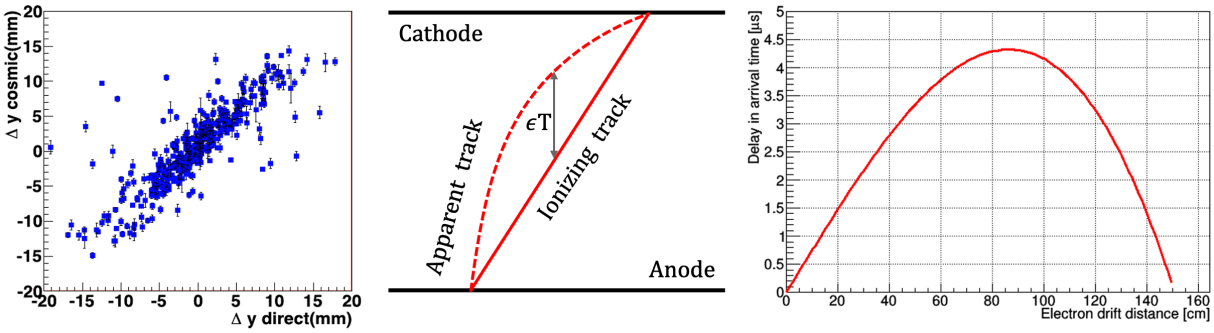


Figure A.10: Left: comparison of direct and indirect (labeled as cosmic) estimations of cathode distortions, taken from Ref. [135]. Middle: Schematic view of the bending parameter $\epsilon T$. Right: delay in arrival time for drift electrons along the full drift. The anode position corresponds to 0 cm in the drift coordinate, while the cathode position is set to 150 cm. Plots from Ref. [180].

Before the measurement, it is important to take into account the completely different situation that the detector is now in. This is mainly due to the large amount of cosmic rays crossing the detector, which generate space charge effects (SCE). The electron drift velocity depends on the electric field, so any distortion of the same will cause a delay in the electron arrival time with respect to the time observed in case of a uniform electric field. Apparent bending of muon tracks along the drift coordinate can be estimated through the time delay $\epsilon T = T_{sc} - T_u$, where $T_{sc}$ is the electron arrival time at the anode when SCE are present, while $T_u$ represents the same magnitude for a uniform electric field, see Figure A.10 middle. The time delay due to the presence of non linear effects (caused by the space charge) as a function of the drift distance was reported in Ref. [180] and shown in Figure A.10 right. The curve indicates that electrons generated at the cathode would have a SCE corresponding to $\approx$ 0.3 mm, being an identical effect in both sides of the cathode. It is then possible to safely neglect the SCE in this study. This assumption would not hold true if positions other than cathode were studied, as the SCE would produce an apparent offset of few mm in the middle of the drift distance.

The same set of data used for TPC wire equalization was employed to address the measurement of the $\Delta$ displacement. Using Eq. A.7 the following cathode maps shown in Figure A.11 were obtained, representing the average displacement in each bin. It is possible to see that local displacements are present in both cryostats, however larger effects were observed for the East module. Absolute variations were found to vary from -6 to 13 mm in the East cryostat, while West cryostat reported values between $\pm$ 9 mm. This indicate a maximum displacement of 13 mm or 8.12 $\mu$s from the nominal cathode position[2].

Figure A.11 has a diagonal line in both cathodes, with mirrored positions (one upstream and the other one downstream) and at 30° with respect to the vertical direction. They could be

[2]Note that this measurement relies on Pandora's capability to stitch the tracks, which assumes a flat cathode. If the cathode is so bend that Pandora cannot associate adjacent segments, this method might be underestimating the flatness of the cathode and a more Pandora independent approach should be used.

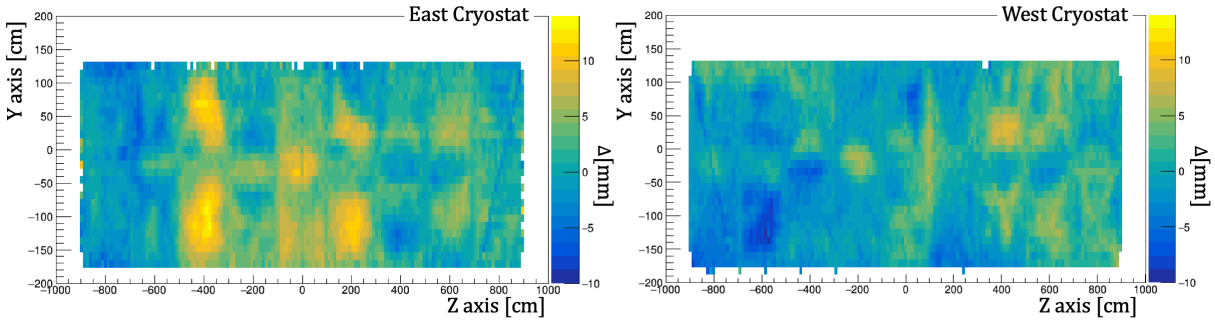


Figure A.11: Cathode map showing the bending present in both cryostats. The Δ is computed with the method explained on the text and here represented with the colour scale in mm units.

related to a wire problem of a plane with that specific wire orientation, preventing the efficient creation of spacepoints in these regions, given the triple charge deposition requirement used in the reconstruction algorithm. The standard deviation errors from the Δ measurements in the West cryostat, are shown in Figure A.12 left. The errors were found to be around 3 or 4 mm depending on the region, with similar values in the other cryostat. It is clear that the study would benefit from larger statistics, and might be repeated in the near future.

The empty bins in the East cryostat of Figure A.11 are related to the EE TPC short, making more difficult to reconstruct tracks crossing the cathode close to boundaries of the detector. On the other hand, the empty space present in the West cryostat at around $z \sim 330$ cm and top face, was found to be related to the known hanging object mentioned at the end of Section A.1.

For the sake of illustration, Figure A.12 right clarifies the meaning of positive and negative displacement of the cathode, where positive values indicate variation on the X axis direction, while negative displacement of Δ are in the opposite direction.

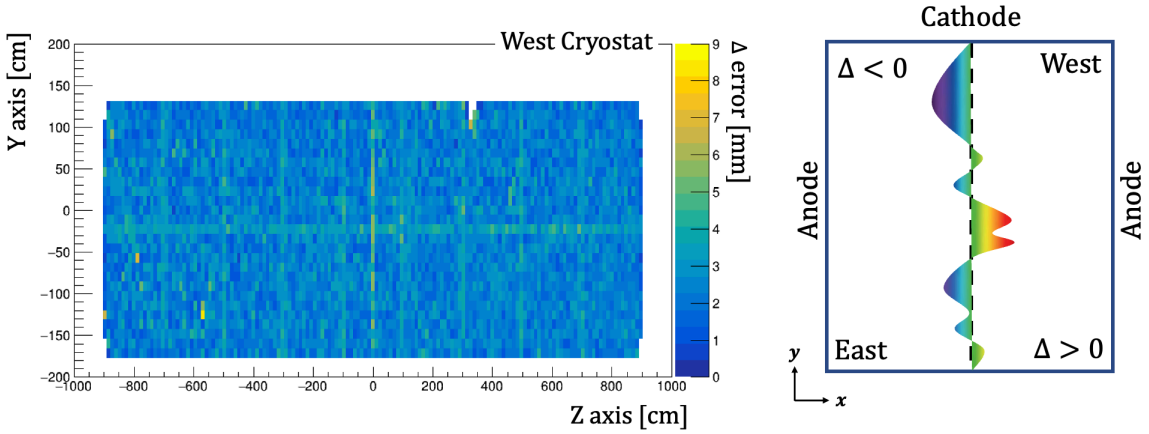


Figure A.12: Left: Standard deviation errors from the Δ measurements of the West cryostat. colour scale in units of mm. Right: Cross section view of the cathode, illustrating the positive and negative bending of the cathode.

It is possible to recognize the cathode mechanical structure in Figure A.11 and A.12 left, however, due to the limited statistics of this study, it was not possible to resolve it in 2D. The cathode plane is composed of 9 punched stainless-steel panels of 2 m long and 3.2 m height, vertically installed within a metallic framework. The supports are made by cylindrical tubes surrounding the cathode borders, and an additional reinforcement bar is located in the middle of each panel. Figure A.13 left shows the layout of the cathode planes inside the detector, while the middle and right images presents some technical details of a single cathode panel. Due to the cathode design, the deformations are usually larger in the middle of each panel and decrease

on the edges. They also tend to diminish at $\sim$ 1.6 m height, where the reinforcement bar is present.

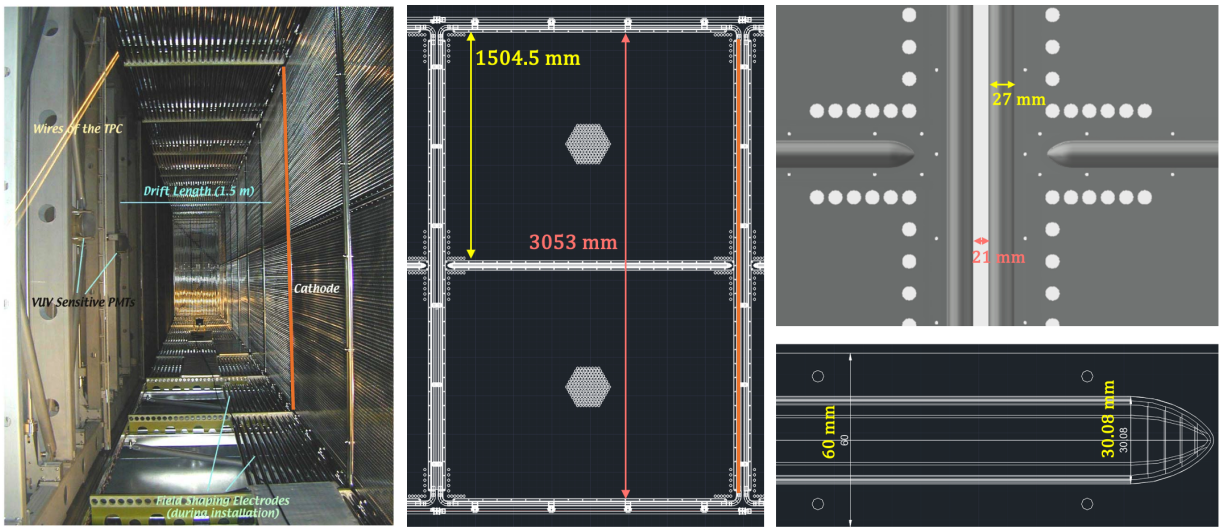


Figure A.13: Left: Picture of the inner detector layout of the first half-module, where the cathode divides the volume in two symmetric TPC. The orange vertical line indicated the position of one of the tube from the mechanical support. Middle: Technical details of one of the 9 cathode panels. Right: Enlarged image of one end of the reinforcement bar, showing the measurements of different elements.

The crossing cathode points of each track were computed by averaging the 3D position of the two closest hits on either side of the cathode. The Y projection obtained with this approach is shown in Figure A.14 where some relevant features were noticed in the data distribution. The first one is a central dip around $y = -24$ cm, in which the number of entries decreases considerably. This could be explained by taking into account the location of the reinforcement bar at $y = -22$ cm, making the correct stitching of the tracks more difficult and biased towards higher or lower positions depending on the incident inclination. The small discrepancy between the two values found might be due to the width of the reinforcement bar or the inclination of the tracks producing slightly different hit distributions. Some technical details regarding the reinforcement bar are shown in Figure A.13 right. No structure was seen in MC events around $y = -24$ cm (see Figure A.14), as expected, since at the moment the cathode is described in the simulation as a flat plane without mechanical reinforcing structures.

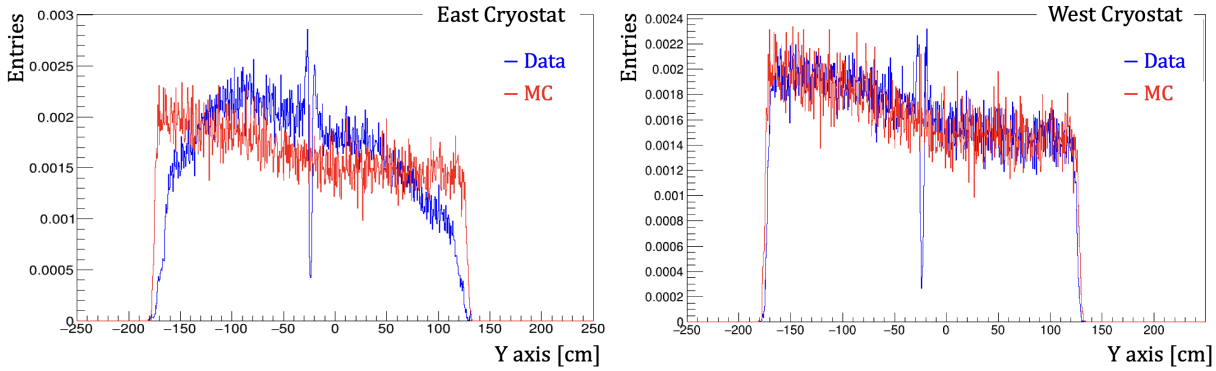


Figure A.14: Projected cathode crossing position in the Y axis. West and East cryostats are shown in left and right plots, where data and MC events are presented as blue and red histograms, respectively. All histograms have been normalized to 1 for the sake of comparison.

On each side of the dip, there was an increase of events. This is probably a combination of the geometrical effect of a missing part of the track and of the electric field distortions created by the reinforcement bars and causing the tracks to curve towards the surroundings. It was also possible to see the different shapes of the two data distributions, evidencing once again the electric field distortions in the East cryostat. The measured fraction of muons reconstructed to cross the cathode above the reinforcement bar ($y = -24$ cm) was $\sim 56\%$, for both East and West cryostats. The non uniform behaviour seen between the upper and lower part of the TPC could be explained by the detector geometry and surrounding features, but also due to the angular distribution of the cosmic rays impinging vertically. Nevertheless, the good agreement seen between data and MC in the West cryostat implied that there was no other source of electric field distortions. It is worth mentioning that in this case SCE was not simulated, showing that the assumption of neglecting its effect when considering cathode positions was sensible. In addition SCE impact is similar in both sides of the cathode, making the effect negligible with respect to other distortions in this particular study.

Finally, the Z projection was calculated for simulated and data events. Once again, discrepancies were found only in areas where the cathode had a structure not simulated in the MC, as shown in Figure A.15 left.

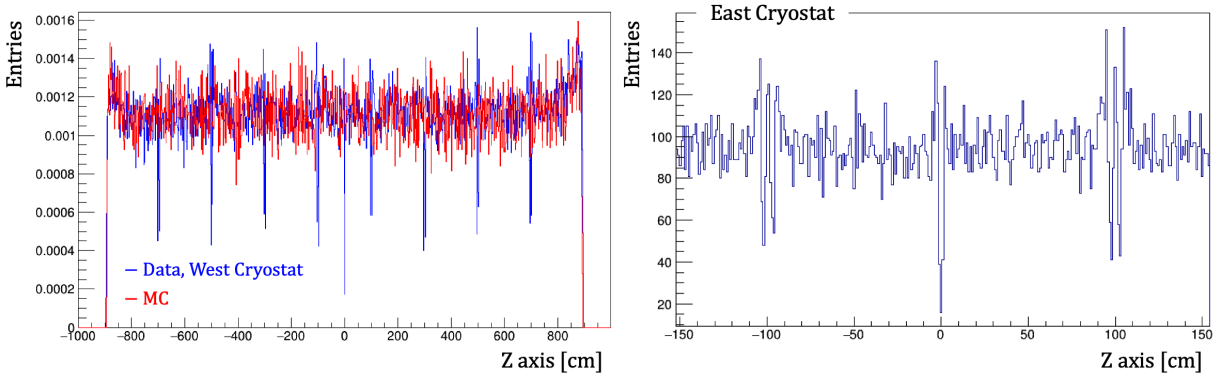


Figure A.15: Left: Z projection of the cathode crossing position, for data and Monte Carlo. The histograms have been normalized to 1. Right: Zoom into the middle area of the detector, to appreciate the minimum at $z = 0$ and two smaller dips at the cathode panel edges, with the characteristic double peak structure.

Similarly to the dip and side accumulations due to the reinforcement bar, 8 small structures were observed in the Z coordinate, corresponding to the boundaries of the 9 panels 2 m long composing the cathode. As before, these dips were the sign of some field distortion, this time caused by the metallic tubes holding the panels. Zooming into each dip it is possible to appreciate a double peak structure, corresponding to each edge tube of the two adjacent cathode panels (see Figure A.13 top right). Figure A.15 right shows the two minima accompanied by their respective increase in nearby coordinates, reproducing similar behaviour seen in the Y projection. However, the Z projection presented a further discrepancy with the simulation. It is known that Induction 1 wires are split at $z = 0$ with a few cm wide region not equipped with them, producing in addition some electric field distortion. This prevents an efficient reconstruction on all three wire planes in that region causing the biggest dip present in Figure A.15 right. The typical distortion that a track suffers when crossing the $z = 0$ surroundings is shown Figure A.16, where a muon track produced by a neutrino interaction is visible in the Collection plane.

Cathode planarity maps are being produced with more statistics and with newer data samples, with the goal of introducing the information inside the reconstruction chain to improve the cathode stitching performance of Pandora and correct for the electric field distortions.

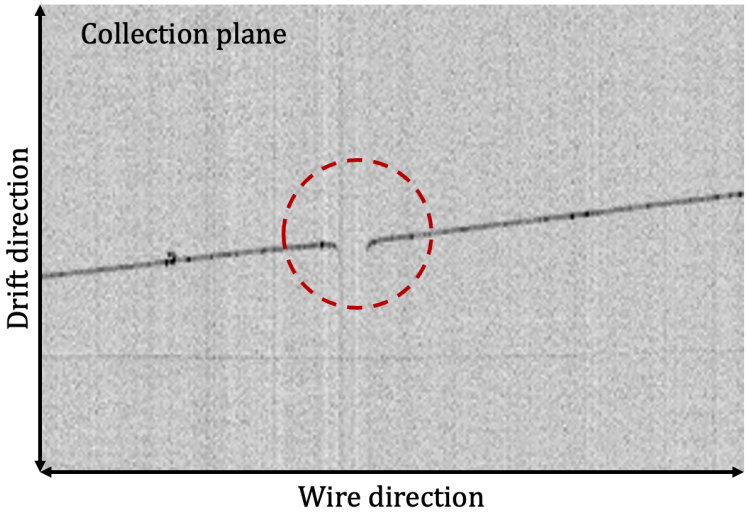


Figure A.16: Muon track from a neutrino interaction affected by the distortion produced due to the split at $z = 0$ of Induction 1 wires.

# Bibliography


[1] J. Chadwick, "Intensitätsverteilung im magnetischen spectrum der $\beta$-strahlen von radium B+ C," *Verhandl. Dtsc. Phys. Ges.*, vol. 16, p. 383, 1914, http://cds.cern.ch/record/262756.

[2] W. Pauli, "Dear radioactive ladies and gentlemen," *Phys. Today*, vol. 31, no. 9, p. 27, 1978.

[3] F. L. Wilson, "Fermi's theory of beta decay," *American Journal of Physics*, vol. 36, no. 12, pp. 1150–1160, 1968, https://doi.org/10.1119/1.1974382.

[4] H. Bethe and R. Peierls, "The "neutrino"," *Nature*, vol. 133, no. 3362, pp. 532–532, 1934, https://www.nature.com/articles/133532a0.

[5] C. L. Cowan Jr, F. Reines *et al.*, "Detection of the free neutrino: a confirmation," *Science*, vol. 124, no. 3212, pp. 103–104, 1956, https://www.science.org/doi/10.1126/science.124.3212.103.

[6] F. Reines and C. Cowan Jr, "Detection of the free neutrino," *Physical Review*, vol. 92, no. 3, p. 830, 1953, https://link.aps.org/doi/10.1103/PhysRev.92.830.

[7] S. H. Neddermeyer and C. D. Anderson, "Note on the nature of cosmic-ray particles," *Physical Review*, vol. 51, no. 10, p. 884, 1937, https://link.aps.org/doi/10.1103/PhysRev.51.884.

[8] B. Pontecorvo, "Electron and Muon Neutrinos," *Zh. Eksp. Teor. Fiz.*, vol. 37, pp. 1751–1757, 1959.

[9] G. Danby *et al.*, "Observation of high-energy neutrino reactions and the existence of two kinds of neutrinos," *Physical Review Letters*, vol. 9, no. 1, p. 36, 1962, https://link.aps.org/doi/10.1103/PhysRevLett.9.36.

[10] K. Kodama *et al.*, "Observation of tau neutrino interactions," *Physics Letters B*, vol. 504, no. 3, pp. 218–224, 2001, https://doi.org/10.1016/S0370-2693(01)00307-0.

[11] T. L. Collaborations, "Electroweak parameters of the z0 resonance and the standard model," *Physics Letters B*, vol. 276, no. 1-2, pp. 247–253, 1992, https://doi.org/10.1016/0370-2693(92)90572-L.

[12] B. Pontecorvo, "Mesonium and antimesonium," *Soviet Journal of Experimental and Theoretical Physics*, vol. 6, p. 429, 1958.

[13] J. Bahcall, A. M. Serenelli, and S. Basu, "New solar opacities, abundances, helioseismology, and neutrino fluxes," *The Astrophysical Journal*, vol. 621, no. 1, p. L85, 2005, https://doi.org/10.1086/428929.

[14] A. Serenelli, "Alive and well: a short review about standard solar models," *The European Physical Journal A*, vol. 52, no. 4, p. 78, 2016, http://doi.org/10.1140/epja/i2016-16078-1.

[15] R. Davis, D. S. Harmer, and K. C. Hoffman, "Search for neutrinos from the sun," *Phys. Rev. Lett.*, vol. 20, pp. 1205–1209, May 1968, https://link.aps.org/doi/10.1103/PhysRevLett.20.1205.

[16] J. N. Bahcall, "Solar neutrinos. i. theoretical," *Phys. Rev. Lett.*, vol. 12, pp. 300–302, Mar 1964, https://link.aps.org/doi/10.1103/PhysRevLett.12.300.

[17] L. Wolfenstein, "Neutrino oscillations in matter," *Phys. Rev. D*, vol. 17, pp. 2369–2374, May 1978, https://link.aps.org/doi/10.1103/PhysRevD.17.2369.

[18] K. S. Hirata *et al.*, "Observation of a small atmospheric v$\mu$/ve ratio in Kamiokande," *Physics Letters B*, vol. 280, no. 1-2, pp. 146–152, 1992, https://doi.org/10.1016/0370-2693(92)90788-6.

[19] S. Fukuda *et al.*, "Determination of solar neutrino oscillation parameters using 1496 days of super-kamiokande-i data," *Physics Letters B*, vol. 539, no. 3, pp. 179–187, 2002, https://www.sciencedirect.com/science/article/pii/S0370269302020907.

[20] P. Anselmann *et al.*, "Solar neutrinos observed by gallex at gran sasso," *Physics Letters B*, vol. 285, no. 4, pp. 376–389, 1992, https://doi.org/10.1016/0370-2693(92)91521-A.

[21] J. N. Abdurashitov *et al.*, "Measurement of the solar neutrino capture rate with gallium metal," *Phys. Rev. C*, vol. 60, p. 055801, Oct 1999, https://link.aps.org/doi/10.1103/PhysRevC.60.055801.

[22] J. Boger *et al.*, "The sudbury neutrino observatory," *Nuclear Instruments and Methods in Physics Research Section A: Accelerators, Spectrometers, Detectors and Associated Equipment*, vol. 449, no. 1-2, pp. 172–207, 2000, https://doi.org/10.1016/S0168-9002(99)01469-2.

[23] Q. R. Ahmad *et al.*, "Measurement of the Rate of $\nu_e + d \rightarrow p + p + e^-$ Interactions Produced by $^8B$ Solar Neutrinos at the Sudbury Neutrino Observatory," *Phys. Rev. Lett.*, vol. 87, p. 071301, Jul 2001, https://link.aps.org/doi/10.1103/PhysRevLett.87.071301.

[24] Nobelprize.org, "The chameleons of space," *Physics Letters B*, Oct 2015, https://www.nobelprize.org/nobel_prizes/physics/laureates/2015/popularphysicsprize2015.pdf.

[25] B. Aharmim *et al.*, "Independent measurement of the total active B 8 solar neutrino flux using an array of He 3 proportional counters at the sudbury neutrino observatory," *Physical Review Letters*, vol. 101, no. 11, p. 111301, 2008, https://link.aps.org/doi/10.1103/PhysRevLett.101.111301.

[26] R. Becker-Szendy *et al.*, "Search for muon neutrino oscillations with the Irvine-Michigan-Brookhaven detector," *Phys. Rev. Lett.*, vol. 69, pp. 1010–1013, Aug 1992, https://link.aps.org/doi/10.1103/PhysRevLett.69.1010.

[27] Y. Fukuda *et al.*, "Evidence for oscillation of atmospheric neutrinos," *Phys. Rev. Lett.*, vol. 81, pp. 1562–1567, Aug 1998, https://link.aps.org/doi/10.1103/PhysRevLett.81.1562.

[28] M. C. Gonzalez-Garcia and Y. Nir, "Neutrino masses and mixing: evidence and implications," *Rev. Mod. Phys.*, vol. 75, pp. 345–402, Mar 2003, https://link.aps.org/doi/10.1103/RevModPhys.75.345.

[29] P. W. Higgs, "Broken symmetries and the masses of gauge bosons," *Phys. Rev. Lett.*, vol. 13, pp. 508–509, Oct 1964, https://link.aps.org/doi/10.1103/PhysRevLett.13.508.

[30] K. Zuber, *Neutrino physics*. Taylor & Francis, 2020, https://doi.org/10.1201/9781315195612.

[31] J. Hewett *et al.*, "Fundamental physics at the intensity frontier," *arXiv preprint arXiv:1205.2671*, 2012, https://doi.org/10.48550/arXiv.1205.2671.

[32] R. P. Feynman, "Very high-energy collisions of hadrons," *Phys. Rev. Lett.*, vol. 23, pp. 1415–1417, Dec 1969, https://link.aps.org/doi/10.1103/PhysRevLett.23.1415.

[33] R. L. Workman and Others, "Review of Particle Physics," *PTEP*, vol. 2022, p. 083C01, 2022, https://academic.oup.com/ptep/article/2022/8/083C01/6651666.

[34] C. Giunti and C. W. Kim, *Fundamentals of neutrino physics and astrophysics*. Oxford university press, 2007, https://global.oup.com/academic/product/fundamentals-of-neutrino-physics-and-astrophysics-9780198508717.

[35] P. A. Machado, "Neutrino properties and interactions," *arXiv preprint arXiv:2206.13449*, 2022, https://doi.org/10.48550/arXiv.2206.13449.

[36] A. Y. Smirnov, "The msw effect and solar neutrinos," *arXiv preprint hep-ph/0305106*, 2003, https://doi.org/10.48550/arXiv.hep-ph/0305106.

[37] A. de Gouvêa *et al.*, "Neutrinos," *arXiv preprint arXiv:1310.4340*, 2013, https://doi.org/10.48550/arXiv.1310.4340.

[38] K. S Hirata. *et al.*, "Observation of $^8$B solar neutrinos in the kamiokande-ii detector," *Phys. Rev. Lett.*, vol. 63, pp. 16–19, Jul 1989, https://link.aps.org/doi/10.1103/PhysRevLett.63.16.

[39] K. Abe *et al.*, "Solar neutrino measurements in Super-Kamiokande-IV," *Phys. Rev. D*, vol. 94, p. 052010, Sep 2016, https://link.aps.org/doi/10.1103/PhysRevD.94.052010.

[40] S. Fukuda *et al.*, "Solar $^8b$ and hep neutrino measurements from 1258 days of super-kamiokande data," *Phys. Rev. Lett.*, vol. 86, pp. 5651–5655, Jun 2001, https://link.aps.org/doi/10.1103/PhysRevLett.86.5651.

[41] Q. R. Ahmad *et al.*, "Direct evidence for neutrino flavor transformation from neutral-current interactions in the sudbury neutrino observatory," *Phys. Rev. Lett.*, vol. 89, p. 011301, Jun 2002, https://link.aps.org/doi/10.1103/PhysRevLett.89.011301.

[42] B. Aharmim *et al.*, "Electron energy spectra, fluxes, and day-night asymmetries of $^8$b solar neutrinos from measurements with nacl dissolved in the heavy-water detector at the sudbury neutrino observatory," *Phys. Rev. C*, vol. 72, p. 055502, Nov 2005, https://link.aps.org/doi/10.1103/PhysRevC.72.055502.

[43] C. Arpesella *et al.*, "First real time detection of 7be solar neutrinos by borexino," *Physics Letters B*, vol. 658, no. 4, pp. 101–108, 2008, https://doi.org/10.1016/j.physletb.2007.09.054.

[44] J. Bergström *et al.*, "Updated determination of the solar neutrino fluxes from solar neutrino data," *Journal of High Energy Physics*, vol. 2016, no. 3, pp. 1–19, 2016, http://doi.org/10.1007/JHEP03(2016)132.

[45] S. R. Elliott, V. Gavrin, and W. Haxton, "The Gallium Anomaly," *arXiv preprint arXiv:2306.03299*, 2023, https://doi.org/10.48550/arXiv.2306.03299.

[46] M. Apollonio *et al.*, "Search for neutrino oscillations on a long base-line at the chooz nuclear power station," *The European Physical Journal C-Particles and Fields*, vol. 27, pp. 331–374, 2003, http://doi.org/10.1140/epjc/s2002-01127-9.

[47] F. Boehm *et al.*, "Final results from the palo verde neutrino oscillation experiment," *Phys. Rev. D*, vol. 64, p. 112001, Nov 2001, https://link.aps.org/doi/10.1103/PhysRevD.64.112001.

[48] Y. Ashie *et al.*, "Measurement of atmospheric neutrino oscillation parameters by super-kamiokande i," *Phys. Rev. D*, vol. 71, p. 112005, Jun 2005. [Online]. Available: https://link.aps.org/doi/10.1103/PhysRevD.71.112005

[49] M. Ambrosio, R. Antolini, G. Auriemma, D. Bakari, A. Baldini, G. Barbarino, B. Barish, G. Battistoni, Y. Becherini, R. Bellotti *et al.*, "Matter effects in upward-going muons and sterile neutrino oscillations," *Physics Letters B*, vol. 517, no. 1-2, pp. 59–66, 2001, https://doi.org/10.1016/S0370-2693(01)00992-3.

[50] M. Sanchez *et al.*, "Measurement of the L/E distributions of atmospheric $\nu$ in Soudan 2 and their interpretation as neutrino oscillations," *Phys. Rev. D*, vol. 68, p. 113004, Dec 2003, https://link.aps.org/doi/10.1103/PhysRevD.68.113004.

[51] W. W. M. Allison *et al.*, "Neutrino oscillation effects in soudan 2 upward-stopping muons," *Phys. Rev. D*, vol. 72, p. 052005, Sep 2005, https://link.aps.org/doi/10.1103/PhysRevD.72.052005.

[52] Z. Li *et al.*, "Measurement of the tau neutrino cross section in atmospheric neutrino oscillations with super-kamiokande," *Phys. Rev. D*, vol. 98, p. 052006, Sep 2018, https://link.aps.org/doi/10.1103/PhysRevD.98.052006.

[53] N. Agafonova *et al.*, "Erratum: Final results of the opera experiment on $\nu_\tau$ appearance in the cngs neutrino beam [phys. rev. lett. 120, 211801 (2018)]," *Phys. Rev. Lett.*, vol. 121, p. 139901, Sep (2018), https://link.aps.org/doi/10.1103/PhysRevLett.121.139901.

[54] M. G. Aartsen *et al.*, "Measurement of atmospheric tau neutrino appearance with icecube deepcore," *Phys. Rev. D*, vol. 99, p. 032007, Feb 2019, https://link.aps.org/doi/10.1103/PhysRevD.99.032007.

[55] A. Albert, M. André, M. Anghinolfi, G. Anton, M. Ardid, J.-J. Aubert, J. Aublin, T. Avgitas, B. Baret, J. Barrios-Martí *et al.*, "Measuring the atmospheric neutrino oscillation parameters and constraining the 3+ 1 neutrino model with ten years of antares data," *Journal of High Energy Physics*, vol. 2019, no. 6, pp. 1–23, 2019, http://doi.org/10.1007/JHEP06(2019)113.

[56] M. G. Aartsen *et al.*, "Measurement of atmospheric neutrino oscillations at 6–56 gev with icecube deepcore," *Phys. Rev. Lett.*, vol. 120, p. 071801, Feb 2018, https://link.aps.org/doi/10.1103/PhysRevLett.120.071801.

[57] S. Adrian-Martinez *et al.*, "Letter of intent for km3net 2.0," *Journal of Physics G: Nuclear and Particle Physics*, vol. 43, no. 8, p. 084001, 2016, http://doi.org/10.1088/0954-3899/43/8/084001.

[58] M.G Aartsen *et al.*, "IceCube-Gen2: the window to the extreme universe," *Journal of Physics G: Nuclear and Particle Physics*, vol. 48, no. 6, p. 060501, 2021, http://doi.org/10.1088/1361-6471/abbd48.

[59] A. Kumar *et al.*, "Invited review: Physics potential of the ical detector at the india-based neutrino observatory (ino)," *Pramana*, vol. 88, pp. 1–72, 2017, http://doi.org/10.1007/s12043-017-1373-4.

[60] K. Abe *et al.*, "Hyper-kamiokande design report," *arXiv:1805.04163*, 2018, https://doi.org/10.48550/arXiv.1805.04163.

[61] B. Abi *et al.*, "Volume i. introduction to dune," *Journal of instrumentation*, vol. 15, no. 08, p. T08008, 2020, http://doi.org/10.1088/1748-0221/15/08/T08008.

[62] K. Eguchi *et al.*, "First results from kamland: Evidence for reactor antineutrino disappearance," *Phys. Rev. Lett.*, vol. 90, p. 021802, Jan 2003, https://link.aps.org/doi/10.1103/PhysRevLett.90.021802.

[63] A. Suzuki, "Antineutrino science in kamland," *The European Physical Journal C*, vol. 74, pp. 1–27, 2014, https://link.springer.com/article/10.1140/epjc/s10052-014-3094-x.

[64] Y. Abe *et al.*, "Indication of reactor $\overline{\nu}_e$ disappearance in the double chooz experiment," *Phys. Rev. Lett.*, vol. 108, p. 131801, Mar 2012, https://link.aps.org/doi/10.1103/PhysRevLett.108.131801.

[65] F.P. An *et al.*, "Observation of electron-antineutrino disappearance at daya bay," *Phys. Rev. Lett.*, vol. 108, p. 171803, Apr 2012, https://link.aps.org/doi/10.1103/PhysRevLett.108.171803.

[66] J.K. Ahn *et al.*, "Observation of reactor electron antineutrinos disappearance in the reno experiment," *Phys. Rev. Lett.*, vol. 108, p. 191802, May 2012, https://link.aps.org/doi/10.1103/PhysRevLett.108.191802.

[67] Z. Atif *et al.*, "Search for sterile neutrino oscillations using reno and neos data," *Physical Review D*, vol. 105, no. 11, p. L111101, 2022, https://journals.aps.org/prd/abstract/10.1103/PhysRevD.105.L111101.

[68] F. An *et al.*, "Neutrino physics with juno," *Journal of Physics G: Nuclear and Particle Physics*, vol. 43, no. 3, p. 030401, 2016, http://doi.org/10.1088/0954-3899/43/3/030401.

[69] T. A. Mueller *et al.*, "Improved predictions of reactor antineutrino spectra," *Physical Review C*, vol. 83, no. 5, p. 054615, 2011, https://doi.org/10.1103/PhysRevC.83.054615.

[70] P. Huber, "Determination of antineutrino spectra from nuclear reactors," *Physical Review C*, vol. 84, no. 2, p. 024617, 2011, https://doi.org/10.1103/PhysRevC.84.024617.

[71] G. Mention *et al.*, "Reactor antineutrino anomaly," *Phys. Rev. D*, vol. 83, p. 073006, Apr 2011, https://link.aps.org/doi/10.1103/PhysRevD.83.073006.

[72] C. Giunti, Y. Li, C. A. Ternes, and Z. Xin, "Reactor antineutrino anomaly in light of recent flux model refinements," *Physics Letters B*, vol. 829, p. 137054, 2022, https://doi.org/10.1016/j.physletb.2022.137054.

[73] M. Danilov and N. Skrobova, "New results from the DANSS experiment," *PoS*, vol. EPS-HEP2021, p. 241, 2022, https://doi.org/10.22323/1.398.0241.

[74] L.-R. Labit and the Stereo collaboration, "The Stereo search for a sterile neutrino at the ILL reactor with full data sample," in *Journal of Physics: Conference Series*, vol. 2156, no. 1. IOP Publishing, 2021, p. 012156, https://iopscience.iop.org/article/10.1088/1742-6596/2156/1/012156.

[75] M. Andriamirado *et al.*, "Improved short-baseline neutrino oscillation search and energy spectrum measurement with the prospect experiment at hfir," *Physical Review D*, vol. 103, no. 3, p. 032001, 2021, https://journals.aps.org/prd/abstract/10.1103/PhysRevD.103.032001.

[76] A.P. Serebrov *et al.*, "Search for sterile neutrinos with the neutrino-4 experiment and measurement results," *Physical Review D*, vol. 104, no. 3, p. 032003, 2021, https://journals.aps.org/prd/abstract/10.1103/PhysRevD.104.032003.

[77] A. Serebrov, R. Samoilov, M. Chaikovskii, and O. Zherebtsov, "The result of the Neutrino-4 experiment, sterile neutrinos and dark matter, the fourth neutrino and the Hubble constant," *arXiv preprint arXiv:2302.09958*, 2023, https://doi.org/10.48550/arXiv.2302.09958.

[78] D. Beavis, A. Carroll, and I. Chiang, "Long baseline neutrino oscillation experiment at the ags," *Physics Design Report Brookhaven National Lab*, (1995), https://doi.org/10.2172/52878.

[79] M. H. Ahn *et al.*, "Measurement of neutrino oscillation by the k2k experiment," *Phys. Rev. D*, vol. 74, p. 072003, Oct (2006), https://link.aps.org/doi/10.1103/PhysRevD.74.072003.

[80] P. Adamson *et al.*, "Combined analysis of $\nu_\mu$ disappearance and $\nu_\mu \to \nu_e$ appearance in minos using accelerator and atmospheric neutrinos," *Phys. Rev. Lett.*, vol. 112, p. 191801, May (2014), https://link.aps.org/doi/10.1103/PhysRevLett.112.191801.

[81] C. Rubbia *et al.*, "Underground operation of the icarus t600 lar-tpc: first results," *Journal of Instrumentation*, vol. 6, no. 07, p. P07011, (2011), http://doi.org/10.1088/1748-0221/6/07/P07011.

[82] K. Abe *et al.*, "Observation of electron neutrino appearance in a muon neutrino beam," *Phys. Rev. Lett.*, vol. 112, p. 061802, Feb 2014, https://link.aps.org/doi/10.1103/PhysRevLett.112.061802.

[83] K. Abe *et al.*, "Improved constraints on neutrino mixing from the T2K experiment with $3.13 \times 10^{21}$ protons on target," *Phys. Rev. D*, vol. 103, Jun 2021, https://link.aps.org/doi/10.1103/PhysRevD.103.112008.

[84] P. Adamson *et al.*, "Constraints on oscillation parameters from $\nu_e$ appearance and $\nu_\mu$ disappearance in nova," *Phys. Rev. Lett.*, vol. 118, p. 231801, Jun 2017, https://link.aps.org/doi/10.1103/PhysRevLett.118.231801.

[85] M. A. Acero *et al.*, "First measurement of neutrino oscillation parameters using neutrinos and antineutrinos by nova," *Phys. Rev. Lett.*, vol. 123, p. 151803, Oct 2019, https://link.aps.org/doi/10.1103/PhysRevLett.123.151803.

[86] C. Athanassopoulos *et al.*, "The liquid scintillator neutrino detector and lampf neutrino source," *Nuclear Instruments and Methods in Physics Research Section A: Accelerators, Spectrometers, Detectors and Associated Equipment*, vol. 388, no. 1-2, pp. 149–172, (1997), https://doi.org/10.1016/S0168-9002(96)01155-2.

[87] B. Louis, V. Sandberg, and H. White, "A thousand eyes: The story of LSND," *Los Alamos Sci.*, vol. 25, pp. 92–115, 1997, https://sgp.fas.org/othergov/doe/lanl/pubs/00326610.pdf.

[88] A. A. Aguilar-Arevalo *et al.*, "Evidence for neutrino oscillations from the observation of $\overline{\nu}_e$ appearance in a $\overline{\nu}_\mu$ beam," *Phys. Rev. D*, vol. 64, p. 112007, Nov (2001), https://link.aps.org/doi/10.1103/PhysRevD.64.112007.

[89] I. Gil-Botella, "Neutrino physics," *arXiv preprint arXiv:1504.03551*, 2015, https://cds.cern.ch/record/2008969.

[90] M. Antonello *et al.*, "Experimental search for the "lsnd anomaly" with the icarus detector in the cngs neutrino beam," *The European Physical Journal C*, vol. 73, pp. 1–9, 2013, https://doi.org/10.1140/epjc/s10052-013-2345-6.

[91] A. Aguilar-Arevalo *et al.*, "The miniboone detector," *Nucl. Instrum. Meth. A*, vol. 599, pp. 28–46, (2009), https://doi.org/10.1016/j.nima.2008.10.028.

[92] T. Katori and J. Conrad, "Beyond Standard Model Searches in the MiniBooNE Experiment," *Adv. High Energy Phys.*, (2015), https://doi.org/10.48550/arXiv.1404.7759.

[93] A. A. Aguilar-Arevalo *et al.*, "Search for electron neutrino appearance at the $\Delta m^2 \sim 1\ \mathrm{eV}^2$ scale," *Phys. Rev. Lett.*, vol. 98, Jun (2007), https://link.aps.org/doi/10.1103/PhysRevLett.98.231801.

[94] A. Aguilar-Arevalo *et al.*, "Updated MiniBooNE neutrino oscillation results with increased data and new background studies," *Physical Review D*, vol. 103, no. 5, (2021), https://doi.org/10.1103/PhysRevD.103.052002.

[95] A. A. Aguilar-Arevalo *et al.*, "Significant excess of electronlike events in the miniboone short-baseline neutrino experiment," *Physical review letters*, vol. 121, no. 22, (2018), https://doi.org/10.1103/PhysRevLett.121.221801.

[96] H. Chen *et al.*, "Proposal for a New Experiment Using the Booster and NuMI Neutrino Beamlines: MicroBooNE," *Fermilab Proposal*, Oct (2007), https://lss.fnal.gov/archive/test-proposal/0000/fermilab-proposal-0974.pdf.

[97] R. Acciarri *et al.*, "A proposal for a three detector short-baseline neutrino oscillation program in the fermilab booster neutrino beam," *arXiv preprint arXiv:1503.01520*, (2015), https://doi.org/10.48550/arXiv.1503.01520.

[98] F. Capozzi, E. Lisi, A. Marrone, and A. Palazzo, "Current unknowns in the three-neutrino framework," *Progress in Particle and Nuclear Physics*, vol. 102, pp. 48–72, 2018, https://doi.org/10.1016/j.ppnp.2018.05.005.

[99] M. o. Aker, "Improved upper limit on the neutrino mass from a direct kinematic method by katrin," *Phys. Rev. Lett.*, vol. 123, p. 221802, Nov 2019, https://link.aps.org/doi/10.1103/PhysRevLett.123.221802.

[100] M. Agostini *et al.*, "Final results of gerda on the search for neutrinoless double-$\beta$ decay," *Phys. Rev. Lett.*, vol. 125, p. 252502, Dec 2020, https://link.aps.org/doi/10.1103/PhysRevLett.125.252502.

[101] N. Abgrall *et al.*, "Legend-1000 preconceptual design report," *arXiv preprint arXiv:2107.11462*, 2021, https://arxiv.org/abs/2107.11462.

[102] A. o. Gando, "Search for majorana neutrinos near the inverted mass hierarchy region with kamland-zen," *Phys. Rev. Lett.*, vol. 117, p. 082503, Aug 2016, https://link.aps.org/doi/10.1103/PhysRevLett.117.082503.

[103] V. Albanese *et al.*, "The sno+ experiment," *Journal of Instrumentation*, vol. 16, no. 08, p. P08059, aug 2021, https://dx.doi.org/10.1088/1748-0221/16/08/P08059.

[104] G. Anton *et al.*, "Search for neutrinoless double-$\beta$ decay with the complete exo-200 dataset," *Phys. Rev. Lett.*, vol. 123, p. 161802, Oct 2019, https://link.aps.org/doi/10.1103/PhysRevLett.123.161802.

[105] A. Simón *et al.*, "Boosting background suppression in the next experiment through richardson-lucy deconvolution," *Journal of High Energy Physics*, vol. 2021, no. 7, 2021, https://doi.org/10.1007/JHEP07(2021)146.

[106] M. A. Acero *et al.*, "White paper on light sterile neutrino searches and related phenomenology," *arXiv preprint arXiv:2203.07323*, 2022, https://arxiv.org/abs/2203.07323v2.

[107] M. Dentler, Á. Hernández-Cabezudo, J. Kopp, P. Machado, M. Maltoni, I. Martinez-Soler, and T. Schwetz, "Updated global analysis of neutrino oscillations in the presence of ev-scale sterile neutrinos," *Journal of High Energy Physics*, vol. 2018, no. 8, pp. 1–35, 2018, https://link.springer.com/article/10.1007/JHEP08(2018)010.

[108] M. Maltoni, T. Schwetz, M. Tortola, and J. Valle, "Ruling out four-neutrino oscillation interpretations of the LSND anomaly?" *Nuclear Physics B*, vol. 643, no. 1-3, pp. 321–338, 2002, https://doi.org/10.1016/S0550-3213(02)00747-2.

[109] P. Abratenko *et al.*, "Search for an excess of electron neutrino interactions in microboone using multiple final-state topologies," *Phys. Rev. Lett.*, vol. 128, p. 241801, Jun 2022, https://link.aps.org/doi/10.1103/PhysRevLett.128.241801.

[110] P. Abratenko *et al.*, "First Constraints on Light Sterile Neutrino Oscillations from Combined Appearance and Disappearance Searches with the MicroBooNE Detector," *Phys. Rev. Lett., American Physical Society*, vol. 130, p. 011801, Jan 2023, https://link.aps.org/doi/10.1103/PhysRevLett.130.011801.

[111] P. A. Machado, O. Palamara, and D. W. Schmitz, "The short-baseline neutrino program at fermilab," *Annual Review of Nuclear and Particle Science*, vol. 69, pp. 363–387, 2019, https://doi.org/10.48550/arXiv.1903.04608.

[112] C. Adams *et al.*, "First measurement of $\nu_\mu$ charged-current $\pi^0$ production on argon with a *lartpc*," *arXiv preprint arXiv:1811.02700*, 2018, https://doi.org/10.48550/arXiv.1503.01520.

[113] P. Abratenko *et al.*, "First measurement of inclusive muon neutrino charged current differential cross sections on argon at e $\nu$ 0.8 gev with the microboone detector," *Physical review letters*, vol. 123, no. 13, p. 131801, 2019, https://link.aps.org/doi/10.1103/PhysRevLett.123.131801.

[114] R. Ainsworth, P. Adamson, B. C. Brown, D. Capista, K. Hazelwood, I. Kourbanis, D. K. Morris, M. Xiao, and M.-J. Yang, "High intensity operation using proton stacking in the fermilab recycler to deliver 700 kw of 120 gev proton beam," *Phys. Rev. Accel. Beams*, vol. 23, p. 121002, Dec 2020, https://link.aps.org/doi/10.1103/PhysRevAccelBeams.23.121002.

[115] A. A. Aguilar-Arevalo *et al.*, "Neutrino flux prediction at miniboone," *Phys. Rev. D*, vol. 79, p. 072002, Apr 2009, https://link.aps.org/doi/10.1103/PhysRevD.79.072002.

[116] M. Catanesi *et al.*, "Particle identification algorithms for the harp forward spectrometer," *Nuclear Instruments and Methods in Physics Research Section A: Accelerators, Spectrometers, Detectors and Associated Equipment*, vol. 572, no. 2, pp. 899–921, 2007, https://doi.org/10.1016/j.nima.2006.11.071.

[117] J. N. Marx and D. R. Nygren, "The Time Projection Chamber," *Physics Today*, vol. 31, no. 10, pp. 46–53, 10 1978, https://doi.org/10.1063/1.2994775.

[118] C. Rubbia, "The liquid-argon time projection chamber: a new concept for neutrino detectors," *Technical report, CERN, Geneva*, 1977, https://cds.cern.ch/record/117852/files/CERN-EP-INT-77-8/.

[119] B. Abi *et al.*, "Deep underground neutrino experiment (dune), far detector technical design report, volume ii: Dune physics," *arXiv preprint arXiv:2002.03005*, 2020, https://doi.org/10.48550/arXiv.2002.03005.

[120] BNL group. (2023) Liquid argon properties (tables and calculators). Accessed: 1/12/2023. [Online]. Available: https://lar.bnl.gov/properties/

[121] D. Whittington, S. Mufson, and B. Howard, "Scintillation light from cosmic-ray muons in liquid argon," *Journal of Instrumentation*, vol. 11, no. 05, p. P05016, may 2016, https://dx.doi.org/10.1088/1748-0221/11/05/P05016.

[122] V. Boccone and (on behalf ofthe ArDM collaboration), "The ardm project: A liquid argon tpc for dark matter detection," *Journal of Physics: Conference Series*, vol. 160, no. 1, p. 012032, apr 2009, https://dx.doi.org/10.1088/1742-6596/160/1/012032.

[123] S. Amoruso *et al.*, "Study of electron recombination in liquid argon with the ICARUS TPC," *Nuclear Instruments and Methods in Physics Research Section A: Accelerators, Spectrometers, Detectors and Associated Equipment*, vol. 523, no. 3, pp. 275–286, 2004, https://www.sciencedirect.com/science/article/pii/S0168900204000506.

[124] R. Acciarri *et al.*, "Construction of precision wire readout planes for the short-baseline near detector (sbnd)," *Journal of instrumentation*, vol. 15, no. 06, p. P06033, 2020, https://iopscience.iop.org/article/10.1088/1748-0221/15/06/P06033.

[125] A. Machado *et al.*, "The x-arapuca: an improvement of the arapuca device," *Journal of instrumentation*, vol. 13, no. 04, p. C04026, 2018, https://iopscience.iop.org/article/10.1088/1748-0221/13/04/C04026.

[126] R. Acciarri, C. Adams, R. An, A. Aparicio, S. Aponte, J. Asaadi, M. Auger, N. Ayoub, L. Bagby, B. Baller *et al.*, "Design and construction of the microboone detector," *Journal of Instrumentation*, vol. 12, no. 02, p. P02017, 2017, https://doi.org/10.1088/1748-0221/12/02/P02017.

[127] C. Adams *et al.*, "Design and construction of the microboone cosmic ray tagger system," *Journal of instrumentation*, vol. 14, no. 04, p. P04004, 2019, https://doi.org/10.1088/1748-0221/14/04/P04004.

[128] P. Abratenko *et al.*, "First constraints on light sterile neutrino oscillations from combined appearance and disappearance searches with the microboone detector," *Physical review letters*, vol. 130, no. 1, p. 011801, 2023, https://link.aps.org/doi/10.1103/PhysRevLett.130.011801.

[129] P. Benetti *et al.*, "A three ton liquid argon time projection chamber," *Nucl. Instrum. Methods Phys. Res., A*, vol. 332, no. DFPD-93-EP-05, pp. 395–412, 1993, https://doi.org/10.1016/0168-9002(93)90297-U.

[130] F. Arneodo *et al.*, "Performance of the 10m3 icarus liquid argon prototype," *Nuclear Instruments and Methods in Physics Research Section A: Accelerators, Spectrometers, Detectors and Associated Equipment*, vol. 498, no. 1-3, pp. 292–311, 2003, https://doi.org/10.1016/S0168-9002(02)01989-7.

[131] S. Amerio *et al.*, "Design, construction and tests of the icarus t600 detector," *Nuclear Instruments and Methods in Physics Research Section A: Accelerators, Spectrometers, Detectors and Associated Equipment*, vol. 527, no. 3, pp. 329–410, 2004, https://doi.org/10.1016/j.nima.2004.02.044.

[132] M. Antonello *et al.*, "Experimental observation of an extremely high electron lifetime with the ICARUS-T600 LAr-TPC," *Journal of Instrumentation*, vol. 9, no. 12, p. P12006, 2014, https://iopscience.iop.org/article/10.1088/1748-0221/9/12/P12006.

[133] M. Antonello *et al.*, "Precise 3D track reconstruction algorithm for the ICARUS T600 liquid argon time projection chamber detector," *Advances in High Energy Physics*, vol. 2013, 2013, https://doi.org/10.1155/2013/260820.

[134] C. Farnese, "Some recent results from ICARUS," *AIP Conference Proceedings*, vol. 1666, no. 1, p. 110002, 07 2015, https://doi.org/10.1063/1.4915574.

[135] M. Antonello *et al.*, "Muon momentum measurement in ICARUS-T600 LAr-TPC via multiple scattering in few-GeV range," *Journal of Instrumentation*, vol. 12, no. 04, p. P04010, 2017, https://iopscience.iop.org/article/10.1088/1748-0221/12/04/P04010.

[136] C. Farnese, "Atmospheric neutrino search in the icarus t600 detector," *Universe*, vol. 5, no. 1, p. 17, 2019, https://doi.org/10.3390/universe5010017.

[137] B. Ali-Mohammadzadeh *et al.*, "Design and implementation of the new scintillation light detection system of icarus t600," *Journal of Instrumentation*, vol. 15, no. 10, p. T10007, 2020, https://iopscience.iop.org/article/10.1088/1748-0221/15/10/T10007.

[138] M. Bonesini *et al.*, "The laser diode calibration system of the icarus t600 detector at fnal," *Journal of Instrumentation*, vol. 15, no. 05, p. C05042, 2020, https://iopscience.iop.org/article/10.1088/1748-0221/15/05/C05042.

[139] L. Bagby *et al.*, "Overhaul and installation of the icarus-t600 liquid argon tpc electronics for the fnal short baseline neutrino program," *Journal of Instrumentation*, vol. 16, no. 01, p. P01037, 2021, https://iopscience.iop.org/article/10.1088/1748-0221/16/01/P01037.

[140] F. Poppi *et al.*, "The cosmic ray tagger system of the icarus detector at fermilab," *PoS ICHEP2022*, vol. 10, no. 1.414, p. 0580, 2022, https://pos.sissa.it/414/580/pdf.

[141] E. Snider and G. Petrillo, "LArSoft: toolkit for simulation, reconstruction and analysis of liquid argon TPC neutrino detectors," *Journal of Physics: Conference Series*, vol. 898, no. 4, p. 042057, oct 2017, https://dx.doi.org/10.1088/1742-6596/898/4/042057.

[142] S. Agostinelli *et al.*, "GEANT4 — a simulation toolkit," *Nuclear Instruments and Methods in Physics Research Section A: Accelerators, Spectrometers, Detectors and Associated Equipment*, vol. 506, no. 3, pp. 250–303, 2003, https://www.sciencedirect.com/science/article/pii/S0168900203013688.

[143] B. Behera *et al.*, "Cosmogenic background suppression at the ICARUS using a concrete overburden," in *Journal of Physics: Conference Series*, vol. 2156, no. 1, 2021, p. 012181, https://iopscience.iop.org/article/10.1088/1742-6596/2156/1/012181/meta.

[144] U. Kose *et al.*, "Icarus: new voyage to sterile neutrino search in the short baseline program," *PoS-Proceedings of Science*, vol. 395, 2021, https://pos.sissa.it/395/1071/pdf.

[145] P. Abratenko, A. Aduszkiewicz, F. Akbar, M. Artero-Pons, J. Asaadi, M. Aslin, M. Babicz, W. Badgett, L. Bagby, B. Baibussinov *et al.*, "ICARUS at the Fermilab Short-Baseline Neutrino program: initial operation," *The European Physical Journal C*, vol. 83, no. 6, p. 467, 2023, https://doi.org/10.1140/epjc/s10052-023-11610-y.

[146] R. Triozzi, "Study of the trigger system performance of the ICARUS T600 detector at Fermilab exposed to the Booster and NuMI neutrino beams," Master's thesis, Università degli studi di Padova, 2022, https://hdl.handle.net/20.500.12608/52881.

[147] J. Serrano *et al.*, "The white rabbit project," *CERN Document Server*, 2013, https://cds.cern.ch/record/1743073/files/thbl2.pdf.

[148] G. L. Raselli *et al.*, "Time calibration and synchronization of the scintillation light detection system in ICARUS-T600," 12 2023, https://www.osti.gov/biblio/2246780.

[149] K. Biery *et al.*, "artdaq: An event-building, filtering, and processing framework," *IEEE Transactions on Nuclear Science*, vol. 60, no. 5, pp. 3764–3771, 2013, https://ieeexplore.ieee.org/document/6495515.

[150] B. Baibussinov *et al.*, "A hardware implementation of Region-of-Interest selection in LArTPC for data reduction and triggering," *Journal of Instrumentation*, vol. 5, no. 12, p. P12006, 2010, https://dx.doi.org/10.1088/1748-0221/5/12/P12006.

[151] C. Adams *et al.*, "Ionization electron signal processing in single phase LArTPCs. Part I. Algorithm Description and quantitative evaluation with MicroBooNE simulation," *Journal of Instrumentation*, vol. 13, no. 07, p. P07006, jul 2018, https://dx.doi.org/10.1088/1748-0221/13/07/P07006.

[152] C. Adams *et al.*, "Ionization electron signal processing in single phase LArTPCs. Part II. Data/simulation comparison and performance in MicroBooNE," *Journal of Instrumentation*, vol. 13, no. 07, p. P07007, 2018.

[153] J. Marshall and M. Thomson, "The pandora software development kit for pattern recognition," *The European Physical Journal C*, vol. 75, pp. 1–16, 2015, https://arxiv.org/abs/1506.05348.

[154] R. Acciarri *et al.*, "The Pandora multi-algorithm approach to automated pattern recognition of cosmic-ray muon and neutrino events in the MicroBooNE detector," *The European Physical Journal C*, vol. 78, pp. 1–25, 2018, https://doi.org/10.48550/arXiv.1708.03135.

[155] A. Abed Abud *et al.*, "Reconstruction of interactions in the protodune-sp detector with pandora," *Eur. Phys. JC*, vol. 83, no. arXiv: 2206.14521, p. 618, 2023, https://doi.org/10.1140/epjc/s10052-023-11733-2.

[156] G. Putnam and D. W. Schmitz, "Diffusion Changes the Peak Value of Energy Loss Observed in a LArTPC," *arXiv preprint arXiv:2205.06745*, 2022, https://arxiv.org/pdf/2205.06745.

[157] P. Abratenko *et al.*, "Measurement of space charge effects in the MicroBooNE LArTPC using cosmic muons," *Journal of instrumentation*, vol. 15, no. 12, p. P12037, 2020, https://dx.doi.org/10.1088/1748-0221/15/12/P12037.

[158] R. Acciarri *et al.*, "A study of electron recombination using highly ionizing particles in the argoneut liquid argon tpc," *Journal of Instrumentation*, vol. 8, no. 08, p. P08005, 2013, https://iopscience.iop.org/article/10.1088/1748-0221/8/08/P08005.

[159] J. B. Birks, "Scintillations from Organic Crystals: Specific Fluorescence and Relative Response to Different Radiations," *Proceedings of the Physical Society. Section A*, vol. 64, no. 10, p. 874, oct 1951, https://dx.doi.org/10.1088/0370-1298/64/10/303.

[160] V. Cataudella, A. de Candia, G. D. Filippis, S. Catalanotti, M. Cadeddu, M. Lissia, B. Rossi, C. Galbiati, and G. Fiorillo, "Directional modulation of electron-ion pairs recombination in liquid argon," *Journal of Instrumentation*, vol. 12, no. 12, p. P12002, dec 2017, https://dx.doi.org/10.1088/1748-0221/12/12/P12002.

[161] R. Acciarri *et al.*, "First measurement of the cross section for $\nu$ $\mu$ and $\nu^-$ $\mu$ induced single charged pion production on argon using argoneut," *Physical Review D*, vol. 98, no. 5, p. 052002, 2018, https://doi.org/10.1103/PhysRevD.98.052002.

[162] D. E. Groom, N. V. Mokhov, and S. I. Striganov, "Muon stopping power and range tables 10 mev–100 tev," *Atomic Data and Nuclear Data Tables*, vol. 78, no. 2, pp. 183–356, 2001, https://doi.org/10.1006/adnd.2001.0861.

[163] M. Z. M.J. Berger, J.S. Coursey and J. Chang. Stopping-Power & Range Tables for Electrons, Protons, and Helium Ions. [Online]. Available: https://physics.nist.gov/PhysRefData/Star/Text/PSTAR.html

[164] C. o. Andreopoulos, "The genie neutrino monte carlo generator: physics and user manual," *arXiv preprint arXiv:1510.05494*, 2015, https://arxiv.org/abs/1510.05494.

[165] G. A. Miller, "Fermi Gas Model," *Nuclear Physics B - Proceedings Supplements*, vol. 112, no. 1, pp. 223–225, 2002, https://www.sciencedirect.com/science/article/pii/S0920563202017863.

[166] A. Bodek and J. L. Ritchie, "Fermi-motion effects in deep-inelastic lepton scattering from nuclear targets," *Phys. Rev. D*, vol. 23, pp. 1070–1091, Mar 1981, https://link.aps.org/doi/10.1103/PhysRevD.23.1070.

[167] J. Nieves, J. E. Amaro, and M. Valverde, "Inclusive quasielastic charged-current neutrino-nucleus reactions," *Phys. Rev. C*, vol. 70, p. 055503, Nov 2004, https://link.aps.org/doi/10.1103/PhysRevC.70.055503.

[168] L. o. Alvarez-Ruso, "Recent highlights from genie v3," *The European Physical Journal Special Topics*, pp. 1–19, 2021, https://doi.org/10.1140/epjs/s11734-021-00295-7.

[169] M. Roda, "Genie overview." Presented at Workshop on Neutrino Event Generators, 2023, https://indico.fnal.gov/event/57388/.

[170] M. Bonesini *et al.*, "An innovative technique for TPB deposition on convex window photomultiplier tubes," *Journal of Instrumentation*, vol. 13, no. 12, p. P12020, 2018, https://arxiv.org/abs/1807.07123.

[171] R. Veenhof, "Garfield, recent developments," *Nuclear Instruments and Methods in Physics Research Section A: Accelerators, Spectrometers, Detectors and Associated Equipment*, vol. 419, no. 2, pp. 726–730, 1998, https://doi.org/10.1016/S0168-9002(98)00851-1.

[172] M. Babicz *et al.*, "A particle detector that exploits Liquid Argon scintillation light," *Nuclear Instruments and Methods in Physics Research Section A: Accelerators, Spectrometers, Detectors and Associated Equipment*, vol. 958, p. 162421, 2020, https://www.sciencedirect.com/science/article/pii/S016890021930991X.

[173] C. M. Hilgenberg, "Cosmogenic background rejection for the sterile neutrino search with the short-baseline neutrino program far detector," Ph.D. dissertation, 1 2021, https://www.osti.gov/biblio/1827375.

[174] A. P. Furmanski and J. T. Sobczyk, "Neutrino energy reconstruction from one-muon and one-proton events," *Physical Review C*, vol. 95, no. 6, p. 065501, 2017, https://journals.aps.org/prc/abstract/10.1103/PhysRevC.95.065501.

[175] A. Bodek and T. Cai, "Removal energies and final state interaction in lepton nucleus scattering," *The European Physical Journal C*, vol. 79, pp. 1–23, 2019, https://doi.org/10.1140/epjc/s10052-019-6750-3.

[176] S. Software. Standard Record Github Repository. [Online]. Available: https://github.com/SBNSoftware/sbnanaobj/tree/develop/sbnanaobj/StandardRecord

[177] A. Heggestuen, "Light detection and cosmic rejection in the icarus lartpc at fermilab," *arXiv preprint arXiv:2312.05684*, 2023.

[178] D. Diretto, "Studies for the selection of the neutrino events collected in ICARUS T600 at FERMILAB," Master's thesis, Università degli studi di Padova, 2022, https://hdl.handle.net/20.500.12608/56463.

[179] J. Conrad and M. Shaevitz, "Sterile neutrinos: An introduction to experiments," *Adv. Ser. Direct. High Energy Phys*, vol. 28, pp. 391–442, 2018, https://arxiv.org/abs/1609.07803.

[180] M. Antonello *et al.*, "Study of space charge in the ICARUS T600 detector," *Journal of Instrumentation*, vol. 15, no. 07, p. P07001, jul 2020, https://dx.doi.org/10.1088/1748-0221/15/07/P07001.